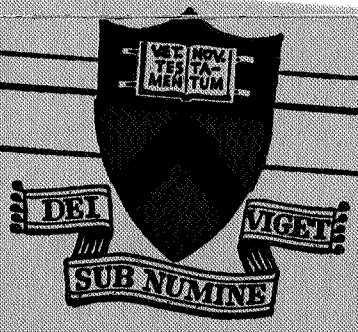

PRINCETON UNIVERSITY

DEPARTMENT OF AEROSPACE AND MECHANICAL SCIENCES

NATIONAL AERONAUTICS AND SPACE ADMINISTRATION

Research Grant NsG-306-63

AN INVESTIGATION OF CURRENT SHEET STRUCTURE IN A CYLINDRICAL Z-PINCH

Report No. 805*

Prepared by William R. Ellis, Jr.
William R. Ellis, Jr.

Approved by Robert G. Jahn
Robert G. Jahn
Professor and
Research Leader

*This report is a reproduction in entirety of the Ph.D. dissertation of Mr. William R. Ellis, Jr. It is submitted to the sponsor and to the distribution list in this form both as a presentation of the technical material, and as an indication of the academic program supported by this Grant.

July 1967

Guggenheim Laboratories for the Aerospace Propulsion Sciences
Department of Aerospace and Mechanical Sciences
PRINCETON UNIVERSITY
Princeton, New Jersey

ABSTRACT

The structure of the propagating current sheet in a large radius cylindrical pinch discharge is investigated experimentally at representative locations in the discharge chamber. Quantitative field measurements and current density distributions are obtained using conventional electric and magnetic probes. Electron number densities, temperatures and collision frequencies are measured with a microwave reflection probe developed for this application. This probe can return quantitative information with a spatial resolution of 2 mm over the density range $10^{12} < n_e < 10^{16}$ cm^{-3}.

The experimental data are related through appropriate continuum models to provide information on the mechanisms of gas acceleration and current conduction in the sheet. The sheet is found to have four interior zones wherein scalar or Hall conduction variously dominate, and ion current is found to be significant in two of these zones. Ionization profiles are obtained and a two step mechanism is suggested wherein initial photo-ionization is abetted by electron collisions. The velocity increase imparted during gas acceleration is found to be comparable with the sheet velocity, and the axial flow deflection is calculated to be small.

ACKNOWLEDGEMENTS

The author wishes to express his thanks and appreciation to all of those who have helped make this work possible. In particular,

To Professor Robert G. Jahn, whose insight and counsel were so essential to this effort.

To Professor Mark Heald of Swarthmore and Dr. Arnold Kelly of Princeton, for their help and comments on the manuscript.

To Mr. Bill Ernst of the Plasma Physics Laboratory, for many helpful discussions on microwave diagnostic problems.

To Mr. J. D. Tregurtha, for his indispensible assistance in the laboratory.

To the staff of the Guggenheim Laboratories for the Aerospace Propulsion Science, especially Mr. Lanny Hoffman of the Computing Group, Mr. Tony Poli and Mrs. Ann Jansak of the Design Group, and Mr. Don Neiler for photography.

To Miss Yolanda Pastor, for her special efforts in interpreting and typing an illegible manuscript.

To the other members of the Electric Propulsion Laboratory, for their camaraderie, support, patience, and many fruitful suggestions.

ACKNOWLEDGEMENTS (cont.)

Financial support for this work was provided by the National Aeronautics and Space Administration, under Grant NsG-306-63. The National Science Foundation is acknowledged for partial support of the computer facilities, under Grant NSF-GP579.

The author wishes especially to thank his parents, for their encouragement and many sacrifices; and his wife Maxcine, without whose devotion and assistance, through many turns of fortune, this work would never have been completed. To her this thesis is dedicated.

TABLE OF CONTENTS

(continued)

(continued)

LIST OF ILLUSTRATIONS

LIST OF ILLUSTRATIONS-cont'd

LIST OF ILLUSTRATIONS-con't

LIST OF ILLUSTRATIONS-con't

LIST OF ILLUSTRATIONS-cont'd

Chapter I

INTRODUCTION

1.1 Planetary Space Missions

A rocket in flight can often be described by the vector equation of motion[1]

$$m\dot{\bar{v}} = \dot{m}\bar{u}_e + \bar{F} \tag{1-1}$$

where $\bar{v}$ is the rocket velocity, m the rocket mass (including stored propellant), $\dot{m}$ the exhaust rate of propellant mass, $\bar{u}_e$ the velocity of the exhaust stream relative to the rocket, and $\bar{F}$ the vector sum of gravitational and aerodynamic forces acting on the rocket.

The first term on the right of eq. (1-1) is identified as the thrust of the rocket

$$\bar{T} = \dot{m}\bar{u}_e \tag{1-2}$$

and in the absence of comparable aerodynamic or gravitational forces the thrust program determines the rocket motion. For the case of constant exhaust velocity the equation of motion then integrates simply to yield

$$\bar{v}_o - \bar{v} = u_e \ln \frac{m_o}{m} \tag{1-3}$$

or conversely

$$\frac{m}{m_o} = \exp\left(-\frac{\Delta v}{u_e}\right) \tag{1-4}$$

This important equation was first derived by Tsiolkovskii

in 1895, and relates the instantaneous mass of the rocket to its instantaneous velocity, initial mass, and exhaust velocity. Eq. (1-4) emphasizes one of the major goals of good rocket performance: the higher the exhaust velocity the larger the deliverable mass for a given mission, all other things being equal.

Consider a mission from earth-orbit to Mars-orbit and return. Jahn[1] gives the typical velocity increment ΔV required for this minimal planetary mission as 14,000 meters per second, and clearly u_e must be comparable with this value to permit a reasonable ratio of final to initial rocket mass.

This requirement on exhaust velocity places even the modest planetary mission of this example beyond the reach of chemical rockets. Laboring under the triple handicaps of intrinsic energy limitation, frozen-flow losses, and tolerable rates of heat transfer to the reaction chamber and nozzle, the conventional chemical rocket can achieve at best a u_e of 3,000 - 5,000 meters per second. Various methods for relieving one or more of these limitations have been advanced, such as exotic fuel combinations, dual stream exhausts for peripheral cooling, nuclear or electrothermic heat sources, and so on. The most challenging of these concepts abandon conventional gas dynamics either completely or in part, and seek thrust producing mechanisms other than the nozzled expansion of heated propellant gas flows.

1.2 Electric Propulsion

Electrostatic and electromagnetic body forces are obvious

candidates for propulsion applications, and were suggested by Robert Goddard[2] as early as 1906 as a means for achieving "high velocity streams of negative and positive particles," i.e. ionized gas flows.

The electrostatic thruster is phenomenologically far simpler than its electromagnetic counterpart, and received a proportionally larger share of early developmental work. Indeed, the ion engine today is an engineering reality, flight-tested in a low-thrust application and comparatively well understood[3]. Electromagnetic thrusters by contrast are very complicated phenomenologically and still poorly understood in many essential features of their operation. Nonetheless this class of device shows perhaps the greatest promise of all presently envisaged space thrusters. The basis for their superiority over the ion engine rests with the inherently greater thrust density (thrust per unit area) which they can deliver. The stress associated with the electrostatic field is $\frac{\epsilon_0 E^2}{2}$, while for the magnetostatic field it is $\frac{B^2}{2\mu_0}$. Thus the stress associated with the rather extreme electric field of 10^7 volts per meter is found to be

$$\frac{\epsilon_0 E^2}{2} \cong 5 \times 10^2 \qquad \text{Newton/meter}^2 \quad \text{(MKS)}$$

while for the relatively modest 10 kilogauss (1 weber/meter^2) magnetic field,

$$\frac{B^2}{2\mu_0} \cong 5 \times 10^5 \qquad \text{Newton/meter}^2 \quad \text{(MKS)}$$

1.3 Electromagnetic Thrusters

Electromagnetic thrusters as a class utilize a combination of electric and magnetic body forces to accelerate a stream of ionized propellant gas to exhaust velocities. Jahn[1] has subdivided the class further to distinguish between steady and pulsed devices, induction and electrode-type devices, and so on, and these vary in their utility for propulsion. The electrodeless machines, for example, such as theta pinch or traveling wave accelerators, have traditionally been troubled by their inability to maintain tight coupling between the fields and the plasma.

Among the electrode-type machines, the (steady) MPD, or magnetoplasmadynamic, arc has generated a great deal of interest by combining high efficiency and exhaust velocity with acceptable levels of electrode erosion. These hybrid arc-jets are relative newcomers (1964) to the propulsion field, however. Their operation is not well understood, and the diagnostic problem is complicated by the destructive, hot, plasma environment in their exhaust plume.

Pulsed plasma accelerators rely upon the interaction of the discharge current with the prevailing local magnetic field to accelerate the plasma in the current zone to exhaust velocities via the resulting $\overline{J} \times \overline{B}$ body forces. (This use of the term "$\overline{J} \times \overline{B}$ forces" in a sense invokes a generic description of a complex field-plasma interaction which can also be consistently described from the particle point of view.) Since the thrust from $\overline{J} \times \overline{B}$ self-field interactions scales quadratically with the arc current, pulsed devices which exploit intermittent

operation to achieve very high current densities for short periods of time can produce useful average thrust without consuming their electrodes.

Three further benefits immediately accrue from pulsed operation. First, the high tolerable levels of current density generate very large self-magnetic fields, and the interaction of the discharge current with its own self-magnetic field is usually sufficient to generate ample thrust without recourse to external magnets and their considerable weight penalty. Second, the transient plasma will usually tolerate internal diagnostic probes for at least the duration of one pulse, simplifying the diagnostic problem. And third, unsteady electromagnetic fields in the plasma can be very useful, the most striking example being the development of a "skin" effect wherein the arc current is constrained to flow in favored geometrical locations, thus further intensifying and localizing the current density.

Figure 1-1 illustrates several geometries which have been developed to exploit $\overline{J} \times \overline{B}$ acceleration of plasmas. While all of these devices will accelerate the gaseous plasma in the current zone, they are not however all equally adaptable to either space thruster applications or laboratory diagnostics. The button gun and rail accelerator are not well suited to experimental purposes because of the strong three-dimensional nature of the $\overline{J} \times \overline{B}$ forces involved. The parallel plate accelerator suffers from flux leakage and other end effect problems, and the coaxial accelerator is complicated by severe geometrical variation of parameters across its radial current sheet. The

FIGURE 1-1

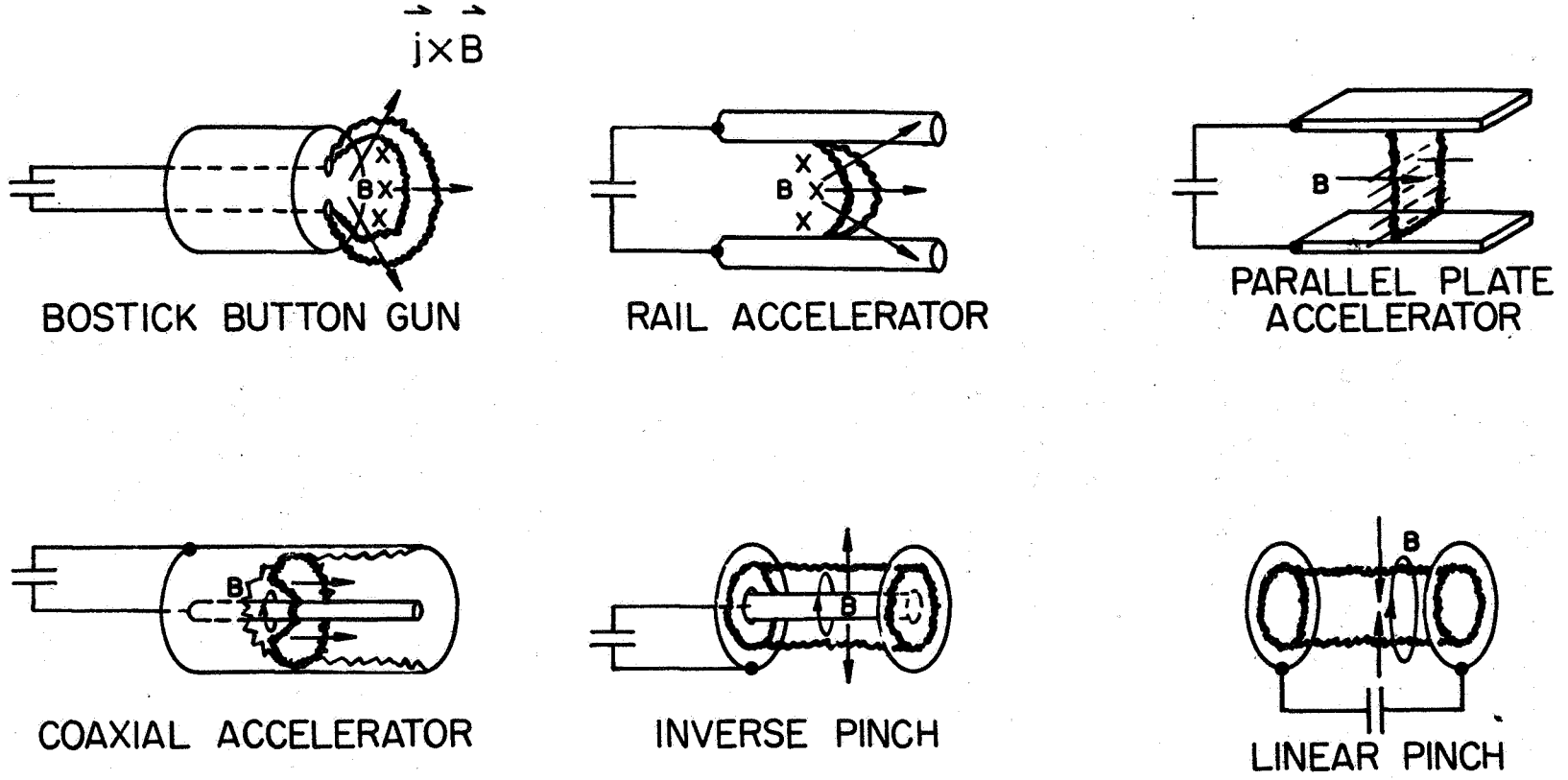

PULSED PLASMA ACCELERATOR GEOMETRIES

remaining two devices are closely related and both the inverse pinch and the direct, or linear pinch develop self-pinching discharges as their names imply. The distinction is between exploding and imploding discharges, the latter situation being more suitable for the production of high thrust densities.

The device chosen for basic studies[4,5,6] at the Electric Propulsion Laboratory at Princeton University, and on which the experiments to be described here were carried out, was a linear (or zeta) pinch machine. The foregoing discussion should make it clear, however, that phenomena associated with one device are in many cases common to all. Among the virtues of the linear pinch geometry not already mentioned are its "endless" current sheet which precludes magnetic flux losses, an approximate two-dimensional geometry, and simplicity of design. An elementary thruster configuration can be achieved simply by supplying a nozzled gas outlet in the center of one electrode.

As a practical matter, the exhausting of a plasma blob which has been accelerated by, and is energetically tied to, a complex ensemblage of electromagnetic fields is far from being a trivial affair. In fact it can be considered as one phase of a three component problem, the first two areas of which deal with discharge initiation and the plasma acceleration process. Recent investigations at Princeton have concentrated on the exhaust phase and are described in references 7 and 8. It is to the second category that this work will primarily address itself, and thus we are led to examine the processes involved in accelerating a current sheet in a manner useful for propulsion.

1.4 Current Sheets

A fundamental obstacle to optimizing pulsed plasma thrusters is the uncertainty which still surrounds many details of the propagating current sheet structure, the gas entrainment process, and the participating current conduction mechanisms. Clearly, gas entrainment in the moving sheet, or "sweeping", is desirable from a propulsion point of view. Mass accumulation however is closely tied to both the dynamics of the pinch and to the density profiles and field structure through the sheet. The composite problem is quite complicated phenomenologically, and has so far resisted comprehensive theoretical treatment. Instead, the historical approach to the problem of current sheet analysis has been a rather arbitrary division into the separate problem areas of sheet structure and sheet dynamics. The dynamics approach suppresses information about the forces acting in the sheet interior by replacing the finite current zone with either a "black box" or an effective discontinuity, and treats the resulting sheet trajectory. The analysis of current sheet structure on the other hand deals with specific fields and particle or fluid motion within a finite structured zone, without explicit reference to subsequent motion of the zone in the laboratory coordinate system. Even so, these separate problem areas are themselves complicated enough that the theoretical formulation of either problem has so far been incomplete.

Dynamical Models. The simplest idealization of the current sheet is perhaps given by the slug model, which assumes that the entire mass of gas to be accelerated is initially present as a thin, incompressible "slug" on the face of the driving current

sheet "piston", and that thereafter no mass is either accumulated or lost as the piston traverses the chamber. The slug model is more appropriate for the electromagnetic cannon for which it was developed [11] than for plasma accelerators, unfortunately.

A more realistic fluid mechanical approach was advanced by M. Rosenbluth[9] at Los Alamos in 1954.+ Rosenbluth formulated a "snowplow" model of the pinch wherein the propagating current sheet was assumed to "shovel-up" the mass ahead of it as it moved, i.e. as if the gas ahead of it were infinitely compressible. The motion of the piston was assumed to be governed by the inertia of the snowplowed gas and the chamber inductance, both of which are clearly functions of the piston position. Colgate[12] substantially improved on the utility of the snowplow model by including the electrical parameters of the external driving circuit in the analysis.

Black[13], working at Princeton, has done a detailed study of current sheet dynamics in a linear pinch geometry, and showed that snowplow dynamics predicted current sheet motion with good overall accuracy. Other recent work at Princeton has treated modified snowplow models which include the effects of a leaky, or porous piston[14] and transmission line power supplies[8].

Rosenbluth[15] has also suggested another dynamical model in which the current sheet is again represented as an impermeable piston, but where particles are assumed to be reflected rather than absorbed by the moving interface. In a

---

+Leontovich and Osovets[10] proposed essentially the same model independently in the U.S.S.R.

cylindrical geometry this leads to the phenomenon of "sheet bounce", an effect which has been observed in cylindrical theta pinches.

The next level of gas dynamic sophistication more realistically treats the finite compressibility of the gas flow, thus falling somewhere between the snowplow (sound speed zero) and slug (sound speed infinite) concepts. The immediate result is to allow a shock wave to propagate ahead of the piston, and several shock wave models have been proposed to describe the gas flow. One model assumes a uniform region between shock and piston as might befit one-dimensional flow. A more realistic assumption, appropriate to cylindrical geometry, has been treated by Chernyi[17] and Rowell[18] for unsteady flow behind the shock. Allen[19] has also treated a strong shock model of the linear pinch, and Burton[14] has recently applied jump conditions across the sheet itself.

It should be pointed out that theoreticians have been much quicker to assume shock waves in their models than experimentalists have been in proving their factual existence. Vlases[20,21] and Sorrel[22] at Caltech have investigated the postulated shock waves in an inverse pinch, and found experimentally that the shock does not achieve separation from the driving piston. In light gases such as hydrogen and helium the "shock" forms in the leading edge of the current sheet; in heavier gases, such as argon, it moves to the center or trailing edge, presenting the interesting phenomenon of a shock trailing the piston which generates it. York[8], at Princeton, has substantiated the interior "shock"

or pressure pulse in current sheets in argon linear pinches. Luminous phenomena associated with the current sheet have been identified with a shock wave by some authors, but any such general identification seems precluded by a variety of experimental evidence which is inconsistent with this interpretation.

Structural Models. Self consistent models of interior sheet structure are inherently more difficult to formulate than the dynamical statements just discussed, and are consequently fewer in number. Rosenbluth[9] proposed an early model which treated sheet structure assuming a collisionless, fully ionized plasma and one-dimensional geometry, and was able to obtain solutions for the fields and particle trajectories. The Rosenbluth model pioneered several fundamental ideas in sheet structure theory, among them the quasi neutral approximation, the dominant role played by internal charge separation (polarization) fields, and the restriction that electron-ion pairs entering the sheet are not at liberty to follow single particle orbits.

Lovberg[25] has advanced several quasi-empirical gas-kinetic arguments to describe particle motions and field distributions in a collisionless sheet, and these methods are instructive although not completely self-consistent. The internal polarization field is important in these models also, but because of the above-mentioned inconsistencies predicts different particle orbits from the Rosenbluth model. Gas kinetic arguments can be intuitively extended to include collisional effects in a straightforward manner.[1,14]

A more consistent (and more complicated) way of handling

the collisional case is through a fluid mechanical approach, wherein the working medium is regarded as a mixture of three fluids, composed of electrons, ions, and neutral atoms, each of which obeys the usual fluid equations of motion, energy, state, and so on. It is possible to simplify the analysis of the three fluid theory by considering one or more of the constitutent fluids in a limiting case, the most obvious being the two-component fluid for fully ionized gases. These models are developed and discussed in Chapter VII of the thesis.

Experiments. The general experimental attack on current sheets and arcs has been extensive. However the variety of experimental geometries which have been used (Fig. 1-1) and the large number of experimental variables--type of working fluid, ambient pressure, operating voltage, external circuitry, etc.--have tended to limit the usefulness of data correlation.

Experiments by Lovberg[24,25,26], Burkhardt and Lovberg[27], and Keck[28] have shown a discouraging disparity of observed three-dimensional effects. The current sheet may develop tilted, paraboloidal, and bifurcated fronts which exhibit unsteady or unstable characteristics. Johansson[29] found that the sheet tilted by as much as 50 degrees in an inverse pinch, and concluded among other things that the current was carried predominantly by ions. Lovberg[27] and Burton[14] found contrarily in other experiments that electron Hall currents predominated in the sheet, in agreement with the gas-kinetic models.

It is apparent that further experimental and theoretical work is necessary to clarify the mechanisms involved in sustaining the current sheet. In this work, quantitative measurements of certain physical

properties of the current sheet have been made, and related to sweeping efficiencies, ionization levels, current conduction mechanisms, internal particle and energy distributions, and so forth, through multifluid theories. The experiments returned information on the electron properties of the plasma and the field components, which were then used to calculate a variety of useful plasma parameters. The experimental variables were chosen to optimize the environment for the current sheet studies, which are described in the following chapters.

Chapter II

PINCH APPARATUS

2.1 Design Philosophy

The selection of a linear pinch geometry for the current sheet studies (Chapter I) specifies the general nature of the discharge event. The current initially assembles itself into a cylindrical layer at the outer-most radius to minimize self-inductance, and then, interacting with its own self-magnetic field, accelerates radially inward under the influence of the resulting $\bar{J} \times \bar{B}$ body forces until it collapses into a filamentary thermal arc column.

The three essential pieces of apparatus necessary to implement this series of events are a cylindrical discharge chamber, a capacitor bank or other energy depot to supply the discharge current, and a switch. Clearly, the large number of geometrical and electrical parameters which must be specified for these three components can exert controlling influence over the resulting electrical discharge. The physical parameters of the apparatus must accordingly be specified with care.

The design objective was to provide stable, narrow, intense, vigorously accelerating current sheets which were reproducible and suited to detailed diagnostic investigation, while maintaining ease of mechanical assembly and minimum electrical hazard for the apparatus. A facility capable of meeting most of these requirements was already in existence at this laboratory, having evolved in concert with other

investigations over a period of several years, and was available for the diagnostic experiments to be described in this work. The consistent, reliable performance of this apparatus contributed heavily to the overall success of the experimental program.

2.2 The Discharge Chamber

The discharge chamber (or pinch chamber, or test chamber) was a cylindrical volume 8 inches (20 cm) in diameter and 2 inches (5 cm) high, as shown in Fig. 2-1. The current sheet, which was typically 1-2 cm wide, thus made a radial incursion of 10 cm and over most of this trajectory the width of the sheet was small compared to its radial position. On this basis it is sometimes possible to invoke one-dimensional assumptions.

The circular electrodes of 3/4-inch thick aluminum were separated by a 1/4-inch thick pyrex glass insulating ring which formed the discharge vessel's radial boundary. O-rings between this insulator and the electrode perimeters sealed the test chamber. The exterior electrode, unlike the interior, provided convenient access to the discharge chamber and at the experimenter's discretion could serve as either anode or cathode. It was typically equipped with a valve for admitting test gas, a diametral slot for streak photography of the pinch, and small probing ports, plugged when not in use, for inserting axial probes into the discharge. The glass insulator ring provided similar ports for radial probing. The probes used in these experiments are described in detail in Chapters IV, V, and VI.

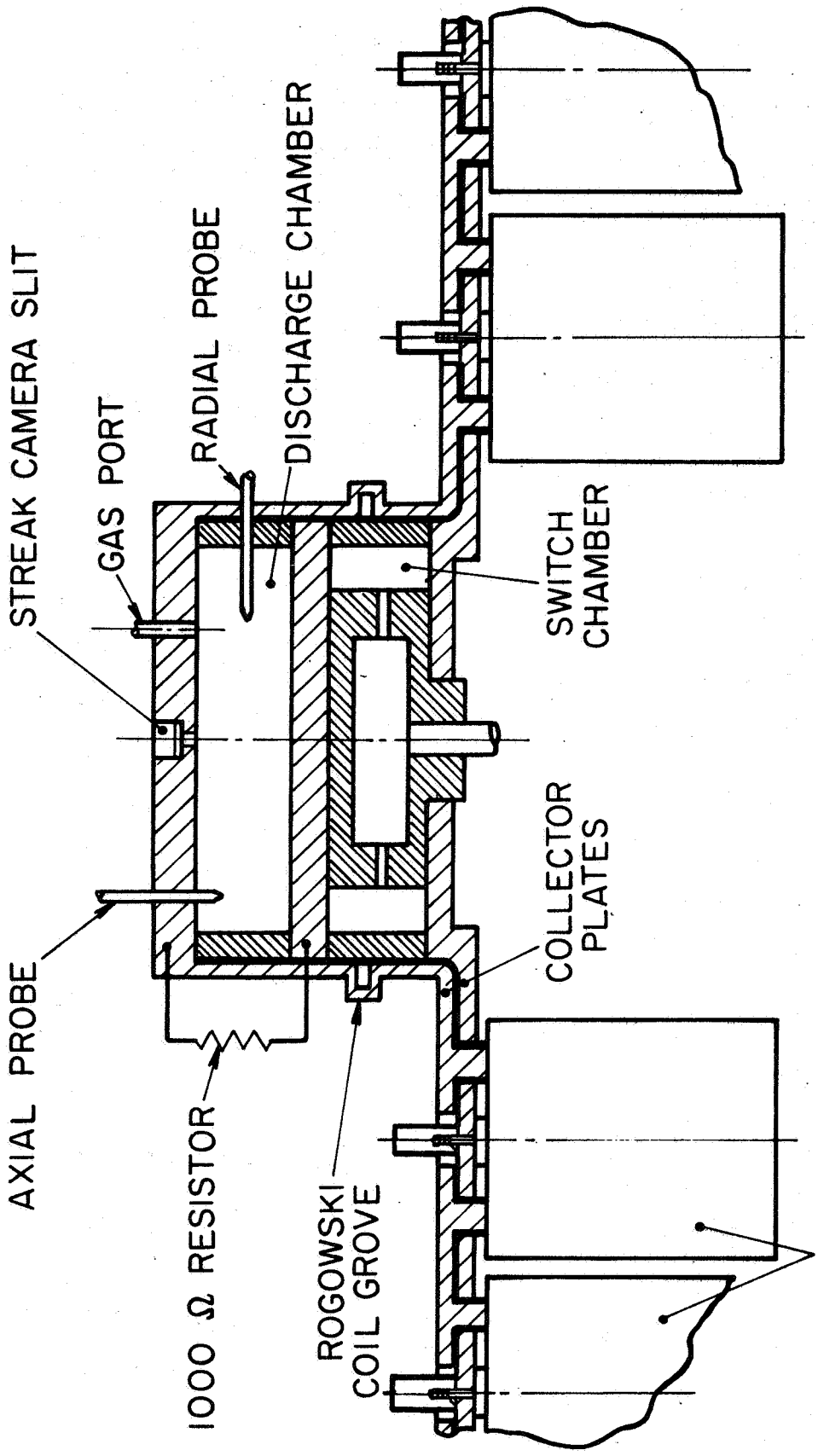

EXPERIMENTAL APPARATUS (SCHEMATIC)

FIGURE 2-1

2.3 The Switch

The switch event was provided by a gas-triggered discharge in an enclosure similar to, and directly below, the test chamber, which however had been provided with a plastic insert to inhibit pinching of the switch current. The switch was characterized by low inductance and a lifetime of several hundred discharges, two features which contributed significantly to the overall utility of the apparatus. The switch design was also evolved at this laboratory, and is described in detail in references 30 and 31.

2.4 The Power Supply

Electrical energy supplied to the discharge was stored in a linear network of capacitors connected by sets of parallel metal plates, each 10 feet long, on opposite sides of the discharge vessel (Figs. 2-2 and 2-3). This "wing" or "T" geometry combined the lumped capacitance of the individual capacitor units with the distributed inductance of the parallel plates to provide a flexible pulse-forming network with electrical properties closely resembling those of an ideal transmission line. This important characteristic allowed a desirable current pulse to be "programmed" by a proper choice of capacitor configuration, thereby bringing the single most important variable under the experimenter's control. The design of the pulse-forming network and its conversion to a useful research tool constituted the basis of Mr. Neville A. Black's 1966 Princeton Ph.D. thesis[13]. The network and its possible applications are also described in references (32) and (33).

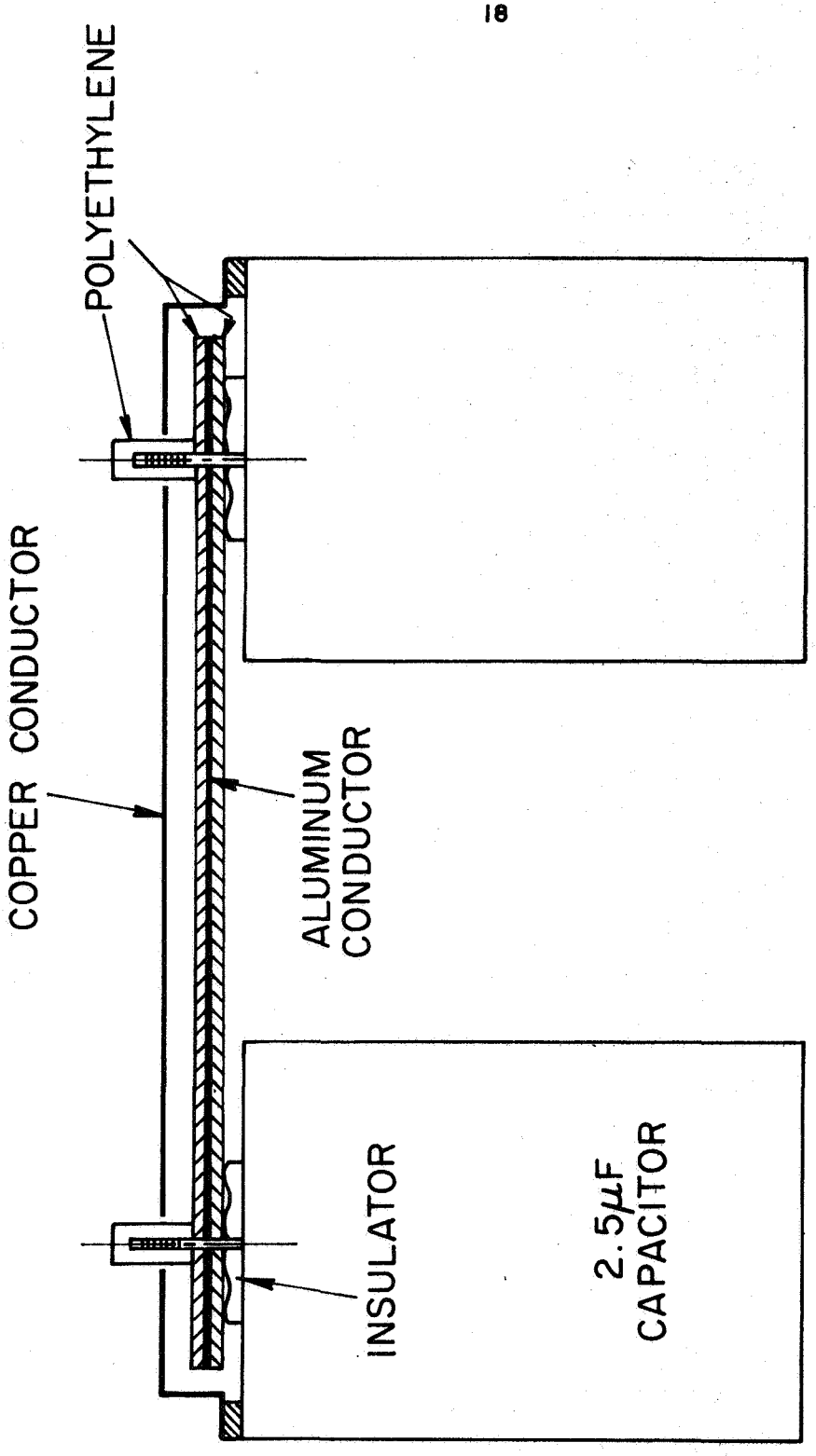

PULSE FORMING NETWORK CROSS SECTION (SCHEMATIC)

FIGURE 2-2

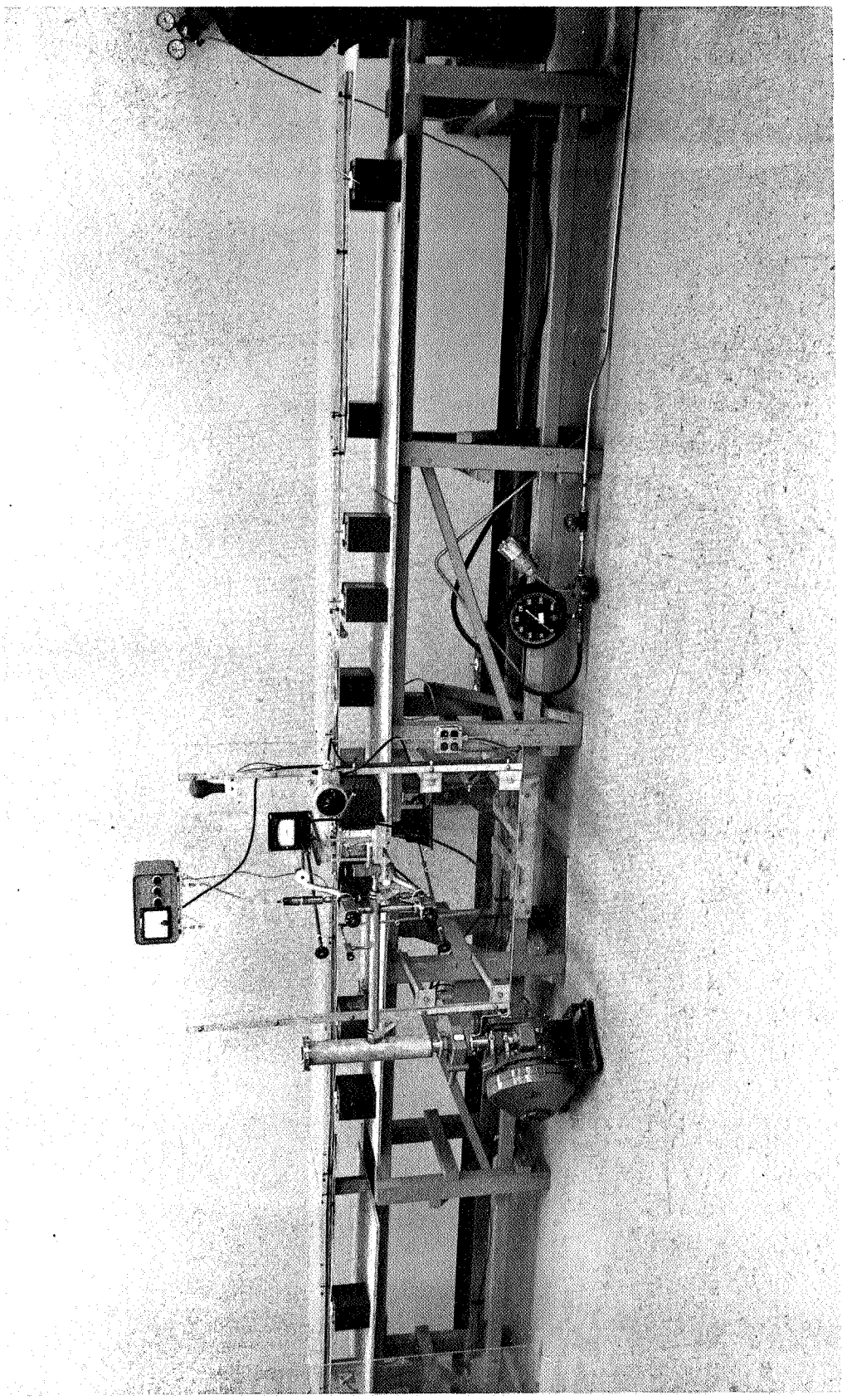

VIEW OF PULSE FORMING NETWORK

FIGURE 2-3

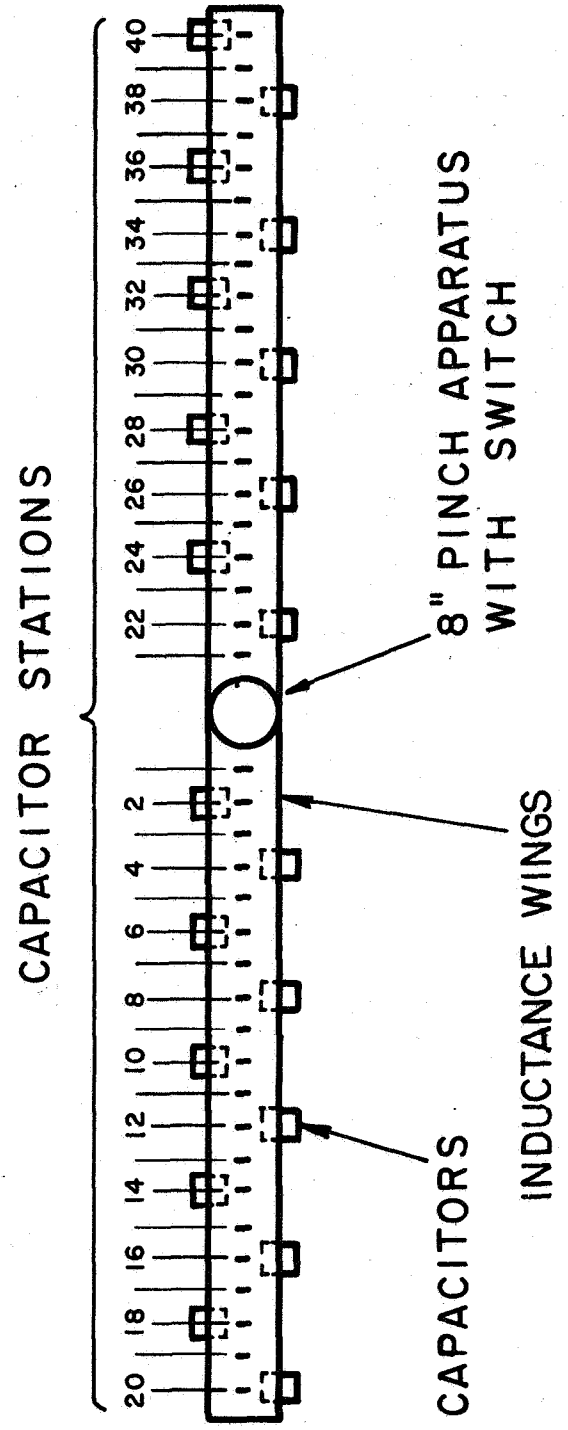

TOP VIEW OF PULSE FORMING NETWORK
(SCHEMATIC)

FIGURE 2-4

2.5 The Current Waveform

If the capacitor units are all lumped together near one spot on each of the two inductance wings, the resulting electrical network behaves much like the classic RLC circuit and, as the current rings down, delivers a waveform as a function of time which closely resembles an exponentially damped sine wave. It is intuitively clear, and experimentally verified, that a useful current waveform must persist long enough to drive the current sheet over the desired trajectory before reversing and beginning the second cycle of the ringdown. If it does not, the phenomenon of secondary, or "crowbar," breakdown, which is inductively favored, decouples the first sheet from the external circuit and causes undesirable complications for both diagnostics and propulsion. The free-ringing circuit, the damped sinusoid, suffers from this deficiency in many instances (Fig. 3-3).

A more attractive waveform is the rectangular pulse, characterized by fast rise times and constant amplitude for the time of interest. (The simplicity of a constant current for analytical formulations is especially appealing, and a useful example of this is discussed in Chapter IV.) A rectangular pulse was best approximated by the pulse-forming network when one 2.5 microfarad capacitor unit was located at each even numbered station of the inductance wings, as shown in Fig. 2-4. The electrical characteristics of the resulting network are given in Table 2-1.

Table 2-1

Circuit Characteristics for Rectangular Pulse

Station-to-station inductance	~ 12 nanohenry
Front section inductance	~ 6 nanohenry
Inductance of capacitor unit and its connection to the line	~ 16 nanohenry
Discharge plus switch inductance	~ 5 nanohenry
Total circuit inductance	~ 100 nanohenry
Discharge impedance	~ 5 milliohm
Switch and network resistance (2-sided). .	~ 5 milliohm
Capacitance of individual capacitor unit .	~ 2.5 microfarad
Total circuit capacitance.	~ 50 microfarad

The current pulse delivered by this network to a discharge in argon under the conditions of the experiments at an initial pressure of 100 mT (millitorr) reached a maximum value of 210,000 amperes in 0.5 microseconds, then leveled off to a nearly constant value of 175,000 amperes for about four microseconds before starting to reverse. The current sheet completed the pinch event in about four microseconds also, and thus for the duration of the experiment an effectively constant driving current prevailed. An oscillogram displaying both $I(t)$ and $\dot{I}(t)$ (a dot denotes time differentiation) for the rectangular pulse is shown in Fig. 3-2, and these waveforms are to be identified with all of the experiments which follow.

From Table 2-1 the inductance of the capacitor network is seen to far exceed the chamber inductance, and it is easy to show[1] that the motion of the current sheet just described

cannot significantly influence the electrical behavior of the total circuit. Thus in the experiments the circuit parameters could be considered independent of time and the driving current waveform was effectively decoupled from the dynamics of the current sheet.

2.6 Other Experimental Parameters

Once the geometry and driving current were specified, the working gas and initial pressure had to be chosen. Noble gases are frequently employed because they are noncorrosive and their atomic-scale interactions can be described by much simpler models than polyatomic gases with their additional internal degrees of freedom. Argon, with an ionization potential of 15.68 volts, was used in the experiments reported here, although both helium and nitrogen were briefly investigated.

The dynamics of the current sheet will clearly be influenced by the amount of overrun gas which is entrained, and it therefore seems plausible, and is easily verified, that sheet structure and motion are very sensitive to the initial gas density, or equivalently the ambient pressure fill. It was found empirically by investigating a range of pressures from 20 mT to 2 T that the optimum pressure for obtaining narrow intense current distributions was close to 100 mT (= 0.1 mm Hg), and this pressure was chosen, in the interest of uniform conditons, for all the experiments described here.

A similar empirical investigation of the optimum initial capacitor bank voltage yielded the expected result that higher voltages produced more intense currents and so the maximum

voltage rating of the capacitors, 10,000 volts, was selected for the experiments. At 10 KV the capacitor bank stored 2.5 kilojoules of energy.

2.7 Supporting Equipment

In addition to the three basic components of chamber, switch, and capacitor bank, the pinch apparatus included a conventional large-duct gas-handling system, vacuum pumps, instrumentation (Chapter III), control panel, and so on.

The argon supply used in all experiments was a 2,500 psi tank of commercial grade argon supplied by the Liquid Carbonic Division of General Dynamics. The impurity level was about 50 ppm (parts per million) from the tank, which was further raised by the addition of small amounts of water vapor, pump oil vapor, and other contaminants which inevitably inhabited the gas lines. The discharge was observed to be insensitive to any prevailing level of argon contamination, however, and gas purity was shown not to be an influential factor in the experiments. The argon was dropped to about 5 psi through a two-stage regulator whence it passed to the test chamber and switch through the gas feed system.

The usual electrical arrangement was for the exterior electrode to serve as the discharge cathode, and the exterior electrode was always maintained at ground potential for safety reasons. Grounding was through a heavy cable conductor which was bolted between the exterior electrode and a pipe buried twenty feet into the earth behind the laboratory.

2.8 Operating Sequence

A typical operating sequence for a data run on the machine proceeded as follows. The probes, if any, were mounted in the pinch chamber and the pinch chamber and switch were both evacuated to a pressure of less than one micron by mechanical pumping. The evacuated switch and the pump were then valved off from the system. Argon was admitted to the test chamber at a pressure of about one millimeter, and the pump was valved in to reduce chamber pressure to 100 microns. The chamber was then closed off by a valve which seated flush in the exterior electrode to present an unbroken electrode surface to the discharge. This sequence typically took several minutes.

The capacitor bank was next charged to operating voltage by a variac-controlled high voltage D.C. power supply. The two discharge chamber electrodes were electrically connected by a 1,000 ohm, 50 watt resistor and in the absence of sensible current were maintained at ground potential. The entire bank voltage appeared across the switch, which had been evacuated below the Paschen limit. Charging continued until the voltage on the capacitor bank and switch was slightly in excess of 10 kilovolts. The high voltage D.C. supply was then disconnected from the charged bank, which was allowed to discharge slowly through a 100 megohm bleed resistor. The total charging procedure also typically required several minutes.

When exactly 10 kilovolts was across the bank and switch, a spring loaded valve was actuated to admit argon from the gas supply into the evacuated switch, which then could no longer

hold off the bank voltage, and so broke down. The now highly conducting switch transferred the entire bank voltage to the pinch chamber, initiating the discharge.

The discharge always originated at the glass insulator because of the skin effect previously mentioned, and quickly built up into a narrow uniform sheet carrying about 210,000 amperes. The sheet then accelerated inward at velocities in excess of 20,000 m/sec, maintaining its overall integrity but altering its internal structure to conform with the entrainment of overrun gas and the compressive geometry of the cylinder, until it collapsed into an intensely hot, radiating, filamentary column several millimeters in diameter on the chamber axis, where it stood until the reversing external circuit robbed it of current.

Chapter III

INSTRUMENTATION AND DIAGNOSTIC TECHNIQUES

3.1 Pressure Gauges

The initial and pump down pressures in the pinch chamber and vacuum system were monitored with Pirani gauges manufactured by Consolidated Vacuum Corporation. These gauges measured pressure over the range one micron to two thousand microns by the cooling effect of the gas on a heated tungsten filament, and were themselves periodically calibrated against a large volume McCleod guage over the operating pressure range. Departures from calibration were never more than a few percent, an error to which the experiments were insensitive.

3.2 Current Measurements

The effective impedance of the overall electrical circuit--capacitor bank, transmission line, switch, and pinch chamber (Figs. 2-2 and 2-3)--was primarily reactive rather than resistive, as evidenced by the circuit parameters of Table 2-1. Consequently, any current measuring device should logically be based upon inductive coupling to the circuit rather than on ohmic voltage-difference type meters.

Rogowski Coil. The current measurements were made with a conventional Rogowski (or Rogovsky) coil, nested in a circular groove (Fig. 2-1) enclosing all current to the discharge chamber. The Rogowski coil or belt is essentially a multi-turn solenoid deformed into a torus which encircles the current

to be measured, and it has the useful property of responding, when properly wound, to the total enclosed current without regard to its spatial distribution. Rogowski coils must be designed to the specific experimental situation, with back-winding to minimize flux leakage and selected electrical characteristics to insure adequate signal strength and frequency response (reference 34, Chapter 1). When properly designed, the Rogowski coil output voltage is proportional to $\frac{dI}{dt}$, the time rate of change of the enclosed (circuit) current. The resulting voltages can be quite high, over 100 volts in these experiments, and careful insulation is necessary to prevent turn-to-turn arcing.

Integrating Circuits. I(t) was obtained from $\frac{dI}{dt}(t)$ by integrating the Rogowski coil output voltage. This was most easily accomplished with a passive R.C. integrator circuit[36], as shown in Fig. 3-1. Here R_o is the characteristic terminating impedance of the 50 Ω cable connecting coil and integrator, the latter being mounted directly on the oscilloscope face in normal operation. R_I (5,000 Ω) and C_I (40 pf) were chosen to give a time constant $\tau = RC = 200$ microseconds, well within the generally accepted requirement that RC exceed the total observation time by a factor of at least ten (for an accuracy of better than one-half percent - Lovberg, ref. 34). Tolerance of electrical components was checked on an impedance bridge before use, and the integrator units were carefully shielded and placed to minimize stray electrical pickup and signal distortion.

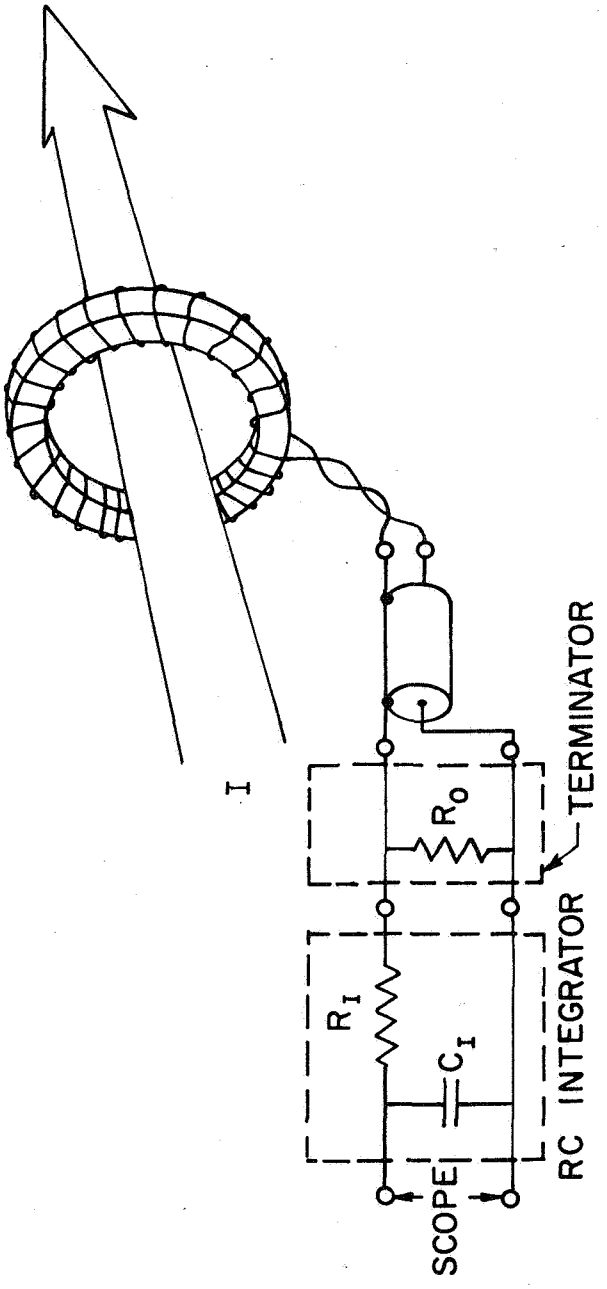

ROGOWSKI COIL CIRCUITRY

FIGURE 3-1

Calibration. Accurate calibration of the Rogowski coil was achieved by arranging the capacitor configuration along the transmission line to simulate a series RLC circuit, thus producing a current waveform which closely resembled an exponentially damped sine wave as discussed in Chapter II. From the known bank voltage and capacitance, the current amplitude and thereby the calibration factor can be inferred by measuring the ringing frequency and damping constant of the waveform. Using these techniques, the standard (rectangular) current waveform I(t) and its time derivative from the Rogowski coil were calibrated. These waveforms are displayed in Fig. 3-2, and with the exception of section 3-4 in this chapter, apply to all experiments described in this work.

3.3 Data Recording

The primary recorder for experimental data was a Tektronix Type 555 dual beam oscilloscope and the oscillogram of Fig. 3-2 is a typical data record. The graticule on this oscilloscope is an integral part of the blue-phosphor cathode ray tube, thus eliminating parallax error. Use of Type 47 Polaroid roll film, with an ASA rating of 3,000, in conjunction with a Hewlett-Packard oscilloscope camera equipped with an f/1.9 lens allowed single shot transients to be photographed readily at sweep speeds up to 0.1 microseconds/centimeter.

The sweep of the oscilloscope was normally triggered by the $\dot{I}$ (Rogowski coil) signal of Fig. 3-2b, the rapidly rising 100 volt pulse having been first attenuated and then fed into the external triggering circuit of the oscilloscope to initiate

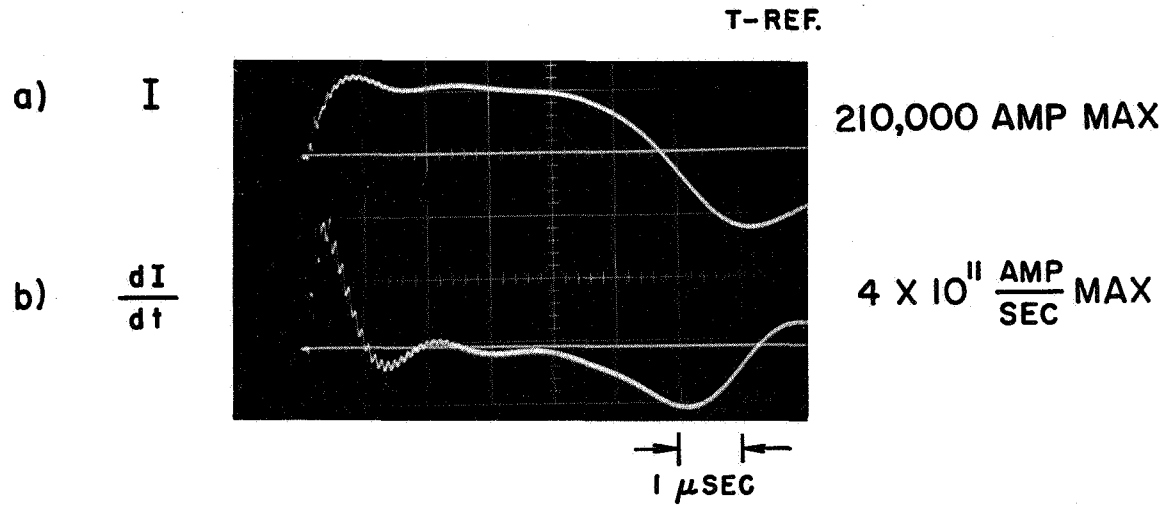

CURRENT WAVE FORM

FIGURE 3-2

a single sweep of both beams. The usual sweep speed was 1.0 microseconds/centimeter, and an internal delay of about 0.2 microseconds allowed the display of the initial event, as is evident in Fig. 3-2.

Electrical Shielding. The matter of noise pickup, whether through the probe tips, probe circuitry, ground loops,[+] oscilloscope power line, and so on, was ever troublesome and was necessarily approached in a semi-empirical fashion. The final details of any probe design were ultimately dictated by a trial and error scheme to determine optimum signal-to-noise ratio. All probe leads were shielded coaxial cable and the probes themselves were impedance matched as closely as possible to commercial cables. These cables were then terminated in their characteristic impedance to suppress spurious cable end-reflection signals. Three types of coaxial cable, having characteristic impedances of 50 ohms, 93 ohms, and 185 ohms, were most commonly employed.

The most troublesome noise signal to suppress was often high-frequency hash or jitter at the beginning of the oscilloscope trace. Some of this hash was eliminated by installing

---

[+]Ground loops are closed circuits completed through the electrical ground connections of the various pieces of apparatus. These loops can easily enclose large areas, and changing magnetic fields can consequently induce large voltages. Ground loops can be avoided by grounding all pieces of equipment to the same point, and to no other point. In these experiments, the common point was the buried grounding pole.

soft indium shims between all mechanical connections in the external circuit to prevent sporadic local arcing. The remaining noise pickup was reduced to an acceptable level by isolating the oscilloscope in a 6'x6'x6' metallic screen room equipped with BNC feed-thru connections for the probe cables and isolation transformers for the 117 volt oscilloscope supply. These low pass filters blocked frequencies higher than 400 cps from the power line and as a consequence could be connected directly to the laboratory electrical service.

The screen room also contained a great deal of microwave probe circuitry (Chapter VI), and thus became, in a sense, an integral part of the probe. It is shown in this capacity in Figs. 6-12 and 6-13.

3.4 Photography

In addition to the obvious use of oscilloscope photography, diagnostic photography which exploited the self-luminosity of the current sheet was often a useful and instructive technique. Two methods were successfully employed to study the pinch: rotating mirror streak photography and Kerr-cell shuttered snapshot photography.

Kerr-cell Camera. Kerr-cell photographs were taken with the aid of a Crown Graphic 4x5 camera equipped with a custom backing plate to accept ASA 3000 Polaroid sheet film. Exposure times of 0.05 microseconds were provided by the particular pulse-forming unit which operated the electro-optical shutter, a time interval which proved adequate to stop the motion of the current sheet while admitting ample light from the self-luminous

plasma. More recently 35 mm color photography has been tried successfully with ASA 180 High Speed Ektachrome color-positive film.

The Kerr-cell technique, when applied to photographing the pinch through a cutaway electrode or cutaway sidewall, was used for preliminary pinch stability studies. These investigations (references 33 and 37) showed that the linear pinch, under the conditions of these experiments, was symmetrical to a high degree with no noticeable tendency to flute or Raleigh-Taylor instability during the implosive phase (Fig. 4-3). It was also established that the self-luminosity associated with the pinch was coincident with the sharply peaked current distribution in the sheet[14], and not with a shock wave somewhere ahead of the sheet (a leading shock wave has never been observed in this laboratory, but other "precursor" effects have been noted and are discussed in Chapter VI). Snapshot photography has obvious limitations, however, and is not appropriate for detailed interior diagnostics in the current sheet.

Streak Camera. Streak photographs of the discharge were made with an AVCO Corporation Type MC300 Model Z rotating mirror streak camera. This camera employed a gas-driven rotating mirror to sweep an image of the diametral slot in the exterior electrode of the pinch chamber (Fig. 2-1) over a cylindrical film sheet, yielding the trajectory of the pinch in an x-t form where x is the 20 centimeter diameter of the pinch chamber.

Current sheet trajectories produced by several driving

current waveforms are shown in Fig. 3-3. These trajectories demonstrate the achievement of intense, narrow, vigorously accelerating current sheets by the rectangular pulse (Fig. 3-3c) chosen for these experiments. The photograph of Fig. 3-3a illustrates typical behavior of a discharge driven by an oscillatory waveform: secondary breakdown causes multiple luminous fronts to be initiated at the wall, at successive half-cycles of the discharge, which quickly coalesce into the primary front and propagate inward with decreasing velocity. In Fig. 3-3b, the diffuseness of the initial luminosity and the relatively long pinch time contrast with the thin, fast pinch of the rectangular pulse in Fig. 3-3c. The difference in this case can be traced to the current rise time: the higher initial current quadratically favors the faster rising pulse. The thin black horizontal lines on the photographs are caused by small wire markers spaced one inch apart in the slot across the diameter of the electrode. They serve as a convenient distance marker and as a check against optical distortion. The dark band across the middle of Figs. 3-3b and c is caused by a neutral density filter placed over the central portion of the slit. The filter reduces glare from the intensely radiating pinch column and permits the progress of the luminous front to be followed to the center.

The streak camera offers a simple and powerful technique for visualizing the general dynamics of the pinch. However, it shares with the Kerr-cell a lack of flexibility for quantitative interior sheet diagnostics.

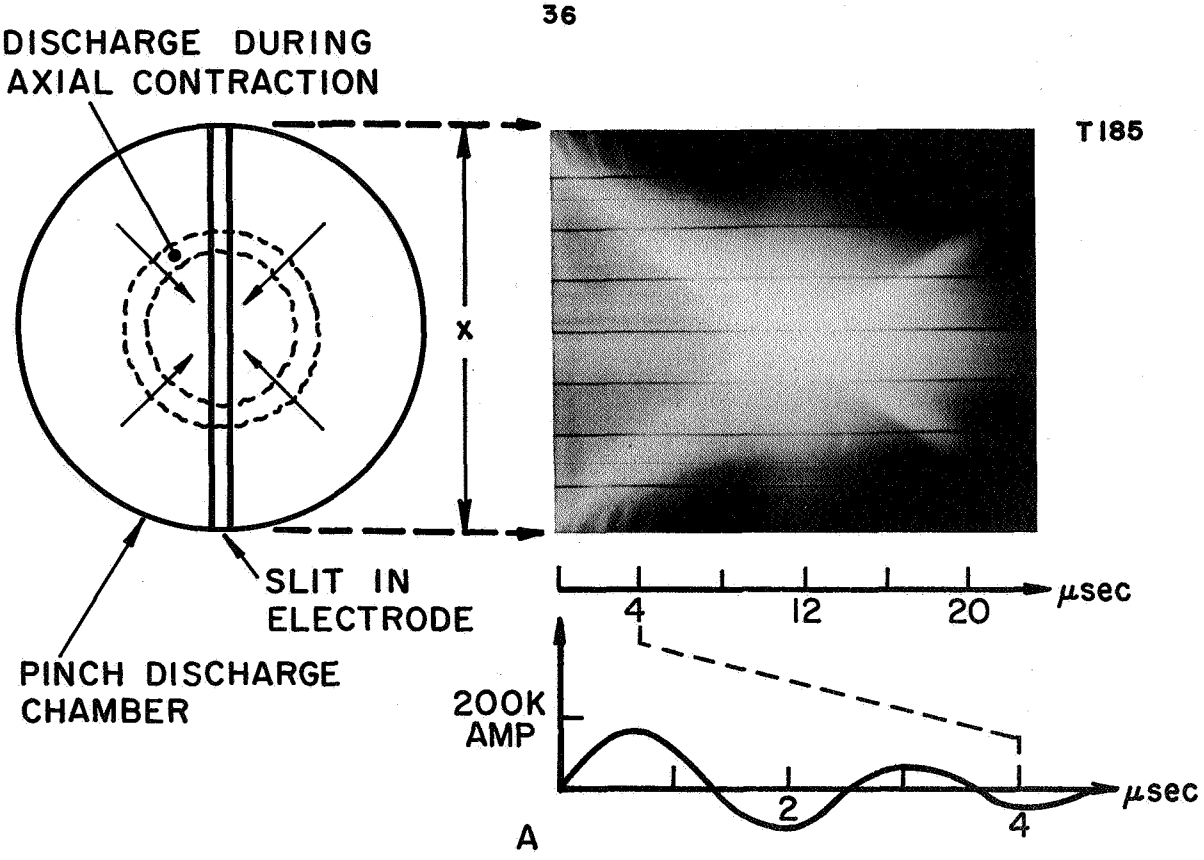

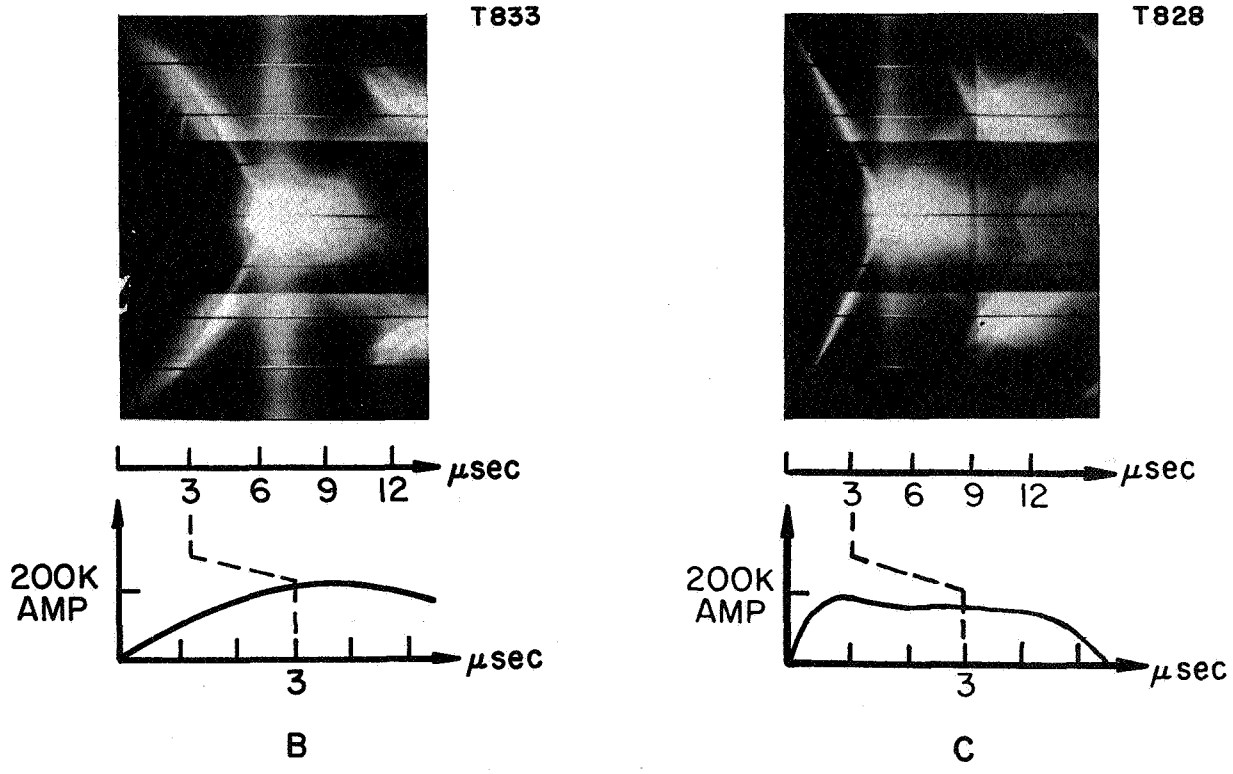

JP2S-P548-66

EFFECT OF VARIOUS DRIVING CURRENTS ON 100 mT ARGON DISCHARGE

FIGURE 3-3

3.5 Probes

For the purposes of discussion we can separate the quantities to be measured in the current sheet into the two distinct groups of field properties and plasma properties. These groups may then be subdivided in any convenient way to relate to the measuring devices.

Magnetic Probes. The first and perhaps most obvious of the field quantities is the magnetic induction field, which is conventionally measured with the aid of small pickup coils. This probing technique has been employed here, and the resulting measurements and their interpretation are discussed in detail in the following chapter.

Electric Probes. The other important field quantity in the sheet is the local electric field, and it too can be obtained from simply-constructed probes by immersing small electrodes in the plasma and measuring the potential between them. When the probe dimensions are properly chosen the probe can be positioned to effectively bracket the position of interest, and thus return electric field (potential gradient) information directly. These probes must be constructed and interpreted with somewhat more care than the B-probes, but the approach is straightforward. These measurements have been made and are discussed in Chapter V.

The $\overline{B}$ field and $\overline{E}$ field measurements, in conjunction with Maxwell's equations, serve to determine the source terms of total current density $\overline{J}$ and net charge density ρ, and these operations are also discussed in the following chapters.

The second important class of current sheet parameters relate to the plasma properties: the free electron and ion densities, n_e and n_I ; the electron and ion temperatures, T_e and T_I; and the collision rates of electrons with the heavier ions and neutrals, ν_{ei} and ν_{en} . These quantities, in the framework of an appropriate plasma theory, lead to other important properties: the electron density, temperature, and collision frequency are usually sufficient to calculate the effective conductivity of the plasma, for example; an equation of state (such as the perfect gas law) yields electron pressure from electron density and temperature measurements, and likewise for other partial pressures; the Hall parameter, which indicates the degree of scalar conduction, follows by definition from the magnetic field and collision frequency, and so on. The electron density and temperature (or collision frequency) are particularly important in this regard, as they appear in many of the equations of plasma physics. Even the ion density follows directly from electron density measurements, when taken together with the net charge density from the divergence of the electric field. This latter term is usually quite small however and the so-called quasi-neutral approximation ($n_e \cong n_I$) applies with high accuracy, as shown in Chapter V. Finally, we note that since the above parameters govern the microscopic and macroscopic conditions in the current sheet, they offer some hope of estimating particle trajectories, current mechanisms, sweeping efficiencies, ionization profiles, and other quantities in the sheet of interest to propulsion.

Measurement of Plasma Electron Properties. There is an abundant literature on plasma diagnostic techniques which return information about the electron component of the plasma. Heald and Wharton[35] have prepared perhaps the most comprehensive review of techniques and references to the literature in Chapter 10 of their book, Plasma Diagnostics With Microwaves (John Wiley and Sons, New York, 1965). A more detailed discussion of the commoner methods is available in Huddlestone and Leonard, ed.,[34] Plasma Diagnostic Techniques (Academic Press, New York, 1965).

There are, in principle, a number of ways to measure the electron properties of a plasma: electrostatic probes, magnetic induction probes, microwaves, spectroscopic and optical techniques, and so on. The development of any of these into a tool for routine investigation has so far been incomplete. Each is applicable over a limited range of experimental conditions, and each has certain characteristic ambiguities in its response to an ionized gas flow. Lacking any "standard source" of uniform, maxwellian plasma to calibrate them, such techniques must rather be justified on the grounds of physical interpretation and the internal consistency of their results.

A few order-of-magnitude considerations will bring the diagnostic requirements into better focus. At an ambient gas fill of 100 mT, there are 3×10^{15} argon atoms per cubic centimeter in the pinch chamber at room temperature. If a variable ionization level from 1% to 100% is anticipated, and allowance made for tenfold compression in the sheet, the expected electron density falls in the range (keeping factors of ten)

$3 \times 10^{13} < n_e < 3 \times 10^{16}$ cm^{-3}. Thus the techniques of spectroscopic line broadening and continuum intensity measurements, as well as optical interferometry, all of which require relatively high free charge densities ($> 10^{16}$ cm^{-3}), are inapplicable.

Some spectroscopic line intensity studies, unresolved in time, have been made of the pinch[14], and indicate an upper limit on the electron temperature, based upon energy balance considerations, of a few ev (one electron volt ≈ 11,600°K). Measured spectral lines from argon III and IV indicate multiple ionization at least in the collapsed pinch column. Trace impurities in the current sheet, such as hydrocarbons and aluminum electrode material, have also been verified spectroscopically. More detailed studies have been hampered by geometrical complications and the spatially integrated nature of the data. The current sheet is a narrow region of rather extreme radial gradients in most properties, and an integrated radial intensity record must be converted into a true radial distribution to be useful. This can be accomplished by Abel inversion only in the case of an optically thin plasma, which is not an accurate description of the intensely self-luminous regions of the current sheet. If the line of sight is chosen axially, the measurements are integrated through a tilted sheet and the diffuse anode attachment region (these features are discussed in Chapter IV).

Langmuir probes[39] and the related double probes[42] are appealing for their simplicity, and earlier diagnostic studies at Princeton employed these devices.[43] However their interpretation is complicated by the aerodynamic, thermal, and electrical

disturbances they introduce into the flow under study, and the inclusion of magnetic fields, potential gradients, and characteristic lengths (Debye length, mean free path, probe dimensions) in the analysis multiplies those difficulties and leaves data interpretation open to serious doubt.

The magnetic induction probe[23] is also relatively simple to use, but it returns information on the gross electrical conductivity instead of the electron properties per se, and calibration in this case would be very difficult (Chapter 10, reference 35).

Microwaves share many of the advantages and disadvantages of the optical techniques, but the lower frequency (gigacycle) range makes them applicable in lower density plasmas. The longer wavelength sacrifices spatial resolution, however, and interest must be restricted to millimeter wavelengths if structural details of the current sheet are to be resolved. Both laboratory sources and circuit components for millimeter microwaves have become commercially available in the past few years, although they are still expensive and somewhat temperamental.

Of the several schemes for actively probing ionized gases with microwaves (as opposed to passive schemes for monitoring self-radiation) the broad distinction is between those involving bounded propagation, as in a waveguide or resonant cavity, and those permitting free propagation of the wave train through the medium. These latter involve launching a microwave signal into the plasma from a suitable antenna and observing phase and amplitude changes in the transmitted and reflected

wavetrains. The hope is then that these wave functions can be related, through a suitable theory, to the free electron density and collision frequency of the plasma. Whenever significant magnetic fields and density gradients are present in the plasma, they must be included in the probe response analysis. In particular cases they may even dominate the problem, as for example in Faraday rotation experiments, which become practical when strong axial magnetic fields are present.

Microwave Probes. Calculations were made for several proposed microwave, spectroscopic, and optical laser interferometry experiments to compare the analytical formulations and numbers involved. On the basis of those calculations, the particular problems posed by the pinch experiments, the state-of-the-art of needed equipment, and the personal preference of the author, one particular microwave technique was selected for further study. This technique proposed measurements of reflected amplitude and phase, in an interferometer whose design was to be specified, to determine electron densities extending all the way into the far cutoff regime. This domain has generally been considered inaccessible to microwave techniques (Chapter 10, reference 34), but the usefulness of such measurements, together with the local sampling properties implied by large reflections, seemed attractive enough to pursue further. Considerable development and refinement proved to be necessary before the desired experiments could be successfully carried out. The reflected phase interferometer and amplitude-measuring bridge circuitry which resulted, and their

application to the pinch experiments, constituted the major experimental effort of this work. Theory and applications are discussed in detail in Chapter VI and the four appendices.

Chapter IV

MAGNETIC PROBES - THEORY AND EXPERIMENT

4.1 Introduction

The transient features of a traveling electrical discharge imply certain experimental liabilities, such as the enhanced noise problems discussed in the previous chapter. On the other hand, transient electrical phenomena are much more amenable to inductive type measurements than are time independent events. This inductive benefit is exploited directly in measuring magnetic field strength.

The $\overline{B}$ probes were essentially small pickup coils inserted into the discharge through probing ports in the exterior electrode and chamber sidewall. Two different but related probe designs were employed. In preliminary experiments to map $\overline{B}$ fields throughout the discharge chamber, the pickup coil and leads were sealed in pyrex glass envelopes to allay destruction by the discharge.

The preliminary surveys furnished a considerable amount of qualitative information and provided a good picture of the shape and propagation characteristics of the current zone. From these data two locations in the chamber were selected for detailed study.

The more detailed, second generation experiments at the selected locations were made with refined versions of the probe, calibrated in position in the discharge chamber, which provided quantitative measurements of the three magnetic field components B_r, B_θ, and B_z. From these the current density and Lorentz force were calculated.

4.2 Magnetic Probe Design

The probe coils were made of three turns of #32 Formvar copper wire, wound into tight, single layer solenoids on a #47 drill shank to an i.d. of 1.9 millimeters. The coil leads were twisted tightly together to circumvent spurious inductive pickup and, in the earlier versions of the probe, were simply sealed with epoxy into pyrex tubing and inserted through O-ring seals into the chamber.

The later calibrated versions of the probe utilized unjacketed construction with brass reinforced nylon sleeves and multiple thin coats of radio cement insulation, as shown in Fig. 4-1. The coil leads were passed through coaxial brass tubing in the probe body, typically 18" in length, to connect with 50 ohm coaxial cable leading to the screen room and oscilloscope.

4.3 Probe Operation

The right-handed cylindrical coordinate system appropriate to the pinch geometry is shown in Fig. 4-2, where R is the radial position of the probe coil and an arbitrary point has coordinates (r, θ, z).

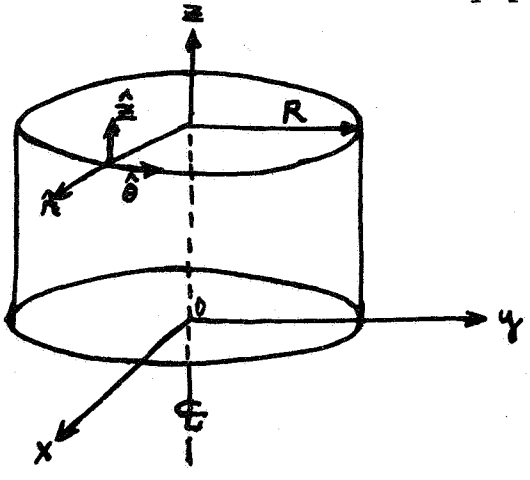

COORDINATE SYSTEM FOR PINCH GEOMETRY

FIGURE 4-2

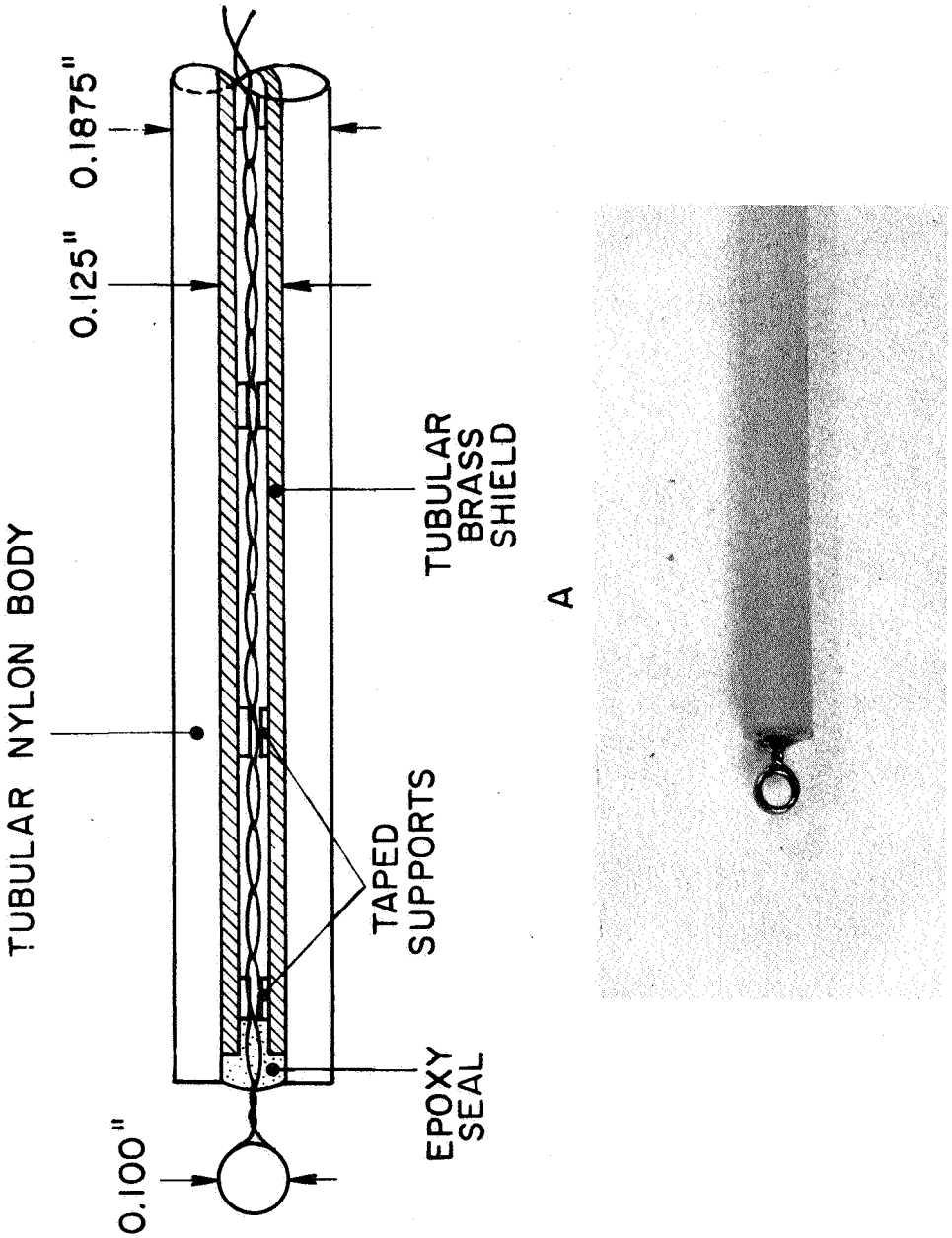

MAGNETIC PROBE

FIGURE 4-1

AP25-MOI-#1

Consider a small probe coil of area A located in the pinch chamber at radius R. Faraday's law in MKS units (Appendix A) integrated over the coil area becomes

$$\int_{\substack{\text{coil}\\\text{Area}}} \nabla \times \bar{E} \cdot d\bar{A} = -\int_{\substack{\text{coil}\\\text{area}}} \frac{\partial \bar{B}}{\partial t} \cdot d\bar{A} \qquad (4\text{-}1)$$

and from Stokes' law

$$V_{coil} = \oint_{\substack{\text{coil}\\\text{perimeter}}} \bar{E} \cdot d\bar{l} \cong -\frac{\partial \hat{B}}{\partial t} N A \cos \theta_{\bar{B},\bar{A}} \qquad (4\text{-}2)$$

where $\frac{\partial \hat{B}}{\partial t}$ is averaged over the probe area and N is the number of turns (three in this case). It will be shown that $\bar{B}$ is essentially constant over a probe diameter, so that $\left|\frac{\partial \hat{B}}{\partial t}\right|$ is a good measure of the local value of $\left|\frac{\partial \bar{B}}{\partial t}\right|$.

With a properly aligned coil the desired component of $\bar{B}$ is normal to the area of the coil, hence cos θ is unity for that component and zero for both other components, giving

$$V_{coil}(R,t) \propto \frac{\partial \hat{B}}{\partial t}(R,t) \cong \frac{\partial B}{\partial t}(R,t) \qquad (4\text{-}3)$$

The probe voltage could then be integrated passively (Section 3.2, Chapter III) to provide simultaneous records of B(R,t) and $\dot{B}(R,t)$ on the same oscillogram.

4.4 Sources of Error

Lovberg (Chapter 3, reference 34) has made a thorough study of major error sources for these probes and the following discussion derives in large part from his analysis. It will be

convenient to define five categories and consider each briefly.

Electrostatic pickup. This effect is caused by capacitive coupling between probe and plasma. The probe coil is normally maintained near ground potential, via the oscilloscope connection, while the local plasma potential may be several thousand volts. The probe coil and plasma are separated by an insulating cover or coating over the probe tip. In the early model jacketed probes the separation between coil and plasma was on the order of one millimeter, large enough to effectively eliminate capacitive coupling. For unjacketed probes the coupling is not so obviously small, but fortunately simple tests for electrostatic pickup can be performed. If the probe coil is rotated by 180 degrees, the magnetic signal should be exactly inverted to give -B(t) while leaving the electrostatic component unchanged in sign. Thus a necessary and sufficient condition for negligible electrostatic pickup is that the two B(t) records obtained in this way be exact mirror images, which was found to be the case. A second test, which consisted of shorting the probe leads during an experiment and recording the probe output voltage, produced very small signals and thus corroborated the finding of negligible capacitive distortion.

Diffusion of Magnetic Flux. Consider the worst situation, wherein the plasma is assumed to flow around the probe coil rather than through it (re the glass jacketed probes). The magnetic field is confined behind the current sheet, and upon reaching the probe must diffuse into the coil area from the streaming plasma particles which are tied to it. Lovberg[34]

gives this characteristic diffusion time as

$$\text{(MKS)} \qquad t_D \cong \frac{\mu_0 \sigma r_0^2}{4} \qquad (4\text{-}4)$$

where r_0 is the coil radius. Clearly jacketed probes have no hope of working in infinite conductivity plasmas.

The plasma conductivity in the current sheet, calculated in Chapter VII using measured values of electron density and temperature, was found not to exceed 10^4 mho/meter. Inserting this value for σ in eq. (4-4) and assuming r_0 = 1 mm, the diffusion time is found to be quite small,

$$t_D = 3 \times 10^{-9} \quad \text{seconds.}$$

For unjacketed probes, t_D is even smaller.

For a 2 mm. coil and the prevailing sheet velocities, $\sim 2 \times 10^4$ meter/second, the probe coil has a time resolution of about 10^{-7} seconds. Thus magnetic flux diffusion into the probe coil can be considered instantaneous, and signal distortion and time lag errors from this source were consequently negligible.

Plasma Cooling by the Probe. The flux of charged particles to the probe body, and hence the transport of heat, is largely controlled by the nature of the negative potential sheath which forms over the probe (or any other insulated body immersed in the plasma). The problem is very difficult to treat analytically. Even in the equilibrium case the plasma thermal conductivity is a strong function of temperature, $\kappa \propto T^{5/2}$, (16) thus making the heat conduction equation $\left(\frac{\kappa}{c_p \rho} \nabla^2 T = \frac{\partial T}{\partial t}\right)$ nonlinear; and plasma flow in the current sheet is not in thermal equilibrium.

Lovberg[34] and Burton[14] have made estimates of this effect, and they concluded that energy loss to the probe in a typical pinch experiment does not exceed 10^{-4} of the energy delivered to the discharge.

It is clear that the probe will also intercept a certain amount of radiation from the gas which might otherwise have been self-absorbed. However, the optically thick regions of the sheet are not likely to be extensive, and the relative volume of the sheet occupied by the probe is a small fraction of one percent, low enough to insure negligible losses from radiation cooling.

It should also be noted that the entire discharge current distribution participates in establishing the net magnetic field at a point, so that the tiny volume of plasma excluded by the probe is not influential enough to perturb the local field severely. This was verified experimentally by comparing B(t) traces from jacketed and unjacketed probes under otherwise identical conditions. The difference was noticeable but not severe, and the conclusion was that jacketed probes were valid for survey studies to within probably 10 percent. The smaller calibrated probes presented a significantly smaller energy sink to the plasma and improved the accuracy to perhaps within 2 - 5 percent.

Probe Boil-off. In the process of cooling the plasma, the probe body and tip sustained heavy-ion bombardment which inevitably blasted off a certain amount of foreign matter into the plasma. This effect is of overriding concern for light fusion plasmas of high purity but, as shown in Chapter III,

impurities found in the pinch chamber (from vaporized electrode material, outgassing, insulator breakup, probe boil-off, and so on) did not noticeably influence the experiments.

Gas Dynamic Effects. The plasma streaming over the probe coil was necessarily diverted somewhat, and the flow deflection unavoidably introduced some distortion into the local flux distribution. The ratio of frontal probe area to sheet area was only 10^{-3} at half radius however, and the probes thus did not represent a major obstacle to the current. Unjacketed probes were superior in this respect.

Of more interest is the question of shock wave generation. Kerr-cell photographs[14] have shown no visible evidence of shock wave formation when the probes are passed over by the current sheet (Fig. 4-3), and pressure surveys with rather large probes have shown no evidence of introducing shock waves into the flow.[8]

To hold gas dynamic effects to a minimum, all field measurements were made with the current sheet running head-on into the probe, except along the electrode surfaces where axial insertion was favored. Radially inserted probes extended across the chamber, through the centerline axis, and out to the radius of interest. Similarly, if the probes were inserted axially through an electrode for any appreciable distance they were bent to face into the oncoming sheet with their coil areas aligned to intercept the desired component of $\overline{B}$.

4.5 Experimental Results

Fig. 4-4 is a cross sectional view of the discharge chamber showing the lattice of interior points where magnetic

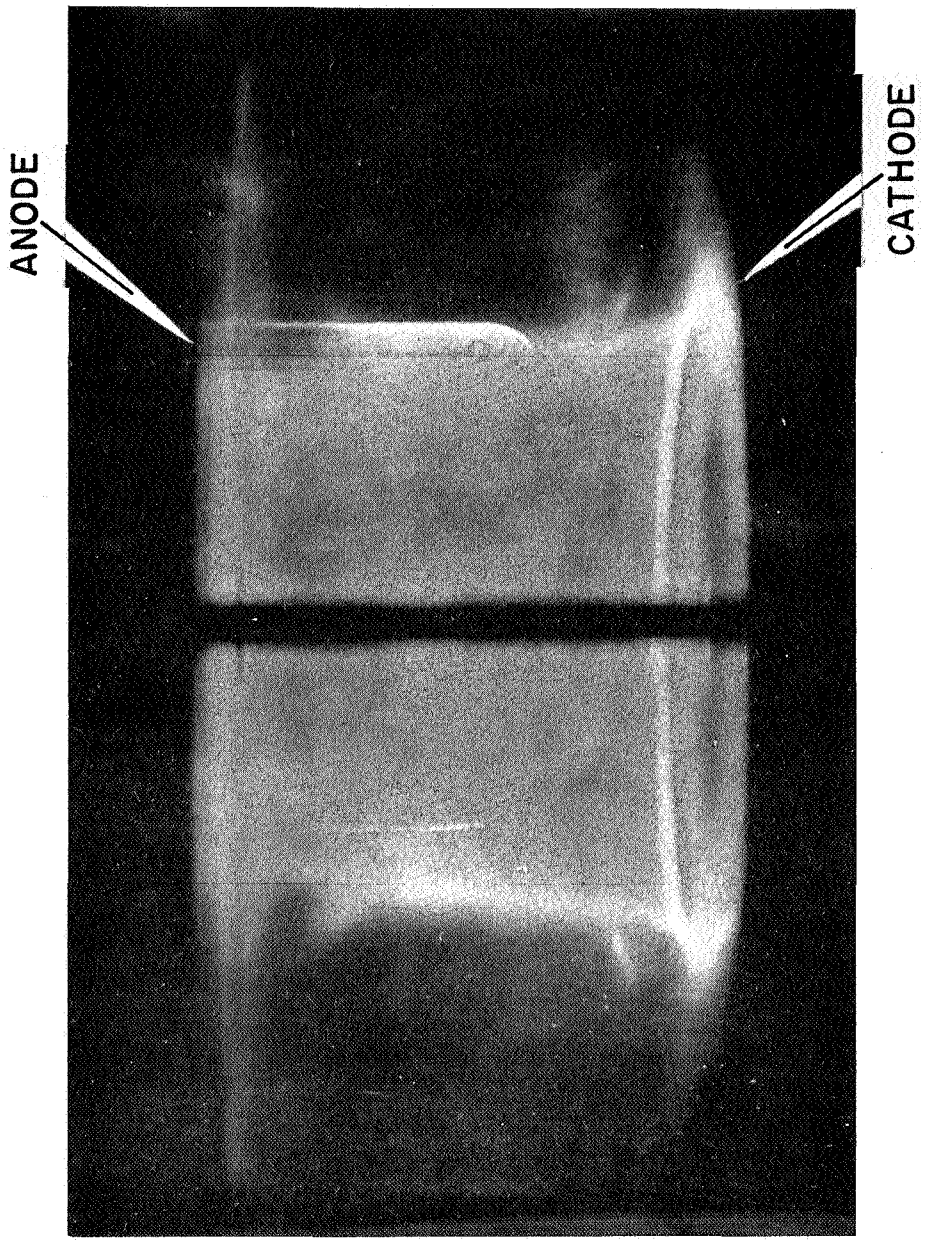

CURRENT SHEET SWEEPING OVER LARGE GLASS-JACKETED B-PROBE †
(5" MACHINE, 120 μA, 10 KV)
† PHOTOGRAPH BY R.L. BURTON

FIGURE 4-3

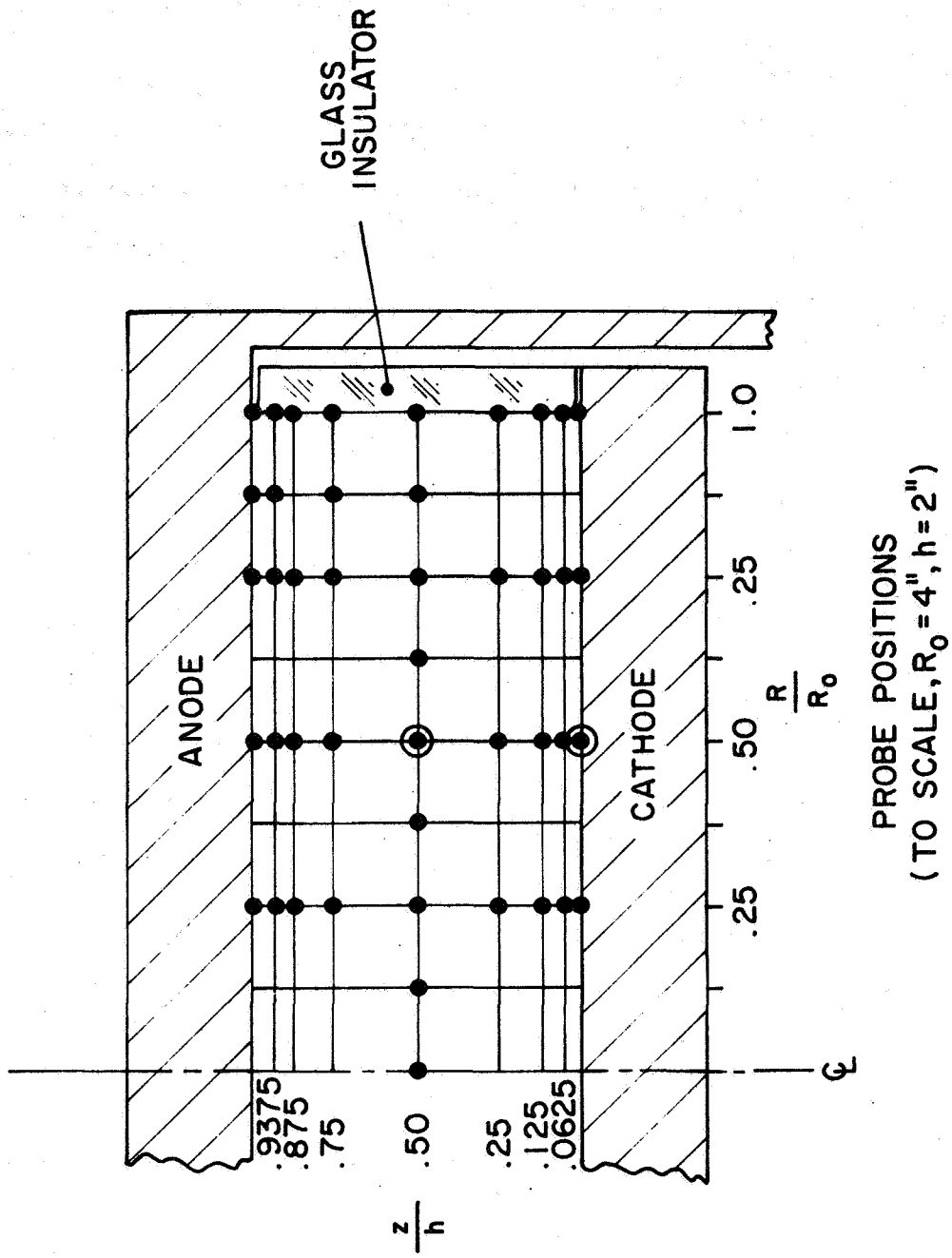
GLASS INSULATOR
ANODE
CATHODE
1.0
.25
.50
.25
R/R₀
PROBE POSITIONS
(TO SCALE, R₀ = 4", h = 2")
.9375
.875
.75
.50
.25
.125
.0625
z/h

FIGURE 4-4

field measurements were made. Surveys over the indicated positions furnished a good picture of current sheet profiles and trajectories. As expected, the predominant $\overline{B}$ field component was found to be azimuthal.

The width of the current sheet can be closely identified with the $\dot{B}_\theta$ signal, a notion which will be given mathematical form in the following section. It is sufficient to note here that, by definition, no current and hence no magnetic field exists ahead of the current sheet; and similarly, by definition, there is no current after the sheet has passed, implying that $\overline{B}$ is constant thereafter in time (assuming constant current and cylindrical symmetry). Therefore, $\dot{B}_\theta$ is significant only during current sheet passage over the probe coil and its spiked profile can be loosely associated with current in the sheet.

Surveys. Fig. 4-5 is an r-t plot of arrival times of $\dot{B}_\theta$ peaks along the anode, cathode, midplane, and intermediate axial positions. The slope of a resulting trajectory at a given radius yields the instantaneous sheet velocity as it passed that point in the chamber.

The trajectories originate from a common origin, indicating the initial formation of a planar sheet of current near the glass sidewall at t = 0 (time is reckoned from the origin of the current trace, Fig. 3-2a). Thereafter $\dot{B}_\theta$ peaks are observed at a given radial position first on the anode, then at midplane, and last on the cathode, indicative of a tilted current distribution having its leading attachment on the anode. This observation is more graphically presented in Fig. 4-6, which is a cross plot of the data of Fig. 4-5 at various times. The development of sheet tilt

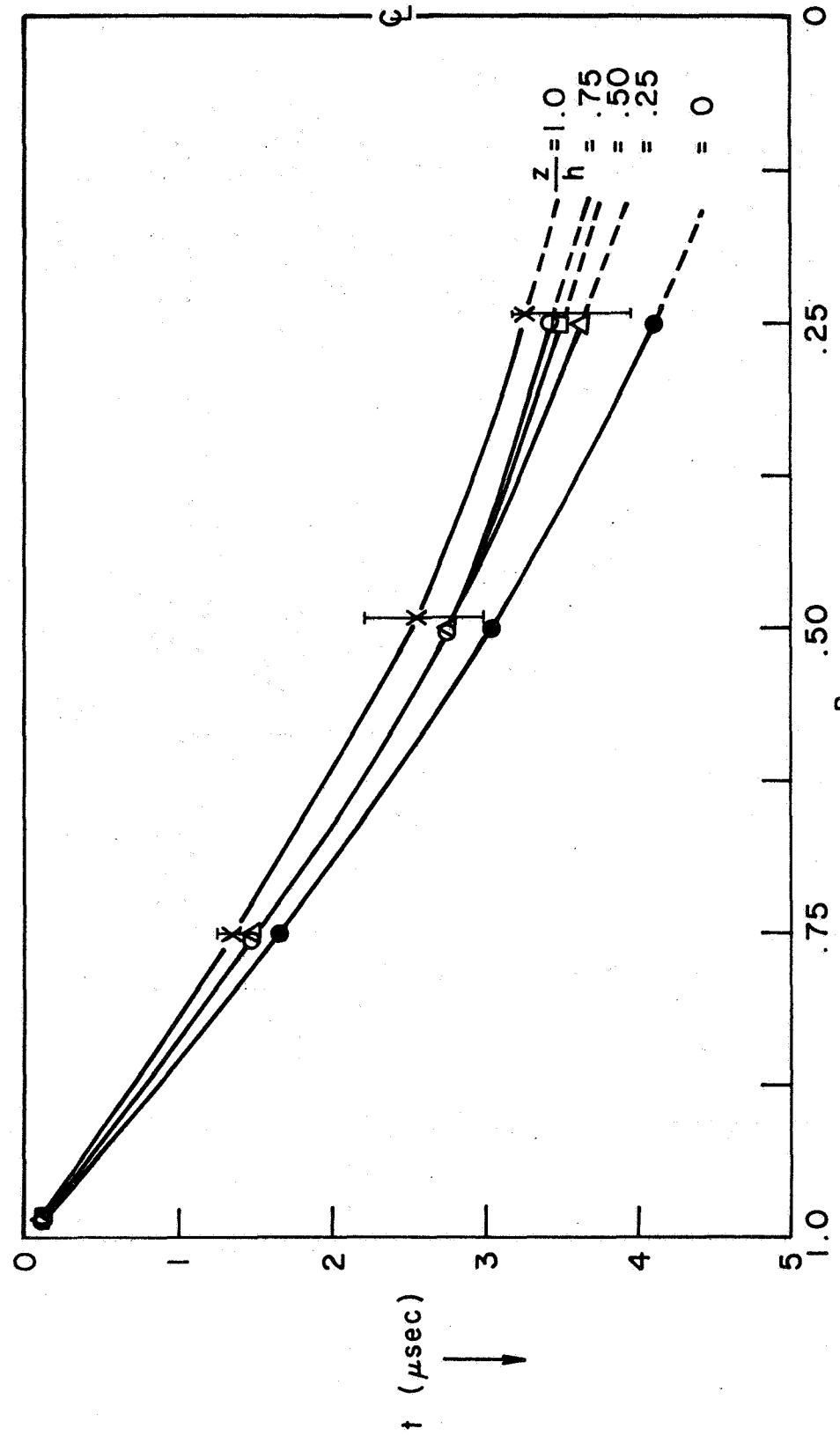
B_θ TRAJECTORIES
$\frac{R}{R_o}$ (R_o = 10 cm)
t (μsec)
$\frac{z}{h}$ = 1.0
.75
.50
.25
0
0
.25
.50
.75
1.0
1
2
3
4
5

FIGURE 4-5

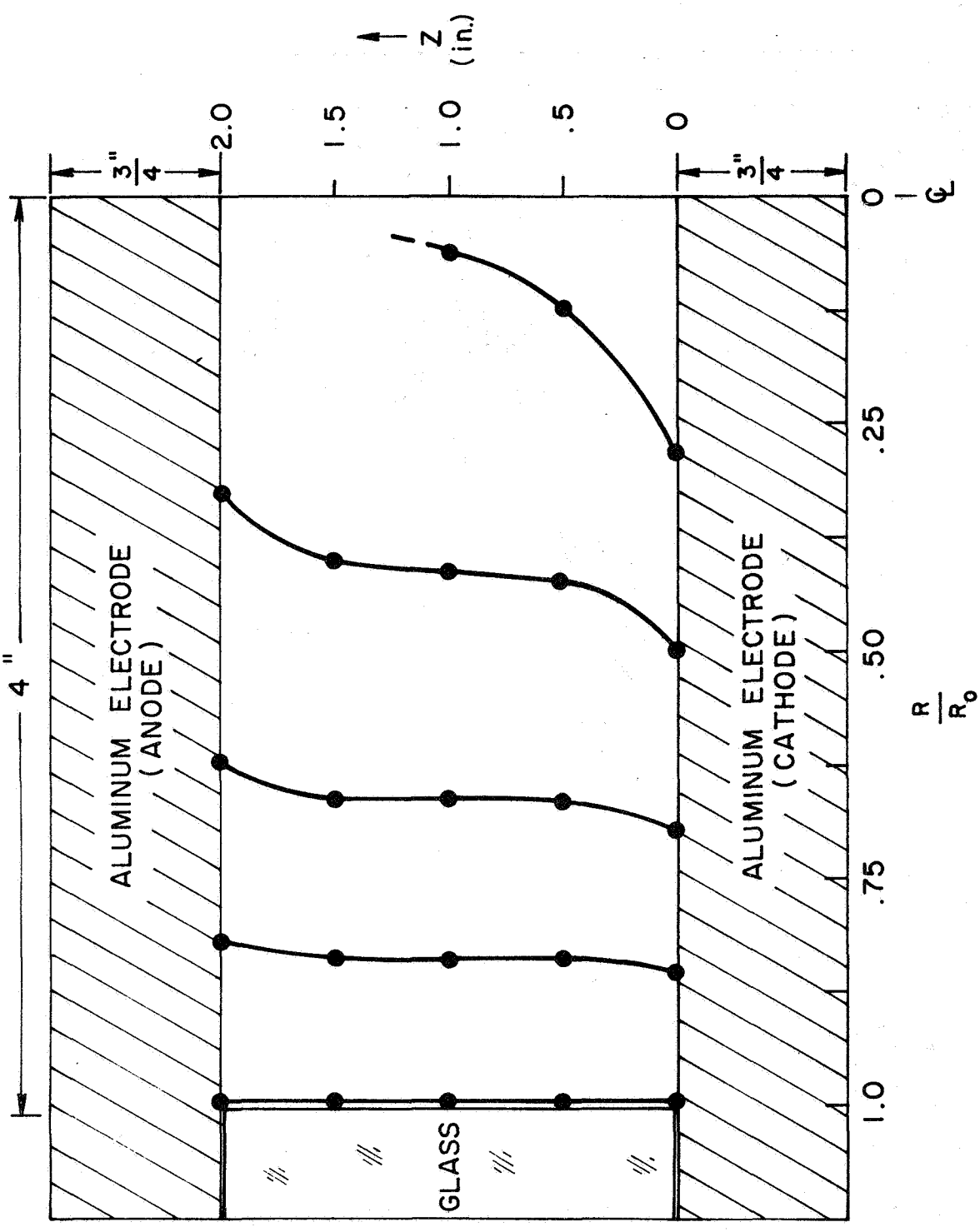

APPS-4264-67

FIGURE 4-6

is clear, and corresponds to the addition of a radial current component:

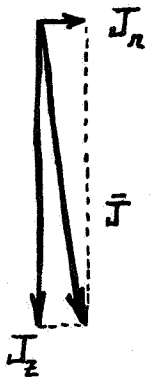

The set of oscillograms in Fig. 4-7 is typical of the raw data, showing in this instance the radial progression of $\dot{B}_\theta$ along the midplane between the two electrodes.

The development of a "foot" on both anode and cathode can be seen in Fig. 4-6. This somewhat pathological attachment behavior is well known and presumably reflects the plasma's reaction to the proximity of metallic boundaries. The representation of the figure is misleading, however, in the sense that the two regions are not very clearly distinguished. In reality a very clear distinction prevails between anode regions and cathode regions in all phenomenological observations of current sheet properties. This different behavior may be due to the relative ease of extracting electrons from the cathode, as compared with the difficulty of obtaining positive ions from the anode. In any event, the fields and other measureable quantities become quite smeared out in a large region near the anode, in distinct contrast with cathode data.

This behavior is illustrated in Fig. 4-8, a typical axial

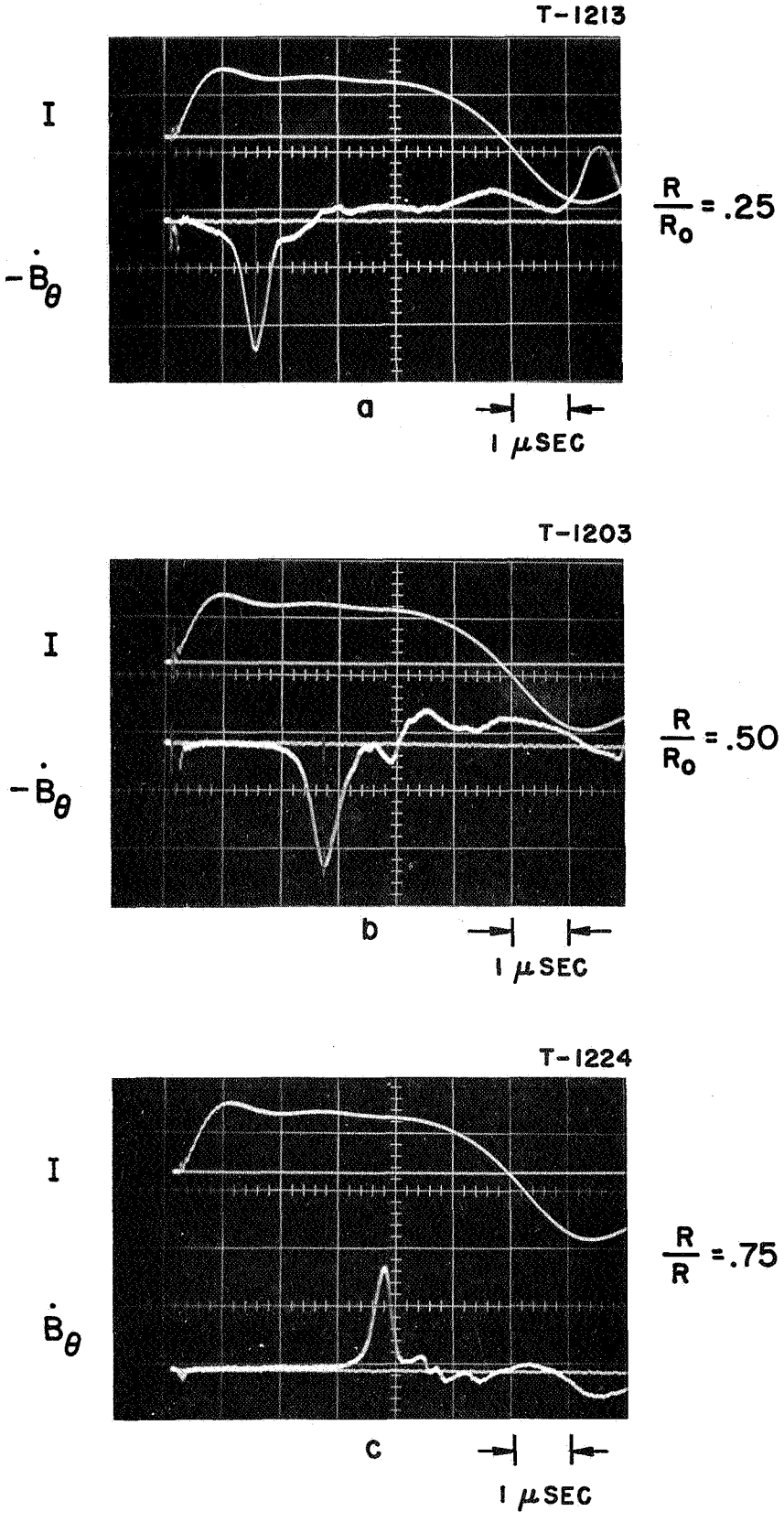

B-PROBE RADIAL SURVEY, MIDPLANE

($\frac{z}{h}$ = .5)

FIGURE 4-7

AP25-P74-61

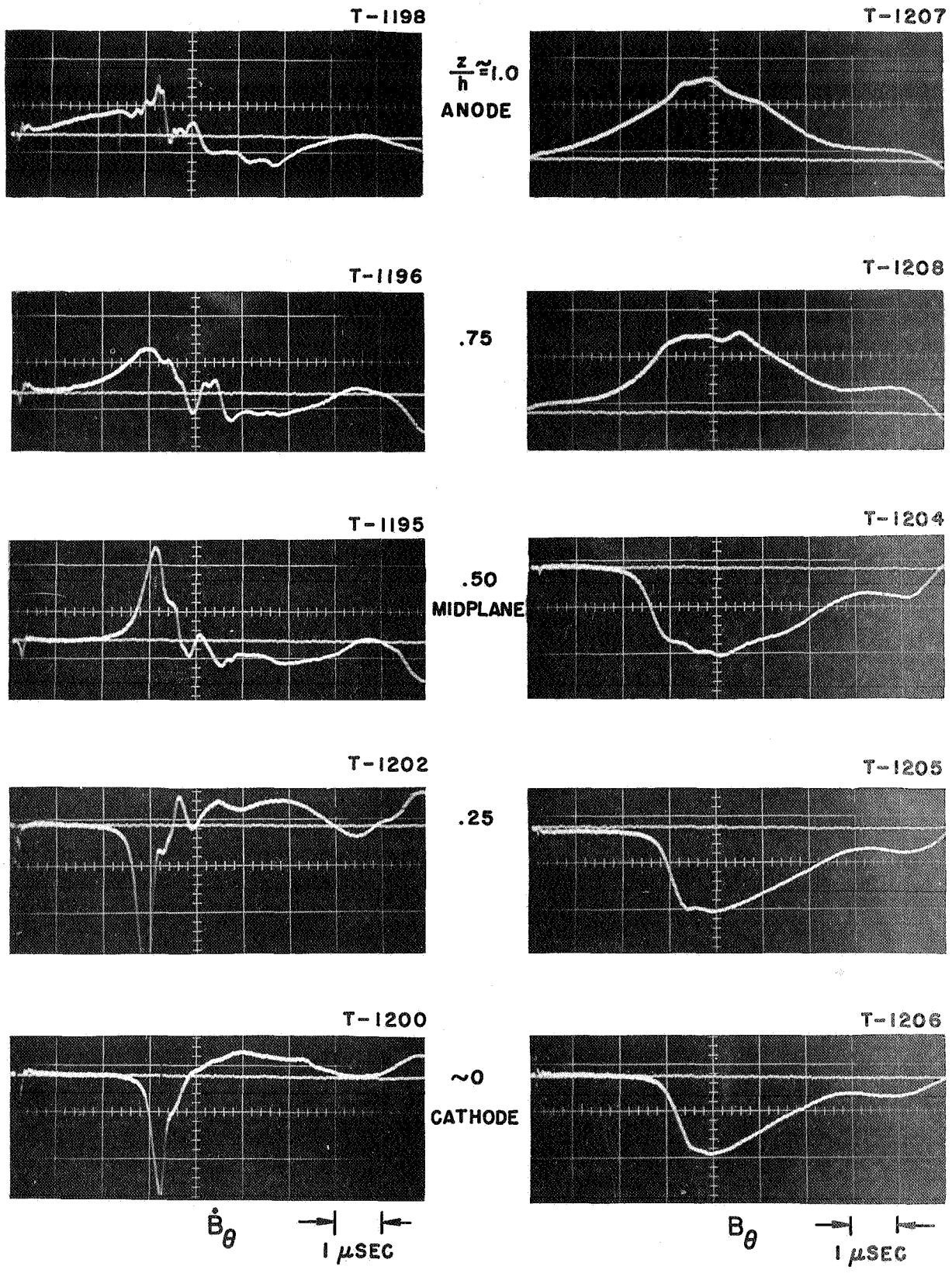

A1235 - P99-67

B-PROBE AXIAL SURVEY, $R/R_0 = .5$

FIGURE 4-8

traverse at half radius. B_θ was detected almost immediately on the anode and increased slowly thereafter. A well-defined sheet cannot be identified. When the probe was positioned closer to the cathode, $\dot{B}_\theta$ became sharper and narrower until on the cathode the current sheet appeared as a thin, sharp spike. The cathode region thus became interesting for further experiments because there the current sheet achieved its best definition.

Another structural feature which emerged from these surveys was a sort of progressive bifurcation or splitting of the current distribution, a phenomenon first noted by Black.[13] A typical "simple bifurcation," or double-sheeted distribution, is shown in Fig. 4-9. The specific conditions which were found to engender bifurcation are hard to describe precisely because the phenomenon was unsteady, exhibited strong radial and axial dependence, and was not notably reproducible. A general conclusion, however, was that bifurcation was favored (a) near the anode, and (b) near the centerline (axis) of the chamber. Hence, the portion of the chamber volume favoring single-sheeted current zone development was bordered by the glass sidewall and cathode surfaces. The bifurcation phenomenon is interesting and perhaps fundamentally important in its own right, and investigations at Princeton[8] are currently focusing on this problem. From the viewpoint of the present research goals, however--the investigation of the simplest current sheets obtainable in a practical device--current bifurcation and multiple-structured zones are complications to be avoided.

On the basis of the findings discussed above, two probing stations were selected for the detailed investigations to follow.

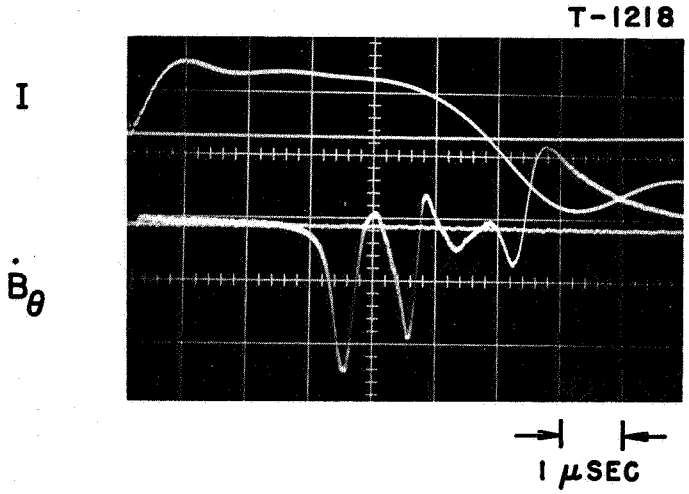

CURRENT SHEET BIFURCATION

FIGURE 4-9

Both locations were at half radius, as shown in Fig. 4-4, the first on the cathode to take advantage of the exceptionally sharp, stable current sheets there, and the second at midplane to exploit the marked planarity of the midplane current sheet. The choice of midradius, common to both stations, locates the sheet equidistant from the axis (r = 0) where the magnetic field has a singular point, and from the sidewall (r = 10 cm) where undesirable transients in the initiation phase and the presence of the dielectric would prejudice the experiments.

From Fig. 4-5, the velocity of the current sheet is found to be 2.04×10^4 meters/second at the cathode station and 2.47×10^4 meters/second at the midplane station. The current sheet profile at midradius is shown in Fig. 4-6.

Calibrated Probe Measurements. Only the unjacketed probes (Fig. 4-1) were calibrated, and these were calibrated in position in the discharge chamber. An aluminum shorting post 1" in diameter was mounted between the two electrodes on the pinch chamber axis and, with the probes connected, the machine was fired. The current in the shorting bar was determined using the current traces and the known Rogowski coil calibration (Chapter III), and the enclosed current was then used to calculate B_θ at the probe position:

$$B_\theta = \frac{\mu_0 I}{2\pi R} \qquad \text{(MKS)}$$

Due to the geometry there were no other components with the shorting post.

All three components of field did in general develop in the sheet, from the more complicated current patterns, and these are shown to scale in raw data form in Figs. 4-10 and 4-11 for

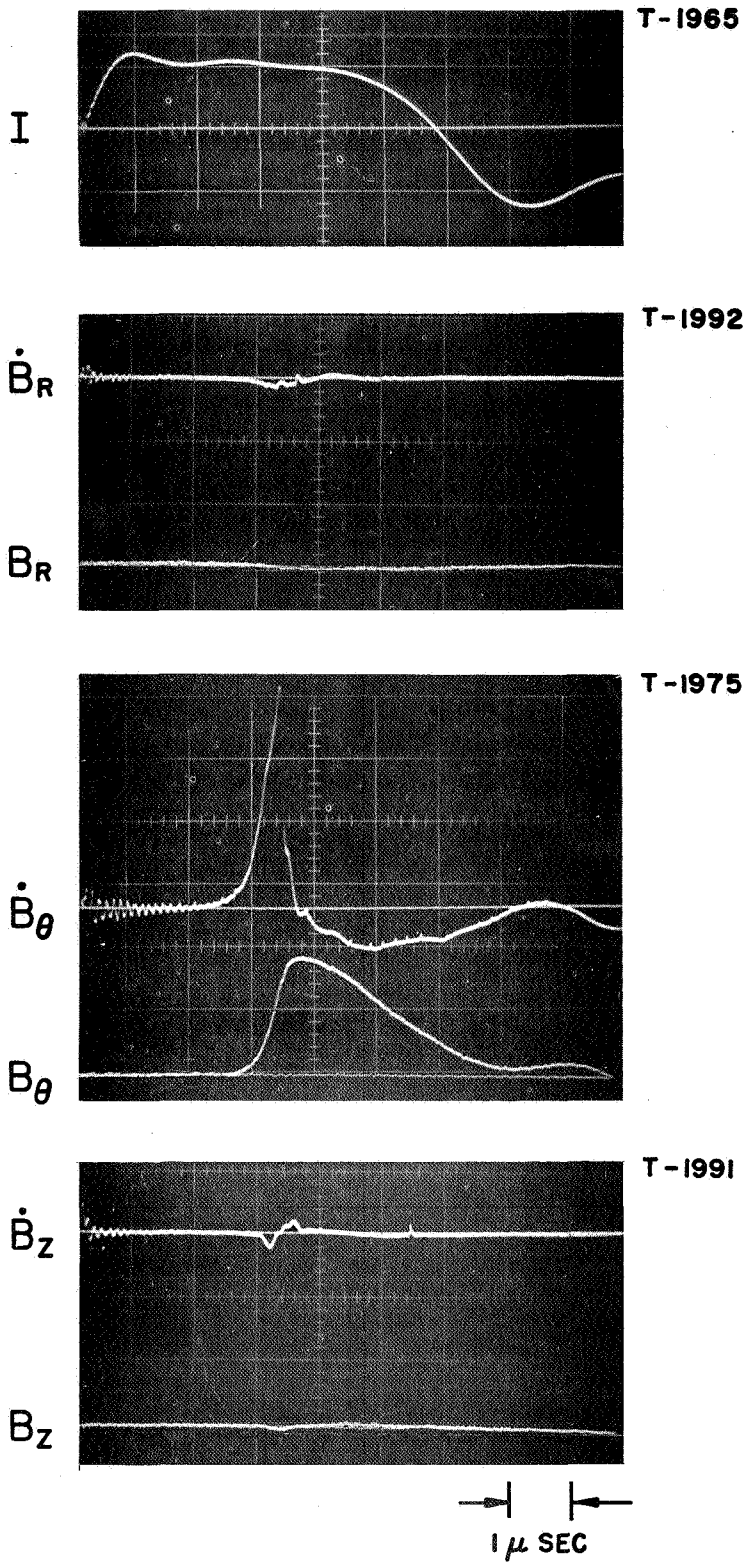

B-PROBE DATA AT CATHODE

$(\frac{R}{R_0} = .5, \frac{z}{h} \cong 0)$

FIGURE 4-10

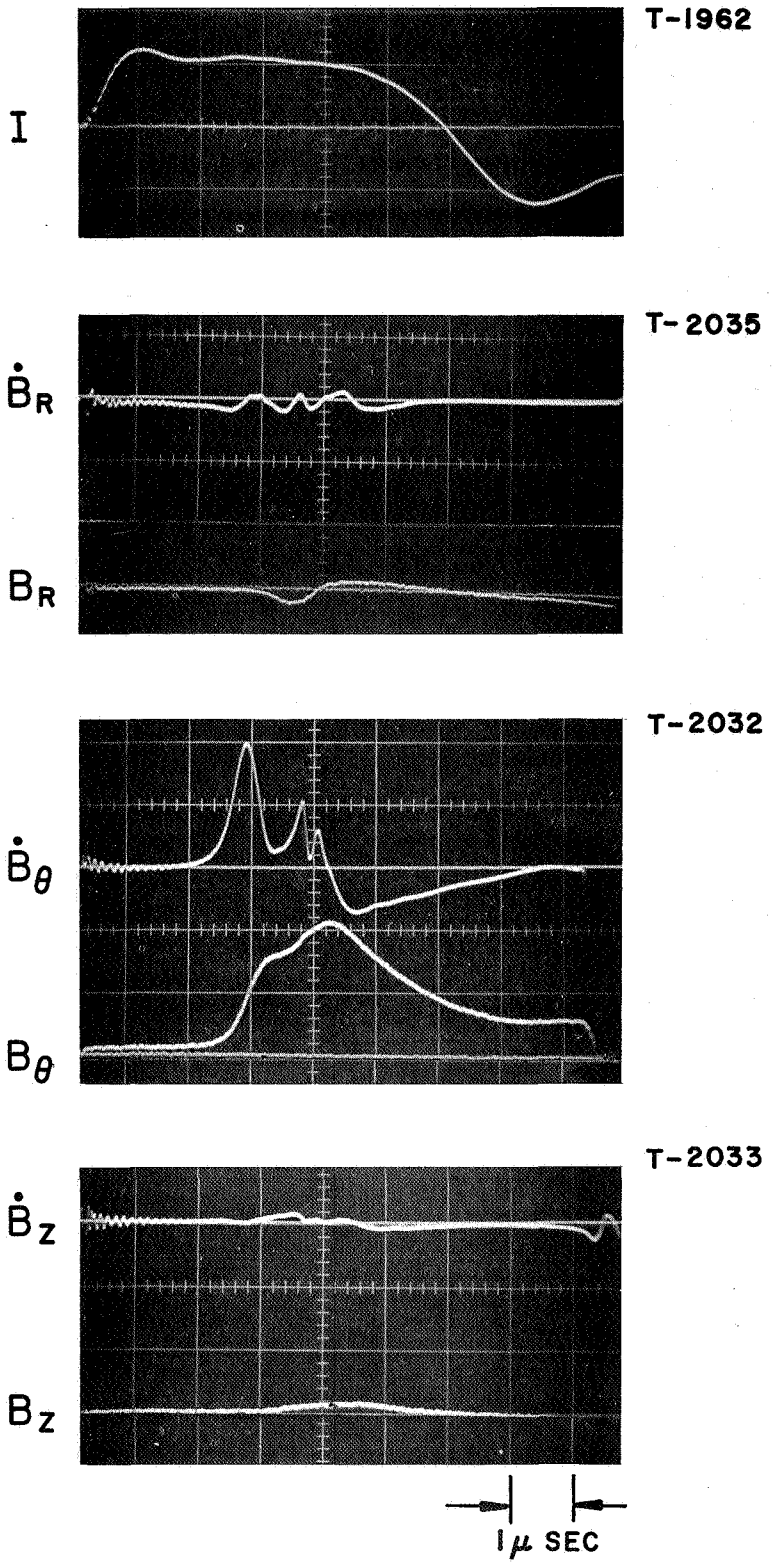

B-PROBE DATA AT MIDPLANE

$\left(\frac{R}{R_o} = .5,\ \frac{z}{h} = .5\right)$

FIGURE 4-11

both selected probing stations. The azimuthal component is clearly dominant at both positions, and the increased tendency for the current distribution to split off a trailing sheet or wake is evident at the midplane location. For the present we shall concentrate on the azimuthal fields, and the calibrated curves for $\dot{B}_\theta(t)$ and $B_\theta(t)$ from these oscillograms are displayed in Figs. 4-12 and 4-13.

4.6 Current Density Distributions

Ampere's law (Appendix A) relates the spatial variation of the magnetic field to the current density

$$\text{(MKS)} \qquad \nabla \times \bar{B} = \mu_0 \bar{J} \qquad (A\text{-}2)$$

since the displacement current is not significant at megacycle frequencies. The current density components are given by

$$\mu_0 J_r = \frac{1}{r}\frac{\partial B_z}{\partial \theta} - \frac{\partial B_\theta}{\partial z} \qquad (4\text{-}5)$$

$$\mu_0 J_\theta = \frac{\partial B_r}{\partial z} - \frac{\partial B_z}{\partial r} \qquad (4\text{-}6)$$

$$\mu_0 J_z = \frac{1}{r}\left[\frac{\partial (r B_\theta)}{\partial r} - \frac{\partial B_r}{\partial \theta}\right] \qquad (4\text{-}7)$$

The second term on the right of eq. (4-7) is negligible compared to the first because azimuthal symmetry precludes θ derivatives and $B_r << B_\theta$ anyway. The other two components of $\bar{J}$ are at best small, and we will concentrate here on J_z:

$$\mu_0 J_z \cong \frac{1}{r}\frac{\partial (r B_\theta)}{\partial r} \qquad (4\text{-}8)$$

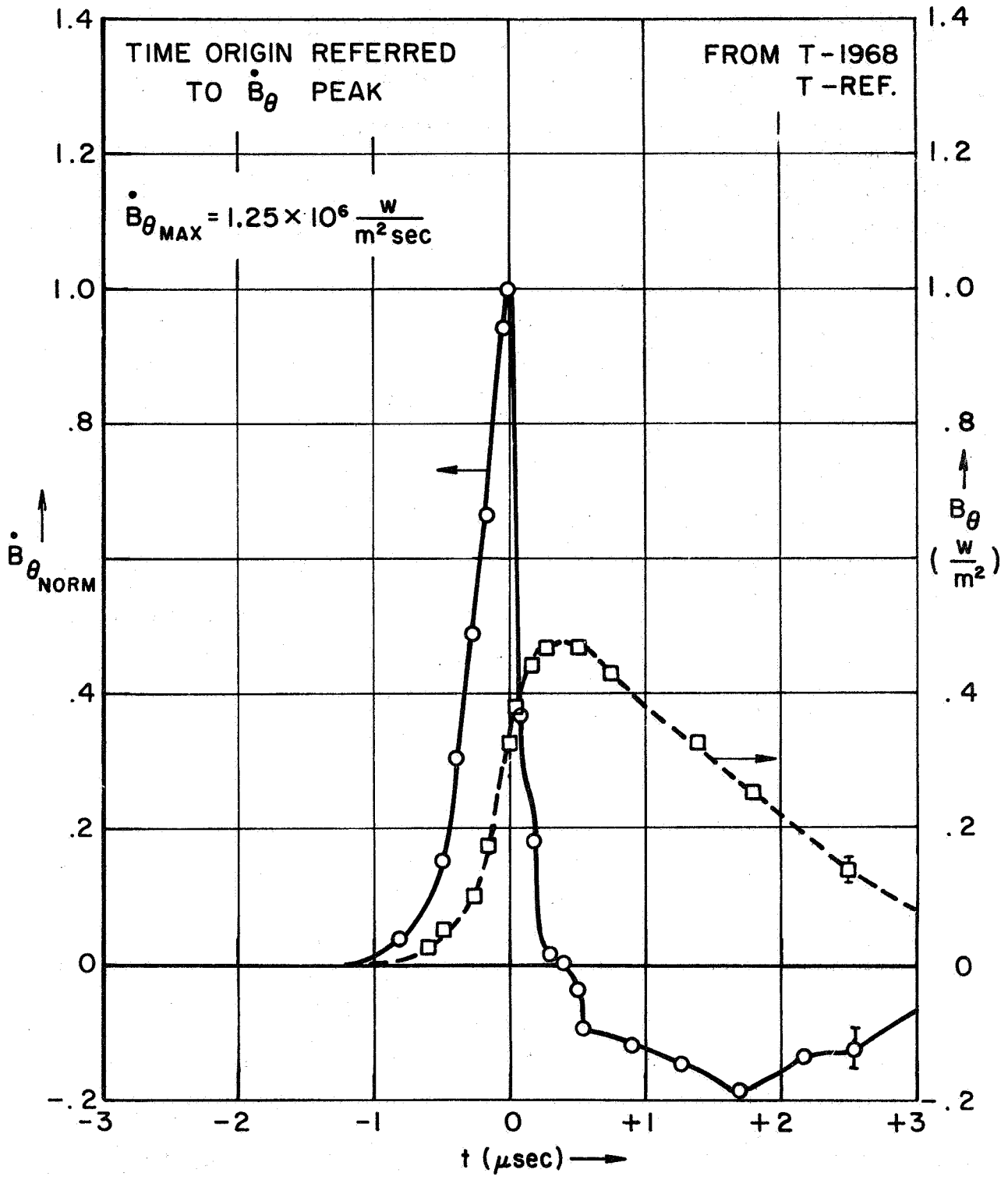

MAGNETIC FIELDS AT CATHODE

$(\frac{R}{R_o} = .5, \frac{z}{h} \cong 0)$

FIGURE 4-12

AP25-4262-67

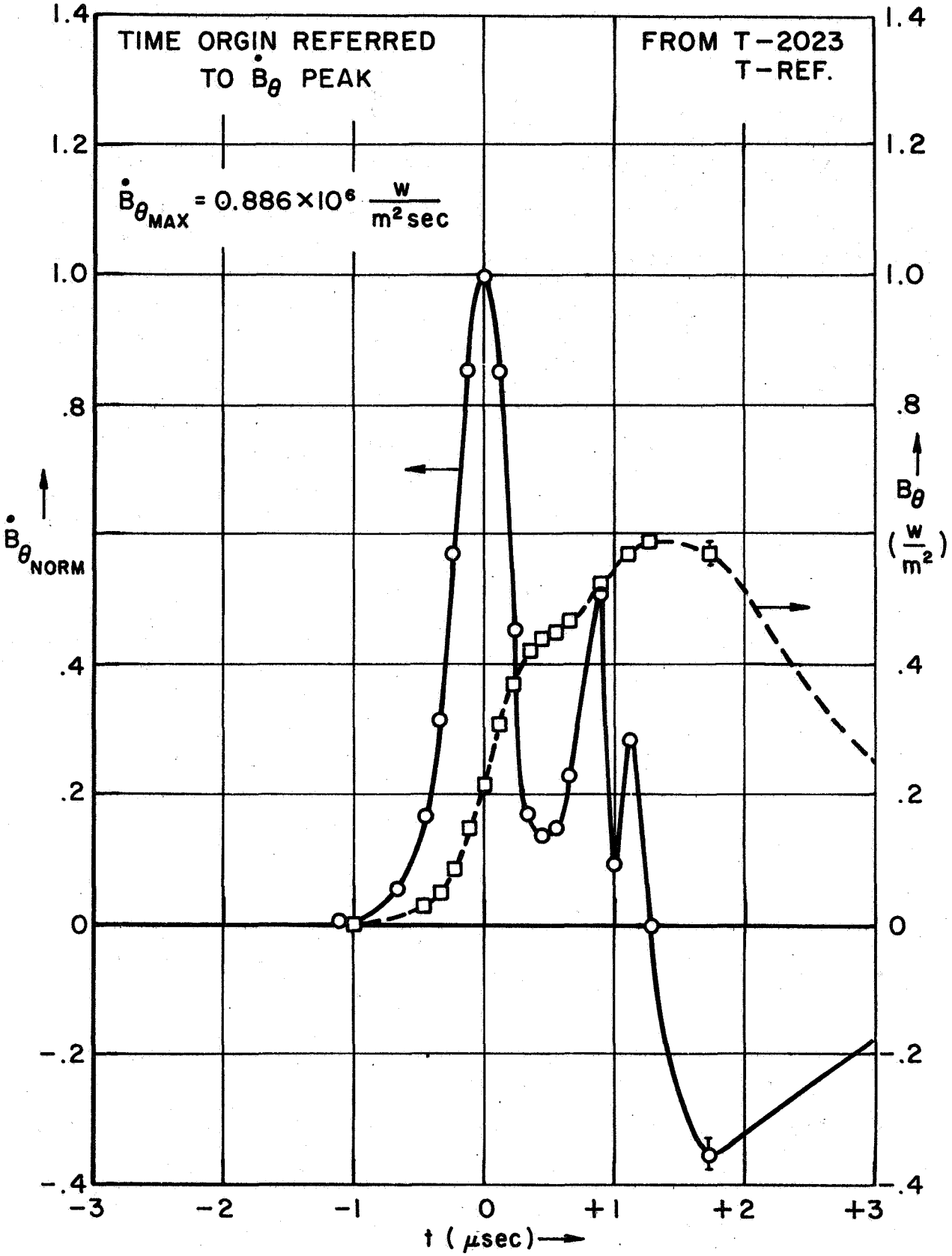

MAGNETIC FIELDS AT MIDPLANE
($\frac{R}{R_o}$=.5, $\frac{z}{h}$=.5)

FIGURE 4-13

or

$$\mu_0 J_z = \frac{\partial B_\theta}{\partial r} + \frac{B_\theta}{r} \qquad (4\text{-}9)$$

Axial Current Density. The two most commonly used methods for obtaining J_z distributions in this geometry follow directly from the last two equations. To use eq. (4-8), one makes a radial probe survey and obtains, by cross plotting this data, a curve of B_θ vs. r for a specific time. The product rB_θ can then be calculated and plotted as a function of r. Finally, graphical differentiation of the rB_θ vs. r curve and division by r yields J_z, point by point, at a given time. An equally convoluted procedure is followed if eq. (4-9) is employed.

While involving no explicit approximations, either of these procedures is both tedious and inexact due to the difficulty of differentiating experimental data accurately, and the large number of measurements and calculations required. The fact that they provide no way for readily visualizing current distributions from the probe records is a further inconvenience.

The following analysis attempts to correct these deficiencies by manipulating integral and differential statements of Ampere's law to obtain a useful relation between $J_z(t)$ and direct B-probe data, $\dot{B}_\theta(t)$ and $B_\theta(t)$.

Assume a small magnetic probe to be located at radius R in the coordinate system of Fig. 4-2, past which an axisymmetric current distribution of the form $J_z(r,t)$ is moving radially inward with velocity U_s.

The total current enclosed interior to the probe

position R is

$$I_{en}(R,t) = \int_0^R 2\pi r\, J_z(r,t)\, dr \tag{4-10}$$

Integration of Ampere's law over the circular electrode area bounded by R gives the familiar result

$$B_\theta(R,t) = \frac{\mu_0}{2\pi R} I_{en}(R,t) \tag{4-11}$$

Since the enclosed current is a function of the enclosure radius R, eq. (4-10) can be differentiated to yield

$$\frac{\partial I_{en}(R,t)}{\partial R} = 2\pi R\, J_z(R,t) \tag{4-12}$$

a result which could also have been obtained directly from eq. (4-11) and Ampere's law.

At a given probe position, the probe responds to $\frac{\partial B_\theta}{\partial t}$. Forming the derivative from eq. (4-11):

$$\frac{\partial B_\theta(R,t)}{\partial t} = \frac{\partial}{\partial t}\left[\frac{\mu_0}{2\pi R} I_{en}(R,t)\right] \tag{4-13}$$

(It should be noted that an analysis entirely equivalent to the following can be carried through using substantial derivatives, $\frac{D}{Dt} \rightarrow \frac{\partial}{\partial t} + \bar{V}\cdot\nabla$, by virtue of the fact that $\bar{B}$ does not actually propagate in the pinching process even though the current source does. More specifically, B_θ exhibits a phase, or interface, velocity but no group, or bulk, motion. Since $\bar{B}$ is also stationary for stationary source currents, it can be inferred that, to first order, $\bar{B}$ is independent of the source motion.)

If the probe is held fixed during a measurement, as of

course it is, then R is not a function of time:

$$\frac{\partial B_\theta}{\partial t}(R,t) = \frac{\mu_0}{2\pi R}\frac{\partial I_{en}}{\partial t}(R,t) \qquad (4\text{-}14)$$

The time rate of change of the enclosed current on the right-hand side arises from two sources: (1) the current in the enclosed portion of the distribution changes due to circuit current changes, and (2) the distribution $J_z(r,t)$ propagates further past the probe position to enclose additional current. Thus, symbolically,

$$\frac{\partial B_\theta}{\partial t} = \frac{\mu_0}{2\pi R}\left[\dot{I}_{circuit} + \dot{I}_{convection}\right] \qquad (4\text{-}15)$$

The second term on the right, arising from the radial motion of the current sheet, can be written

$$\dot{I}_{convection} = -U_s\frac{\partial I_{en}}{\partial r}(R,t) \qquad (4\text{-}16)$$

provided the current distribution maintains a self-similar profile during its incursion over the probe. U_s can then be identified with the sheet velocity.

The other term in eq. (4-15) accounts for changes in the enclosed current due to circuit current fluctuations, and thus can be expressed as the product of $\frac{dI}{dt}$ and the enclosed current fraction. $\frac{dI}{dt}$ or $\dot{I}$ can be obtained from the Rogowski coil, viz Fig. 3-2, and the enclosed current at time t is given by inverting eq. (4-11):

$$I_{en}(R,t) = \frac{2\pi R}{\mu_0}B_\theta(R,t) \qquad (4\text{-}17)$$

Therefore the unsteady term arising from the circuit current may

be written

$$\dot{I}_{circuit} = \frac{dI}{dt} \times \left(\frac{I_{eq}}{I}\right) = \left(\frac{\dot{I}}{I}\right) \times \frac{2\pi R B_\theta}{\mu_0} \qquad (4\text{-}18)$$

Substitution of eqs. (4-18), (4-16), and (4-12) into eq. (4-15) yields the desired result:

$$J_z(R,t) = -\frac{1}{\mu_0 u_s}\left[\dot{B}_\theta(R,t) - B_\theta(R,t) \times \frac{\dot{I}}{I}(t)\right]$$

This expression relates the current density at the probe location, as a function of time, to directly measurable quantities. It can be simplified to include only time dependence explicitly, since R is fixed for any given experiment:

$$J_z(t) = -\frac{1}{\mu_0 u_s}\left[\dot{B}_\theta(t) - f_I(t)\, B_\theta(t)\right] \qquad (4\text{-}19)$$

where the ratio $\frac{\dot{I}}{I}(t)$ has been denoted by f_I. Since the external current waveform determines both $I(t)$ and $\dot{I}(t)$, f_I is a predetermined function once the waveform is specified, i.e. it does not depend on the particular experiment, the probe location, and so on. For a <u>constant</u> driving current f_I vanishes by definition, and $J_z(t)$ is determined solely by $\dot{B}_\theta(t)$ and the sheet velocity, which is nearly constant for the short transit time over the probe.

f_I for the rectangular current waveform of these experiments was calculated from the data of Fig. 3-2 and the results are shown in Fig. 4-14. Notice that over the time interval of interest, $1\,\mu\text{sec} < t < 4\,\mu\text{sec}$, f_I is very nearly zero, justifying the close identification of J_z with $\dot{B}_\theta$. Current distributions can thus be quickly and accurately estimated from a single oscillogram.

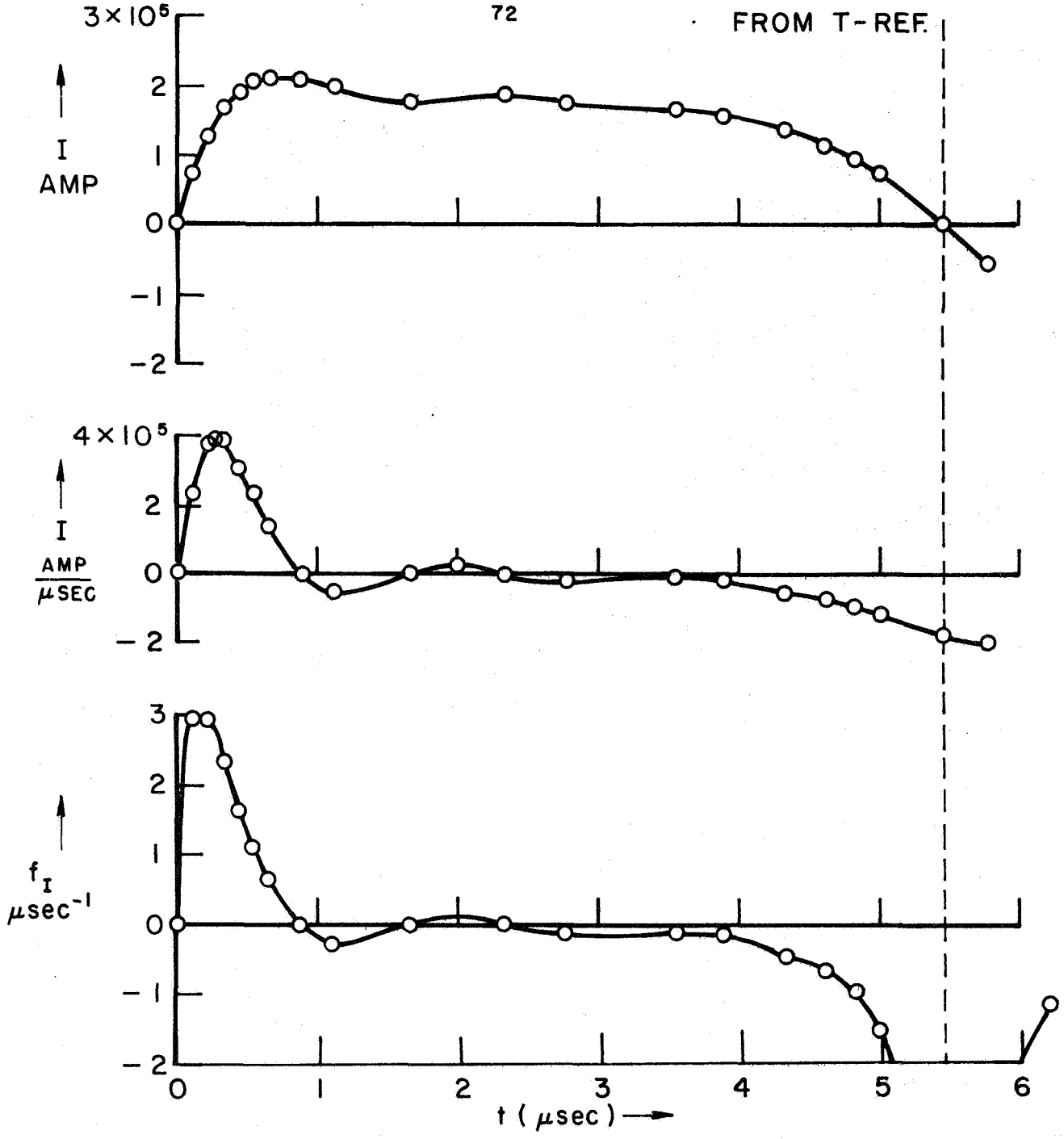

AP25-4269-C7

CIRCUIT CURRENT AND ASSOCIATED WAVEFORMS

FIGURE 4-14

Current densities calculated in the sheet from the data of Figs. 4-12, 4-13, and 4-14, using eq. (4-19), are shown in Fig. 4-15 and 4-16. The maximum value of J_z, measured on the cathode, was just over 5×10^7 amperes/meter^2.

These results can be checked by calculating enclosed currents from eq. 4-10 with the aid of a Galilean coordinate transformation. Thus

$$I_{enl} = \int_0^R 2\pi r \; J_z(r,t)\, dr \tag{4-20}$$

$$\stackrel{u}{=} 2\pi R\, u_s \int_{\substack{\text{across}\\ \text{sheet}}}^{t} J_z(R,t)\, dt \tag{4-21}$$

where the time integration is most easily carried out by plotting Figs. 4-15 and 4-16 on graph paper and counting squares.

The total enclosed current at the cathode probe position as calculated by this procedure almost exactly equals the current carried by the primary midplane sheet, about 125,000 amperes. The second and third "sheets" at midplane add another 35,000 amperes to give a total current of 160,000 amperes passing the midplane location. Since the external circuit delivers a nearly constant 175,000 amperes to the discharge, it is concluded that the remaining current does not participate directly in the pinching process but elects instead to remain in the ionized environment swept over by the primary sheet. The calibrated magnetic probe data of Figs. 4-12 and 4-13 confirm these conclusions and show the fractional division of current calculated by these methods to be quite accurate.

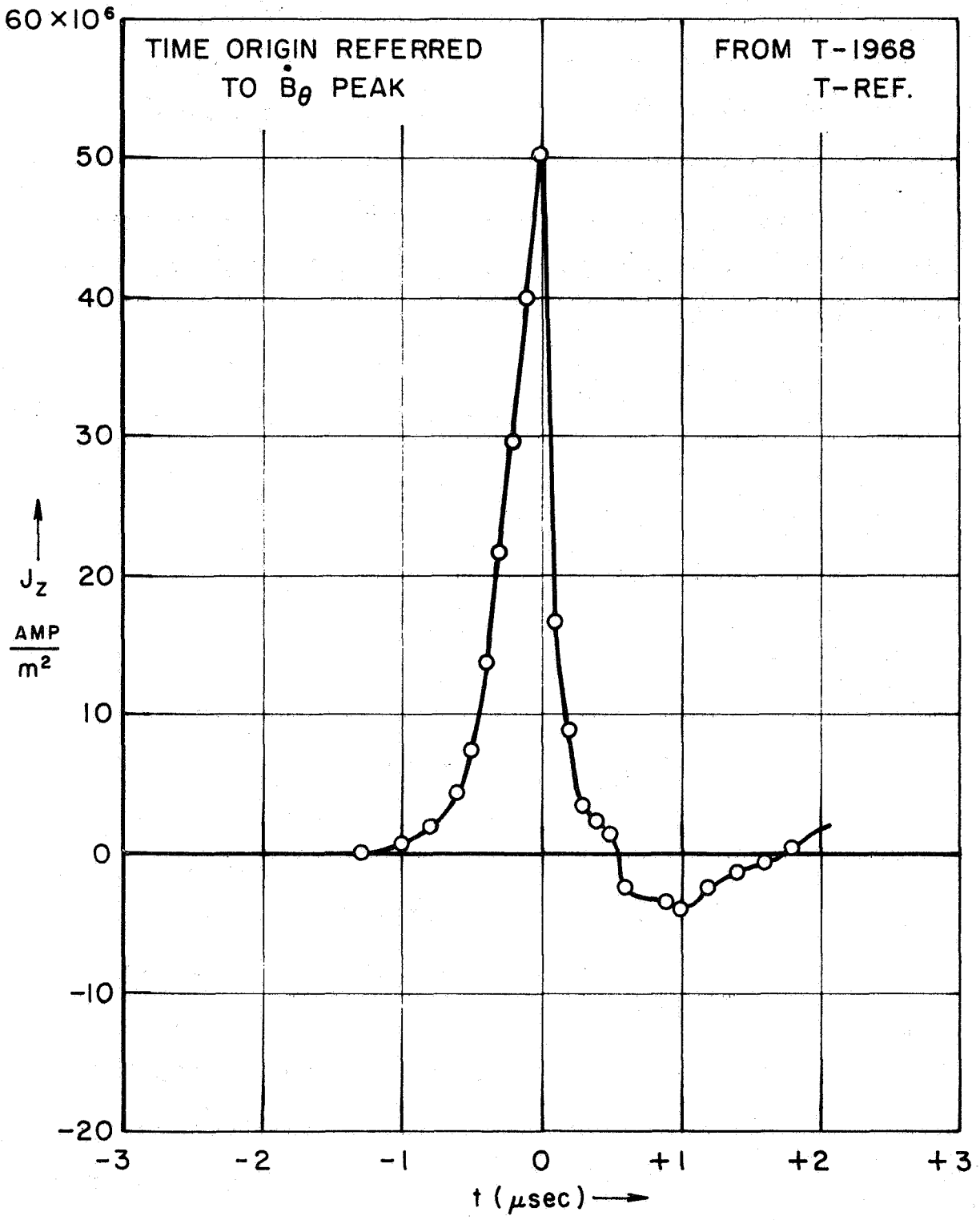

CURRENT DENSITY AT CATHODE

$\left(\frac{R}{R_0}=.5, \frac{z}{h}=0\right)$

FIGURE 4-15

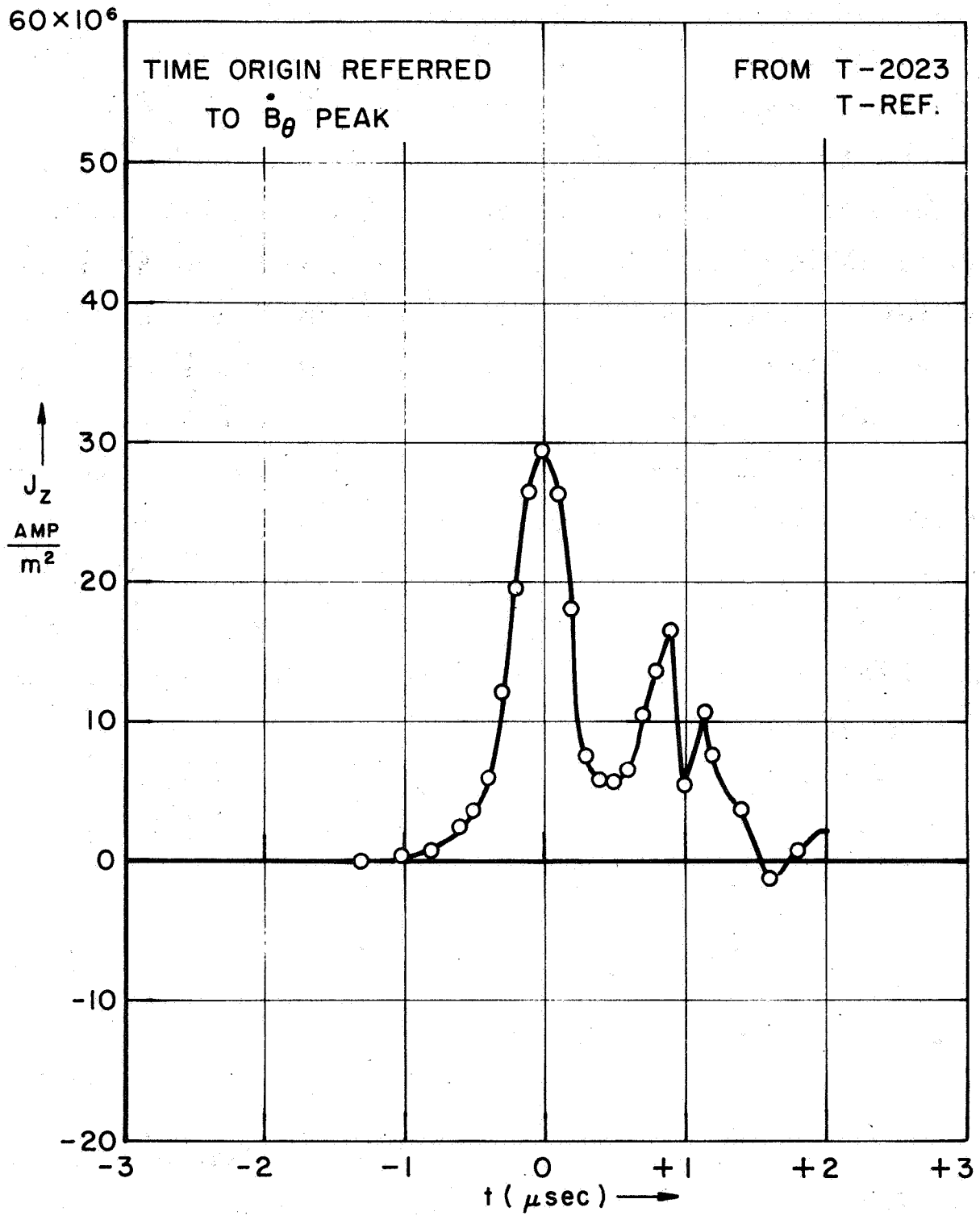

CURRENT DENSITY AT MIDPLANE

$\left(\frac{R}{R_o} = .5, \frac{z}{h} = .5\right)$

FIGURE 4-16

The fact that more current is enclosed at the same radius at midplane than at the cathode suggests that the overall current pattern contains circulating components, stationary attachment points, and/or other complicated features. The persistence of such internal circulating currents is responsible for the measured residual B_θ field which remains even after the external circuit current reverses (Fig. 4-10). Thus eq. (4-19) is valid only as long as the loop currents are dominated by the axial conduction current, and the computed current density profiles are terminated when this criterion fails. Such current pattern irregularities are primarily confined to the downstream or wake regions of the flow field behind the sheet and are not a serious hinderance to experiments on the primary sheet structure. The cathode-adjacent regions of the sheet are obviously superior in this respect.

Radial and Azimuthal Current Density. Exact calculations for the other two components of current density are more difficult to make. From eqs. (4-5) and (4-6) we find

$$J_\theta \cong 0 \tag{4-22}$$

$$J_r \cong -\frac{1}{\mu_0}\frac{\partial B_\theta}{\partial z} \tag{4-23}$$

The axial gradient in B_θ is evident from Fig. 4-8, but numerical calculations are jeopardized by the graphical differentiation procedure required. Furthermore, radial polarization currents arising from the radial electric field are possible on the scale of the probe coil dimensions, and hence would be

undetectable with these probes. For these reasons radial current densities were calculated by an entirely different technique, presented in Chapter VII.

$\overline{J} \times \overline{B}$ Forces. The Lorentz force on the conducting gas, $J_z B_\theta$, has been calculated for the two probe locations and is shown in Figs. 4-17 and 4-18. The implosive force density acting on the sheet at the cathode was about 2.5 times the corresponding midplane force density, reaching a maximum of 1.6×10^7 newton/meter^3. The large contribution from the trailing sheet structure at midplane reflects the large magnetic field associated with the primary sheet.

4.7 Comments on Probe Resolution

The time resolution of a 2 mm probe coil at the prevailing sheet velocities is $\sim 10^{-7}$ sec, as mentioned in section 4.4. As a consequence, data points were taken from the oscillograms in 0.1 μs steps through the sheet, and were assumed to represent an average value over the probe dimensions, e.g. 2 mm, at each point. The fact that many experimental profiles in this chapter (and in later chapters) change considerably between data points, e.g. over a probe diameter, shows that spatial resolution may still be troublesome. The profiles are generally smooth peaked functions of time, which ameliorates the problem somewhat, but the maximum value of the more sharply peaked functions still may escape the resolution of the probes. Therefore the peak values at t = 0 (see section 5.4 for a discussion of this notation) should perhaps be regarded more in a qualitative than in a quantitative sense.

The problem could perhaps be overcome with the B probes by

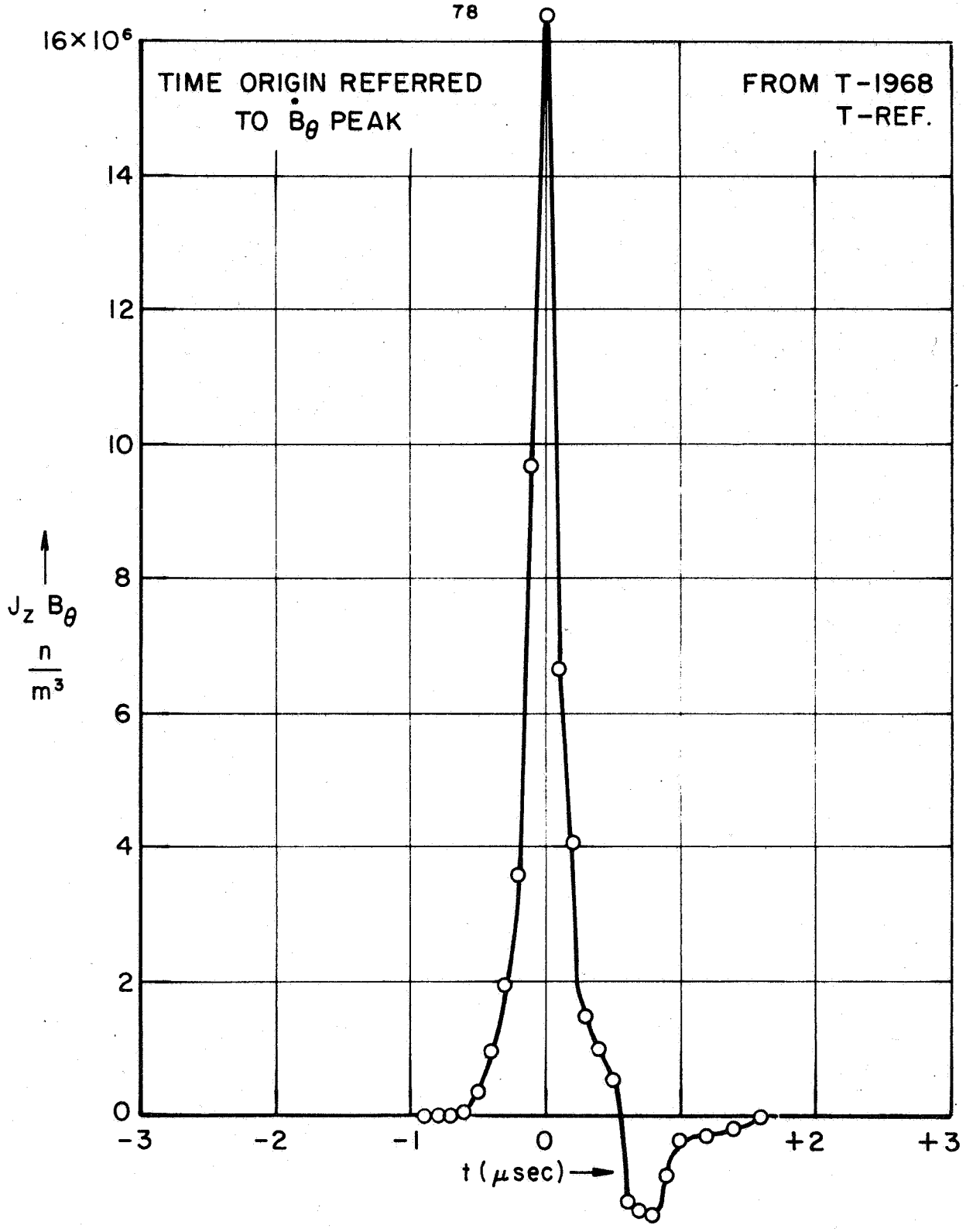

LORENTZ FORCE AT CATHODE

$\left(\frac{R}{R_0} = .5, \frac{z}{h} = 0\right)$

FIGURE 4-17

AP25-4258-67

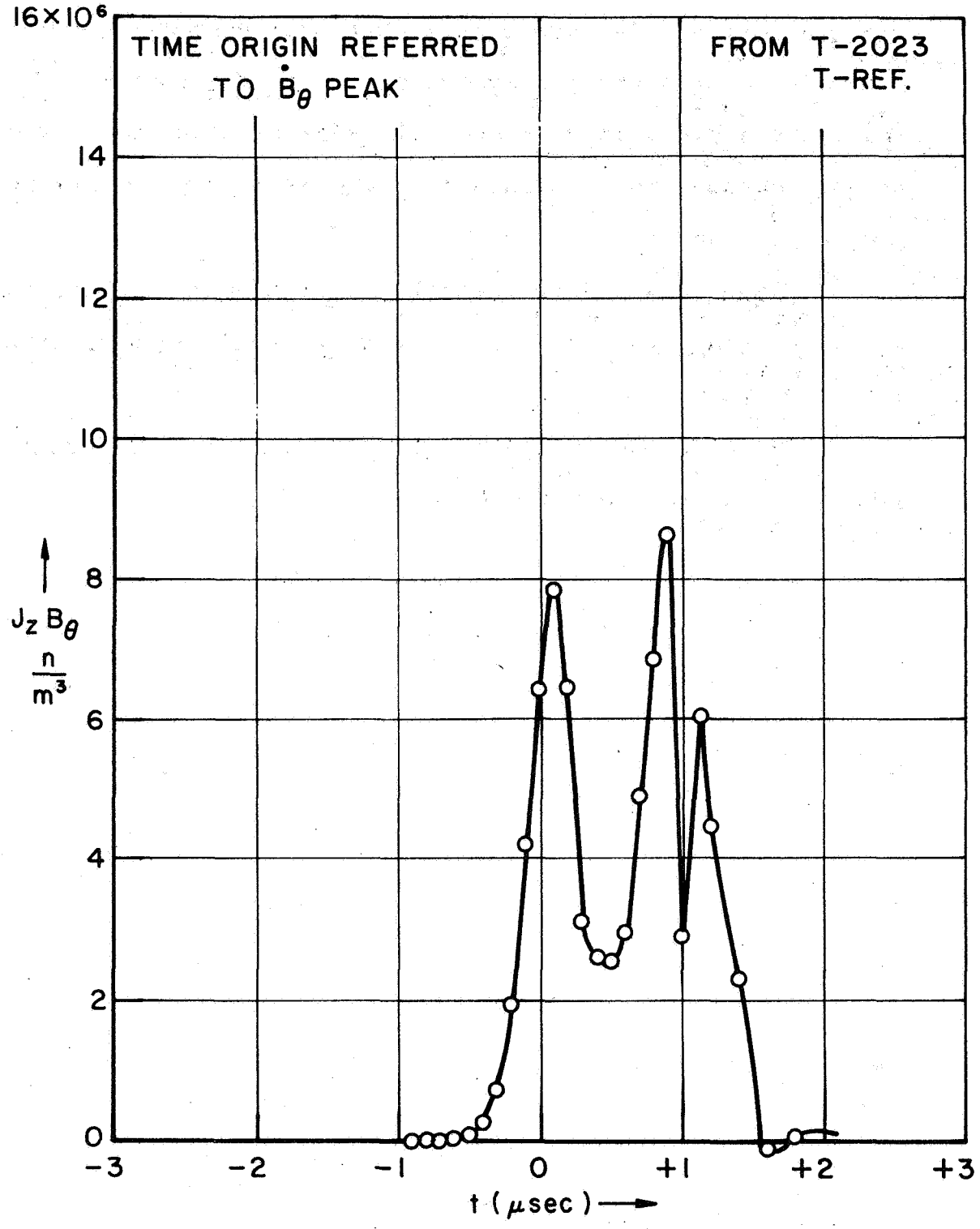

LORENTZ FORCE AT MIDPLANE

$(\frac{R}{R_0} = .5, \frac{z}{h} = .5)$

FIGURE 4-18

using a much smaller probe coil, but such economy is not possible for the other diagnostic probes (Chapters V and VI), which are limited to 2 mm spatial resolution for more fundamental reasons, to be discussed. Therefore 2 mm probes were used here also.

These remarks apply equally to the probes discussed in following chapters, and the maximum value of the steeper profiles obtained there.

The next chapter deals with electric field measurements within the current distribution.

Chapter V

ELECTRIC PROBES - THEORY AND EXPERIMENT

5.1 Introduction

It has previously been shown, in Chapter IV, that the self-magnetic field of the current sheet has effectively a single, azimuthal component. The interior electric field by contrast has two significant components, both normal to B_θ, which are related to the current density through a tensor conductivity.

The plasma conductivity components are finite (Chapter VII), and thus an applied E_z field is maintained because of resistive voltage drop in the reference frame of the moving current sheet. In the laboratory frame E_z is measured somewhat larger because of the inclusion of the $U_s B_\theta$ induced field.

If the applied electric field were the only component present, the charged particles would attempt to execute crossed field $E_z B_\theta$ drift parallel to the sheet motion, the ratio of radial to axial current depending on the relative frequency of particle collisions, through the Hall parameter. This process is not a self-consistent description however, for it leads to a streamwise separation of electrons and ions which rapidly gives rise to an opposing radial electric field. This E_r polarization field, arising from a radial displacement of the centroids of the electron and ion density distributions within the sheet, serves the useful function of accelerating the overrun ions in the ambient plasma from rest to the stream velocity, thus supplying the fundamental mechanism for sweeping and accumulating mass.

The particle trajectories will develop in accordance with the net electric field, which has both transverse (applied) and streamwise (polarization) components, and the crossed magnetic field. Particle dynamics are considered in Chapter VII. In this chapter quantitative measurements of the radial and axial electric field strength distributions in the sheet are presented and the principal sources of error are discussed.

5.2 Probe Design

The measurement of potential difference between two points in a plasma can be most easily carried out by inserting small electrodes directly into the plasma at these points, in such a way that they assume the local floating potential. Burkhardt and Lovberg[27] (1962) developed and used this method of measuring electric fields associated with a moving current distribution, and their basic techniques have been adopted for these experiments.

The pair of probe conductors entered the discharge chamber as a small coaxial line, exposing to the plasma a pair of metallic electrodes in the form of a circular outer ring and central conducting wire, as shown in Fig. 5-1. The effective separation distance between probe electrodes was thus along the probe axis and in these experiments was fixed at 2 millimeters. This spacing was substantially less than the total sheet thickness of two centimeters, permitting generally adequate spatial resolution of the interior electric field structure.

The electric probe had an outer sleeve of nylon, similar to the later model B-probes after which it was patterned, and it derived structural rigidity from the interior hollow coaxial brass

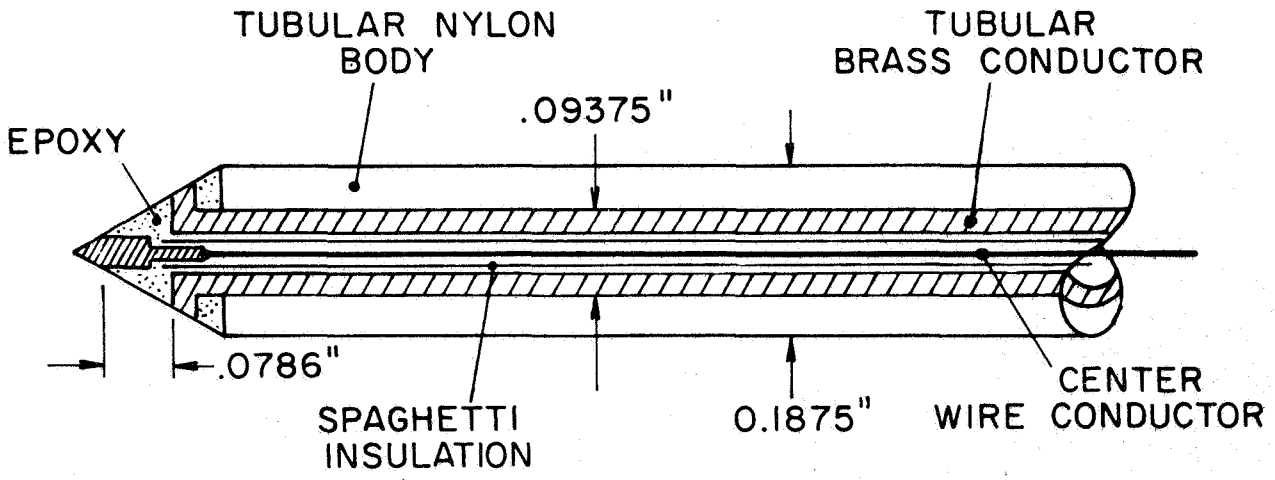

A

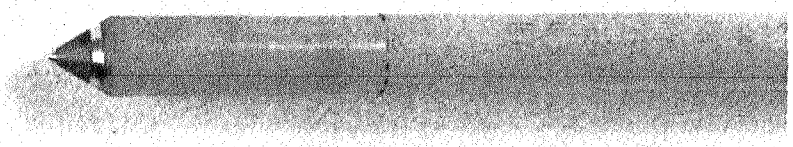

B

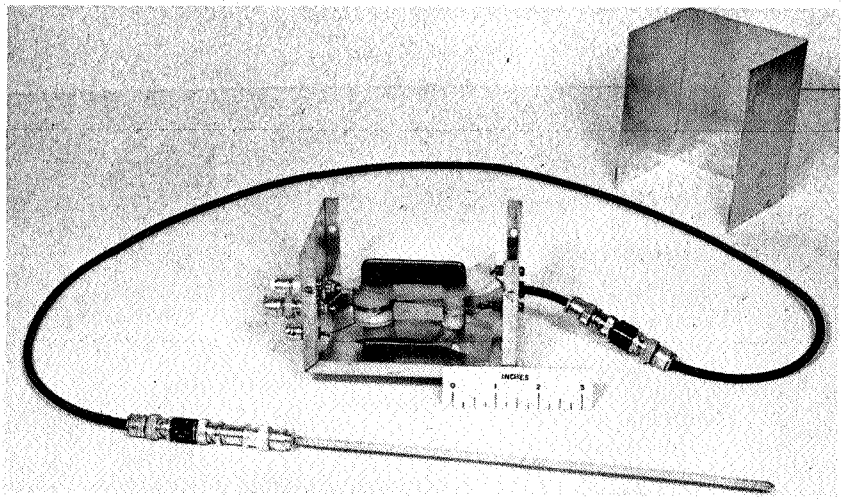

C

ELECTRIC PROBE

FIGURE 5-1

conductor which joined the ring electrode. A truncated cone of machine-turned epoxy separated the concentric electrodes and provided a vacuum seal. The resulting probe was axisymmetric and when inserted into the discharge chamber through an O-ring sealed probing port, could be bent to any reasonable shape and restraightened without affecting either its vacuum properties or structural integrity.

The probe leads outside the chamber were connected to the electrical circuit of Figs. 5-1c and 5-2. This circuit, based on the Burkhardt-Lovberg design, was adapted for linear pinch experiments by Burton[14] and Turchi[8] at Princeton.

The transformer served to pass the difference signal between probe electrodes, typically 10 volts, while eliminating the common mode signal, typically a kilovolt. Thus its presence in the circuit effectively isolated the oscilloscope from the potentially dangerous voltages existing in the plasma and inductively coupled the probe to the outside world.

The two variable resistors shown in Fig. 5-2 controlled the probe circuit response characteristics. Resistor R_1 provided electrical loading and terminated the 50 ohm probe cable. For the majority of experiments, proper termination in the 50 ohm characteristic impedance was satisfactory.

Resistor R_2 was chosen to provide adequate frequency response. The optimum value was found to be about 200 ohms, allowing the circuit to pass a square wave of 45 nanosecond rise time over the frequency range from one kilocycle to ten megacycle, the range of interest for the 1 μsec/cm sweep speeds employed. The entire circuit was heavily shielded and insulated

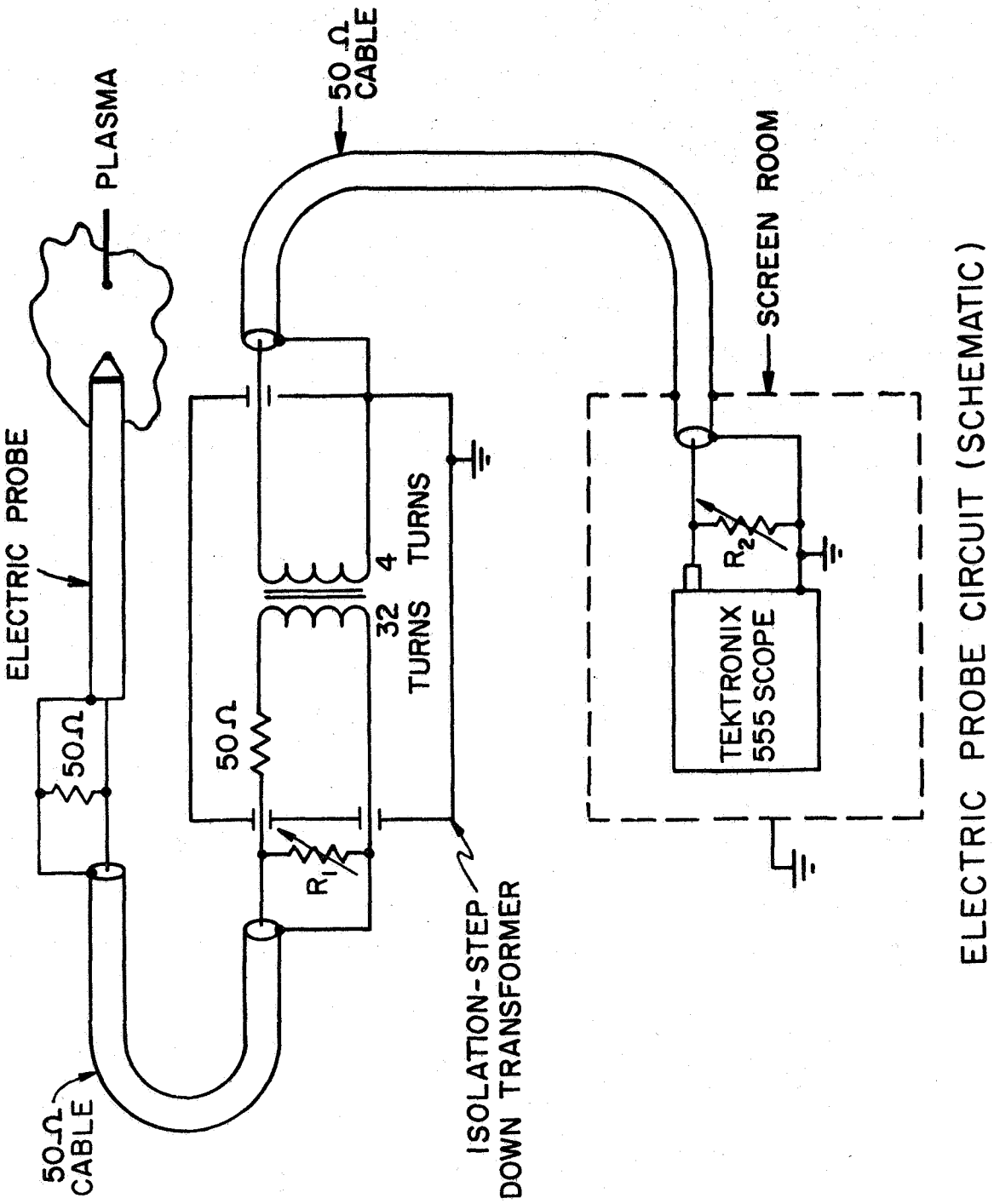

FIGURE 5-2

AP25-40550 65

and in operation was mounted on the side of the screen room. Further details of the circuit design, including an equivalent circuit representation of the ferrite core transformer and various parasitic electrical parameters, can be found in reference 14.

5.3 Probe Operation

Since the electric probe described above measures potential difference, as opposed to probe current, the net current drawn from the plasma was purposefully kept small. In this respect the electric probe differs fundamentally from the better known Langmuir probe, and reaps the benefit of greatly reduced sensitivity to the presence of magnetic fields, departures from thermal equilibrium, precise determination of electrode area, etc., which habitually beset the biased versions. The stipulation of small probe current thus ameliorates many traditional problems of interpretation by allowing the probe to float, and in the process improves the accuracy of the measurement of plasma potential. Indeed, as Lovberg points out, it is extremely difficult to prevent a floating electrode from assuming the local plasma potential, minus about $\frac{kT_e}{|e|}$ (34). This correction term is associated with voltage drops across the thin (typically 10^{-4} mm) Debye sheath which forms over the probe surface. The sheath effect is shown schematically in the potential diagram of Fig. 5-3.

The floating potential difference sensed by the probe is seen to be the difference in plasma potential plus the difference in sheath potential:

$$V_{f_2} - V_{f_1} = (V_{P_2} - V_{P_1}) + (V_{S_2} - V_{S_1}) \qquad (5\text{-}1)$$

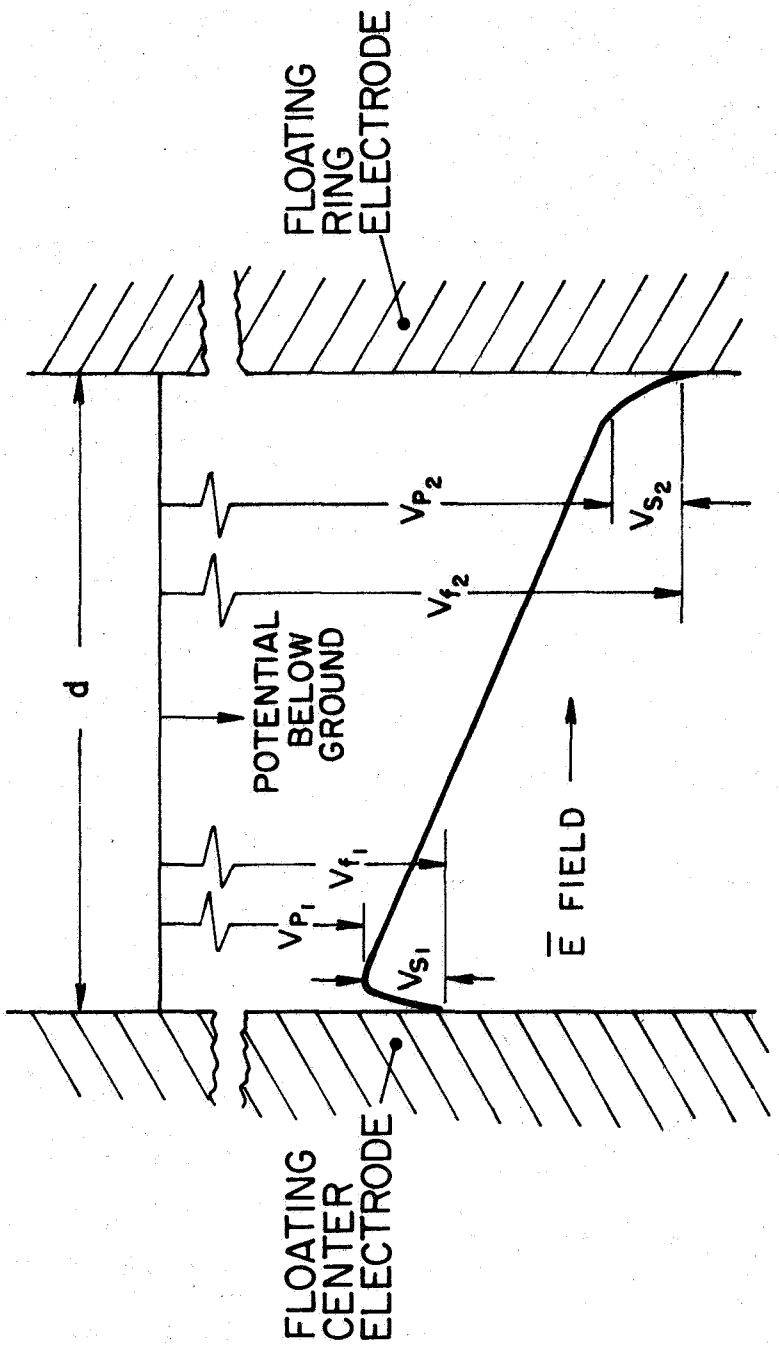

POTENTIAL DISTRIBUTION BETWEEN TWO FLOATING PROBE ELECTRODES

FIGURE 5-3

Thus a direct measurement of plasma potential requires a small net contribution from the sheath term. Biased probes, on the other hand, would seek the opposite ordering to facilitate detailed measurement of the sheath potentials.

A detailed, analytical model of sheath formation on the probe electrodes which faithfully incorporates the variable magnetic field, flow velocity, property gradients, etc., would be very difficult to formulate. Fortunately such an analysis is not necessary because of the ordering of terms in eq. (5-1), as will be shown. However, some useful insight into the roles played by the flow parameters can be obtained by considering the case of flow over the probe tip at zero angle of attack, corresponding to radial insertion.

Lam and Greenblatt[38] have recently treated the problem of collisionless plasma flow over a negatively biased cone. They concluded that the potential drop between the cone and the far flow field could be subdivided into a drop φ_1 occurring in the conical flow field up to the edge of the Debye sheath, and a further drop φ_2 occurring across the sheath. The actual relevance of the potential φ_1 to real probe measurements is not clear, but it can be eliminated in any case, according to the authors, provided the condition

$$\theta_c \geq \arcsin\left[\frac{kT_e}{m_i u_\infty^2}\right]^{\frac{1}{2}} \equiv \theta_0 \qquad (5\text{-}2)$$

between ion kinetic energy, electron temperature, and cone half angle θ_c can be satisfied.

As the front part of the current sheet approaches the probe, both electrons and ions have essentially random thermal

motion with respect to laboratory and probe and hence their flow velocity is zero. As the sheet passes the probe tip the plasma flow develops, with the rear portions of the sheet sweeping ions past the probe at nearly the sheet velocity, imparting to them a streaming energy in excess of 100 ev (Chapter VII).

It is clear from inspection that U_I cannot assume its initial small values in eq. (5-2) while restricting θ_c to real angles. However gas dynamic effects are clearly most serious for well-developed flows, i.e. when U_I is large, and if the measured values $\frac{kT_e}{|e|} \simeq$ 1 ev, $U_I \simeq U_s = 2.5$ centimeters/microseconds are inserted, θ_0 is found to be less than 5 degrees, a very mild restriction on the cone half angle. In these experiments θ_c was chosen rather arbitrarily as 30 degrees, a compromise between gas dynamic streamlining and ease of probe construction.

The assumption of approximately zero net probe current is equivalent to requiring equal net ion and electron fluxes to the probe electrodes. The zero-current, or floating potential, point on Langmuir probe characteristics is well-known, and is always negative with respect to thermalized plasmas because random electron flux to the probe is favored, by the square root of the mass ratio. Thus negligible probe current may be interpreted as any current significantly less than the random ion flux to the probe, and with this restriction it can be shown[14,22,27,34] that

$$V_s \simeq \frac{3kT_e}{|e|} \quad \text{volts} \qquad (5\text{-}3)$$

Using measured values (Chapter VI), the maximum possible kT_e variation over a probe dimension was found to be a few tenths

of an electron volt, near the center of the current distribution. Thus the maximum possible sheath contribution was perhaps one volt, or about 10 percent of the measured potential difference.

Dropping the sheath term and recognizing that the probe will average any potential gradient variations over the electrode gap d, we have from eq. (5-2)

$$E = -\nabla V \cong \frac{V_{f_2} - V_{f_1}}{d} \qquad (5\text{-}4)$$

and thus the probe output voltage can be interpreted as a direct measurement of average electric field strength between the electrodes.

5.4 Sources of Error

The discussion up to this point has dealt with the most obvious source of error, and has endeavored to show that probe dimensions were to a large extent dictated by the characteristic lengths appearing in the problem. A probe much larger would have sacrificed too much spatial resolution, while a probe much smaller would have had such greatly diminished output that errors incurred in sheath potential drops would have become intolerable (i.e. the probe would become sensitive to electron temperature gradients). Two other important sources of error, statistical scatter in the data, and liabilities inherent in the coaxial design, can impair the accuracy of electric probe measurements, and these will be considered next.

Shot-to-shot Reproducibility. The first type of error deals with shot-to-shot variations in the data. It was found generally that magnetic field measurements exhibited less

scatter than any other data, electric fields and plasma properties included. This can probably be attributed to the fact that the magnetic field strength at a point is established by the entire current distribution enclosed within the probe radius, whereas the electric field for example is established by rather more local conditions, such as neighboring charge distribution, and therefore is subject to greater statistical fluctuations.

Other effects also entered in. It was soon found that the E-probe had to be frequently and thoroughly cleaned with acetone or some other solvent to remove any microscopic conducting film which the discharge deposited over the probe tip. This required frequent removal and replacement of the probe assembly, which introduced a certain amount of error in probe position from shot-to-shot.

A large number of experiments were done under essentially identical conditions to furnish a statistical picture of overall shot-to-shot reproducibility. The E(t) traces, typically peaked profiles in time, were found to have variations in both arrival time and peak amplitude while exhibiting geometrically similar profile shapes. The radial electric field was more unpredictable than the axial field, with amplitude variations sometimes reaching nearly 50 percent near the cathode from shot to shot even when the probe tip was cleaned after every measurement. This behavior indicated that the sheet did not necessarily develop in quite the same way each time, perhaps due to slight variations in the initial conditions or from some related cause. Some of the amplitude variation was attributed to the difficulty of removing all traces of conducting film from the probe tip, and the largest

measured fields were assumed to be most representative of conditions in the sheet.

The other observed discrepancy, in profile arrival time, constituted a serious potential error source in time correlation, a problem common to all experiments relying on the indistinguishability of successive data runs. The problem was solved in this instance by noting that the current distribution, shown in Chapter IV to be closely related to $\dot{B}_\theta$, and the other measurables, such as the electric field, exhibited the same degree of scatter. The arrival time of the sheet at midradius was generally uncertain to within about half a microsecond, and the same uncertainty was manifest in all measurable quantities investigated. Thus it appeared plausible, and was soon confirmed, that it was not the structure and velocity of the sheet which shifted significantly from shot-to-shot so much as the time lag associated with striking and stabilizing the arc current during the initial formation of the current sheet.

A series of experiments employing B-probes and E-probes simultaneously showed that $\dot{B}_\theta(t)$ and, say, $E_r(t)$ gave close agreement for profile arrival time, within about 0.1 microsecond, even though exhibiting an unacceptable amount of scatter individually. Thus a method of time correlation evolved wherein $\dot{B}_\theta$ was taken as the time reference and recorded simultaneously with the quantity of interest, the time origin being taken as the $\dot{B}_\theta$ peak. In this system $t = 0$ corresponds to the peak of the current density and defines the center of the current sheet, negative time refers to the leading half of the sheet, and positive time refers to the trailing half.

Successful binary probing requires that the two probes be mounted in such a way as not to interfere appreciably, and the small size of the nylon sleeved B-probes was an important aid in this respect. The following example will illustrate the method.

To record $\dot{B}_\theta(t)$ and $E_r(t)$ simultaneously at the midplane probing station, the E-probe was inserted radially through the opposite side of the discharge chamber, as shown in Fig. 5-4, while the B-probe was inserted axially, bent through an angle of 90 degrees, and positioned with the same radial and axial coordinates as the E-probe but displaced a small distance in the azimuthal direction. A series of test shots showed well-reproduced time correlation between B(t) and E(t) with the dual probes in this position, reflecting the azimuthal symmetry of the pinch. The minimum separation distance was found to be about 1/4" to avoid mutual interference. Gas dynamic effects were held to a minimum since the current sheet encountered both probes head-on.

Cross-Talk Components. The second major source of error reflects the finite dimensions of the E-probe. The probe electrodes present a coaxial sampling system to the plasma in order to avoid magnetic pickup. If linearly aligned point electrodes were used instead of the coaxial arrangement, for example, the conducting path completed through the plasma would form an effective one turn pickup coil, i.e. a functional magnetic probe (section 4-3). This effect is negated with the coaxial arrangement, but at the expense of heightened sensitivity to transverse electric field gradients. An example will illustrate the problem.

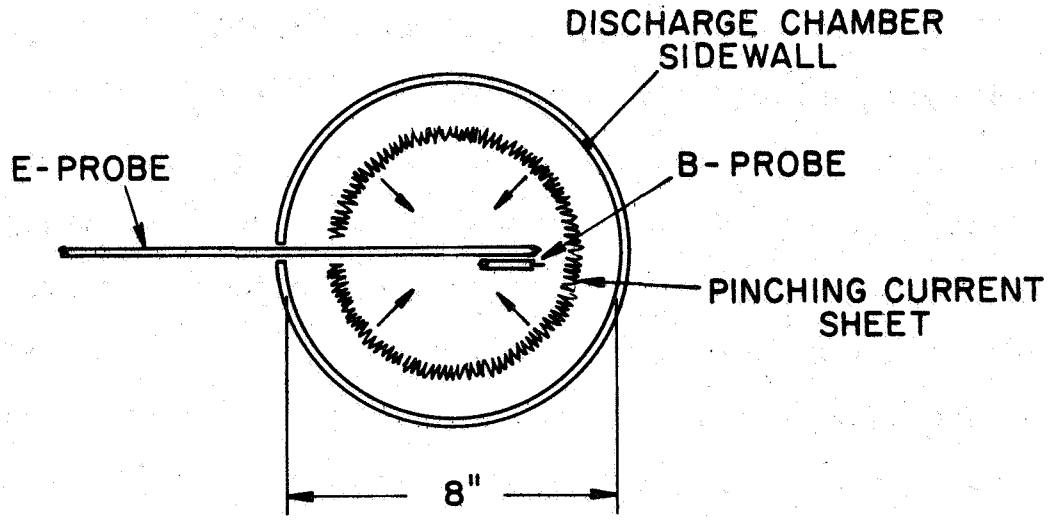

TOP VIEW OF DUAL PROBE ARRANGEMENT

FIGURE 5-4

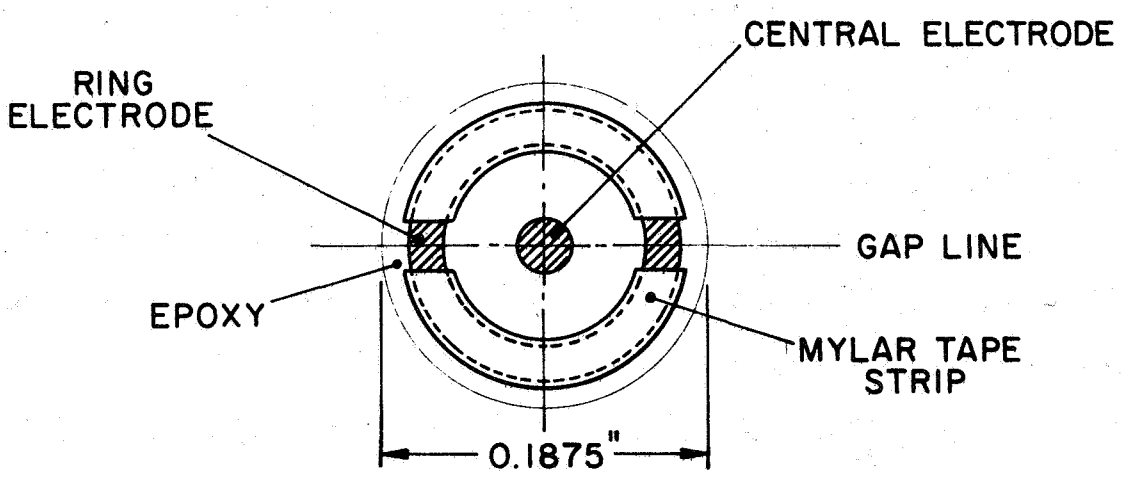

E-PROBE TIP CONFIGURATION FOR ∇E EXPERIMENTS

FIGURE 5-5

Consider the E-probe to be positioned radially as in Fig. 5-4, to measure $E_r(t)$. If an E_z field is also present, but approximately constant over the diameter d of the ring electrode, the probe will respond correctly to E_r alone. If a strong axial gradient in E_z is present, however, the potential assumed by the ring electrode (an equipotential surface) will accurately represent not the potential which exists at the axis of the ring but rather the average value, and thus the probe output will have an erroneous "cross-talk" component. Stated mathematically, the inequality

$$\frac{\partial E_z}{\partial z} \Delta z \ll E_r \qquad (5\text{-}5)$$

must be satisfied, where Δz is identified with d, the diameter of the ring electrode. Similarly, accurate measurement of the axial field requires

$$\frac{\partial E_r}{\partial r} d \ll E_z \qquad (5\text{-}6)$$

The effect of satisfying these inequalities is that the probe will respond to first derivatives in the potential along the probe axis, but to neither first nor second derivatives normal to the axis, thus assuring that the primary object of the experiments remains the measured quantity.

Sensitivity to field gradients was checked in the laboratory with a modified taped probe as shown in Fig. 5-5. Two thin strips of mylar tape covered the ring electrode except for two opposed points or gaps, and the probe circuit was completed through the plasma as two adjacent loops whose axes were perpendicular to the gap line.

E_r measurements were checked by aligning the gap first along $\hat{\theta}$ and then along $\hat{z}$, using the coordinate system of Fig. 4-2. The traces so obtained were identical with each other and with the traces from the coaxial probe, and this was considered sufficient evidence that local E_z gradients were not severe at the two probing stations, a reasonable result. E_r measurements were thus assumed free of this type of error with a good deal of confidence.

E_z measurements, on the other hand, would seem more susceptible to cross talk errors because of the known strong radial property variations through the current sheet, and this was found to be the case. With the gap aligned along r, traces identical with the coaxial arrangement were obtained. However with the gap along $\hat{\theta}$, where severe gradients can be presumed nonexistant, a noticeable difference appeared in the traces for positive times, i.e. in the trailing half of the current sheet. This was considered evidence that the coaxial probe had indeed fallen victim to radial component cross-talk, and consequently the $\hat{\theta}$ gap orientation was used in E_z probing. The error was not great however, less than 25 percent, and no difference was noticed in the leading half of the sheet at all.

The various sources of error considered above, including shot-to-shot data scatter, the uncertain gas dynamic disturbances introduced into the flowing plasma, electric field gradients, finite probe current, etc. all contribute toward making electric field measurements less precise than magnetic field measurements. The complicated way in which the various errors change with time makes the assignment of error bars difficult, but the overall

accuracy of the quantitative measurements was judged to be between 20% and 50%.

5.5 Experimental Results

The probe circuit was calibrated in place by applying a known voltage to the probe tips and measuring the resulting signal at the oscilloscope.

With the dual probe arrangement at the cathode location, $R/R_o = .5$, the oscillograms of Fig. 5-6 were obtained. The peak of $\dot{B}_\theta$ on the lower beam trace locates $t = 0$, and the calibrated E_r and E_z fields are reproduced in Figs. 5-7 and 5-8.

Note that the extremely rapid variation of E_r near $t = 0$ prevents precise evaluation of the radial field there. It is possible that the maximum amplitude of E_r in the plasma is considerably higher than the indicated maximum of 6,000 volts/meter, because both the rise time of the oscilloscope (20 ns) and the spatial resolution of the probe (2 mm) have been exceeded.

The electric field felt by the plasma is not the same field measured in the laboratory of course, the fields differing by the inductive term $\vec{v} \times \vec{B}$ where $\vec{v}$ is the plasma velocity. As the sheet sweeps past the probe the velocity of the plasma with respect to the probe is not constant, and in fact constitutes one of the major unknowns of the problem (Chapter VII). A coordinate system which will be useful in some of the discussions to follow is one fixed in the sheet, i.e. moving radially inward with the local velocity of the $\dot{B}_\theta$ peaks. In the sheet coordinate system, the measured radial electric field would be identical to that measured in the laboratory, but the axial field would be

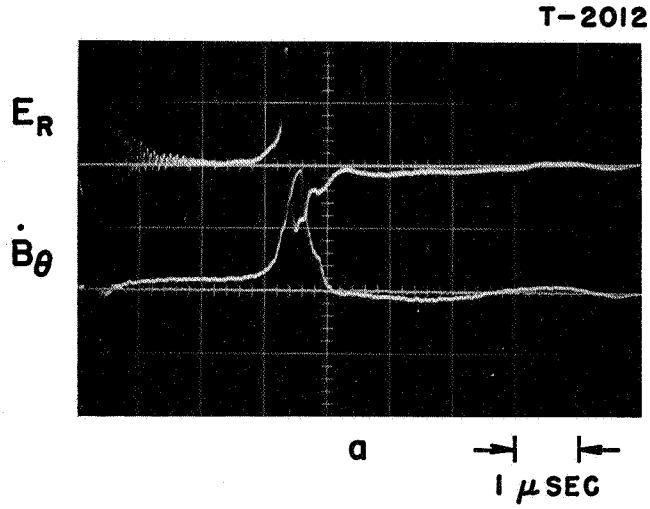

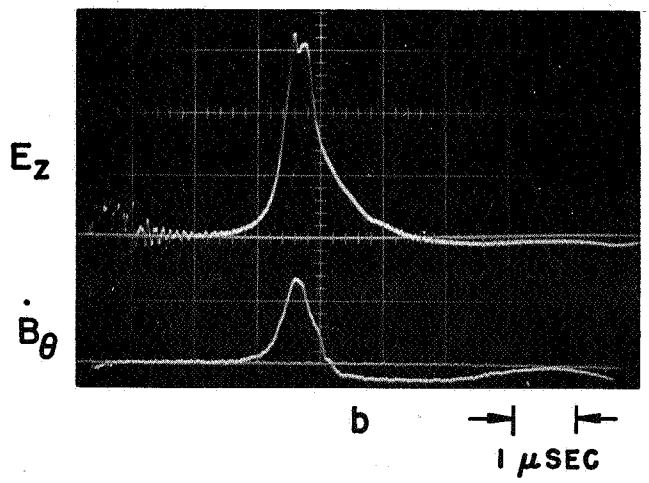

E-PROBE DATA, CATHODE

$\left(\frac{R}{R_0}=.5, \frac{z}{h}\cong 0\right)$

FIGURE 5-6

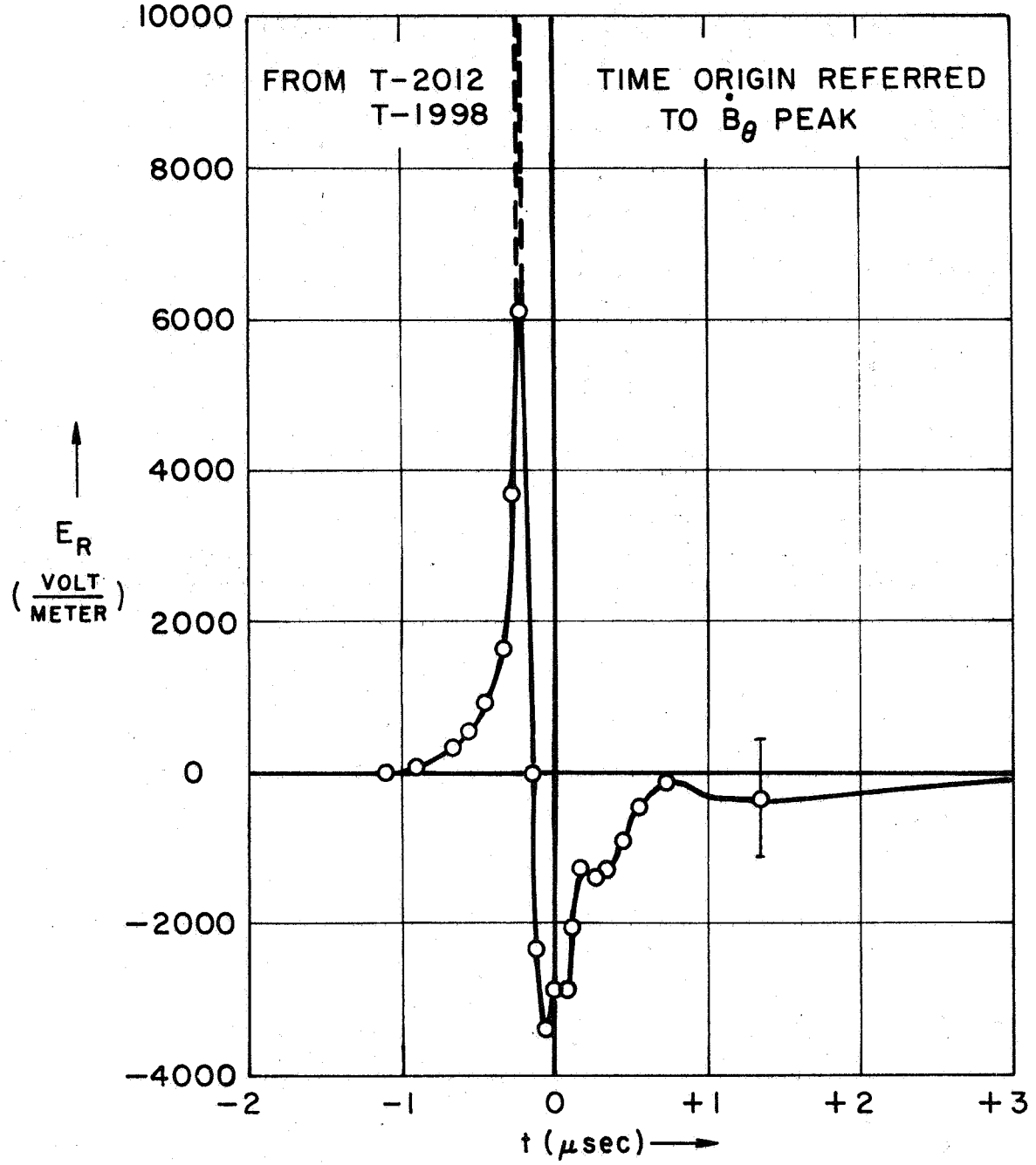

RADIAL ELECTRIC FIELD AT CATHODE

$\left(\frac{R}{R_0}=.5, \frac{z}{h}\cong 0\right)$

FIGURE 5-7

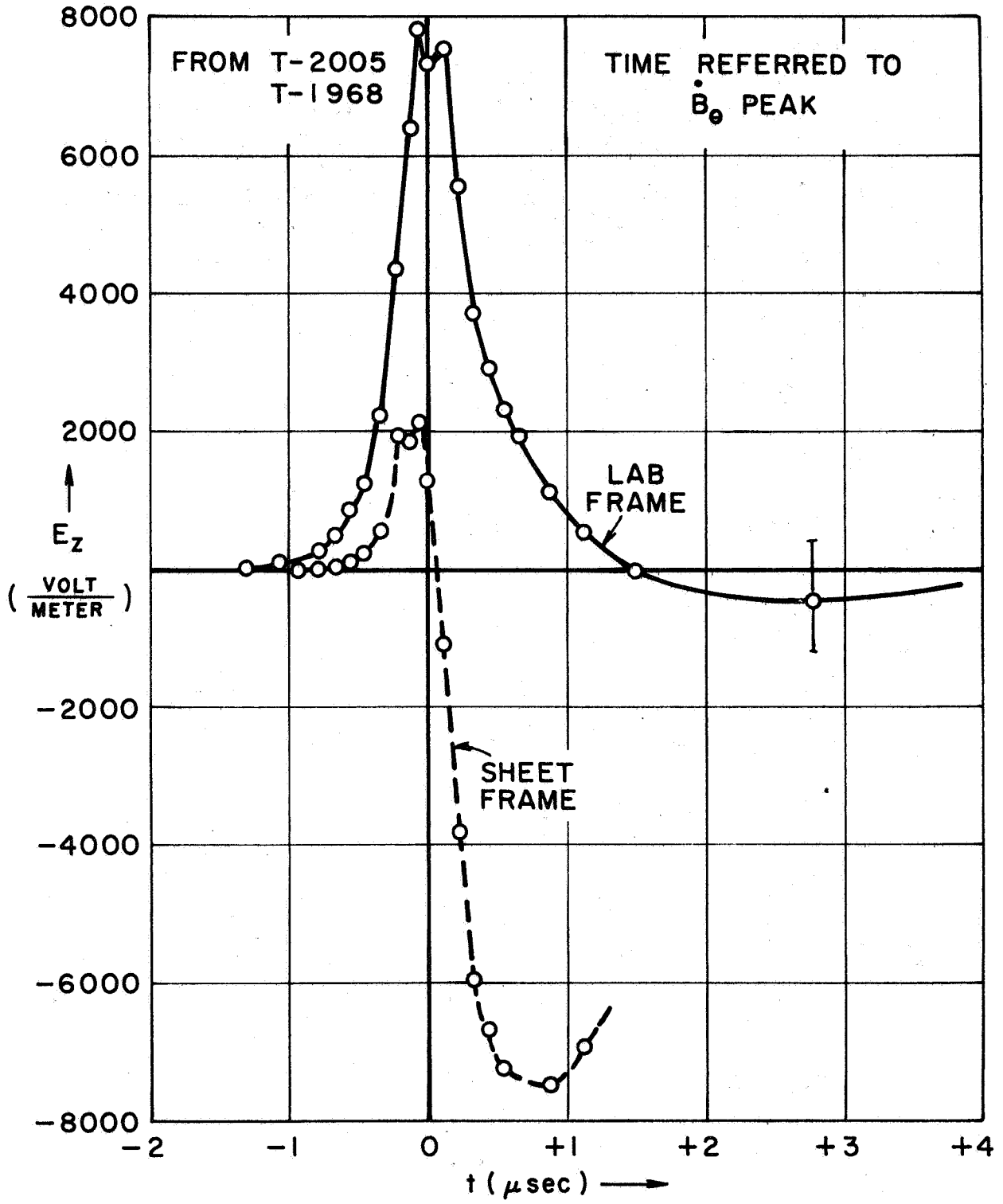

AXIAL ELECTRIC FIELD AT CATHODE

$\left(\frac{R}{R_0} = .5, \frac{z}{h} \cong 0\right)$

FIGURE 5-8

AP25-4255-67

diminished by the amount $U_s B_\theta$. The two coordinate systems are shown in Fig. 5-9, and the cathode E_z field in both systems has been plotted in Fig. 5-8.

These measurements were repeated at the midplane location, $R/R_o = .5$, and the data are displayed in Fig. 5-10. The calibrated field components obtained from these oscillograms are plotted in Figs. 5-11 and 5-12. As expected, the midplane fields are similar to the cathode fields in the leading portions of the current sheet, but become somewhat more smeared out in the trailing edge.

Several observations can be made immediately on the basis of these data. The area under the $E_r(t)$ curve can be readily converted, via the Galilean transformation $\Delta r \cong u_s \Delta t$ (i.e. near t = 0, .1 μs corresponds to about 2.5 mm), to the spatial integral

$$\varphi = \int_{sheet} E_r \, dr \qquad \text{[volts]} \qquad (5\text{-}7)$$

which represents the energy lost by an argon ion in traversing the sheet. Thus the incoming ion, in the sheet coordinate system, is decelerated by the large opposing radial field in the leading edge of the current sheet, whereas in the laboratory frame it is accelerated from rest (see Chapter VII).

Since the divergence of the electric field is dominated by the radial term, a good estimate of the net charge imbalance can be obtained from the Poisson equation

MKS $$\frac{\partial E_r}{\partial r} \cong \rho/\epsilon_o \qquad (5\text{-}8)$$

From the curves of Figs. 5-7 and 5-12, the maximum possible net

FIGURE 5-9

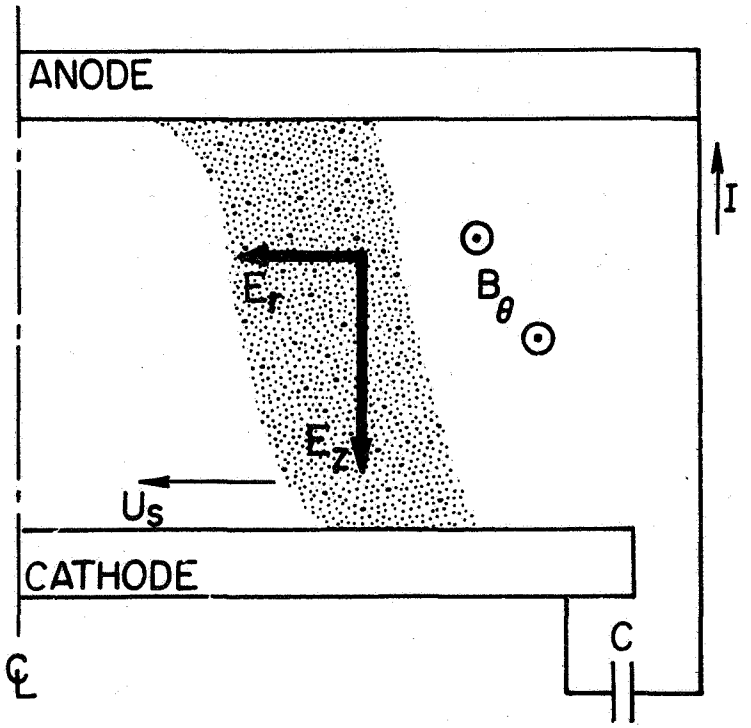

LABORATORY COORDINATES

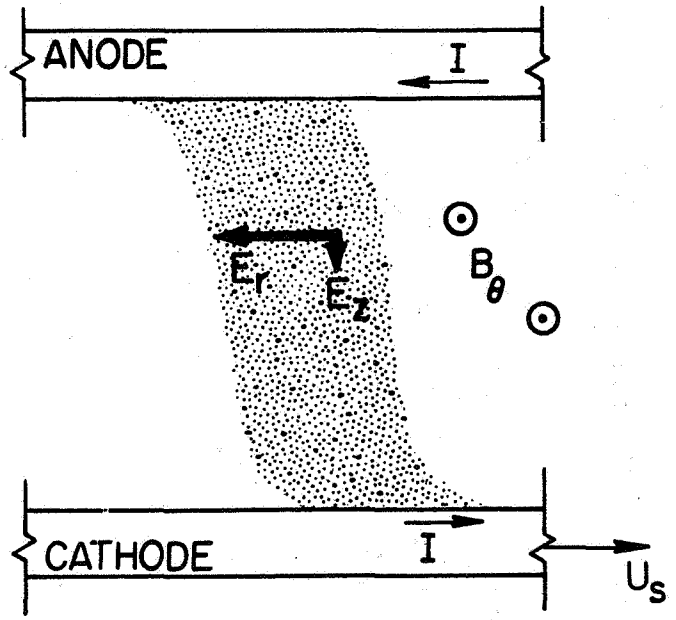

MOVING COORDINATES

ELECTRIC FIELD COMPONENTS

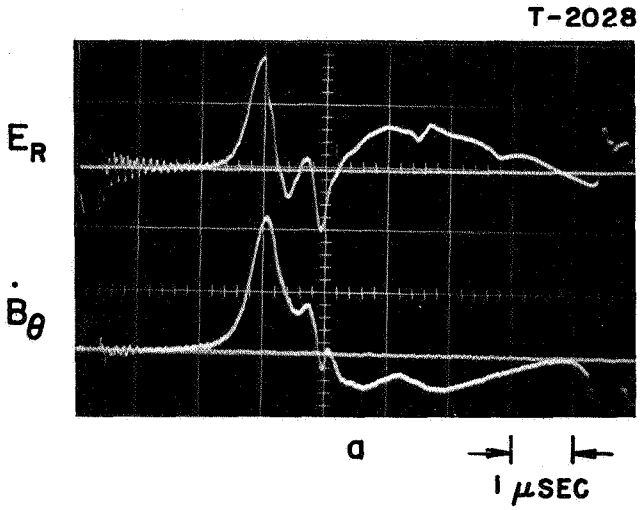

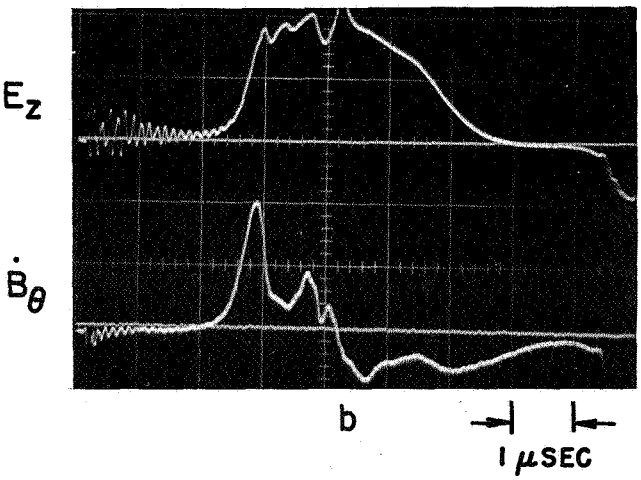

E-PROBE DATA, MIDPLANE

$\left(\frac{R}{R_o}=.5, \frac{z}{h}=.5\right)$

AD25-P95-61

FIGURE 5-10

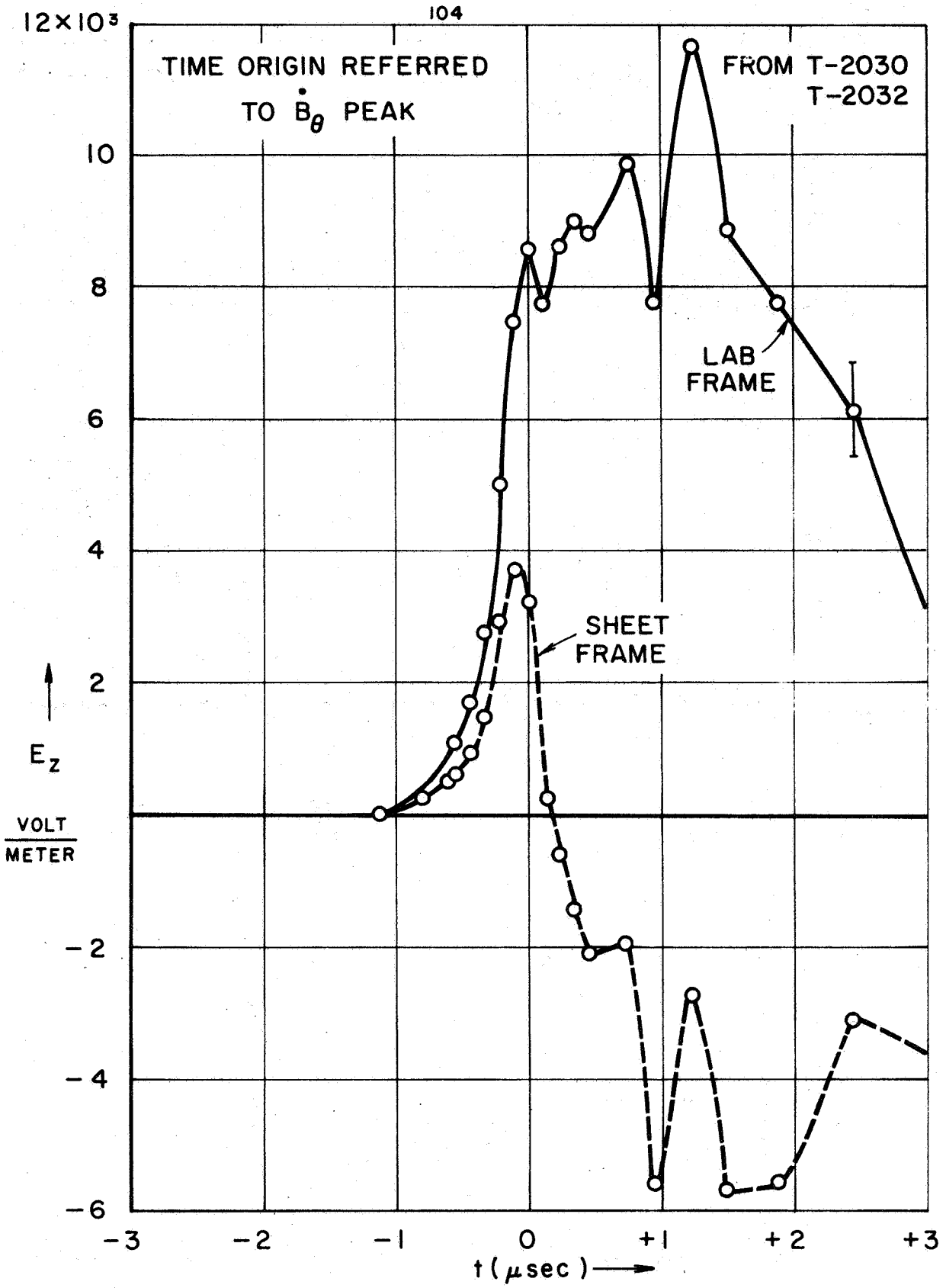

AXIAL ELECTRIC FIELD AT MIDPLANE

$\left(\frac{R}{R_o} = .5, \frac{z}{h} = .5\right)$

FIGURE 5-11

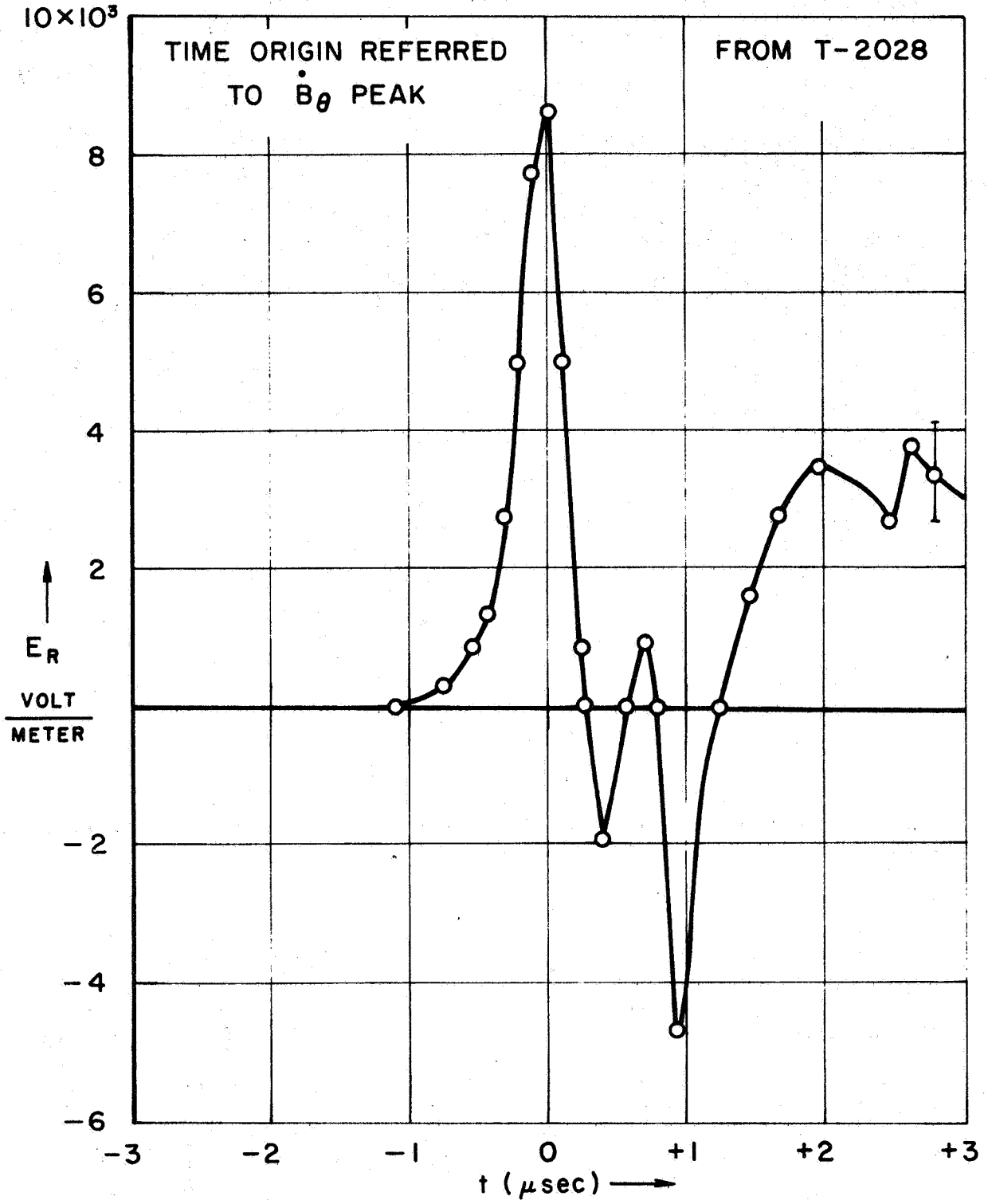

RADIAL ELECTRIC FIELD AT MIDPLANE

$\left(\frac{R}{R_0} = .5, \frac{z}{h} = .5\right)$

FIGURE 5-12

charge density was calculated to be less than 10^{-12} coulomb/cm^3, or about 10^7 electrons/cm^3. The maximum net charge imbalance is thus less than 10^{-8} of the prevailing charge densities (Chapter VI), and the measured electron density can thus be equated to the ion density for all other purposes with negligible error.

The measurement of these densities is considered in detail in the following chapter.

Chapter VI

MICROWAVE PROBES - THEORY AND EXPERIMENT

6.1 Introduction

Microwave-plasma interactions can and often do become quite complicated, encompassing simultaneously a variety of different physical effects. Heald and Wharton[34] have described the plasma in a magnetic field, viewed as a medium for electromagnetic wave propagation, as refractive, lossy, resonant, dispersive, anisotropic, nonreciprocal, inhomogeneous, and possibly nonlinear in the general case. Clearly such a medium requires some simplifying assumptions if it is to afford mathematical tractability.

In addition to its strong, multifaceted interaction with electromagnetic waves and fields, the laboratory plasma is characterized by another distinguishing feature, a direct result of its finite extent. The plasma must be bounded, whether by $\overline{B}$ field or chamber wall, and its interaction with this container inevitably will introduce some diffuseness into its perimeter regions. Thus if external radiation is to penetrate the plasma, it must negotiate an inhomogeneous transition region arising solely from boundary effects, which separates the body of plasma from its environment. Boundary layer formation and sheath envelopment have been encountered previously in the chapters on B and E probes, and indeed pose a potential error source for any plasma experiments involving internal probing.

Actually the appearance of diffuse boundaries is not unique to laboratory plasmas but rather is a universal charac-

teristic of all wave interactions with material media. Strictly speaking, Maxwell's equations are not applicable to regions of discontinuity in constitutive parameters, nor are the constitutive parameters definable on an atomic scale over which macroscopic discontinuities are present. Thus similar arguments must be applied to any medium, and its "boundary conditions" must derive from a limiting process about a narrow transition zone.

An important feature of the plasma problem, however, is the width of the transition zone, which, for the millimeter waves being contemplated, may be comparable with or exceed the incident wavelength. It is not possible in such cases to relegate changes in the wave, brought about by the region of inhomogeneous propagation, to a "boundary" condition, and this modification introduces considerable mathematical difficulty into an already complicated problem.

In this chapter, some important physical features of plasma-wave interactions are first presented for the simplest realistic case, treating uniform, isotropic plasmas, plane waves, and slab boundaries. The insights gained from this analysis are applied to the design of a microwave probe, an interferometer sensitive to reflected waves. The influence of static magnetic fields (i.e. B_θ) and inhomogeneities near the boundary are then included in more detailed analyses and laboratory sources of error are examined in detail. Finally, techniques of data reduction are discussed and time histories of the plasma electron properties are obtained.

6.2 Wave Propagation in an Infinite, Linear, Homogeneous, Isotropic Medium

The theory of electromagnetic wave-plasma interactions has been considered extensively at many different levels of sophistication.[44,45,46,47] Here only a very simple approach is outlined, felt to display adequately the relevant physical phenomena involved in interpreting the microwave probe data.

We will consider the simplest case with any hope of experimental realization, a linearly polarized electromagnetic plane wave with harmonic time dependence, propagating in a linear, homogeneous, isotropic medium of finite conductivity but net charge neutrality, far from any boundaries.

From Appendix A, the harmonic forms of the Faraday and Ampere laws are

$$\nabla \times \bar{E} = -i\omega\mu_0 \bar{H} \tag{6-1}$$

$$\nabla \times \bar{H} = (\sigma + i\omega\epsilon_0)\bar{E} \tag{6-2}$$

where we have assumed vacuum permeability and permittivity as discussed in the Appendix. Taking the curl of eq. (6-1) and substituting in eq. (6-2) yields

$$\nabla \times \nabla \times \bar{E} = \nabla(\nabla \cdot \bar{E}) - \nabla^2 \bar{E} = (-i\omega\mu_0\sigma + \omega^2\epsilon_0\mu_0)\bar{E} \tag{6-3}$$

For net charge neutrality, Gauss' law (A-3) shows the $\bar{E}$ field to be divergenceless, and eq. (6-3) reduces to

$$\nabla^2 \bar{E} + (\omega^2\epsilon_0\mu_0 - i\omega\mu_0\sigma)\bar{E} = 0 \tag{6-4}$$

or

$$\nabla^2 \bar{E} + k^{*2} \bar{E} = 0 \qquad (6\text{-}5)$$

the familiar harmonic wave equation for electromagnetic waves. The plane wave solutions of eq. (6-5) are transverse, in the form

$$\bar{E} = \bar{E}_0 \, e^{i(\omega t \mp k^* z)} \qquad (6\text{-}6)$$

where the minus sign applies for propagation in the +z direction, and

$$k^* = \frac{\omega}{c} \left[1 - i \frac{\sigma}{\epsilon_0 \omega} \right]^{\frac{1}{2}} \qquad (6\text{-}7)$$

is the complex propagation coefficient, indicative of the wavelength and the attenuation of wave motion in the conducting medium.[+] $\bar{E}_0$ is the vector amplitude of the wave, constrained to lie in the x-y plane.

[+] k^* is explicitly complex, with its real and imaginary parts conventionally designated as

$$k^* = \alpha - i\beta$$

Note that if the solution to eq. (6-6) is taken to be of the form

$$\bar{E} = \bar{E}_0 \, e^{i\omega t \mp \gamma z}$$

then $$\gamma = i k^* = \beta + i\alpha$$

i.e. the real and imaginary parts are <u>interchanged</u>. Both notations are common, and variations in the choice of signs abound in the literature.

To complete the solution of eq. (6-5) we need to evaluate σ. The entire concept of plasma conductivity is somewhat poorly defined, as discussed in Appendix B. The conventional solution for σ proceeds by identifying an "ensemble-average" electron, whose drift velocity defines the current per particle and satisfies the heuristic equation of motion

$$m_e \dot{\bar{v}} + m_e \nu \bar{v} = -|e| \bar{E}(t) \tag{6-8}$$

Solution of eq. (6-8), for times long enough to suppress the transient, yields

$$\bar{v} = \frac{-|e|}{m_e(\nu + i\omega)} \bar{E}(t) \tag{6-9}$$

The current density follows directly,

$$\bar{J}_e = -n_e|e|\bar{v} = \frac{n_e e^2}{m_e(\nu + i\omega)} \bar{E} \tag{6-10}$$

and by analogy to Ohm's law, $\bar{J} = \sigma \bar{E}$, identifies a complex conductivity

$$\sigma = \frac{n_e e^2}{m_e} \frac{1}{\nu + i\omega} = \epsilon_0 \left(\frac{\omega_p^2}{\nu + i\omega} \right) \tag{6-11}$$

which we have written in terms of

$$\omega_p = \left[\frac{n_e e^2}{\epsilon_0 m_e} \right]^{\frac{1}{2}} \tag{6-12}$$

the electron plasma frequency. ω_p is the natural frequency of oscillation of the free electron component of the plasma and is a function only of the local electron density.

When the plasma frequency equals the probing frequency, a resonance occurs. Thus we are led to define a resonant, or

critical, electron density for a given probing frequency

$$n_p = \frac{\epsilon_0 m_e \omega^2}{|e|^2} \tag{6-13}$$

The complex refractive index of the plasma, from Appendix A, is

$$\mu^* = (\kappa^* \kappa_m)^{\frac{1}{2}} = \sqrt{1 - i \frac{\sigma}{\epsilon_0 \omega}} \tag{6-14}$$

which by comparison to eq. (6-7) is seen to be simply the non-dimensional complex propagation coefficient

$$\mu^* = \frac{k^*}{k_0} = \frac{\alpha}{k_0} - i \frac{\beta}{k_0} \tag{6-15}$$

where we identify the nondimensionalizing constant as

$$k_0 = \frac{\omega}{c} = \frac{2\pi}{\lambda_0} \tag{6-16}$$

the reciprocal radian wavelength in vacuum or air.

When eq. (6-11) for σ is substituted in eq. (6-14), we find

$$\mu^* = \left[1 - i \frac{\omega_p^2}{\omega(\nu + i\omega)}\right]^{\frac{1}{2}} \tag{6-17}$$

from which the real and imaginary parts of the complex refractive index follow in convenient nondimensional form,

$$\frac{\alpha}{k_0} = \left[\frac{1}{2}\left[1 - \frac{(\omega_p/\omega)^2}{1+(\nu/\omega)^2}\right] \pm \frac{1}{2}\left\{\left[1 - \frac{(\omega_p/\omega)^2}{1+(\nu/\omega)^2}\right]^2 + \left[\frac{(\omega_p/\omega)^2}{1+(\nu/\omega)^2}\left(\frac{\nu}{\omega}\right)\right]^2\right\}^{\frac{1}{2}}\right]^{\frac{1}{2}} \tag{6-18}$$

$$\frac{\beta}{k_0} = \left[-\frac{1}{2}\left[1 - \frac{(\omega_p/\omega)^2}{1+(\nu/\omega)^2}\right] \pm \frac{1}{2}\left\{\left[1 - \frac{(\omega_p/\omega)^2}{1+(\nu/\omega)^2}\right]^2 + \left[\frac{(\omega_p/\omega)^2}{1+(\nu/\omega)^2}\left(\frac{\nu}{\omega}\right)\right]^2\right\}^{\frac{1}{2}}\right]^{\frac{1}{2}} \tag{6-19}$$

the plus sign being chosen in both cases to keep α and β real as defined. α/k_0 and β/k_0 are known as the phase coefficient (or real refractive index) and attentuation coefficient (or attentuation index) respectively, and they completely specify the propagation of a plane, transverse, electromagnetic wave in the plasma in terms of its basic properties. α, which determines the wavelength (or phase velocity), and β, which determines the attentuation of the wave train, depend only on ω_p and ν, which in turn involve only the density and temperature of the electrons, collision cross-sections, and some fundamental constants. Measurements of phase shift and attenuation should thus suffice, in principle, to determine both electron density and temperature in an equilibrium plasma of known collision properties.

Figs. (6-1) and (6-2) display nondimensional α and β as a function of ω_p/ω, with ν/ω as a parameter.

It is instructive to examine the collisionless limit. Figs. (6-1) and (6-2) show how the quantity ω_p/ω sharply divides the plasma behavior into two distinct regimes for low collision frequencies. When $\omega_p/\omega \ll 1$, the wave will propagate through the plasma with almost no attenuation $(\beta \doteq 0)$; when $\omega_p/\omega > 1$, i.e. when $n_e > n_p$, the wave motion becomes evanescent and propagation ceases $(\alpha \doteq 0)$. The real part of the Poynting vector can be shown to be zero in this case, and no energy transport through the plasma can occur. The physical picture here is that enough free electrons are present to "screen out" the electromagnetic wave so that the fields cannot penetrate the plasma. Below the critical density n_p, the physical picture is that

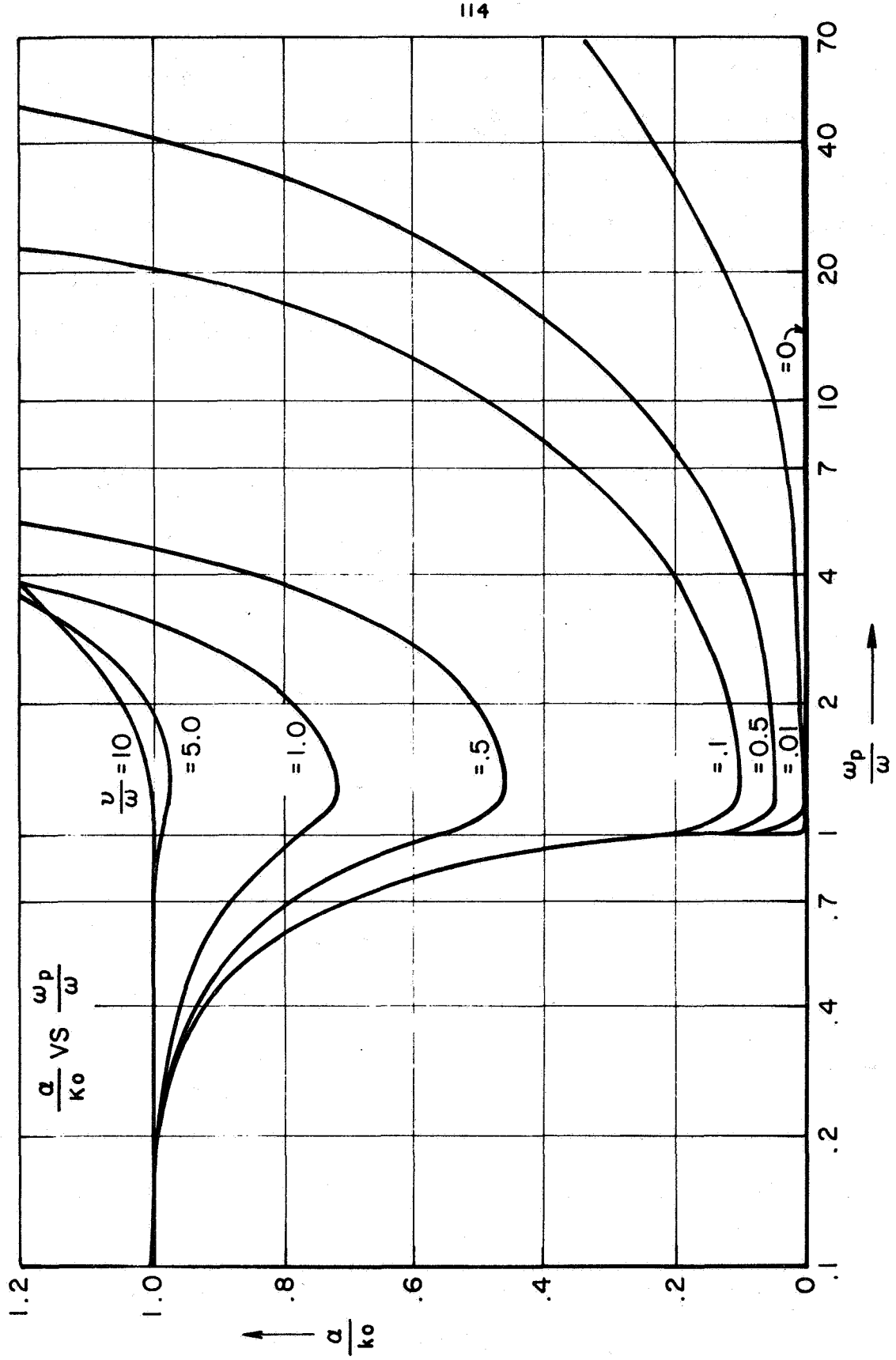

FIGURE 6-1

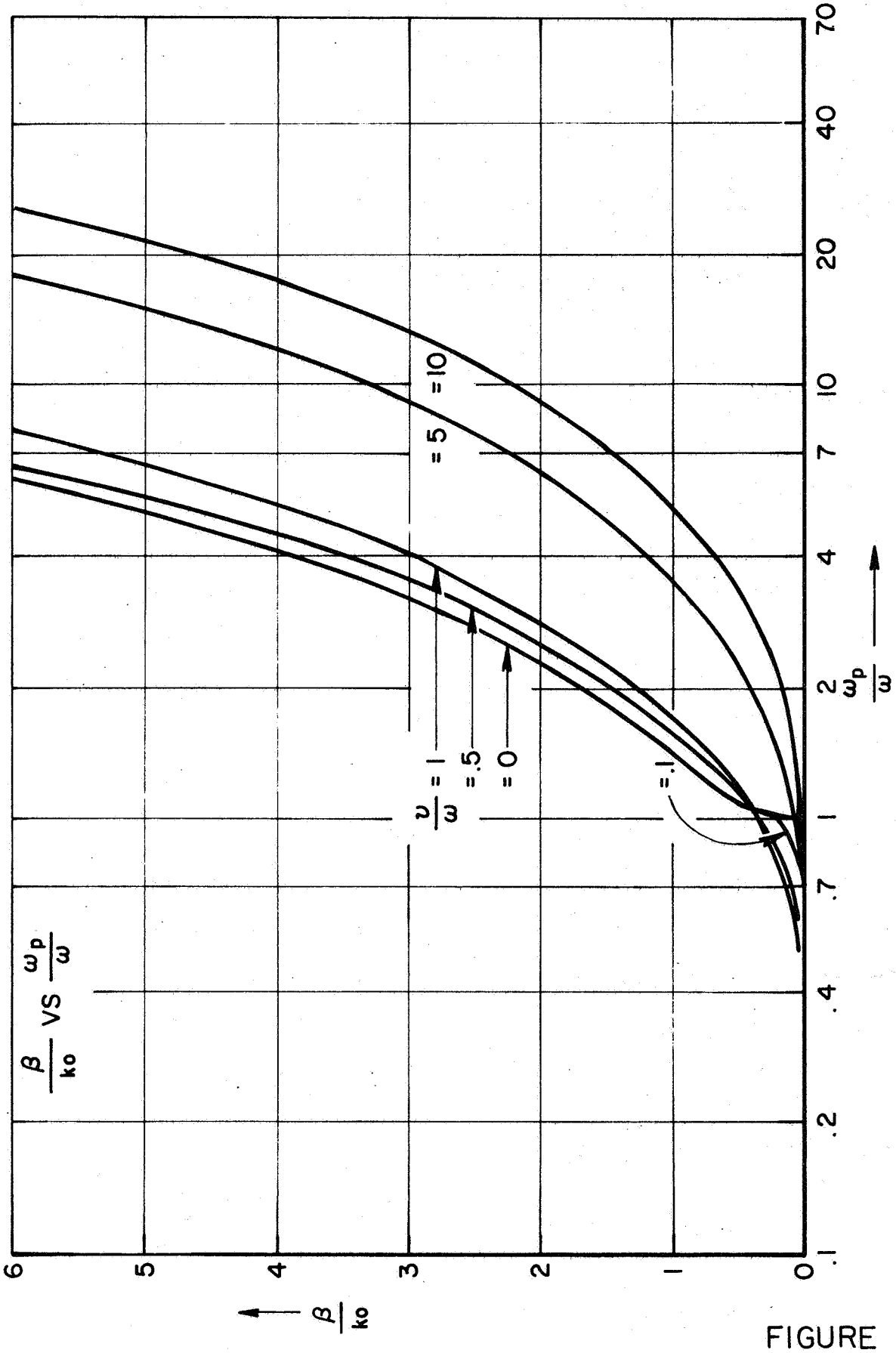

FIGURE 6-2

of the electrons being unable to follow the rapid field variations completely, hence acting somewhat like the bound electrons in dielectric materials. Indeed the medium may be formally treated as a dielectric (Appendix A), with a complex dielectric constant given by

$$K^* \triangleq \mu^{*2} = 1 - \frac{(\omega_p/\omega)^2}{1 - i\nu/\omega} \triangleq 1 - \left(\frac{\omega_p}{\omega}\right)^2 \qquad (6\text{-}20)$$

in the collisionless limit.

When appreciable collisions are present during one oscillation of the field, Figs. (6-1) and (6-2) show how this sharp division of the behavior of the plasma into dielectric and reactive regimes degenerates into a smooth transition as the electron density (ω_p) is increased, leaving a hybrid absorptive-reactive medium over the domains adjacent to the former discontinuity.

6.3 Propagation Across an Interface Between Conducting and Nonconducting Media

The containment problem is common to many experiments in plasma physics. In most laboratory situations it is necessary to confine the ionized gas under study between walls or isolate it in some other way from the transmitter and detector of the electromagnetic waves. The wave train, normally monochromatic at some selected probing frequency ω, will thus have to cross interfaces separating regions of different refractive index, at which it will suffer reflection losses and phase changes in addition to those from the plasma itself.

To specify these considerations for our particular problem, consider the wave train to be incident upon the plasma through a dielectric probing port in one of the electrodes, thus propagating in the z direction in the coordinate system of Fig. (4-2). If the electromagnetic wave is to be generated in the laboratory and beamed through the plasma, it must negotiate two air-dielectric interfaces, two dielectric-plasma interfaces, and the plasma itself before reaching a transmission detector, as shown in Fig. (6-3a). The reflected signal in general will also involve components from each interface.

The analysis of this problem can be considereably simplified by judicious design of the bounding dielectric slabs. For example they may be the dielectric lenses in a matched set of focused microwave horns; they may be exact half-wave or multiple-wave plates; or they may be arbitrary flats whose outer surfaces have been modified with grooves or a prescribed refractive coating in such a way as to contribute negligibly to the composite interference process.[48] Such matching techniques are based upon wavelength, and clearly are exact only for one probing frequency (and appropriate harmonics).

The matching technique used for these experiments involved multiple-wave plates, and will be discussed in section 6-4. Regardless of the method used, however, the desired result is the same: to make the containing walls drop out of the problem. To illustrate the method, consider the case of half-wave plates. If media ①, ③, and ⑤ of Fig. (6-3a) are considered to be initially identical, the successive reflections from the front and back surfaces of the walls interfere destructively and, in

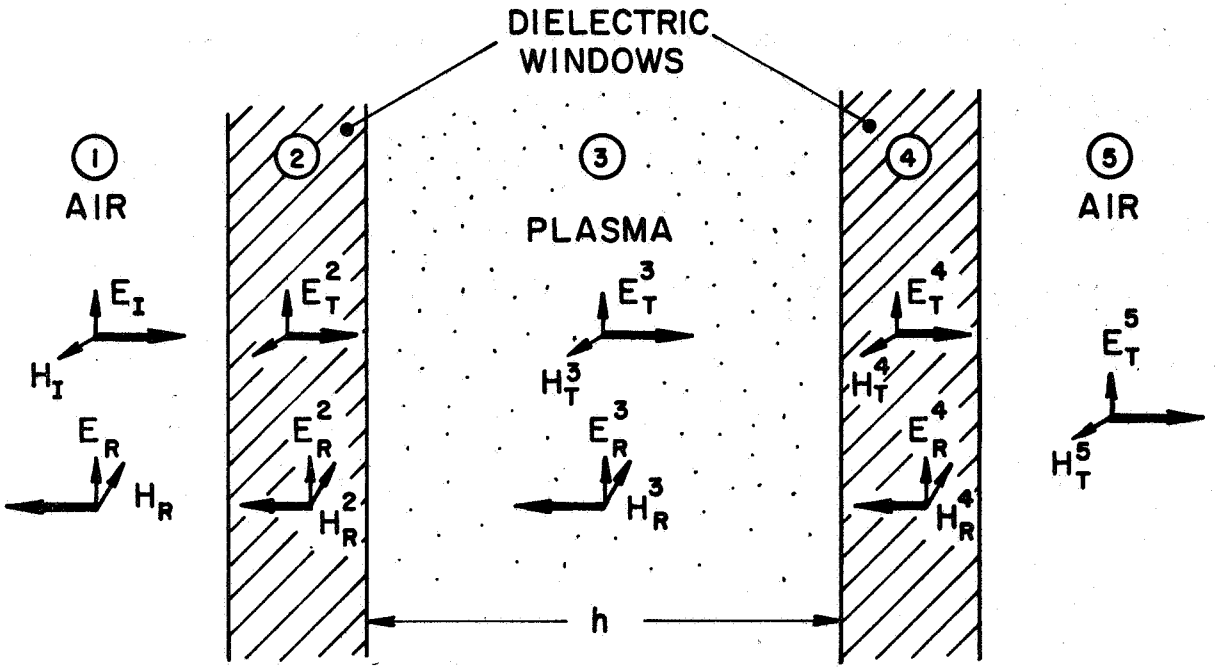

a) REFLECTION AND TRANSMISSION AT DIELECTRIC WINDOWS

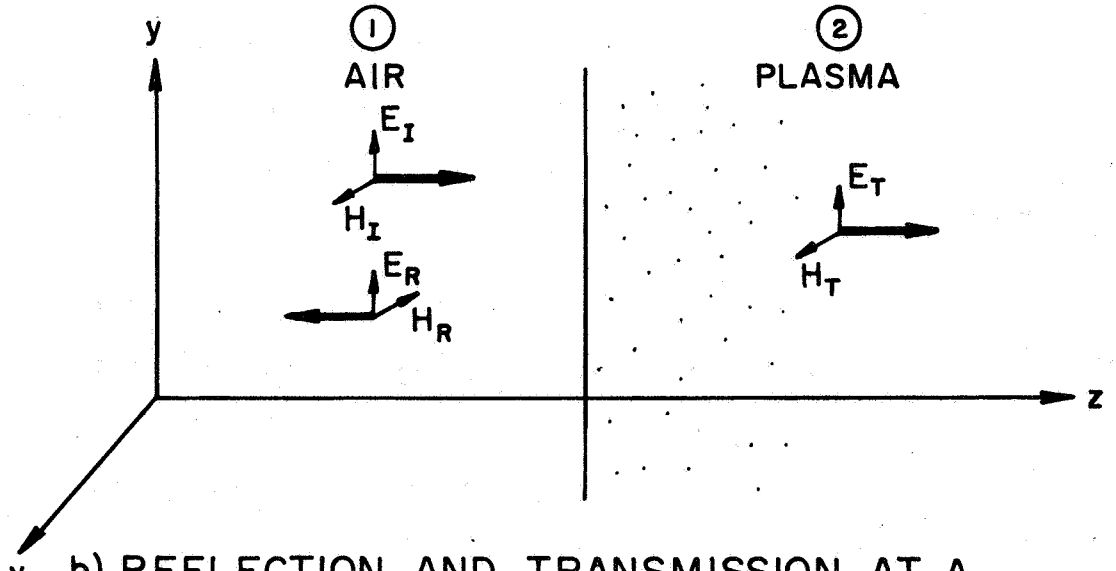

b) REFLECTION AND TRANSMISSION AT A PLANE INTERFACE

FIGURE 6-3

the absence of losses within the dielectric, the beam is totally transmitted. The analogy with classical optics is obvious, and the result is that the dielectric becomes "invisible." The introduction of plasma into region ③ then produces a mismatch in the system, and the net reflection and/or transmission of the incident signal is the same as would prevail if the slab of plasma, medium ③, were bounded directly by media ① and ⑤ (i.e. air) with no intervening half-wave slabs of dielectric window.[44]

A further simplification results if h in Fig. (6-3a), the chamber height, is taken to be so large that the plasma effectively screens out the second interface. This is what, in fact, occurs in these experiments, and the problem then reduces to a wave train incident on a semi-infinite plasma slab, Fig. (6-3b).

Consider a plane, linearly polarized wave incident normally from the left on the plane interface between a dielectric medium (i.e. air) and the plasma, with polarizations as shown in Fig. (6-3b). From section 6-2 we have the result that plane waves traveling to the right are represented by the phase factor $\exp\left[i(\omega t - k^* z)\right]$, and waves traveling to the left by $\exp\left[i(\omega t + k^* z)\right]$, where k^* is the complex propagation coefficient of eq. (6-15). Thus the wave functions are

Incident wave:

$$\tilde{E}_x(z,t) = \hat{x}\, E_{0I}\, e^{i(\omega t - k_1^* z)} \tag{6-21}$$

$$\tilde{H}_y(z,t) = \hat{y}\, H_{0I}\, e^{i(\omega t - k_1^* z)} \tag{6-22}$$

Reflected wave:

$$\bar{E}_R(z,t) = \hat{x}\, E_{oR}\, e^{-i(\omega t + k_1^* z)} \tag{6-23}$$

$$\bar{H}_R(z,t) = \hat{y}\, H_{oR}\, e^{-i(\omega t + k_1^* z)} \tag{6-24}$$

Transmitted wave:

$$\bar{E}_T(z,t) = \hat{x}\, E_{oT}\, e^{-i(\omega t - k_2^* z)} \tag{6-25}$$

$$\bar{H}_T(z,t) = \hat{y}\, H_{oT}\, e^{-i(\omega t - k_2^* z)} \tag{6-26}$$

where $\hat{x}$ and $\hat{y}$ are the x- and y-unit vectors of Fig. (4-2), and the amplitudes E_{oI}, H_{oI}, E_{oR}, H_{oR}, E_{oT}, H_{oT}, may be complex numbers to allow for phase changes.

The waves are all transverse, and integration of Maxwell's equations over hypothetical plane surfaces piercing the interface parallel to the field vectors yields the boundary conditions that $\overline{E}$ and $\overline{H}$ be continuous across the interface. If the z-origin is taken at the interface, the boundary conditions take the simple form

$$\bar{E}_I(0,t) + \bar{E}_R(0,t) = \bar{E}_T(0,t) \tag{6-27}$$

$$\bar{H}_I(0,t) + \bar{H}_R(0,t) = \bar{H}_T(0,t) \tag{6-28}$$

Application of the Faraday law, eq. (A-1), to the assumed right and left going waveforms relates the amplitudes of the electric and magnetic fields

$$\frac{E_o}{H_o} = \pm \frac{\mu_o \omega}{k^*} \tag{6-29}$$

the sign depending on the polarization. Using this result, the boundary conditions are simplified to two relations between the electric field amplitudes:

$$E_{0I} + E_{0R} = E_{0T} \tag{6-30}$$

$$k_1^*(E_{0I} - E_{0R}) = k_2^* E_{0T} \tag{6-31}$$

From the simultaneous solution of these equations, it follows that the amplitude reflection and transmission coefficients are, respectively

$$R = \frac{E_{0R}}{E_{0I}} = \frac{k_1^* - k_2^*}{k_1^* + k_2^*} \tag{6-32}$$

$$T = \frac{E_{0T}}{E_{0I}} = \frac{2k_1^*}{k_1^* + k_2^*} \tag{6-33}$$

both of which are complex numbers, indicative of phase and amplitude changes at the interface for the reflected and transmitted waves. Now if medium (1) is specified to be free space or air, and medium (2) to be the uniform plasma of section 6-2, the relevant propagation coefficients are

$$k_1^* = \frac{\omega}{c} = \frac{2\pi}{\lambda_0} = k_0 \quad (\underline{\text{real}}) \tag{6-34}$$

$$k_2^* = \alpha - i\beta \tag{6-35}$$

where α and β are given by eqs. (6-18) and (6-19). Substituting eqs. (6-34) and (6-35) into eqs. (6-32) and (6-33), nondimensionalizing, and converting to polar form, we finally

obtain

$$R = |R|\, e^{i\varphi_R} \tag{6-36}$$

$$|R| = \frac{\left\{\left[1-(\alpha/k_0)^2-(\beta/k_0)^2\right]^2 + 4(\beta/k_0)^2\right\}^{\frac{1}{2}}}{\left[1+(\alpha/k_0)^2\right]^2+(\beta/k_0)^2} \tag{6-37}$$

$$\varphi_R = \tan^{-1}\left[\frac{2(\beta/k_0)}{1-(\alpha/k_0)^2-(\beta/k_0)^2}\right] \tag{6-38}$$

$$T = |T|\, e^{i\varphi_T} \tag{6-39}$$

$$|T| = \frac{2}{\left[1+(\alpha/k_0)^2+(\beta/k_0)^2\right]^{\frac{1}{2}}} \tag{6-40}$$

$$\varphi_T = \tan^{-1}\left[\frac{(\beta/k_0)}{1+(\alpha/k_0)}\right] \tag{6-41}$$

Due to the semi-infinite extent of the plasma in this model, the reflection coefficient is the one accessible to measurement. For a given probing frequency, $|R|$ and φ_R are functions of the electron density through the parameters α/k_0 and β/k_0.

It is instructive to examine the limiting case of high density and few collisions ($n/n_c > 1$, $\nu/\omega \ll 1$; hence $\alpha/k_0 \ll 1$),

a domain where the plasma becomes perfectly reflecting:

$$|R| = 1.0 \tag{6-42}$$

$$\varphi_R = \begin{cases} 0^\circ, & \beta/k_0 = 0 \\ 90^\circ, & \beta/k_0 = 1.0 \\ 180^\circ, & \beta/k_0 = \infty \end{cases} \tag{6-43}$$

When the transmission coefficient is calculated for this case, it is found to be nonzero:

$$|T| = \frac{2}{\sqrt{1+(\beta/k_0)^2}} \tag{6-44}$$

$$\varphi_T = \begin{cases} 0^\circ, & \beta/k_0 = 0 \\ 45^\circ, & \beta/k_0 = 1.0 \\ 90^\circ, & \beta/k_0 = \infty \end{cases} \tag{6-45}$$

The appearance of a finite transmitted amplitude in addition to a "total reflection" is perhaps noteworthy. Actually, no contradiction of energy balance is involved since the energy carried away from the interface by the transmitted wave is zero. This can be shown by calculating the complex Poynting vector in this region.[44] In general,

$$\bar{S} = \pm \bar{E} \times \tilde{H}$$

$$= \frac{1}{2} E_{0T} e^{i(\omega t - \alpha z)} e^{-\beta z} \left[\frac{\alpha + i\beta}{\mu_0 \omega} \tilde{E}_{0T} e^{-i(\omega t - \alpha z)} e^{-\beta z} \right] \tag{6-46}$$

$$= \frac{\alpha + i\beta}{2\mu_0 \omega} |E_{0T}|^2 e^{-2\beta z} \tag{6-47}$$

the real part of which represents the net energy transport per unit area per second, and is clearly zero for $\alpha = 0$. This result is reasonable in view of the degeneration of wave motion under these circumstances. As $\alpha \rightarrow 0$, $\lambda \rightarrow \infty$ and no space-wise propagation occurs; the $\overline{E}$ and $\overline{H}$ fields exercise standing oscillations, the wave amplitudes decreasing exponentially away from the interface.

Although no net energy propagates away from this region, the energy density within it is not zero because of the standing wave pattern. It is actually this finite zone, rather than the surface itself, which is the reflector, re-radiating just as much energy back into the laboratory in the form of the reflected wave as it absorbs from the incident wave. The penetration distance, or "skin depth," is the distance in which the wave pattern attenuates to $\frac{1}{e}$ of its maximum amplitude, and is given simply by

$$z = d_p = \frac{1}{\beta} \tag{6-48}$$

From this standpoint, it is clear that inhomogeneities in the vicinity of the interface are capable of introducing first-order changes into the reflected wave, even for supercritical, or "cut-off" plasmas, and this problem is treated in detail in section 6-6.

In the more general problem where collisions are allowed, both $|R|$ and φ_R incorporate the new variable, and the computations become sufficiently awkward to justify machine solution. The computed curves are shown in Figs. 6-4 and 6-5, which are plots of $|R|$ and φ_R as a function of $n_e/n_p = (\omega_p/\omega)^2$, with ν/ω as a parameter.

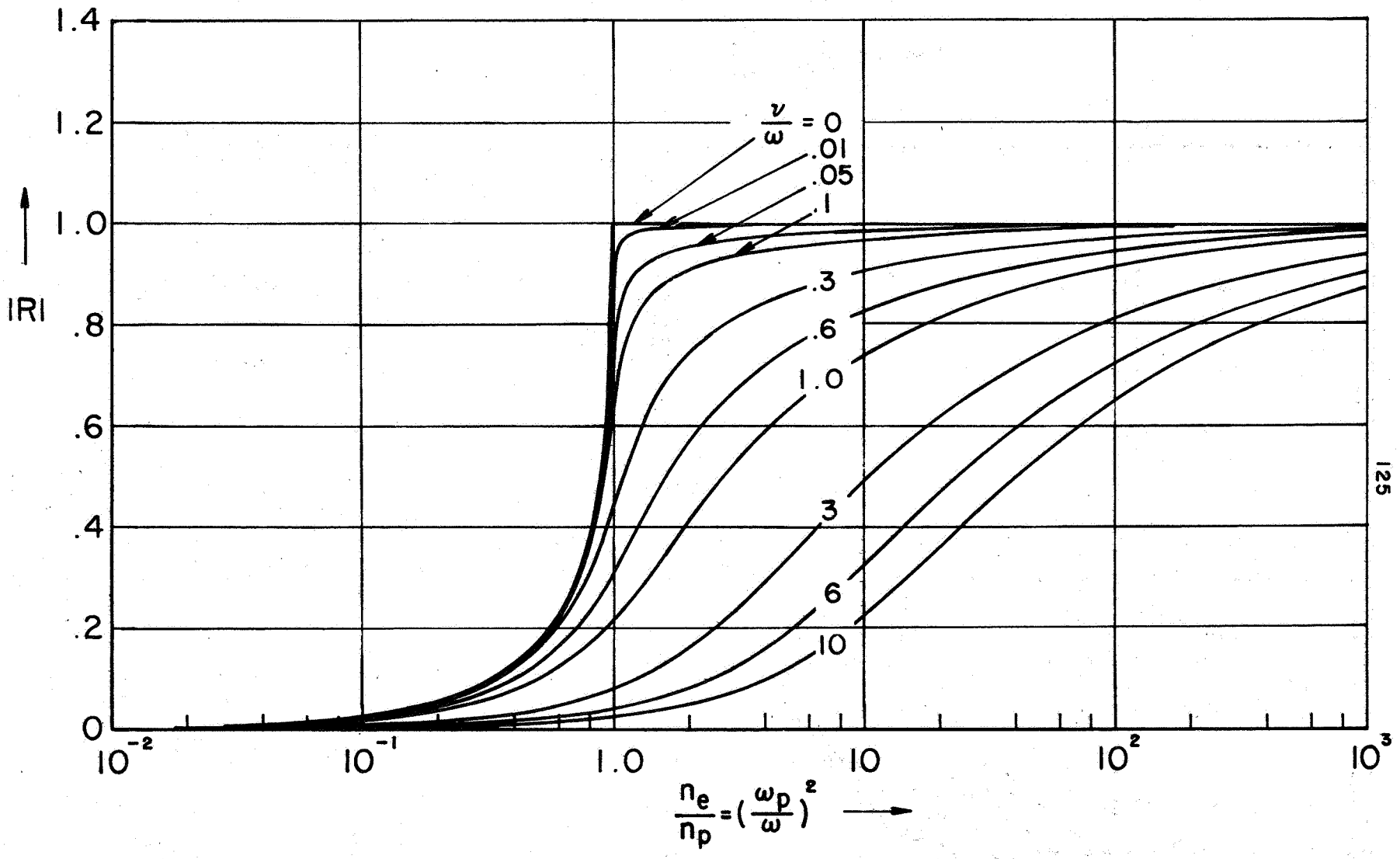

FIGURE 6-4

REFLECTED AMPLITUDE FROM A UNIFORM PLANE PLASMA INTERFACE

FIGURE 6-5

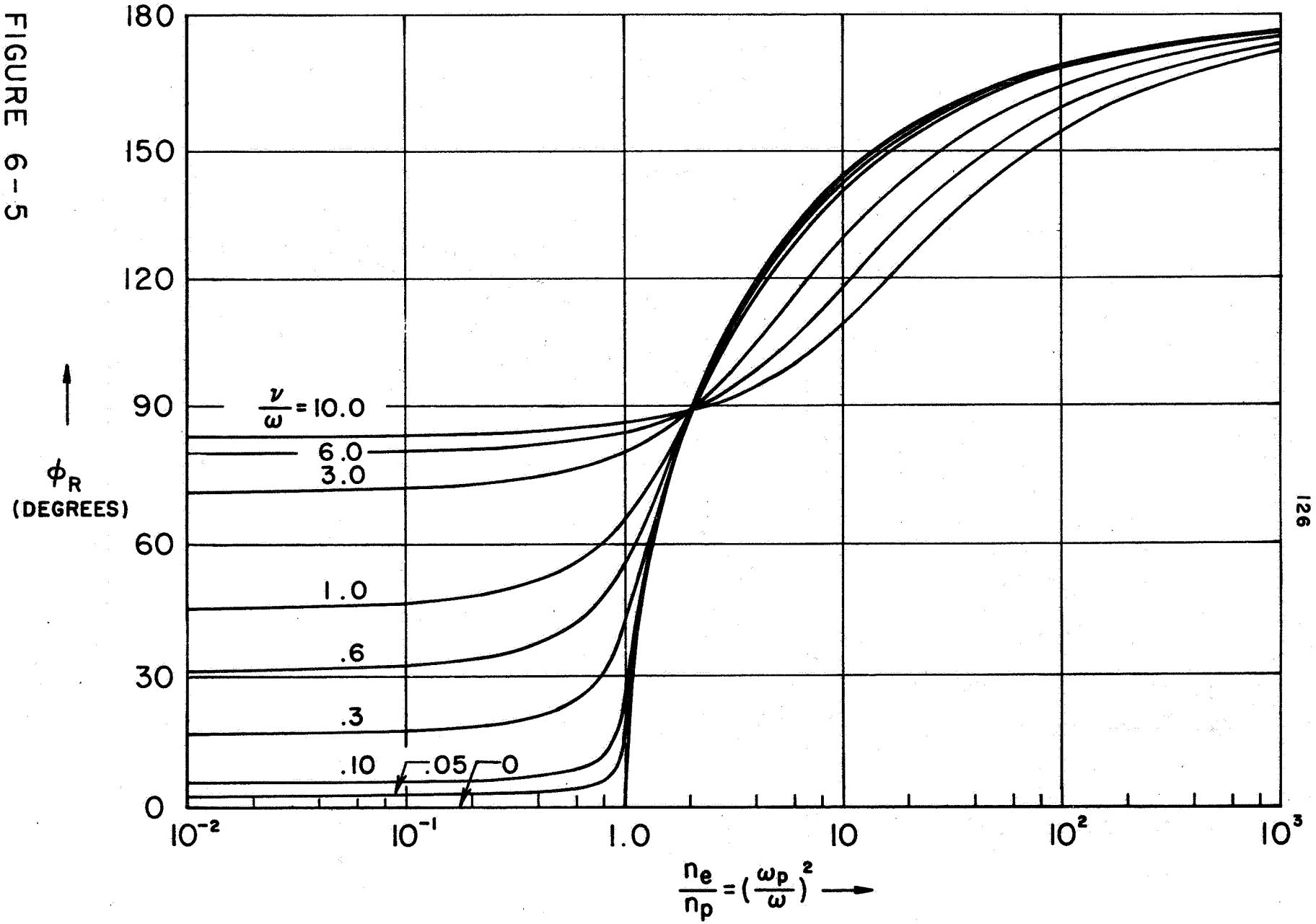

REFLECTED PLANE ANGLE FROM A UNIFORM PLANE PLASMA INTERFACE

Physically, the damping process seems clear: free electrons, driven by the oscillating $\overline{E}$ field, lose some energy upon collision with atoms and ions which otherwise would have been re-radiated as coherent electromagnetic waves. The energy transferred to the heavy particles must appear as a macroscopic heating of the gas at the expense of reflected wave intensity. The rate of such energy absorption per unit volume per second can be calculated from the negative divergence of the real part of the Poynting vector, or, by invoking energy conservation, it can be attributed to an absorption coefficient

$$|A|^2 = 1 - |R|^2 - |T|^2 \qquad (6\text{-}49)$$

In order that the probing wave train introduce negligible disturbance into the plasma under study, it is necessary both that the net energy increase per particle from macroscopic microwave heating be small and that the instantaneous kinetic energy of the nondrifting particles be close to their thermal energy. In the experiments to be described both criteria were satisfied.

The appearance in Fig. 6-5 of a constant, finite phase shift for low electron densities in the highly collision-dominated regime is perhaps surprising, but the effect is academic because of the vanishingly small reflected amplitude prevailing under these conditions.

From the general appearance of the phase curves in Fig. 6-5, the phase of the reflected wave, relative to the incident wave, is seen to undergo significant change only when the electron density is higher than critical. The amplitude curves of Fig. 6-4 show generally the opposite effect for $|R|$, for ν/ω

small, with changes in reflected amplitude tending to occur at densities below critical. Thus the two taken together offer an effective method for measuring electron density over a range of values centered about the critical, or cut-off density.

The fact that reflected phase measurements, in principle, extend the useful range of microwave diagnostics considerably beyond the cut-off density is apparently not universally recognized by workers in the field, and allegations that microwave diagnostics inherently fail above the critical density appear commonly in the literature.

In 1961 Jahn[44] published some of the characteristics of reflected radiation from a partially ionized gas, and in the same year Takeda and Roux,[49] and Hermansdorfer[61] independently in Germany, suggested basic diagnostic experiments incorporating reflected phase measurements. The former authors concluded erroneously that nonuniformities near the boundary would always be confined to within a Debye length of the container wall (re the discussion of section 6-6) and they considered only simple plane boundaries, as did Hermansdorfer. The quiescent plasma-plane boundary model was discussed further in subsequent papers by Takeda and Tsukishma[50,51] for a shock tube experiment, and in a more recent report (1965) these authors gave formal recognition to the boundary problem in reflected phase experiments but made no serious attempt to treat the problem analytically.[52] A recent publication by Hermansdorfer[53] reports reflected phase measurements with a theta pinch, assuming the validity of the uniform plane boundary approximation.

In the following section a probe is described for making reflection measurements in the transient plasma environment of the passing current sheet.

6.4 Microwave Probe Design

Adequate sensitivity to density variations required that the experiments measure both $|R|$ and φ_R. Measurement of the reflected amplitude was straightforward in principle, although somewhat subtler in the execution as described in section 6-7. At microwave frequencies the available detection devices approximately measure power, whence their name of "square-law" detectors. In these experiments solid state diodes were employed to insure adequate transient response. Under ideal conditions they would respond approximately to $|R|^2$, hence delivering the amplitude measurable directly. The phase angle φ_R, on the other hand, was only indirectly measurable, through the interference of the reflected wave train with an undisturbed component of the signal in some type of bridge arrangement.

Consider a steady normalized reference signal to be made available at the detector, which initially sees only this signal with no reflected wave present, corresponding to reflection from a very low density plasma. As the electron density increases, a reflected signal of finite strength appears at the detector superimposed on the reference signal. If the initial phase relationship is such that these two signals initially add, then as the electron density approaches the critical value the reflected signal grows to unit amplitude with essentially

unchanging phase until the net amplitude at the detector has doubled and the power output has increased by a factor of four.

Further increases in electron density rotate the phase of the reflected signal without appreciably changing its amplitude, until at very high densities the two signals are 180° out of phase and the net amplitude vanishes. Thus the resultant amplitude ρ of the interfering signals follows the rules of vector addition, as shown in Fig. 6-6,

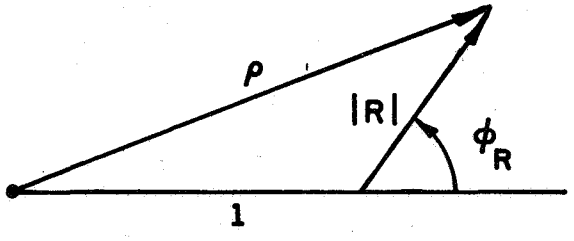

VECTOR ADDITION OF AMPLITUDES

FIGURE 6-6

and the net electric field at the detector may be expressed as the vector sum of a unit reference signal and the complex reflection coefficient in the normalized form

$$E_{Net} = \frac{\rho_{\pm}}{2} = \frac{\sqrt{1 + |R|^2 \pm 2|R| \cos \varphi_R}}{2} \leq 1 \qquad (6\text{-}50)$$

The choice of the + or - sign in eq. (6-50) is in the hands of the experimenter, for the interferometer can be adjusted to yield a critical null or antinull with equal ease. It will be

convenient to refer to use of the + sign as "low-mode" operation and to use of the - sign as "high-mode" operation for reasons which will become apparent. The modes differ significantly, and the particular virtues of each will be examined later in the chapter.

The net electric field, eq. (6-50), is plotted in Figs. 6-7a and 6-8a as a function of the electron density, $\frac{n_e}{n_p} = \left(\frac{\omega_p}{\omega}\right)^2$ with $\frac{\nu}{\omega}$ as a parameter. To the "square law" approximation the detector output was proportional to E_{net}^2, i.e. ρ^2, and Figs. 6-7b and 6-8b display this phase measurable. The designation "high" or "low" mode is now seen to refer to the detector output for asymptotically high values of electron density.

As anticipated, the composite detector output exhibits either a null or antinull at the critical density, according to the mode of bridge operation selected, followed by a region of monotonic sensitivity to n_e and ν as φ_R undergoes an excursion of approximately 180 degrees beyond cutoff. The result is thus a kind of single fringe interferometer, whose operation is distinguished from the usual fringe counting methods by the necessity to make quantitative measurement of a fractional fringe shift. Detector nonlinearity and other experimental variables are thus more critical here than in the usual interferometer experiment.

A compensating advantage offered by this approach is the marked sensitivity of cusp height to collisional damping, particularly in the low mode operation of Fig. 6-7b, which suggests a simple inspection method for inferring electron collision frequencies quickly.

FIGURE 6-7a

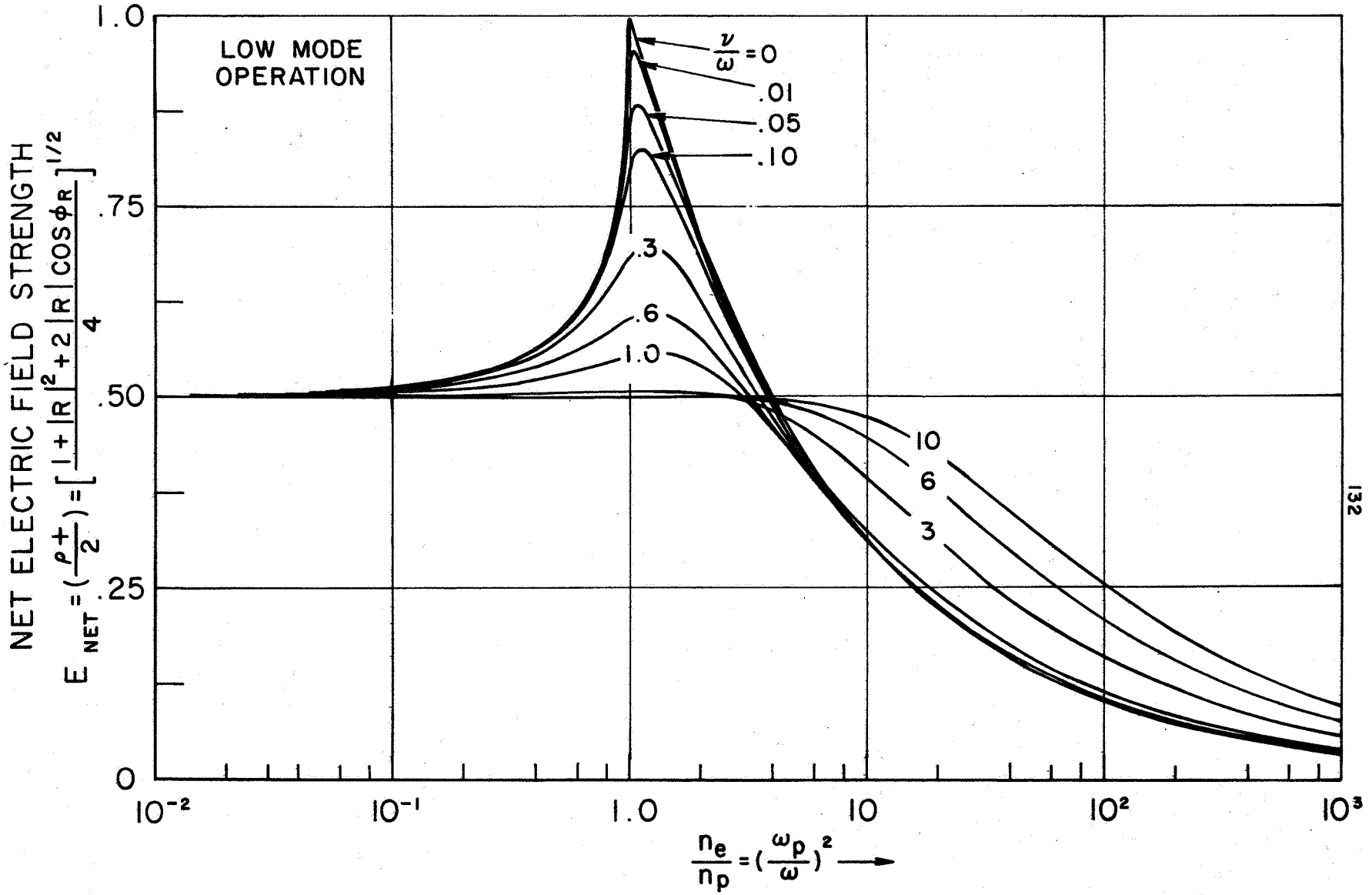

COMPUTED INTERFEROMETER RESPONSE FROM A UNIFORM PLANE PLASMA INTERFACE

APPS-4280-01

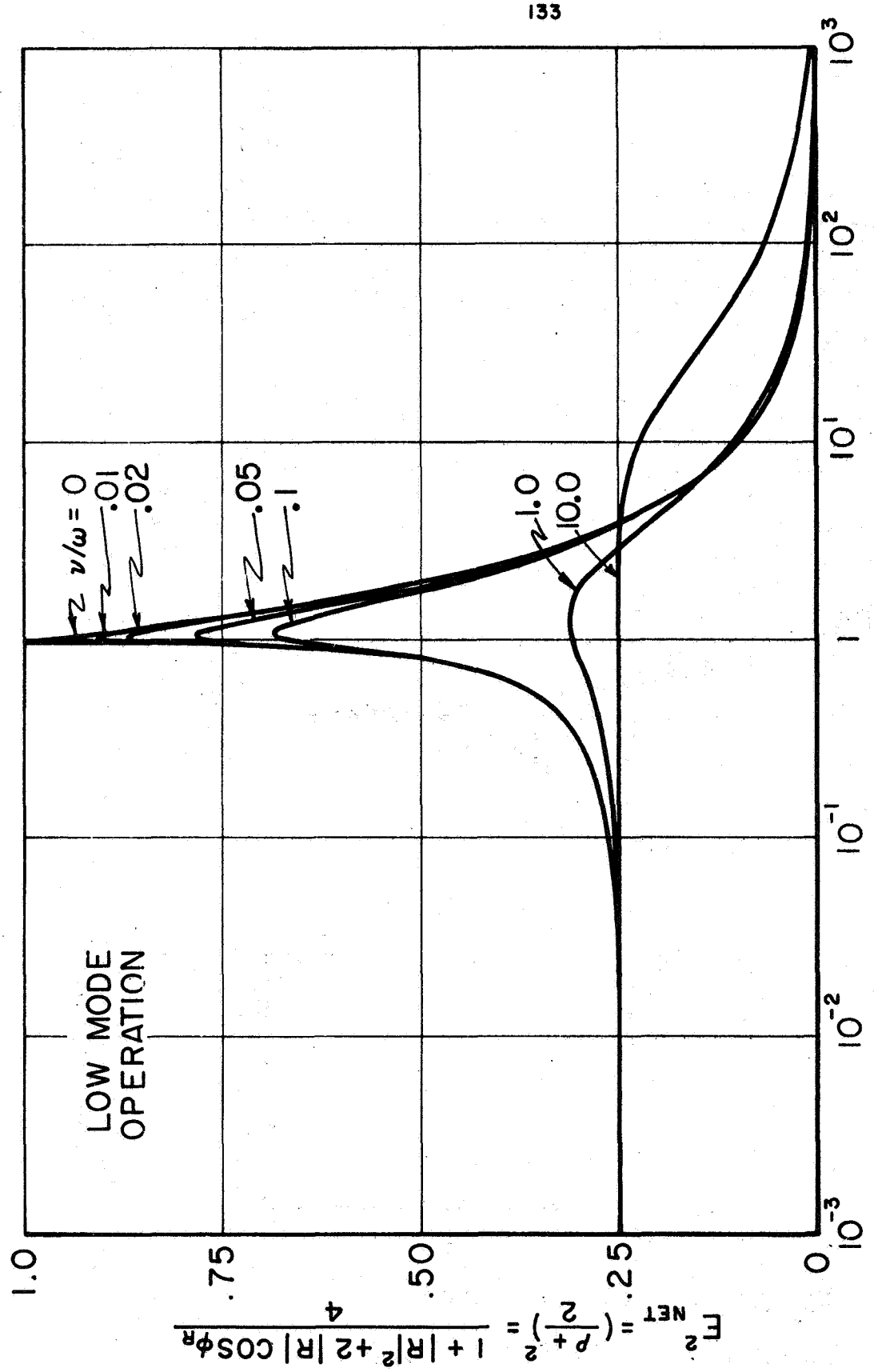

COMPUTED INTERFEROMETER RESPONSE FROM A UNIFORM PLANE PLASMA INTERFACE

FIGURE 6-7b

FIGURE 6-8a

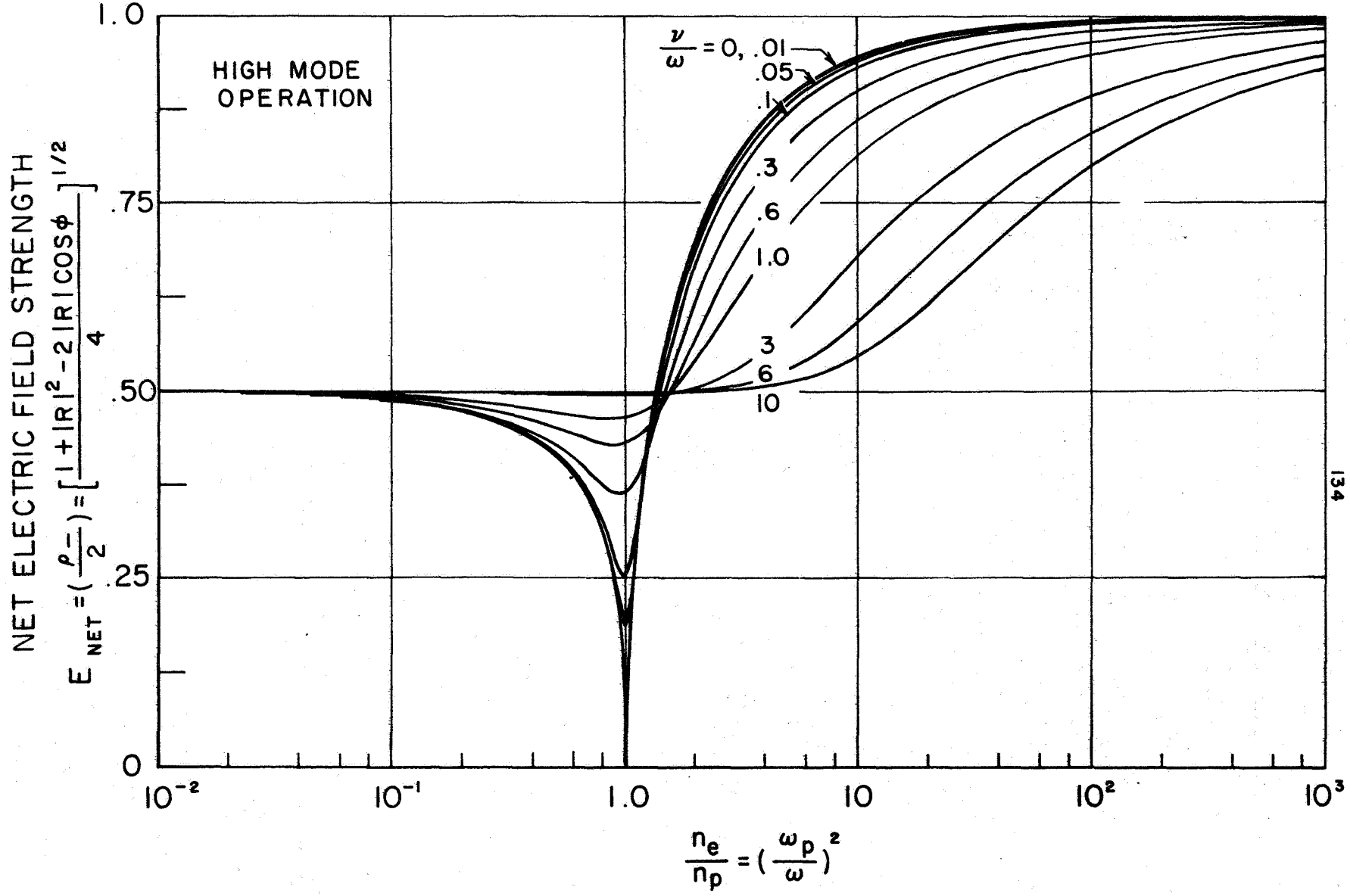

COMPUTED INTERFEROMETER RESPONSE FROM A UNIFORM PLANE PLASMA INTERFACE

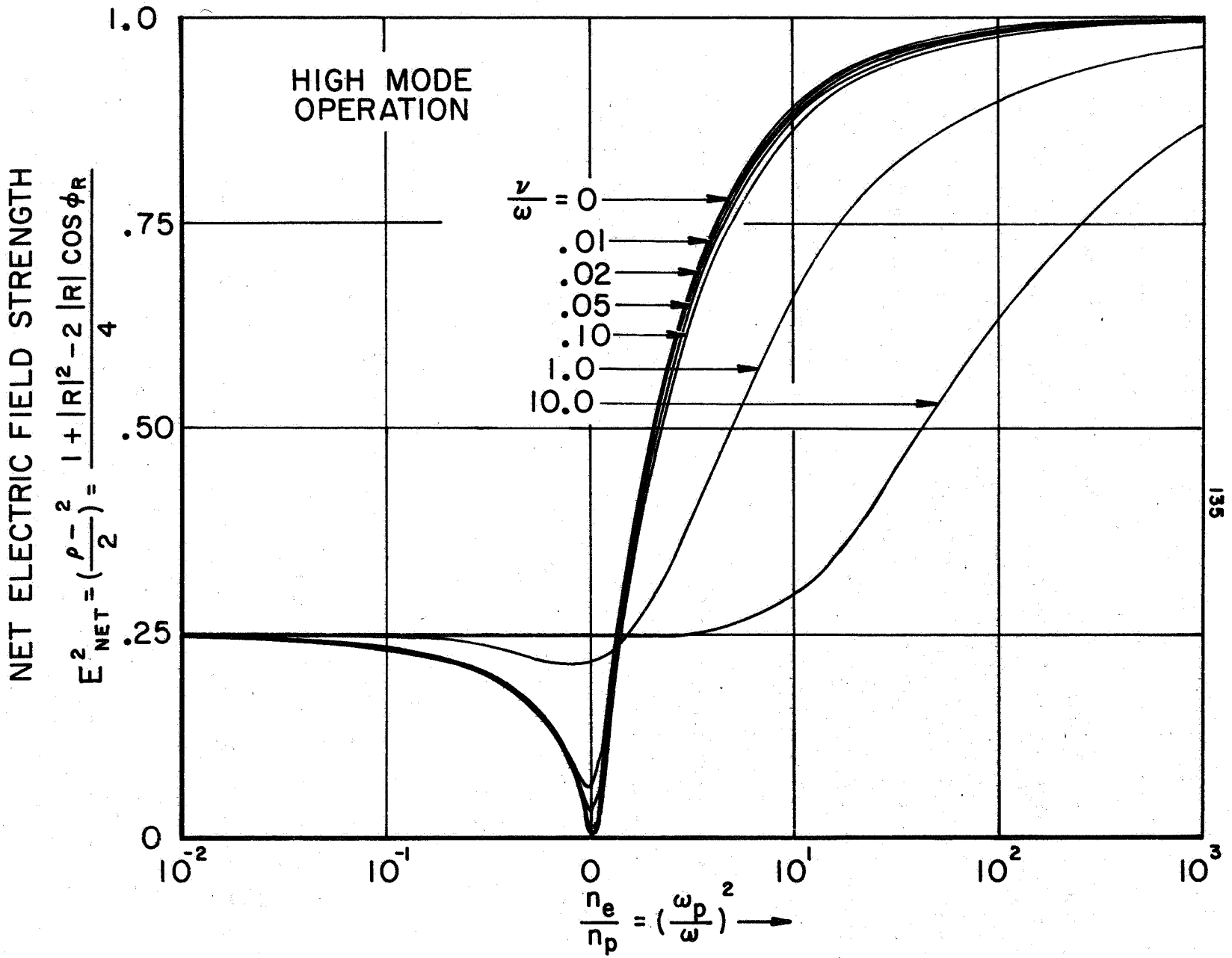

FIGURE 6-8b

COMPUTED INTERFEROMETER RESPONSE FROM A UNIFORM PLANE PLASMA INTERFACE

The probing frequency was selected as the best compromise between spatial resolution, the need to measure high densities, and the equipment problems of the shorter millimeter wavelengths as discussed in section 3-6. Comparison tests were made in the laboratory with 35 GHz ($\lambda \cong 8$ mm) and 70 GHz (4 mm) equipment, the two most readily available millimeter wavelengths. 140 Gc (2 mm) was rejected for reasons of high cost and questionable mechanical and electrical reliability. On the basis of these tests and the considerations mentioned, 70 GHz (kilomegacycles per second) was selected as the best available probing frequency for the proposed experiments, and all subsequent work was done at this frequency. Fig. 6-9 is a chart of the absorption bands for microwave frequencies in air, and 70 GHz is seen to be a relatively good choice in this respect. From eq. (6-13),

$$n_p = 6.1 \times 10^{13} \ cm^{-3} \tag{6-51}$$

As discussed in section 3-6, the electron density variations anticipated in 100μ discharges fall in the range

$$10^{13} \lesssim n_e \lesssim 10^{16} \ cm^{-3} \tag{6-52}$$

and thus we require sensitivity roughly over the range

$$10^{-1} < \frac{n_e}{n_p} < 10^{2} \tag{6-53}$$

This requirement is seen to be well met by the range of sensitivity of the reflected-phase interferometer (RPI), from Figs. 6-7 and 6-8.

More than a dozen bridge configurations were tested in the laboratory, and the only consistently satisfactory design

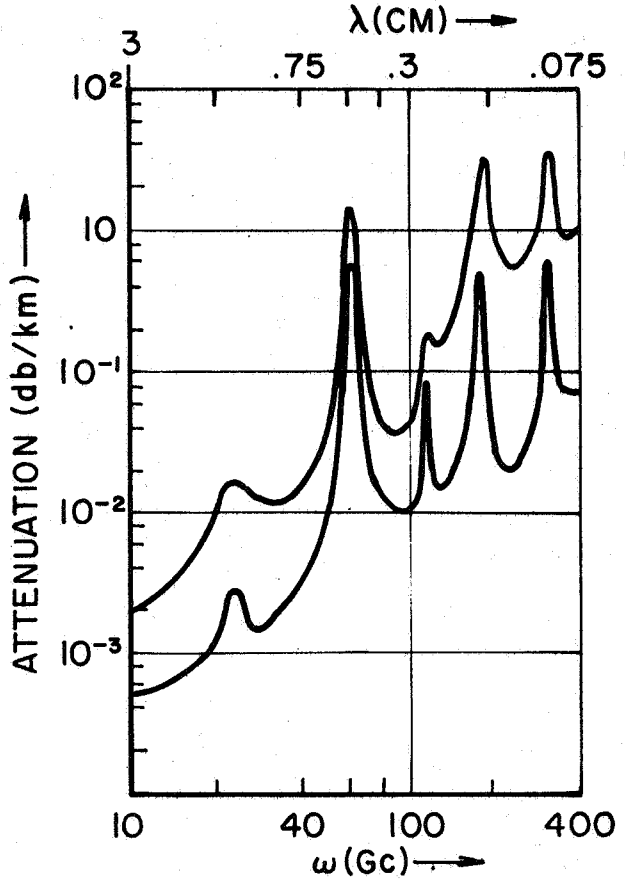

APPROXIMATE ATMOSPHERIC ATTENUATION FOR MICROWAVES †
(† TRG HANDBOOK)

FIGURE 6-9

which was found is diagrammed schematically in Fig. 6-10. The basis for this component configuration was the need for a bridge sufficiently adaptable to precision balancing. This is a practical problem shared by many interferometer designs, and is discussed in section 6-7 under sources of error.

The waveguide components were furnished primarily by TRG, Inc., of Boston, Massachusetts. The waveguide was standard RG-98/U V-band (50-75 GHz) supplied with standard UG-385/U flanges, with the exception of two quick-break claw flanges which were installed for safety reasons. The waveguide sections were fabricated from silver stock, silver plated and protected with a rhodium flash coat to reduce transmission losses. Ten feet of oversized 8 mm guide was employed between the discharge chamber and the screen room which housed the interferometer to further reduce losses (the problem of guide attenuation was especially severe in these experiments because of the two-way transmission of power). The few special pieces of waveguide which were not available commercially were fabricated at Princeton[+] of copper stock in RG-98/U dimensions (0.148"x0.074" I.D.) and fitted with silver soldered brass flanges. The entire assembly was mounted on a removable, ventilated 3'x6' wooden platform which was accommodated inside the screen room on metal runners, Figs. 6-11 and 6-12. The waveguide link between screen room and pinch

---

[+]The assistance of the Microwave Division, Plasma Physics Laboratory, Princeton University, for the loan of certain specialized equipment needed in fabricating these waveguide components is gratefully acknowledged.

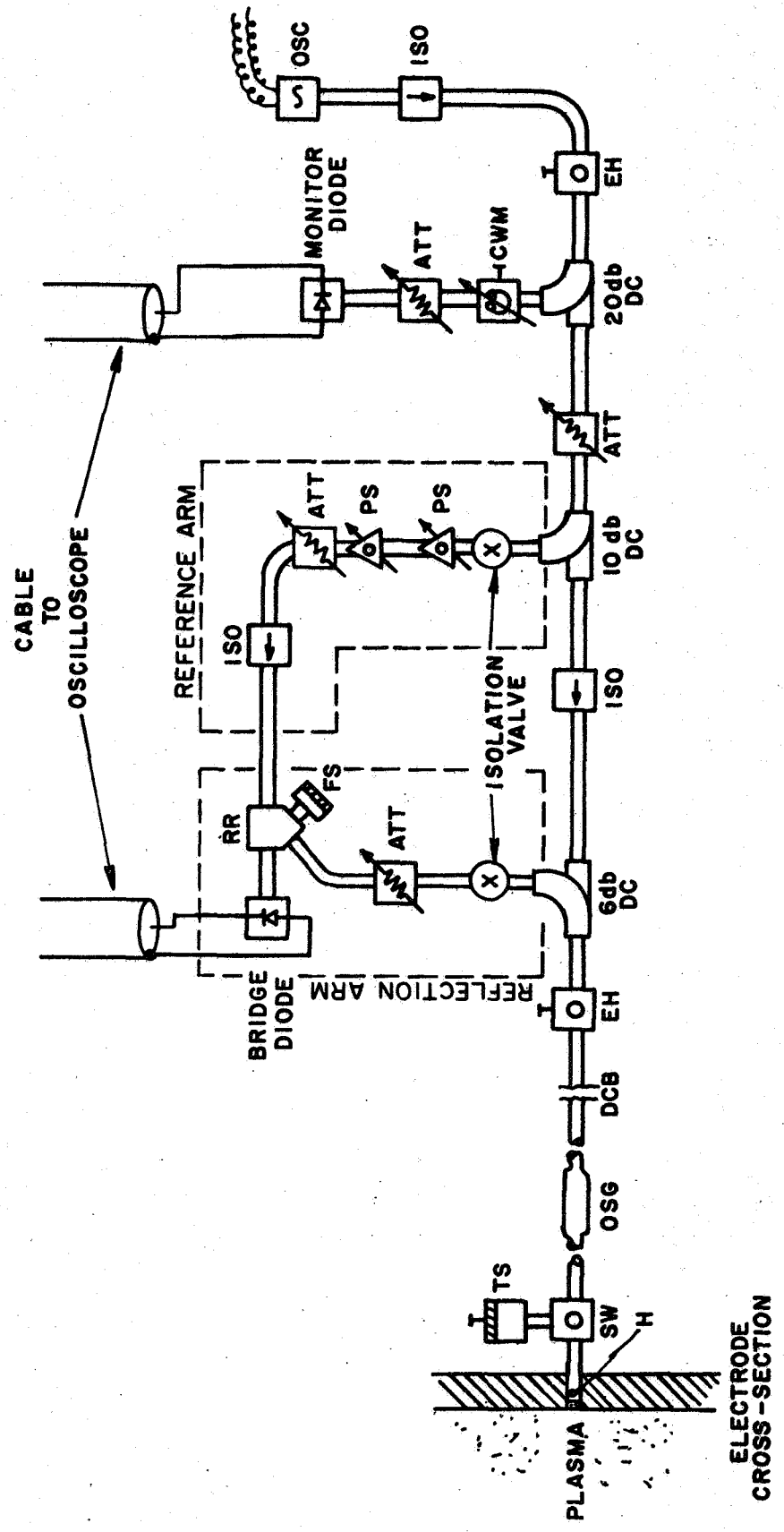

Notation: H, horn; SW, 3-port switch; TS, tunable short; OSG, oversize guide; DCB, direct current break in waveguide; EH, $\overline{E}$ and $\overline{H}$ plane tuner; DC, directional coupler; ATT, variable attenuator; Diode, square-law crystal detector; FS, fixed short; RR, rat race; ISO, isolator; PS, variable phase shifter; CWM, cavity wave meter; OSC, reflex klystron oscillator.

DIAGRAM OF REFLECTED PHASE INTERFEROMETER

FIGURE 6-10

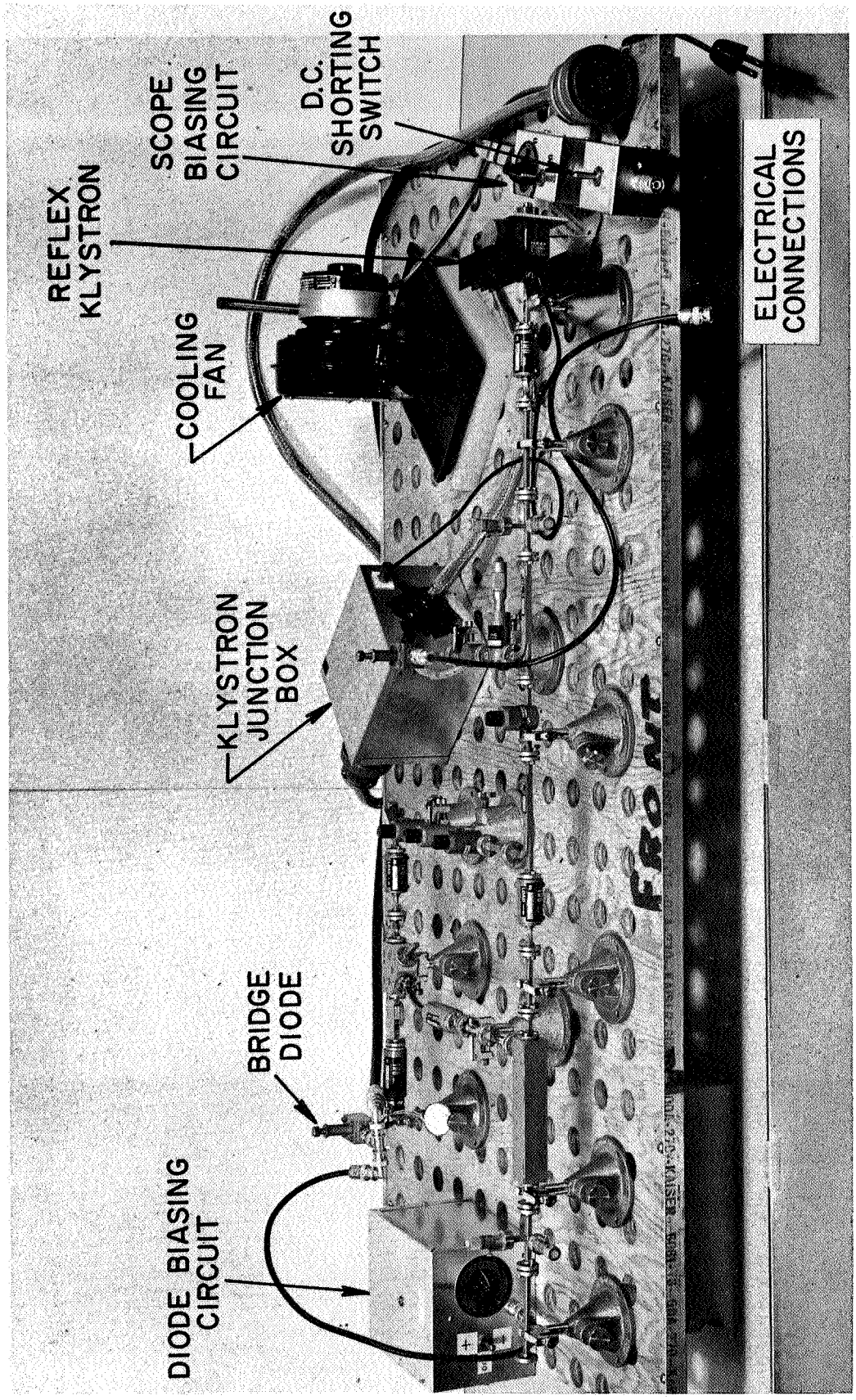

REFLECTED PHASE INTERFEROMETER ON SCREEN ROOM PLATFORM

FIGURE 6-11

AP25-P105-6T

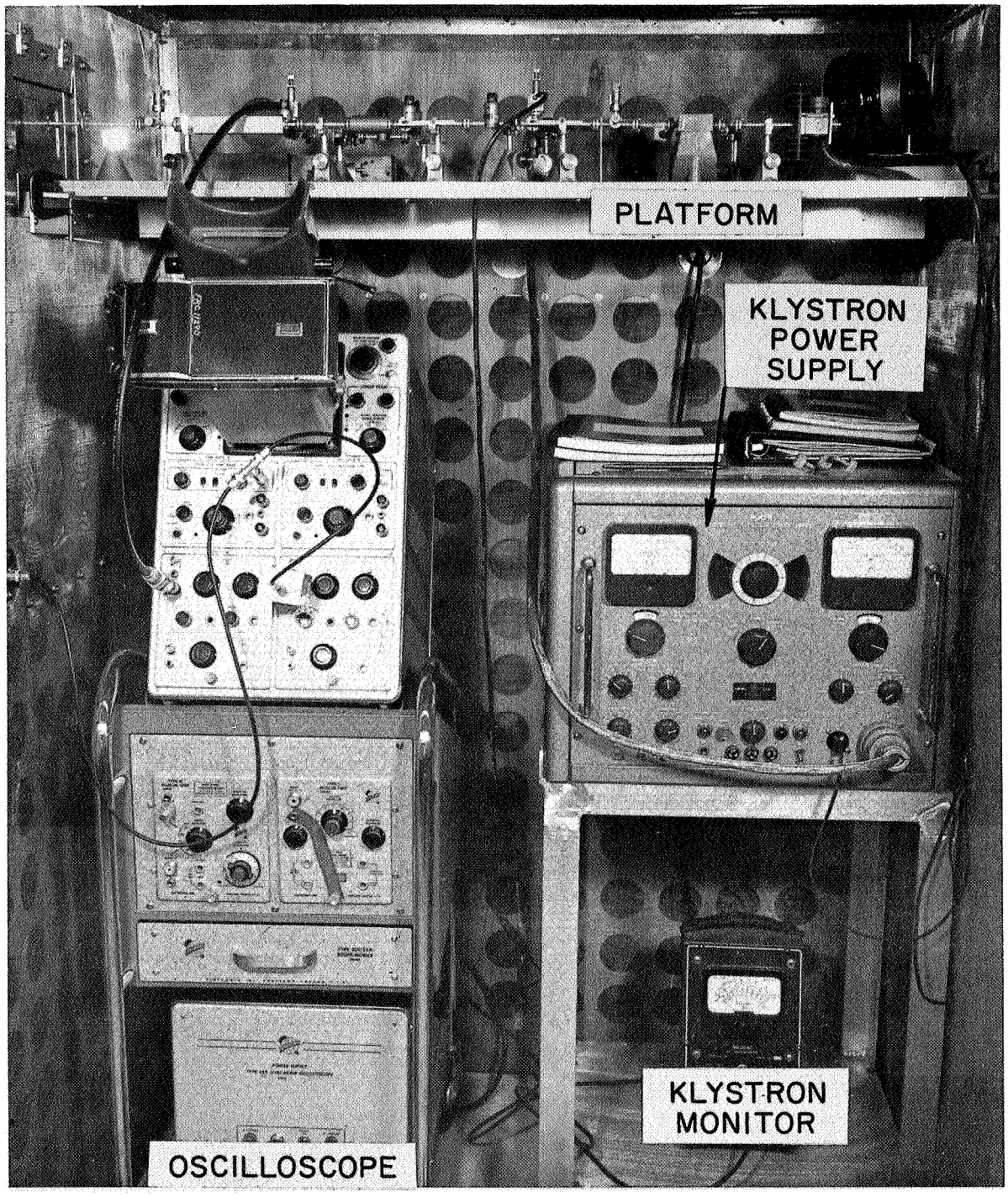

INTERIOR VIEW OF SCREEN ROOM

FIGURE 6-12

AP25-P104-67

apparatus is shown in Figs. 6-13 and 6-14. These figures also show the Rogowski coil and probe connections to the screen room, the microwave probe and B-probe mounted simultaneously in the discharge chamber, and the screen room exit panel to accommodate the waveguide. This latter item incorporated a specially fabricated waveguide section and a sliding metal plate, held by strap fasteners, which permitted movement of the exiting guide in any direction plus rotation about the long dimension. These precautions were taken to avoid undue mechanical stresses in the waveguide linkage between RPI and test chamber, while maintaining electrical shielding for the bridge components. A direct current mylar break was provided in the waveguide near the screen room exit.

The three components of the RPI requiring the greatest amount of individual attention were the reflex klystron wave source, the diode detectors, and the microwave horn. These components are described briefly and separately below.

Klystron. The microwave energy source was a VA-250 reflex klystron manufactured by Varian Associates, Ltd., of Ontario, Canada, on special order. This tube was selected for its high cw (continuous wave) output power of up to 500 milliwatts and its operating stability. The high power output was necessary to establish the very good signal-to-noise ratio obtained in the experiments. The tube was operated at about 80% maximum output cw on the resonance peak shown in Fig. 6-15, and the observed frequency drift was less than 0.1 GHz over a two-year period. The tube had a guaranteed life of 100 hours, and in view of its high cost a log was kept of its operation. The tube

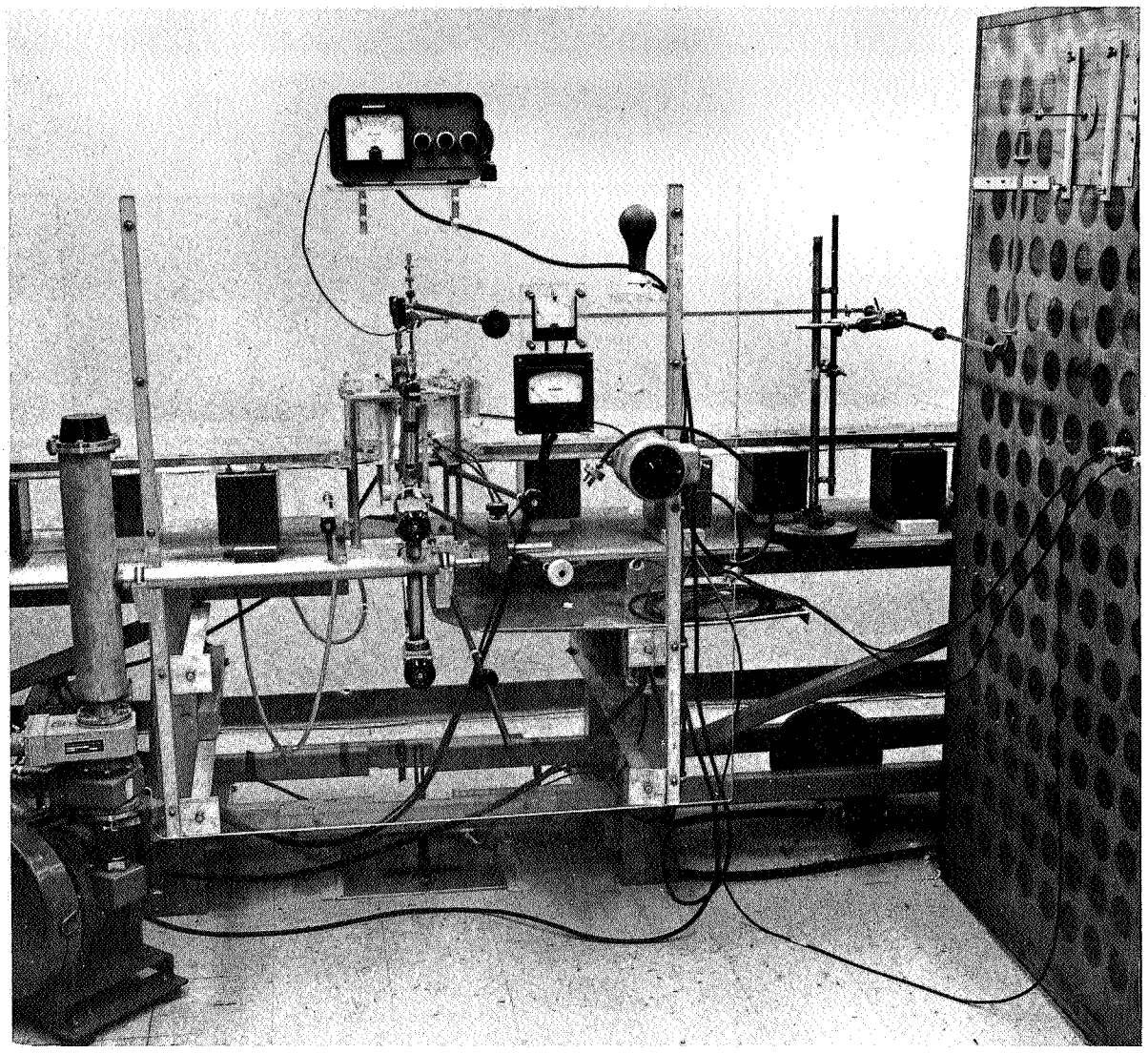

OVERALL VIEW OF APPARATUS AND PROBE CONNECTIONS

AP25-P102-67

FIGURE 6-13

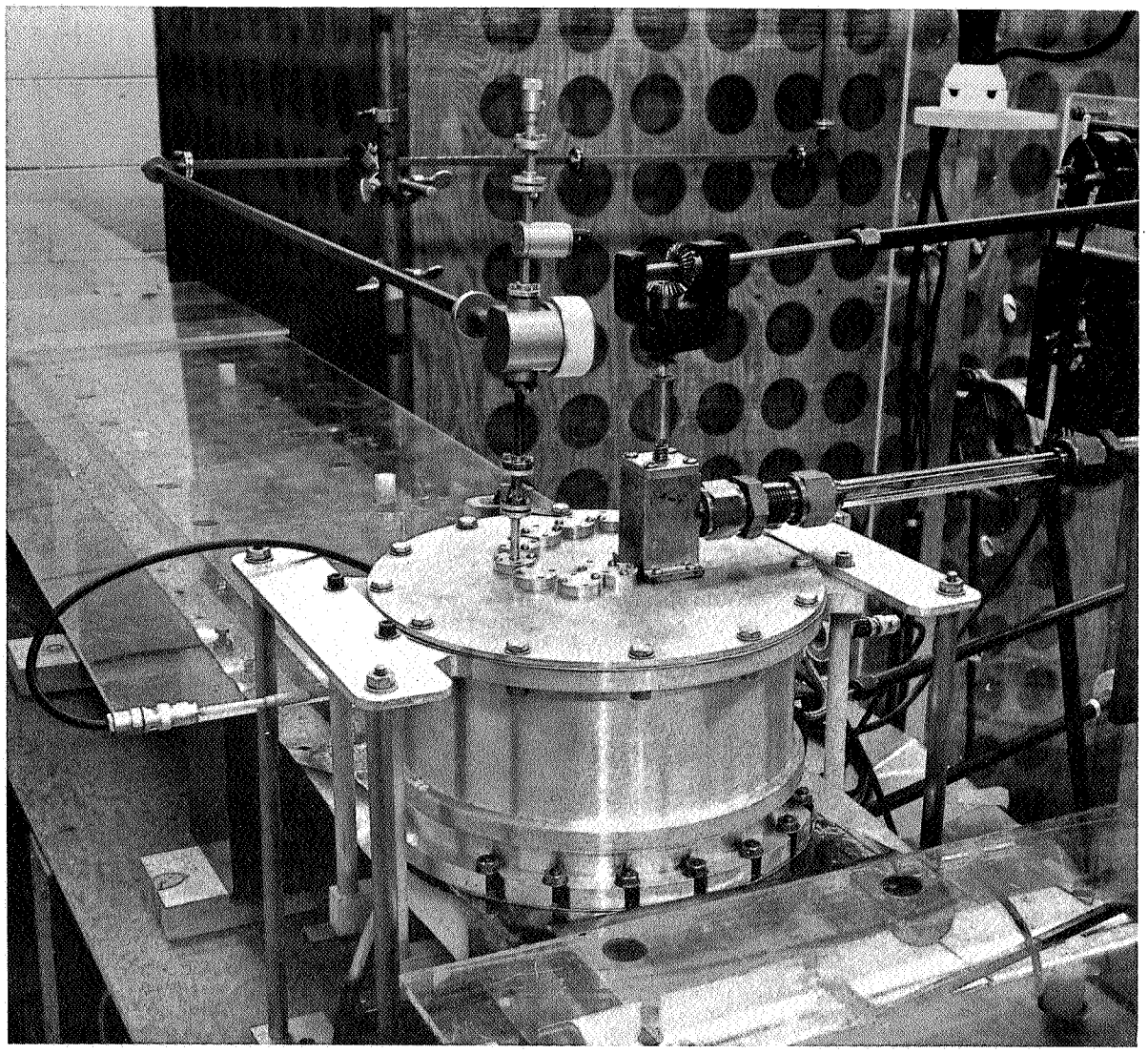

AXIAL MICROWAVE PROBE AND RADIAL B-PROBE
MOUNTED IN 8" DISCHARGE CHAMBER

AP25-P103-67

FIGURE 6-14

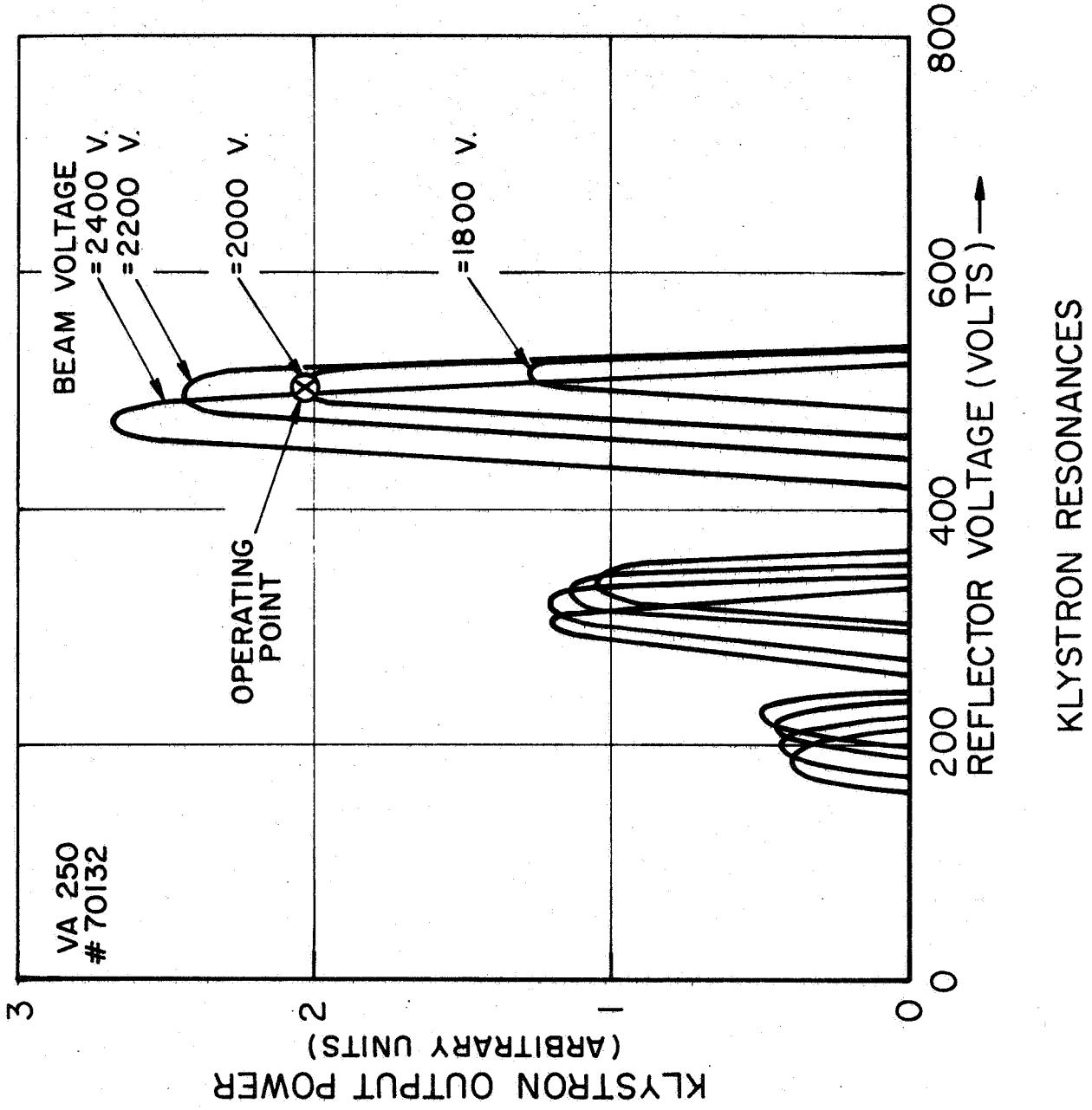
KLYSTRON OUTPUT POWER
(ARBITRARY UNITS)
3
2
1
0
0
200
400
600
800
REFLECTOR VOLTAGE (VOLTS) ⟶
KLYSTRON RESONANCES
BEAM VOLTAGE
=2400 V.
=2200 V.
=2000 V.
=1800 V.
OPERATING POINT
VA 250
#70132

FIGURE 6-15

was still functioning after two hundred hours of recorded operation, although at greatly diminished output.

Cooling was provided by a fabricated aluminum jacket with blackened cooling fins, and a small centrifugal fan mounted beside the tube on a shock absorbing pad to reduce vibration (Fig. 6-12). The tube was protected from feedback resonance with an impedance-matching, ferrite isolator-tuner combination mounted between the tube and the other bridge components. The output power of the klystron was read continuously from a separate monitoring circuit located between the isolator-tuner section and the bridge (Figs. 6-10 and 6-12).

Klystron power was supplied by an FXR Universal Klystron Power Supply Model Z-815-B, shown in Fig. 6-12. The power supply was accommodated in the screen room on its own fabricated aluminum dolly, and was connected to the laboratory electrical service through a low pass isolation transformer.

Two modifications were required to adapt this power supply to the operating specifications of the klystron. The power supply reflector grid circuit impedance was too high, and had to be reduced below 100,000 ohms to prevent possible positive excursions of the reflector voltage (which would prove instantly fatal to the tube); and the heater leads had to be converted from a floating arrangement to tie in with the cathode, to prevent the possibility of an internal cathode-to-heater short circuit. Since the cathode potential was nearly 2,500 volts below ground, this required extensive rewiring of the power supply output circuit and plug configuration. The rewiring was done at the factory to the supplied specifications, and the klystron was then wired to

the power supply through an intermediary shielded junction box, visible in Fig. 6-11, which was tested to withstand 8,000 volt surges between terminals. The junction box provided safe access to the hot leads, and allowed the addition of a variable heater voltage supply unit, if desired, to revive the klystron output power.

Diode Detectors. The detectors were hermetically sealed germanium diodes, Philco Model #IN2792, which were selected for maximum output voltage at 70 GHz. These diodes were mounted in standard TRG Model V995 crystal holders available for this purpose, and normally two were employed in the RPI, one to monitor the klystron and the other to respond to the reflected wave as previously described.

This latter detector, the bridge diode, was an important link between the standing wave pattern in the guide and the data display on the oscilloscope screen because of the part it played in noise pickup, the electrical and mechanical connections between interferometer and oscilloscope, and the quantitative behavior of the oscilloscope input signal.

When the transient $|R|$ signal reached the diode during an experiment, the diode rectified the sinusoidal 70 GHz signal as would any ordinary half wave rectifier, and the resulting pulsed dc voltage appeared across the terminals of the germanium crystal.

The specific electrical characteristics of the diode are a strong function of the electrical loading, and the internal resistance R_i varies from about 1,000 Ω, drawing small current, to several hundred ohms under maximum current loading. The internal

capacitance, C_i , is well regulated at several picofarads. Thus the maximum time constant of the diode is

$$\tau \cong 10^{-9} \text{ sec.} \qquad (6\text{-}54)$$

and the unit would pass no frequencies higher than about 1 GHz. Thus the rectified 70 GHz signal was effectively filtered at the diode terminals into a "dc" output voltage with time variations commensurate with the microsecond time scale of the experiment.

As a result the diode exhibited excellent frequency response for these experiments, but required high impedance cable for adequate matching and high output voltage. Within the restriction to use commercially available cable with real (i.e. non-reactive) characteristic impedance, 185 ohm cable was the best available match to the loaded diode. As no commercial terminators were available for this cable, 186 ohm terminators (the closest match) were constructed using 1/2 watt, 1% precision resistors in Tektronix housings. Cable reflections were practically undetectable using this arrangement, and the overall signal-to-noise ratio was very good.

At first the diode response characterisitcs, which must be known for accurate data reduction, underwent undesirably large day-to-day variations, generally exhibiting something between linear and quadratic behavior. The diodes also showed a lack of sensitivity at very low power levels, exacerbating the already delicate problem of bridge balance. These problems were alleviated by employing a forward biasing voltage on the diode in conjunction with a compensating reverse bias for the oscilloscope. Fig. 6-16 is a schematic diagram of the biasing circuits employed, including

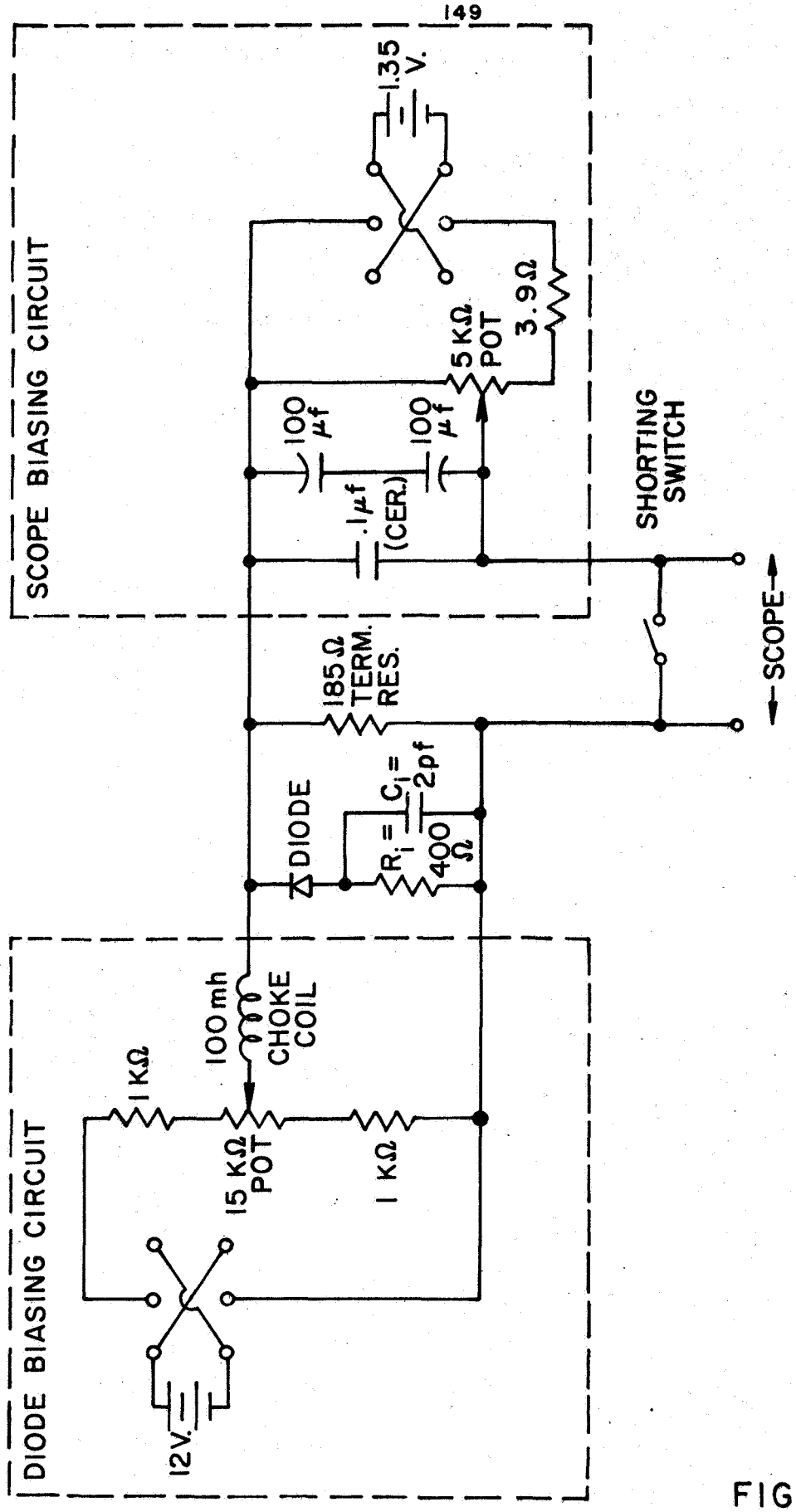

SCHEMATIC DIAGRAM FOR BIASING CIRCUITS

FIGURE 6-16

a low pass choke filter to block high frequency diode transients from the voltage divider.

It was determined by trial and error that a forward bias of 0.2 volts on the diode resulted in very nearly quadratic response, good stability of the biasing circuit, and near maximum diode sensitivity, and the diode was so biased whenever quantative data were taken.

The question of precise diode calibration will be deferred to the discussion of errors in section 6-7.

70 GHz Horn. The microwave horn was considered, in the theory of section 6-2, to irradiate the plasma with plane waves. The virtue of the plane wave theory lies in its simple one dimensionality, i.e. lack of transverse energy flow. Since the microwave radiation was incident in these experiments on a strongly reflecting plasma, Fig. 6-17a, the effect on a guided wave was similar

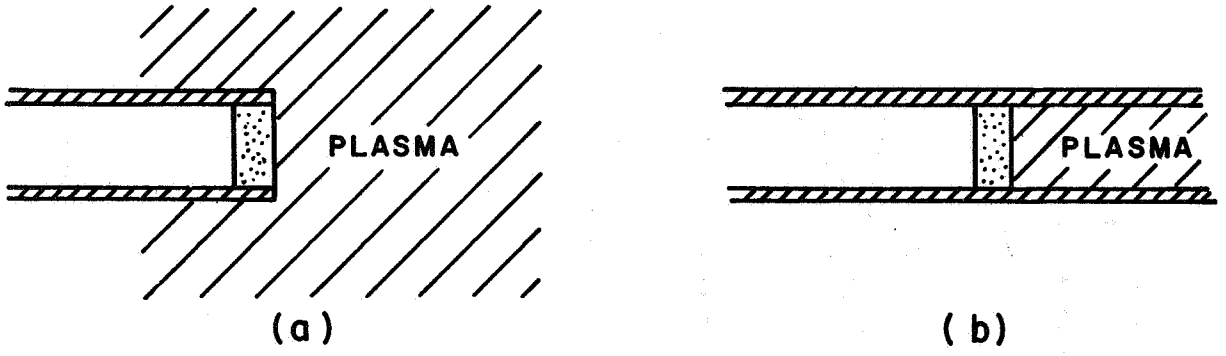

FIGURE 6-17

to what would prevail if the wave encountered a plasma discontinuity in the waveguide, Fig. 6-17b. Indeed, if the reflection coefficient from a waveguide discontinuity is calculated[54] it

turns out to be identical with eq. (6-32), demonstrating that if all the incident energy is reflected back down the waveguide the situation is indistinguishable, mathematically, from the plane wave case.

Thus we are led to one of the major advantages of a reflected wave experiment: the "radiator" can be made as small as the fundamental-mode waveguide dimension, which means that for a 70 GHz probing frequency the spatial resolution will be about $\frac{\lambda}{2}$, or 2 mm, the same spatial resolution obtained with the B-probes and E-probes.

With this criterion in mind, a series of design experiments was undertaken by TRG to determine the most favorable horn geometry for reflection measurements. The designs tested included W and V band rectangular waveguides, and equivalent circular guides, both with and without terminating ground planes, supplied with various dielectric end windows. The tests included beam focusing, symmetry effects, and the influence of reflecting elements introduced into the radiation patterns.

The final design incorporated a linearly polarized (TE_{11} mode) circular waveguide horn fed from standard V-band rectangular waveguide (WR-15) through a smooth rectangular to circular waveguide transition. A UG-385/U waveguide flange was used at the rectangular input end, and a quartz window was sealed into the circular aperature with epoxy cement. A cross section view of the horn assembly is shown in Fig. 6-18, and all three probes are compared in Fig. 6-19.

The horn was designed to mount in a 0.250 inch diameter hole in the exterior electrode. A Parker #2-11 O-ring in the hub

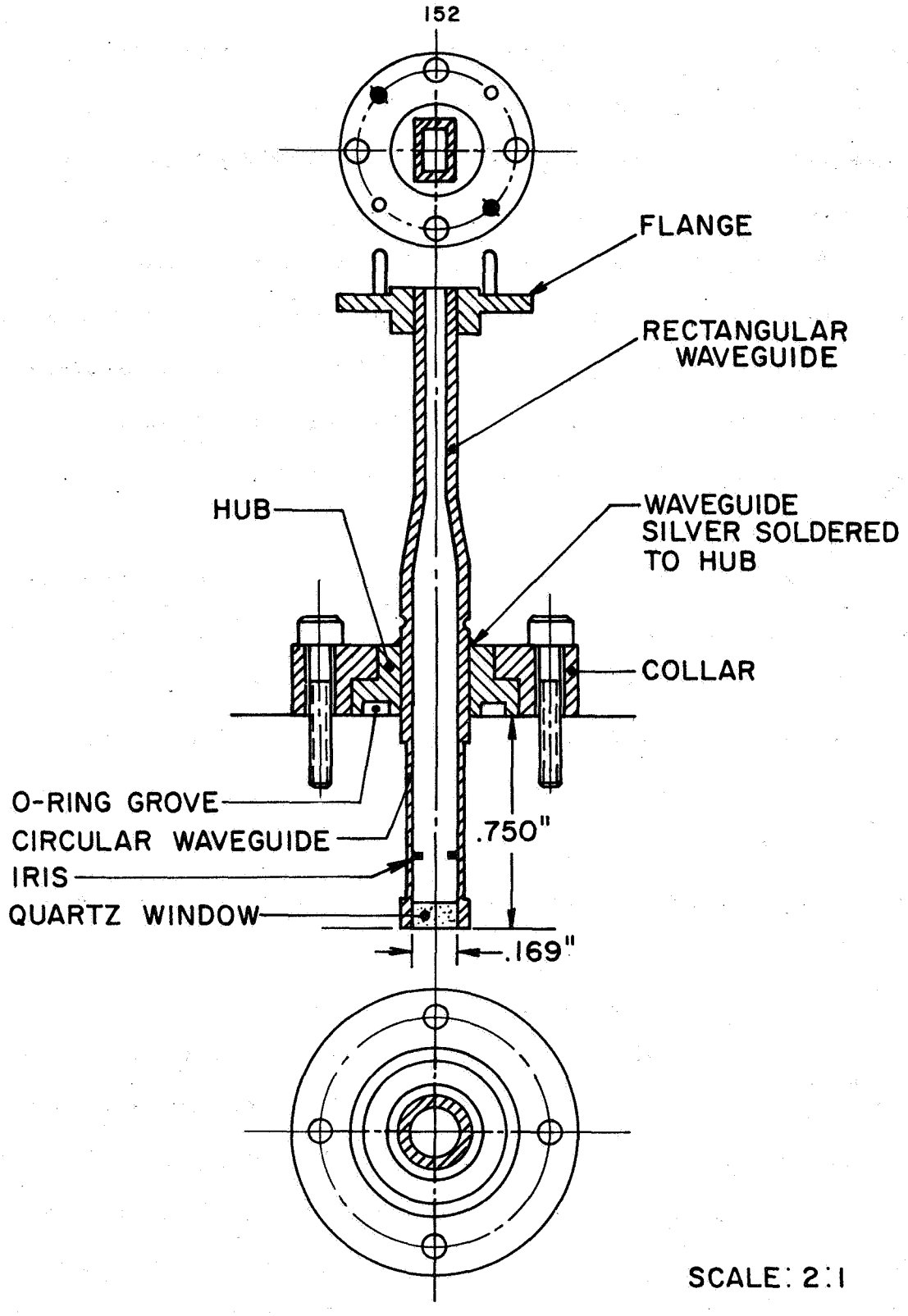

CROSS-SECTION VIEW OF 70 GHz HORN

FIGURE 6-18

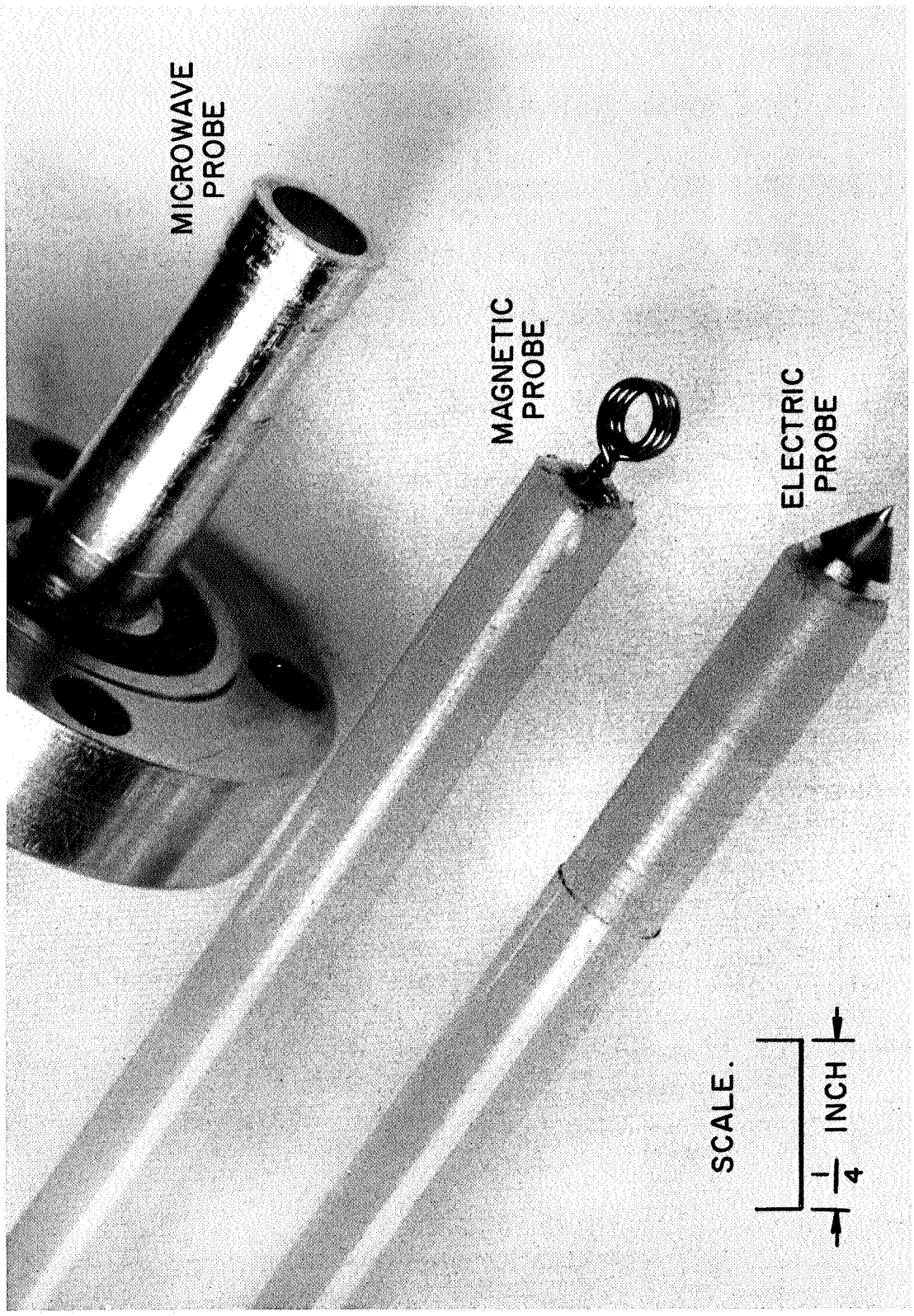

MICROWAVE PROBE, MAGNETIC PROBE AND ELECTRIC PROBE USED IN 8" MACHINE CLOSED CHAMBER EXPERIMENTS

FIGURE 6-19

plus the quartz window provided the vacuum seal. A collar was used to hold the horn in position, and prior to securing allowed the horn polarization to be rotated through 360°.

Several electrodes were constructed to accept the horn. Fig. 6-20a shows the horn mounted flush in an electrode equipped with radial probing ports every 1/2 inch, arranged in a spiral to minimize mutual interference. Fig. 6-14 is an exterior view of this electrode mounted on the discharge chamber, with nine probing ports visible. Figs. 6-20b and c show two views of an electrode adapted for axial probing. The radial glass slot was used for streak photography. The thin teflon flow isolator, shown mounted on the horn, was used to minimize gas dynamic effects at off-electrode probing positions, e.g. when the horn protruded into the path of the propagating sheet. For the several μsec duration of the experiments, it effectively divided the flow field into two regimes: the unimpeded flow over the horn aperture, and the stagnated flow (beneath the isolator) which had impacted against the horn body.

Before fitting the quartz window to the horn, the match of the unit was very good, with a voltage standing wave ratio, defined as

$$VSWR = \frac{1-|R|}{1+|R|} \qquad (6\text{-}55)$$

of less than 1.05:1 at 70 GHz. By using a dielectric constant of 3.78 for the quartz, a window thickness one wavelength long in quartz filled guide was determined to be 0.091 inches. This dimension was verified when the window was inserted well inside the guide. However at the aperature a thickness of 0.095 produced a slightly better VSWR, 1.25:1 as against 1.35:1 for the

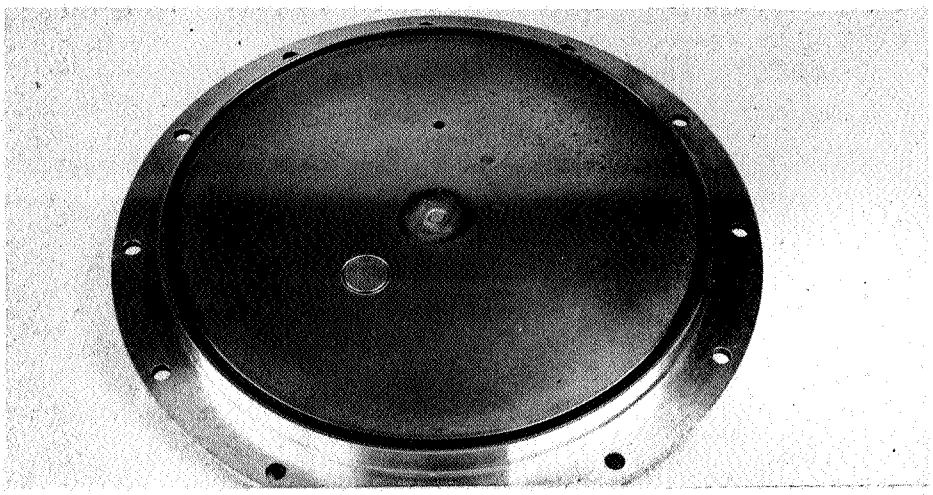

a

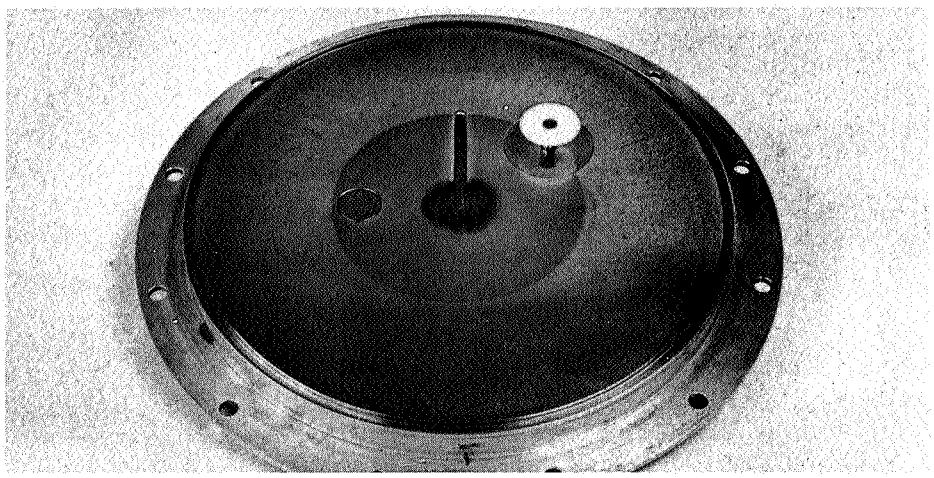

b

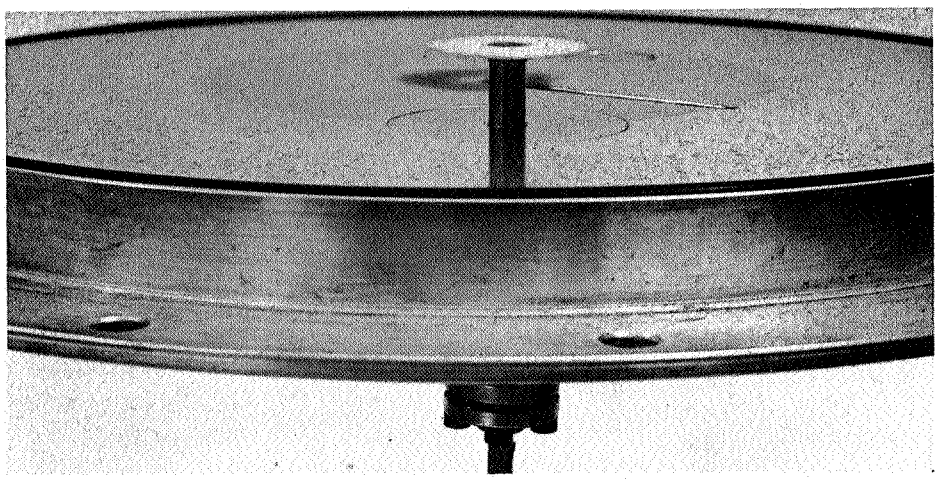

c

MICROWAVE PROBE MOUNTED IN VARIOUS 8" ELECTRODES

FIGURE 6-20

.091 window. In either case, a matching iris was needed to reduce the VSWR to a satisfactory level.

A final test with the .095 window sealed flush with the aperture and matched with an iris produced a VSWR of 1.04:1 at 70 GHz. The VSWR was less than 1.15:1 from 68 to 71 GHz, a minimum VSWR of 1.01:1 being measured at 69.5 GHz. Substitution of the measured VSWR of 1.04:1 at the probing frequency into eq. (6-55) evaluates the internal reflection coefficient from the quartz window as

$$|R|_{win.} = 0.0196 \qquad (6\text{-}56)$$

amounting to an error of less than 2 percent.

The general problem of radiation from the open end of a waveguide could be discussed in principle from several points of view. Rigorously, the radiation can be considered to arise from the current distribution on the inside walls of the guide, which is just the current distribution associated with the fields propagated in the interior of the guide, together with the currents flowing from the open end out upon the exterior guide surfaces. Were it not for difficulties in the analysis this current distribution and the radiation field at an external point could be calculated; but so far this type of problem has defied exact solution.

On the other hand, the approximate methods of diffraction theory have been applied to the problem with some degree of success.[55,56,57] The guide opening or aperature is presumed to act like a hole in an infinite screen, the transverse fields in the aperture being assumed to be identical with those in a

parallel cross section inside the guide. The vector Huygens principle is then applied to obtain the radiation field from the aperture field distribution. The field patterns for the dominant TE_{01} mode in rectangular guide and TE_{11} mode in circular guide are shown in Fig. 6-21. Details of the field derivations can be found in the standard texts.[58,59]

Unfortunately, the diffraction theory is in serious error near the aperture. Over a cross section inside the guide sufficiently far from the aperture, any component of the field is indeed the vector sum of the components associated with incident and reflected waves of the dominant mode. In the aperture, however, additional higher-mode fields exist locally, excited by the discontinuity in the guide. The generation of higher modes arises from the necessary distortion of the electric and magnetic fields due to the edge of the aperture and its metal surface. The electric field lines must be normal to the latter, a condition that clearly cannot be met by the dominant mode alone, adapted as it is to the waveguide interior. Due to the waveguide dimensions, the higher modes cannot propagate; except within a very short distance of the aperture, on the order of a wavelength, the fields in the waveguide consist essentially of dominant mode waves. The higher mode waves represent electric and magnetic field energy stored at the junction, and as such may be interpreted as a storage, or induction, field.

This interpretation gives rise to a third approach to antennae problems: the fields set up by the horn, or any radiating system, may be arbitrarily divided into two components, the induction field and the radiation field. The induction field

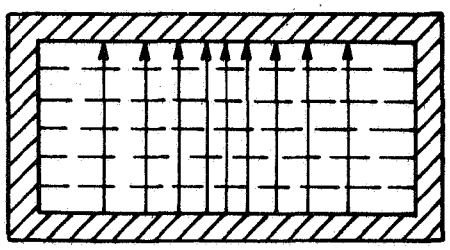

a. TE_{10} MODE

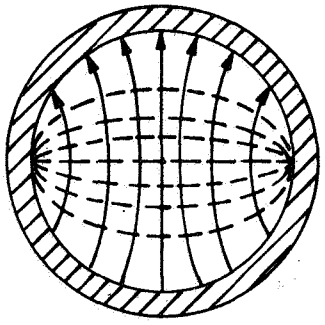

b. TE_{11} MODE

DOMINANT MODE FIELDS

FIGURE 6-21

is important only in the immediate vicinity of the radiating system; the energy associated with it pulses back and forth between the radiator and nearby space. At large distances the radiation field is dominant; it represents a continual flow of energy directly outward from the radiator, with the energy density varying inversely with the square of the distance and, in general, depending on the direction from the source.

It is this radiation component of the aperture fields which diffracts out of the horn mouth in a roughly spherical wave front, and--prior to the ionization event--disperses in the discharge chamber. A negligible amount ever finds its way back into the unfocused horn and reconverts into a rearward propagating dominant mode wave, and this is the reason why the microwave horn never "sees" the opposing electrode, even when no plasma intervenes. In this sense, the semi-infinite slab model is the appropriate one.

It was established by a series of bench tests that the effective interaction zone between radiation and reflector was quite small and confined near the aperture, a result which confirmed similar findings by S. C. Lin[60] in shock tube experiments. When the field near the aperture was probed with a small reflecting wire, the strongest reflections occurred on the horn axis within a very small distance of the mouth. A radiation pattern, or more appropriately, a field pattern for the horn was established in this way by defining the one-tenth power points as those off-axis points where the reflected power, $|R|^2$, has dropped 10 db with respect to the axis. This experimental pattern is displayed in Fig. 6-22, to scale.

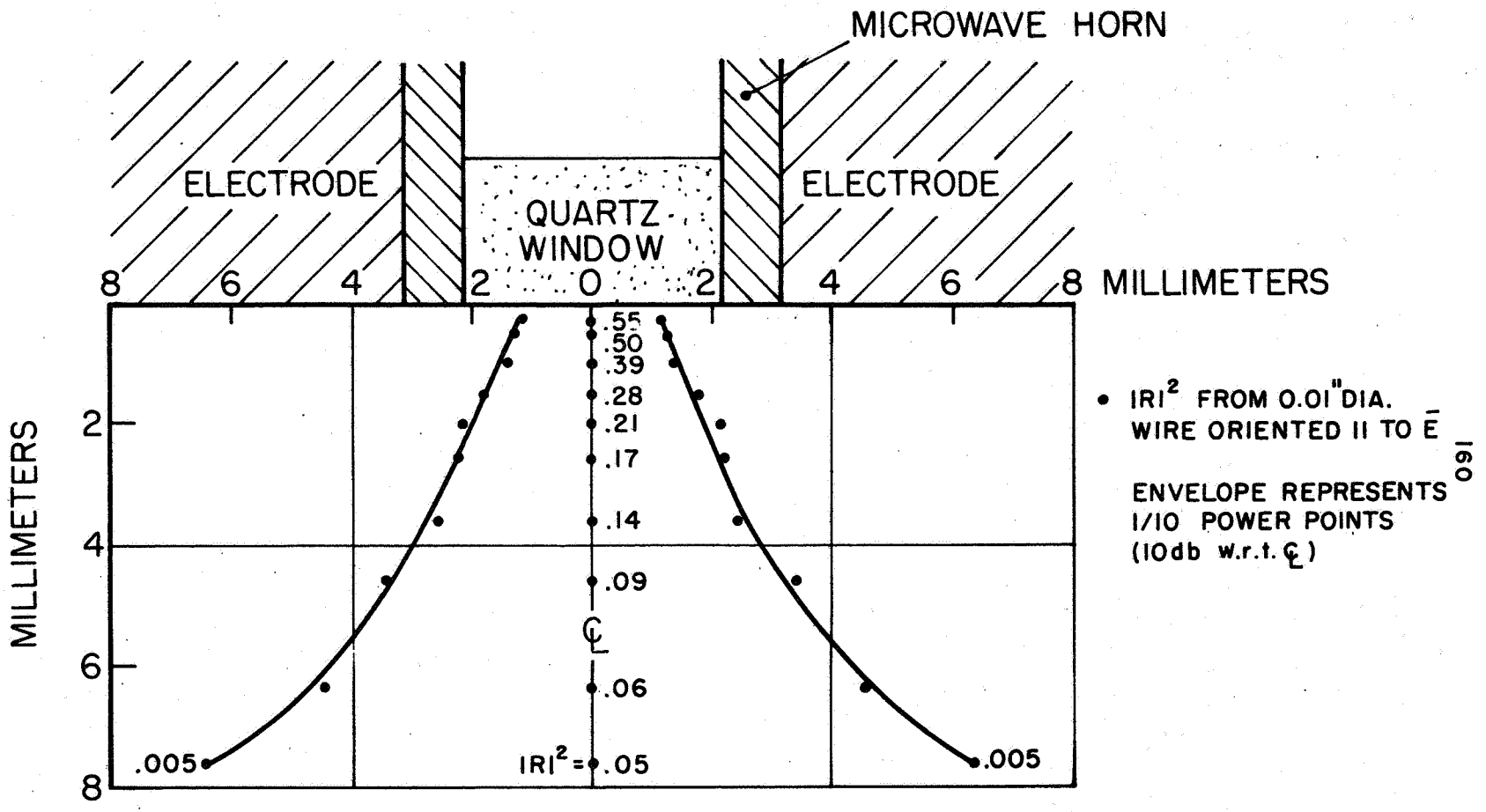

RADIATION PATTERN OF MICROWAVE HORN

FIGURE 6-22

This brief discussion has attempted to delineate a few of the characteristics of the near field radiation pattern to be expected from the 70 GHz horn. A more mathematical description can be obtained from the referenced literature. The exact nature of the radiation pattern is not essential to the experiments, however, since it has been experimentally verified that reflection from a metallic block adjacent to the quartz window and also from the ionized argon in the test chamber both produced unit reflection, $|R|_{max} = 1$. Thus the reflection characteristics of the plasma interface effectively duplicate those of an interior waveguide discontinuity, Fig. 6-17, which, as previously shown, is adequately described by the plane wave-slab boundary model developed in section 6-3.

With the reflected phase interferometer installed in the screen room and the microwave horn mounted in the exterior electrode, the current sheet was probed at various locations in the test chamber. Because of the slight penetration depth of the microwaves into the cutoff plasma (typically 0.1 λ_o, or half a millimeter), the measurements were localized very close to the horn aperture, thus permitting meaningful axial and radial surveys of local conditions in the sheet to be made. Upon this property a great deal of the success of the experiments rested, and clearly such a procedure would not have been possible with the traditional reflection and transmission techniques employed for subcritical plasmas, which involve interaction regions extending over many wavelengths, and which consequently return integrated rather than local plasma properties.

Typical traces obtained for the physical measurables $|R|$ and ρ are shown in Fig. 6-23. The signal-to-noise ratio is seen to be very good, and fine details are readily discernible. The unbiased diode response falls between linear and quadratic behavior, as determined by the ratio of reference lines on the oscillogram for ρ, and the electron density variations are seen to be well within the sensitivity of the probe (i.e. the ρ trace lies well inside the asymptotic reference lines for critical and saturation densities; see section 6.7 for a discussion of reference line placement and calibration). The good shot-to-shot reproducibility of the data is evidenced by the typical double overlay for $|R|$.

The main features of the discharge, as they are manifested in the electron properties, can be seen from Fig. 6-23. Comparison of these experimental traces with the theoretical curves of Figs. 6-4 and 6-8 reveals some striking similarities. Consider the phase measurable of Fig. 6-23b, which was obtained at half radius, 1/2 inch from the anode, using the flow isolator of Fig. 6-20. (This position was selected for illustration because the relatively gentle variations near the anode are ideal for good space and time resolution.) The nearly identical appearance of predicted curves of Fig. 6-8 and the experimental trace of Fig. 6-23b clearly shows that the electron density initially increases as a smooth, monotonic function of time, and the well-defined null (high mode) pinpoints the attainment of critical density ($6.1 \times 10^{13} cm^{-3}$) at about 1/2 microsecond. This early, abrupt density increase signals the passage of a preionizing wave-front considerably ahead of the bifurcated current sheet, whose

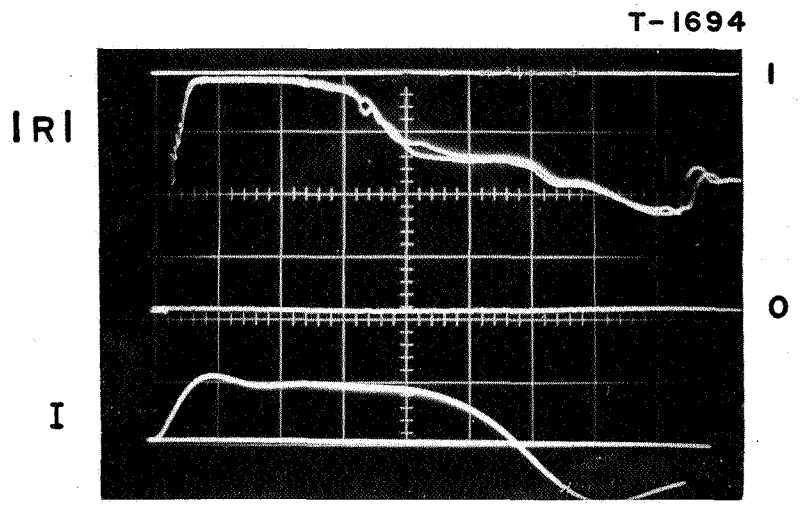

a. REFLECTED AMPLITUDE

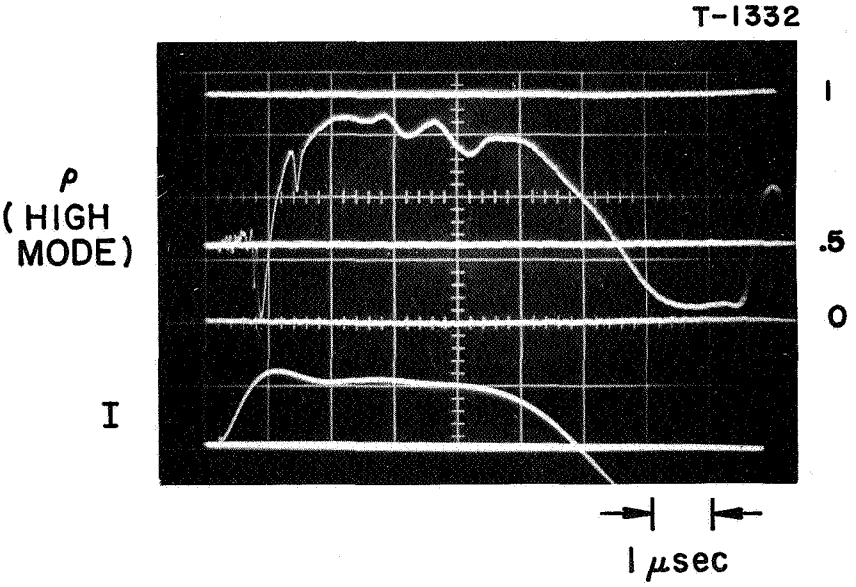

b. REFLECTED PHASE

TYPICAL MICROWAVE MEASURABLES

FIGURE 6-23

arrival at the probe at around 3 microseconds is marked by the double peaks (note that small ρ variations in the high density regime bespeak large density variations because of the nonlinear definition of ρ in eq. (6-50)). This ionizing precursor was not detectable with either B-probes or E-probes, indicating that the fundamental mechanisms involved are not conduction current, which would have an associated magnetic field, or electron diffusion ahead of the current sheet, which would produce large charge-separation electric fields. Precursor mechanisms will be discussed further in section 6-8; here it is sufficient to note simply that the precursor does exist, and can be investigated with the present probe. The fact that it preionizes the gas to a level of at least a few percent is very significant, for it means that the current sheet advances, not into cold argon gas, but into a neutral plasma where the electron population is already appreciable and electron-ion collisions dominate. The electron collision frequency behind the precursor is still much lower than the probing frequency, however, since the undamped "cusp" or spike at the critical density null implies $\nu/\omega \ll 1$. Thus the plasma "entering" the current sheet is essentially collisionless as far as the microwave experiments are concerned. This conclusion is also supported by the $|R|$ data of Fig. 6-23a, which shows $|R|$ to be approximately constant and equal to unity after precursor passage, but to undergo significant damping when the current distribution passes. This is an important effect, and will be discussed in more detail in section 6-8. Since ρ involves $|R|$ explicitly, it too must be damped when the current sheet passes, and this is seen to be the case.

The observation that $|R|$ and ρ are compatible within the framework of the present theory is in reality only one of several possible tests on the internal consistency of the model. For example, it might be postulated that the passage of the current sheet, instead of increasing the collision frequency, tends to pull the interface away from the quartz window enough to permit energy leakage from the horn. But bench tests, performed with a metal reflector mounted on a precision micrometer drive, show this effect to be contradicted by the data; if the reflector is removed far enough from the horn to allow sufficient transverse energy loss ($\sim \lambda/2$), the phase change associated with the displaced reflecting surface is more than sufficient to drive the interferometer through a complete additional fringe, an event which was never observed.

The data, when properly recorded (some of the practical difficulties are discussed in section 6-7), always exhibited a high degree of internal consistency, thereby strongly suggesting that the uniform plane plasma boundary approximation was not seriously in error. To the extent that this is true, simultaneous measurements of ρ and $|R|$ are sufficient to determine n_e and ν uniquely at each instant of time from the calculated curves of Figs. 6-4 through 6-8. However before the raw data of Fig. 6-23 can be used with confidence to obtain quantitative information, the errors incurred in assuming isotropy and homogeneity must be examined in detail. In the following section the influence of the self-magnetic field of the discharge on the reflection coefficient is investigated.

6.5 Effects of Anisotropy

The analysis of a uniform, isotropic plasma, presented in sections 6-2 and 6-3, yielded a complex refractive index

$$\mu^* = \left[1 - \frac{(\omega_p/\omega)^2}{1 - i\nu/\omega}\right]^{\frac{1}{2}} = \frac{k^*}{k_0} = \frac{\alpha}{k_0} - i\frac{\beta}{k_0} \qquad (6\text{-}17)$$

and complex reflection coefficient

$$R = \frac{1-\mu^*}{1+\mu^*} \qquad (6\text{-}32)$$

which were functions of the two nondimensional frequencies ω_p/ω, representing the electron density, and ν/ω, representing an effective electron collision frequency.

The presence of a static magnetic field in the plasma introduces a third characteristic frequency[+]

$$\omega_b = \frac{|e|B}{m_e} \qquad (6\text{-}56)$$

into the analysis, and the dimensionless variable $(\omega_b/\omega)^2$ serves as a measure of the error incurred in neglecting propagation anisotropy caused by $\bar{B}$. From the data of Chapter IV, the maximum measured B_θ field is approximately 0.5 w/m^2 at the rear of the current sheet and correspondingly less in the sheet interior. Thus

---

[+] ω_b is called the cyclotron or gyro-frequency and specifies the orbital frequency of a gyrating electron in a magnetic field. It should not be confused with the Larmour frequency, $\frac{|e|B}{2m_e}$, which describes the precession frequency of a spinning electron in a magnetic field.

at 70 Gc ($\omega = 4.4\times10^{11}\,\mathrm{sec}^{-1}$)

$$(\omega_b/\omega)^2 \leq 0.16\,(B_\theta)^2_{max} \leq 0.04 \qquad \text{(MKS)}$$

suggesting that the B_θ field probably plays a weak role in the reflection process.

The mathematical development of this problem is the subject of Appendix C, where it is shown that waves can propagate normal to the azimuthal B_θ field of the discharge in either the ordinary mode

$$\mu^{*2}_{ord} = 1 - \frac{(\omega_p/\omega)^2}{1 - i\,\nu/\omega} \qquad (6\text{-}57)$$

or the extraordinary mode,

$$\mu^{*2}_{ex} = 1 - \frac{(\omega_p/\omega)^2}{1 - i\,\nu/\omega - \dfrac{(\omega_b/\omega)^2}{1 - (\omega_p/\omega)^2 - i\,\nu/\omega}} \qquad (6\text{-}58)$$

The ordinary mode corresponds to waves whose polarization is locally colinear with B_θ, in which case the motion of the oscillating electrons is unhampered by the magnetic field, and the refraction index reverts to the familiar form for uniform isotropic plasmas (compare eqs. (6-57) and (6-17)).

The extraordinary mode corresponds to wave polarization normal to B_θ, in which case the magnetic field, the propagating electric vector, and the propagation direction along the z axis form a mutually orthogonal set. The refractive index for the two modes differs by a term proportional to $(\omega_b/\omega)^2$ as anticipated, and the anisotropy effect thus scales quadratically with B_θ in this quantity.

It is instructive to examine the collisionless case. The domains of propagation for the two modes are derived in Appendix C,

and are shown in Fig. 6-24 in the $\left(\frac{\omega_b}{\omega}\right)$ — $\left(\frac{\omega_p}{\omega}\right)^2$ (i.e. $B_\theta - n_e$) plane.

The sequence of events seen by the probe at midradius, for example, is the early precursor ionization event, followed by a relatively quiescent period of 1-2 microseconds, followed by the current sheet traverse and the concomitant buildup of an azimuthal magnetic field. The horn orientation predetermines whether the microwaves couple to the plasma in the ordinary or extraordinary mode, since the length of circular guide is too short to exhibit any appreciable degree of rotational instability in the field pattern.[41] The presence of the B_θ field can affect the experiment if either the reflection coefficient or the skin depth are sensitive functions of ω_b/ω.

From Appendix C, the skin depth in the extraordinary mode is given by

$$d_p = \frac{1}{\beta} = \frac{c}{\omega}\left\{\frac{\left(\frac{\omega_b}{\omega}\right)^2 + \left(\frac{\omega_p}{\omega}\right)^2 - 1}{\left[1-\left(\frac{\omega_p}{\omega}\right)^2\right]^2 - \left(\frac{\omega_b}{\omega}\right)^2}\right\}^{\frac{1}{2}} \qquad (6\text{-}59)$$

defined for real β, and this quantity is plotted in Fig. 6-25. The skin depth for the ordinary mode is a special case of eq. (6-59), and is given by the $\omega_b = 0$ line of Fig. 6-25. Clearly, for the magnetic fields and high densities of these experiments, the skin depth is not appreciably increased; transverse energy leakage from the horn thus does not become a factor, and the validity of the one-dimensional model for the reflection process is preserved.

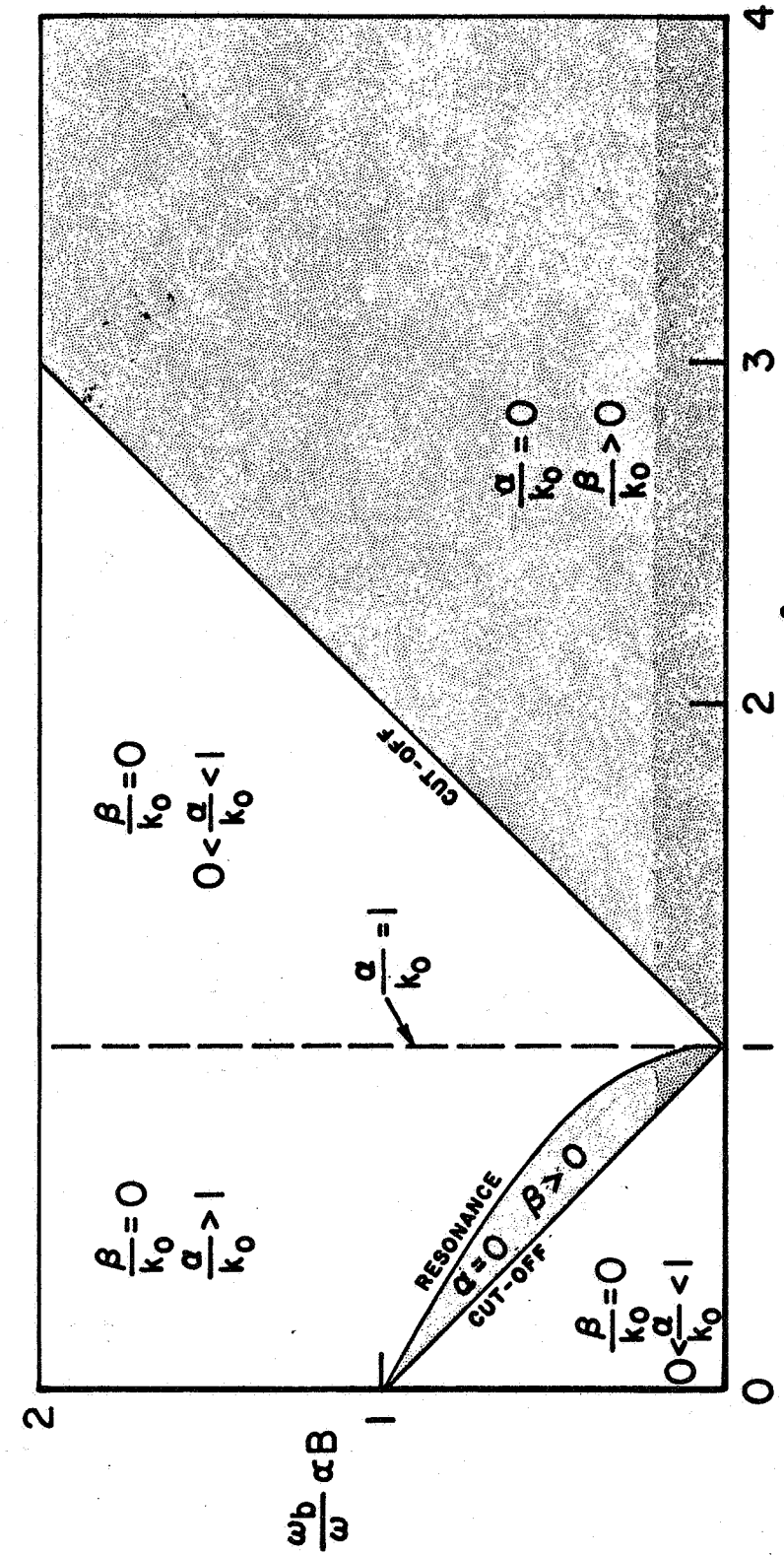

PROPAGATION DOMAINS FOR EXTRAORDINARY WAVE, $\frac{\nu}{\omega}=0$

AD25 4278-67

FIGURE 6-24

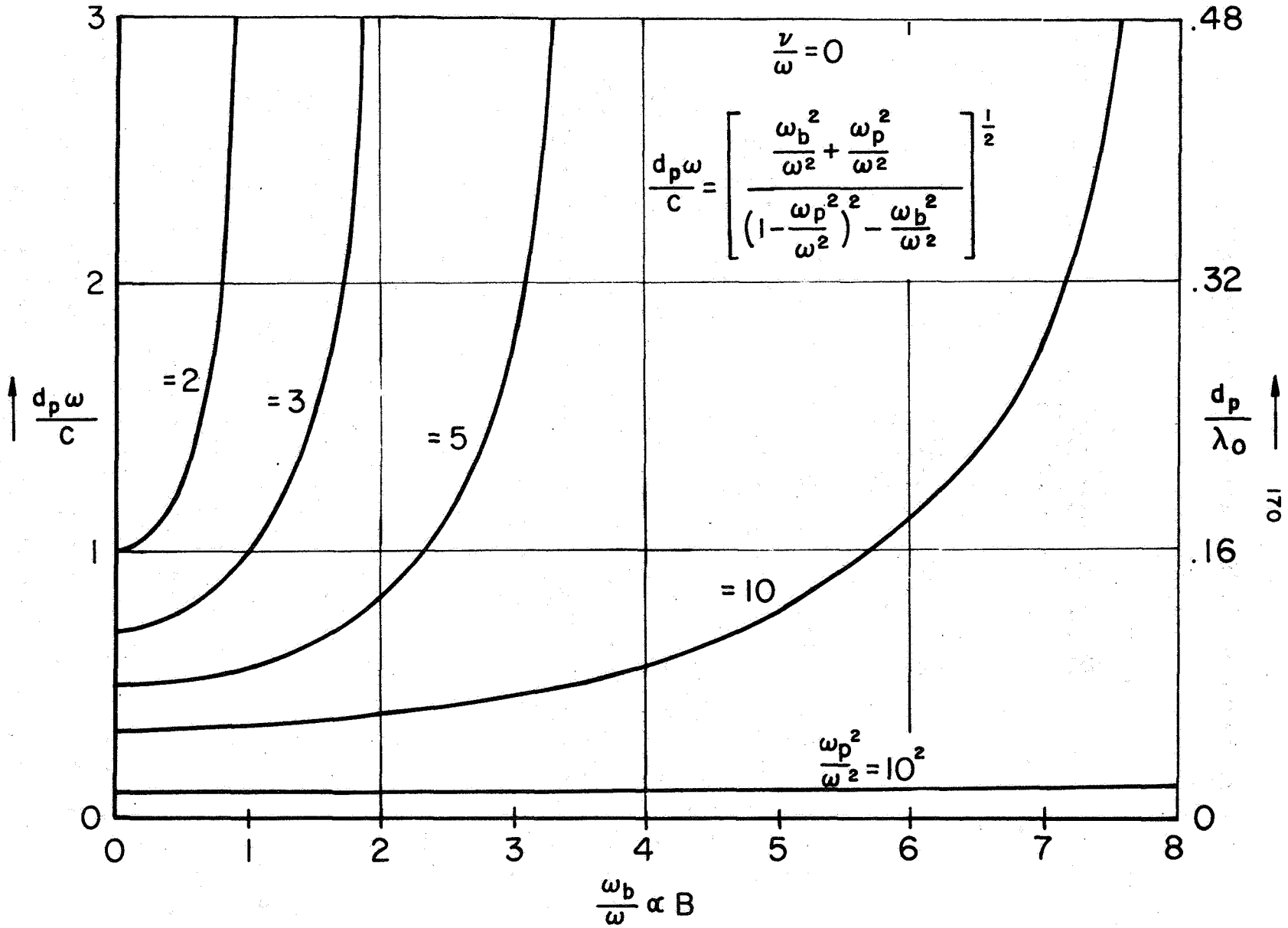

FIGURE 6-25

SKIN DEPTH IN EXTRAORDINARY MODE VS STATIC MAGNETIC FIELD

The reflection coefficients for the two modes are, from Appendix C

$$R_{ord} = \frac{1-\mu^*_{ord}}{1+\mu^*_{ord}} \tag{6-60}$$

$$R_{ex} = \frac{1-\mu^*_{ex}}{1+\mu^*_{ex}} \tag{6-61}$$

so that, as might be expected, the ordinary wave is identical with the special case of extraordinary waves for $\omega_b/\omega = 0$. The reflection coefficient modulus is plotted in Fig. 6-26 for several values of ω_b/ω, and significant changes are seen to be confined to near-critical or subcritical densities. Thus, since B_θ becomes significant only after the plasma density is far above critical, the reflection coefficient should be insensitive to the particular mode of propagation, and thus to the horn orientation.

This result was confirmed experimentally as shown in Fig. 6-27. Also the useful observation was made that data were generally more reproducible when the microwaves coupled to the plasma in the extraordinary mode, and the waves were consequently launched into the plasma with their polarization normal to B_θ to exploit this advantage. Similar studies confirmed the insensitivity of the phase measurable to the prevailing anisotropy, showing that magnetic effects could be safely neglected in the data calculations.

In the following section the possible effects of boundary diffuseness on the reflection coefficient are examined.

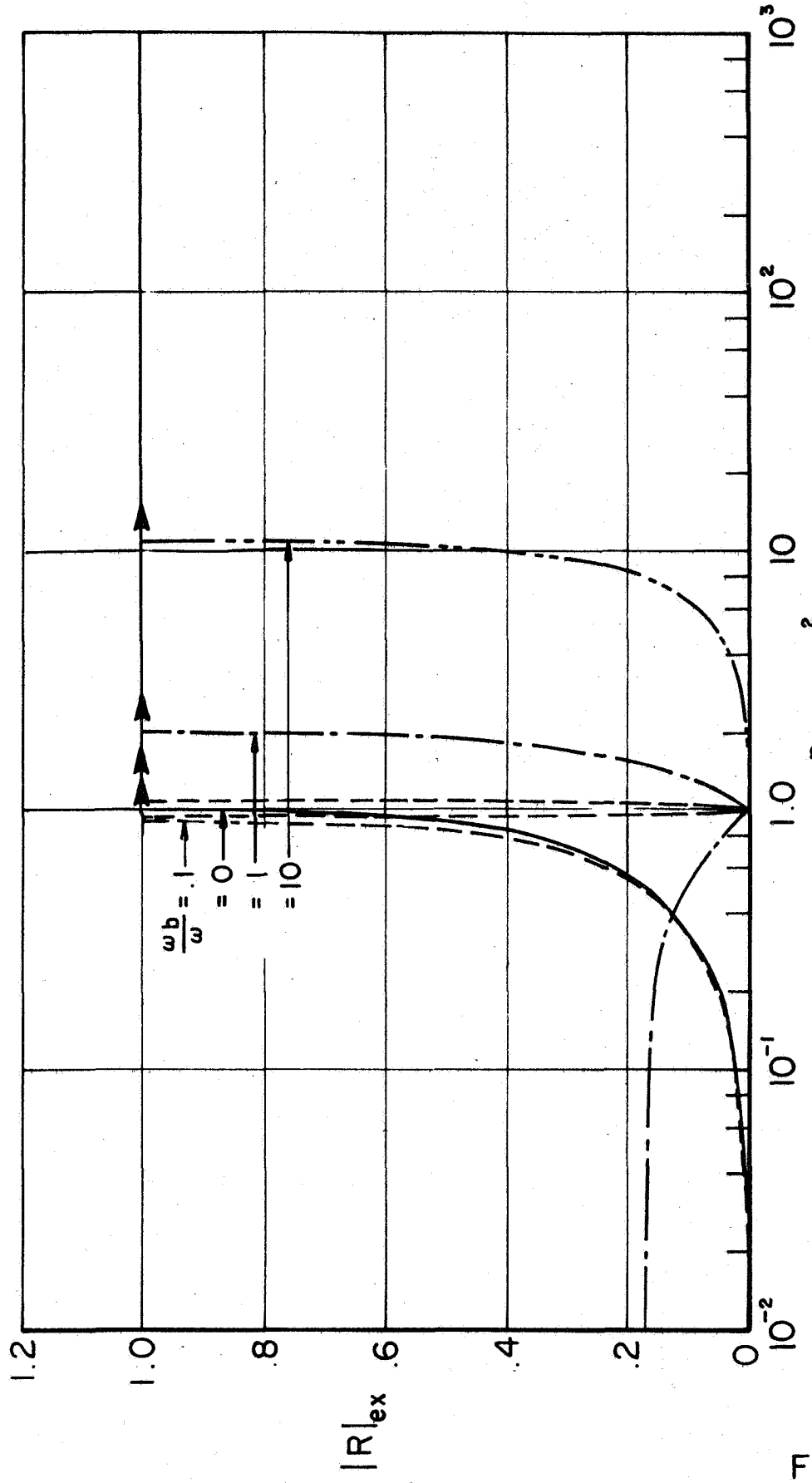

REFLECTED AMPLITUDE FROM ANISOTROPIC PLANE PLASMA INTERFACE, EXTRAORDINARY MODE, $\frac{\nu}{\omega} = 0$

FIGURE 6-26

T-1692

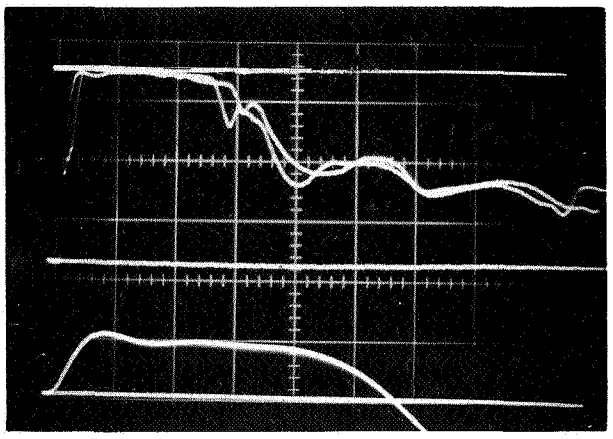

a. ORDINARY MODE, $E \| B_\theta$

T-1691

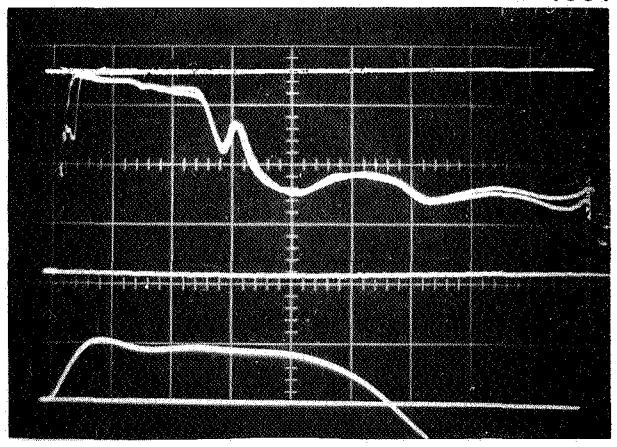

b. EXTRAORDINARY MODE, $E \perp B_\theta$

REFLECTION COEFFICIENT, ORDINARY AND EXTRAORDINARY MODES

$\left(\frac{R}{R_0} = .5, \frac{z}{h} \cong 0\right)$

FIGURE 6-27

6.6. Effects of Inhomogeneity

The analysis presented up to this point has dealt with reflections from uniform plasmas having semi-infinite plane boundaries. In this section a more general theory is developed which includes the possibility of thermal boundary layers or similar transition zones embodying free electron density gradients near the plasma interface through which the probing wave train must pass.

If the gradients are mild and extend over many wavelengths, an adiabatic or WKB approximation can be used to analyze the wave motion. In addition to treating an unrealistic model of the transition zone, however, this type of analysis explicitly excludes reflections and interference effects and thus cannot be used to calculate reflection coefficients.

The only appropriate mathematical approach to the problem involves examining the inhomogeneous zone explicitly in terms of Maxwell's equations to determine permitted modes of wave propagation. Rather general studies of allowed modes of propagation for incident plane waves have been undertaken by Bachynski,[66] who has shown that isotropic inhomogeneous plasmas will support TEM modes, to the exclusion of TE or TM modes, as long as the density gradients are in the same direction as the wave motion. This case incorporates the one-dimensional boundary layer and is considered in detail below.

The harmonic wave equation of section 6-2,

$$\nabla \times \nabla \times \bar{E} = \nabla(\nabla \cdot \bar{E}) - \nabla^2 \bar{E} = (-j\omega\mu_0\sigma + \omega^2 \epsilon_0 \mu_0)\bar{E}$$

was simplified for uniform plasmas on the basis of net charge neutrality, implying $\epsilon_0 (\nabla \cdot \bar{E}) = 0$. However, in general a net alternating space charge exists in regions of density gradients, as can be seen from the continuity equation (A-5)

$$\nabla \cdot \bar{J} = -\frac{\partial \rho}{\partial t} \tag{6-62}$$

whose harmonic form

$$\nabla \cdot (\sigma \bar{E}) = -i\omega \rho \tag{6-63}$$

can be expanded to give

$$\sigma \nabla \cdot \bar{E} + \bar{E} \cdot \nabla \sigma = -i\omega \rho \tag{6-64}$$

Equation (6-64) together with the third Maxwell equation, (A-24c), yields

$$\rho = \epsilon_0 \nabla \cdot \bar{E} = -\epsilon_0 \left[\frac{\bar{E} \cdot \nabla \sigma}{\sigma + i\omega\epsilon_0} \right] \tag{6-65}$$

so that, in general, charge neutrality and Debye length concepts cannot be invoked to restrict the size of the transition zone, and the wave equation must include a conductivity gradient term

$$\nabla^2 \bar{E} + \nabla \left[\frac{\bar{E} \cdot \nabla \sigma}{\sigma + i\omega\epsilon_0} \right] + (\omega^2 \epsilon_0 \mu_0 - i\omega\mu_0\sigma) \bar{E} = 0 \tag{6-66}$$

This equation reduces to the familiar form if $\nabla\sigma$ is taken to

be in the direction of propagation, so that $\sigma = \sigma(z)$:

$$\nabla^2 \bar{E} + \left[\omega^2 \epsilon_0 \mu_0 - i\omega \mu_0 \sigma(z)\right] \bar{E} = 0$$

or (6-67)

$$\nabla^2 \bar{E} + \frac{\omega^2}{c^2}\left[1 + \frac{\sigma(z)}{i\omega \epsilon_0}\right] \bar{E} = 0$$

In terms of the complex propagation coefficient

$$k^{*2}(z) = k_0^2 \left[1 - i\frac{\sigma(z)}{\omega \epsilon_0}\right] \tag{6-68}$$

the inhomogeneous wave equation becomes simply

$$\nabla^2 \bar{E} + k^{*2}(z) \bar{E} = 0 \tag{6-69}$$

As before, a dynamical description is necessary to evaluate σ and k^* in terms of properties of the medium.

The first time integral of the Lorentz force equation

$$m_e \dot{\bar{v}} + m_e \nu \bar{v} = -|e| E_0 e^{i(\omega t - k^* z)} \tag{6-8}$$

proceeds as in section 6-2, even when ν and k^* are considered to be functions of z , to yield the velocity and thus (since $\bar{J} = -n_e |e| \bar{v} = \sigma \bar{E}$) the conductivity

$$\sigma(z) = \frac{n_e(z)|e|^2}{m_e} \frac{1}{\nu(z) + i\omega} \tag{6-70}$$

as a nonlinear function of the longitudinal coordinate.

An important mathematical simplification results in the following analysis if $\nu(z)$ is assumed to be approximately constant through the transition zone. This is a good approximation as long as electron-neutral collision processes dominate, in an equilibrium plasma. However, as soon as electron-ion collisions become dominant, which is the usual situation, then the effective collision frequency ν becomes approximately linear in $n_e(z)$ and inversely proportional to the three halves power of $T_e(z)$, the electron temperature. These two effects may be expected to cancel one another to some extent, but the conductivity will remain nonlinear in both n_e and z, and no solution to the wave equation exists in terms of known simple functions. In order to obtain analytical solutions, it will be assumed below that $\nu(z) \cong \nu =$ constant, implying that $\sigma(z)$ is linear in electron number density.

A variety of $n_e(z)$ profiles have been treated in the literature with varying degrees of success, and Fig. 6-28 displays three models which might be used for the present study. Epstein,[68] Poincelot[69] and Budden[63] contributed to early analytical work in the field, while Albini and Jahn[67] have more recently made extensive numerical calculations of reflection and transmission coefficients for linear and "kinked" profiles. Taylor[70,71,72] has studied reflections from several ramp shapes, including the linear and inverse parabolic profiles. Wait[64] has given formal methods for treating stratified media and Yen[73] has studied asymptotic solutions for an inverse exponential geometry.

Clearly, "infinite" or unbounded exponential, linear, or

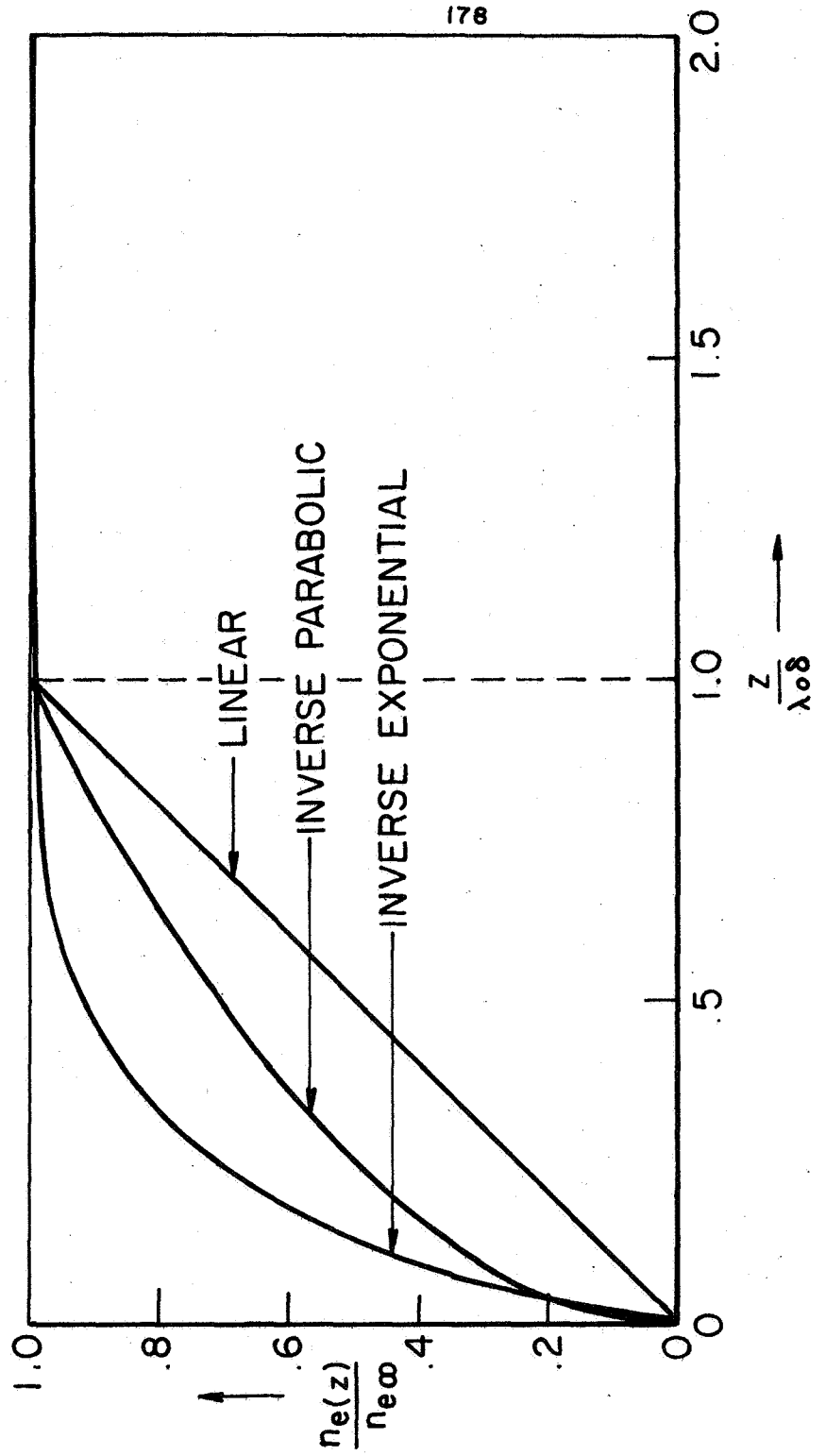

VARIOUS ELECTRON DENSITY PROFILES COMPARED

FIGURE 6-28

power-law ramps, attractive to ionospheric workers, are unsuitable for the present problem. The linear ramp, which leads to solutions involving Bessel functions of real, fractional order (or alternatively, Airy functions) lends itself poorly to machine calculations because of the difficulty of obtaining rapidly converging series solutions for the prevailing range of parameters. It also is of limited appeal from a physical viewpoint, since a smooth density profile and steepening gradients near the boundary are reasonable properties to be expected in a realistic situation. The discontinuity in slope experienced by the linear ramp profile occurs at maximum density, a fault shared by the parabolic and all other power-law profiles, and hence these models can introduce spurious interference effects into the mathematics.

In spite of these difficulties, Albini and Jahn,[67] by studying various linear and kinked ramps, were able to arrive at the important general result that the reflection and transmission coefficients from a transition zone are very sensitive to its width, less sensitive to its detailed profile shape. This result has been essentially confirmed by Wharton and Slager,[74] in microwave experiments, and Greene and Hornig,[75] for optical frequencies in shock-width experiments. Thus the specific choice of profile is not especially critical and can be made on the basis of comparative physical appeal and mathematical tractability.

The Inverse Exponential Density Profile. In view of these considerations, the inverse exponential was selected as an optimum compromise. This profile describes a smooth density variation,

$$n_e(z) = n_{e\infty}\left[1 - e^{-2mz/\lambda_0}\right] \qquad (6\text{-}71)$$

whose derivatives are continuous and steepest at the boundary, and by suitable choice of the folding parameter m it reverts to either a linear ramp or a uniform plane slab (discussed in section 6-3).

In terms of the dimensionless ratio $n_e(z)/n_{e\infty}$, the complex propagation coefficient in the transition zone can be written as

$$k^{*}(z)^2 = k_0^2 - (k_0^2 - k_\infty^{*2}) \frac{n_e(z)}{n_{e\infty}} \tag{6-72}$$

or

$$\mu^{*2}(z) = 1 - (1 - \mu_\infty^{*2}) \frac{n_e(z)}{n_{e\infty}} \tag{6-73}$$

where the z-origin is taken to be the boundary,

$$\frac{n_e(z)}{n_{e\infty}} = 0 \qquad \text{for} \quad z \leq 0$$

In terms of the refractive index, the wave equation within the transition zone becomes

$$\frac{d^2E}{dz^2} + k_0^2 \left[1 - (1 - \mu_\infty^{*2})(1 - e^{-2mz/\lambda_0})\right] E = 0 \tag{6-74}$$

The problem statement is then as follows. It is desired to find analytical solutions of the inhomogeneous wave equation (6-74) to describe the propagation of plane transverse waves parallel to the assumed exponential density gradient in n_e. These solutions, together with appropriate statements of the boundary conditions

at $z = 0$ and $z = \infty$, will then determine the reflection coefficient R as a function of the dimensionless plasma parameters $\left(\frac{\omega_p}{\omega}\right)^2$ and $\frac{\nu}{\omega}$, and the "ramp parameter" m or its equivalent.

By making a change of variable

$$V = \frac{\lambda_0 k_0}{m}\left(1 - \mu_\infty^{*2}\right)^{\frac{1}{2}} e^{-mz/\lambda_0} \tag{6-75}$$

such that

$$E(z) = E\left(V(z)\right) \tag{6-76}$$

$$\frac{dE}{dz} = \frac{dE}{dV}\frac{dV}{dz} \tag{6-77}$$

and

$$\frac{d^2E}{dz^2} = \frac{d^2E}{dV^2}\left(\frac{dV}{dz}\right)^2 + \frac{dE}{dV}\frac{d^2V}{dz^2} \tag{6-78}$$

the wave equation (6-74) is reduced to Bessel form[76]

$$V^2\frac{d^2E}{dV^2} + V\frac{dE}{dV} + (V^2 - P^2)E = 0 \tag{6-79}$$

where

$$P = i\frac{\lambda_0 k_0}{m}\mu_\infty^* \tag{6-80}$$

Solutions to eq. (6-79) are given by

$$E = A\,J_p(V) + B\,J_{-p}(V) \tag{6-81}$$

with arbitrary constants A and B to be determined from the boundary conditions.

The appearance of Bessel solutions is not uncommon to inhomogeneous wave problems, and the quasi-periodic behavior of their slowly changing wavelength and amplitude seems in character with the wave motion they describe. The appearance of complex order and argument for these functions is more unusual, and unfortunately tabulated values of complex Bessel functions do not exist, due no doubt to the problems of adequately mapping between the three complex planes represented by $J_R + iJ_I$, $V_R + iV_I$, and $P_R + iP_I$. Watson's Treatise on the Theory of Bessel Functions[77] includes many theorems for the general complex case, and is the authority for the algebraic operations which follow.

Consider a wave of unit amplitude, $E_I = e^{i(\omega t - k_0 z)}$, incident on the boundary from the left in Fig. 6-29. Assume a reflected wave of the form $E_R = R e^{i(\omega t + k_0 z)}$ and a transmitted wave $E_T = T e^{i(\omega t - k^* z)}$ which, because of the asymptotic nature of η_e, is defined only at infinity.

The Faraday law, eq. (A-1), reduces the continuity of $\bar{H}$, in the absence of discontinuities in $\mu^*(z)$, to the requirement that $\frac{dE}{dz}$ be continuous, and thus the boundary conditions may be conveniently handled in terms of the electric field alone. Eliminating the common time variation, the first-boundary conditions can be written

at $z = 0$:

$$E_I(0) + E_R(0) = \left[E(V)\right]_{z=0} \qquad (6\text{-}82)$$

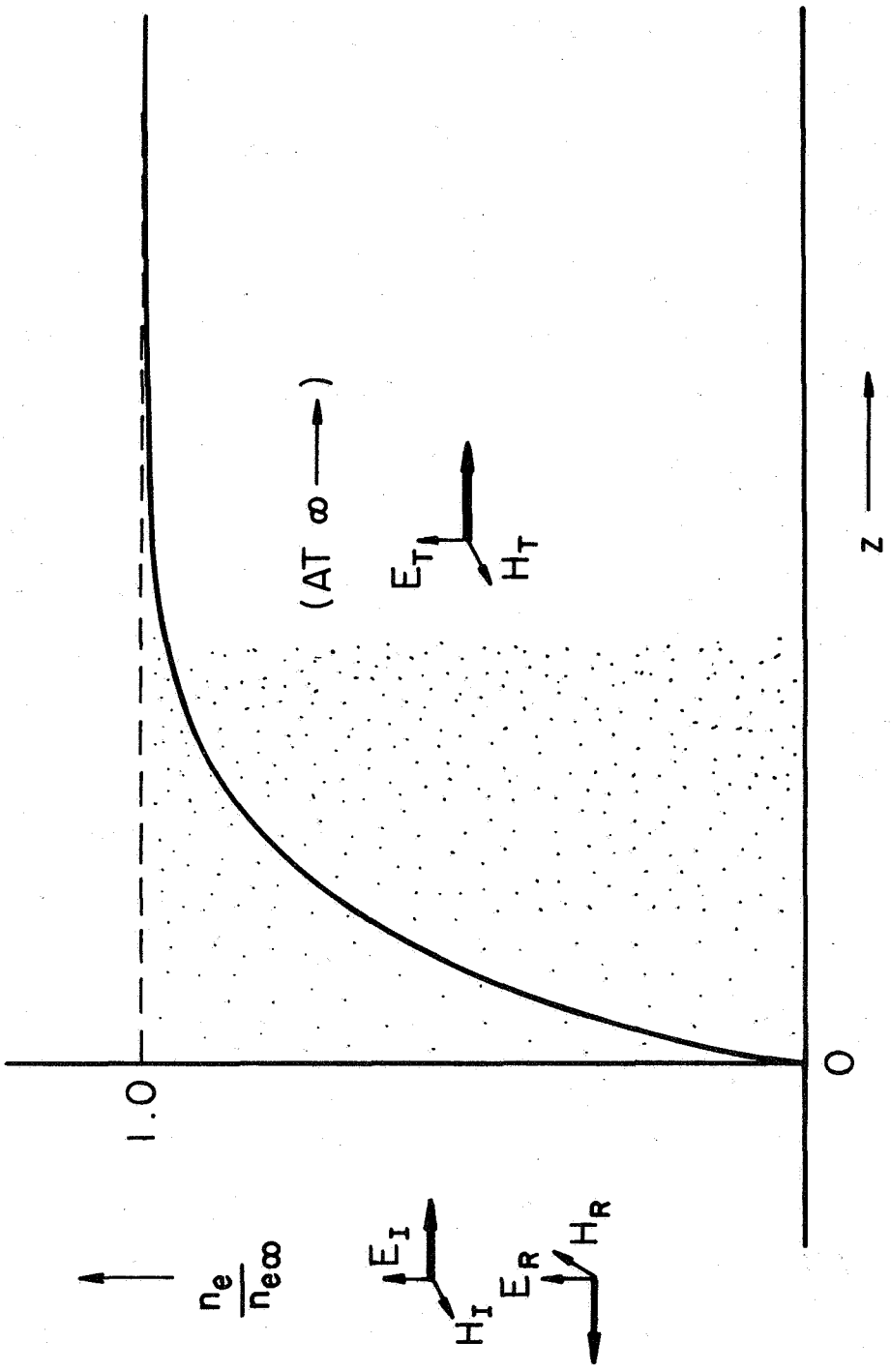
INVERSE EXPONENTIAL DENSITY PROFILE, $n_e(z) = n_{e\infty}(1-e^{-2m(z/\lambda_0')})$
z
0
1.0
$\frac{n_e}{n_{e\infty}}$
(AT ∞)
E_T
H_T
E_I
H_I
E_R
H_R

FIGURE 6-29

and

$$\frac{dE_I(0)}{dz} + \frac{dE_R(0)}{dz} = \left[\frac{dE(V)}{dz}\right]_{z=0} \tag{6-83}$$

or

$$1 + R = A\left[J_p(V)\right]_{z=0} + B\left[J_{-p}(V)\right]_{z=0} \tag{6-84}$$

and

$$-ik_0(1-R) = A\left[\frac{dJ_p(V)}{dz}\right]_{z=0} + B\left[\frac{dJ_{-p}(V)}{dz}\right]_{z=0} \tag{6-85}$$

in which form they are most conveniently handled by defining the dimensionless group

$$X = V(z=0) = \frac{\lambda_0 k_0}{m}\left(1-\mu_\infty^{*2}\right)^{\frac{1}{2}} \tag{6-86}$$

The second boundary condition is a little more subtle. Because of the exponential nature of the density gradient, a uniform region of plasma does not exist in the finite half plane $z \geq 0$, and the mathematical statement of the problem does not allow straightforward application of the boundary conditions at $z = +\infty$. A limiting process must be employed instead.

From the definition of the Bessel function,

$$J_p(V) = \sum_{l=0}^{\infty} \frac{(-1)^l}{l!\,\Gamma(p+l+1)}\left(\frac{V}{2}\right)^{p+2l} \tag{6-87}$$

and the asymptotic behavior of the argument,

$$V \to 0 \qquad \text{as} \qquad z \to \infty$$

we can express the solution for E_T to any desired accuracy for large positive z by taking the first term of the expansion:

$$J_{\pm p}^{(V)}\Big]_{z\to\infty} \propto V^{\pm p} \propto e^{\pm i \frac{2\pi}{\lambda_0} z} e^{\mp \beta z} \tag{6-88}$$

Since in general the attenuation coefficient β does not vanish for large z, the boundary condition commensurate with finite amplitudes at infinity requires that the coefficient B in eq. (6-81) be identically zero. The boundary conditions thus reduce to the two equations

$$1 + R = A\, J_p(X) \tag{6-89}$$

$$i\,(1-R) = A\left(\frac{mX}{k_0 \lambda_0}\right) J_p'(X) \tag{6-90}$$

where a prime denotes differentiation with respect to the argument. Upon eliminating the coefficient A,

$$\frac{1-R}{1+R} = -i\sqrt{1-\mu_\infty^{*2}}\;\frac{J_p'(X)}{J_p(X)} \tag{6-91}$$

the reflection coefficient is found to be

$$R = \frac{J_p(X) + i\sqrt{1-\mu_\infty^{*2}}\, J_p'(X)}{J_p(X) - i\sqrt{1-\mu_\infty^{*2}}\, J_p'(X)} \tag{6-92}$$

Any of the recursion formulas can be used to express R in related terms, the most useful being

$$J_p'(X) = \frac{P}{X} J_p(X) - J_{p+1}(X) \tag{6-93}$$

and

$$\frac{2P}{X} J_p(X) = J_{p-1}(X) + J_{p+1}(X) \tag{6-94}$$

Rearranging R and collecting results,

$$R = \frac{(1-\mu_\infty^*) J_p(X) + i\sqrt{1-\mu_\infty^{*2}}\, J_{p+1}(X)}{(1+\mu_\infty^*) J_p(X) - i\sqrt{1-\mu_\infty^{*2}}\, J_{p+1}(X)} \tag{6-95}$$

where

$$X = \frac{\lambda_0 k_0}{m}\sqrt{1-\mu_\infty^{*2}} \tag{6-86}$$

$$P = i\frac{\lambda_0 k_0}{m}\mu_\infty^* \tag{6-80}$$

and

$$\mu_\infty^* = \left(\frac{\alpha}{k_0}\right)_\infty - i\left(\frac{\beta}{k_0}\right)_\infty \tag{6-15}$$

The ∞ subscript refers to the uniform values far from the boundary, and α/k_0 and β/k_0 are given by eqs. (6-18) and (6-19).

These expressions completely describe the character of the reflected wave in terms of the folding constant m and the asymptotic values of electron density $(\omega_p/\omega)^2$ and collision frequency ν/ω, albeit in a rather complicated functional form.

Note that for the interesting case of $\nu/\omega \cong 0$, $(\omega_p/\omega)^2 \geq 1$, μ^*_∞ becomes a purely imaginary quantity, making both X and P real. For real argument and order, the Bessel functions and their derivatives are both real, so that from eq. (6-91) the ratio $(1 - R)/(1 + R)$ is pure imaginary. Let $R = X + iy$ and let γ be any real number. Then eq. (6-91) can be written

$$\frac{1 - X - iy}{1 + X + iy} = i\gamma \tag{6-96}$$

from which it follows directly that

$$X^2 + y^2 = |R|^2 = 1 \tag{6-97}$$

The fact that $|R|$ is unity for lossless, critically dense plasmas implies that no power can be transmitted into the medium regardless of the transition zone thickness. As in the previous case of a uniform plasma, T does not vanish under these conditions, but the Poynting vector in the plasma has no real part. Hence no energy transport away from the interface is possible in the medium.

Although the expressions derived above for R are exact they do not lend themselves to easy calculation, nor can the general

behavior of the reflection coefficient be deduced from inspection. There are many asymptotic expansions which in principle may be invoked for complex Bessel functions to yield a variety of small and large argument expansions. In addition, since X and P differ only slightly for $\mu_{00}^{*}>1$, an expansion in terms of their small difference quantity ϵ becomes possible (ref. 77, page 245). The narrow ramp (large m) approximation is perhaps the most useful and is derived below.

Consider an expansion in terms of the recursion relation, eq. (6-94). Letting $P \rightarrow P+1$,

$$\frac{J_{p+1}(X)}{J_p(X)} = \frac{X}{2(P+1)}\left[1 + \frac{J_{p+2}(X)}{J_p(X)}\right] \tag{6-98}$$

which may be substituted in R, rearranged as

$$R = \frac{(1-\mu_{00}^{*}) - i\sqrt{1-\mu_{00}^{*2}}\left[\frac{J_{p+1}(X)}{J_p(X)}\right]}{(1+\mu_{00}^{*}) + i\sqrt{1-\mu_{00}^{*2}}\left[\frac{J_{p+1}(X)}{J_p(X)}\right]} \tag{6-99}$$

to yield

$$R = \frac{(1-\mu_{00}^{*}) - i\sqrt{1-\mu_{00}^{*2}}\,\frac{X}{2(P+1)}\left[1 + \frac{J_{p+2}(X)}{J_p(X)}\right]}{(1+\mu_{00}^{*}) + i\sqrt{1-\mu_{00}^{*2}}\,\frac{X}{2(P+1)}\left[1 + \frac{J_{p+2}(X)}{J_p(X)}\right]} \tag{6-100}$$

This process can be continued to include as many terms as desired, the numerator and denominator yielding identical series. In the nth term of the polynomial, the Bessel function order becomes

real and integral as n becomes large, and

$$\lim_{n\to\infty} \frac{J_{p+n}(X)}{J_p(X)} = \lim_{n\to\infty} \frac{J_n(X)}{J_p(X)} \to 0 \qquad (6\text{-}101)$$

leaving a polynomial solution for R in terms of μ_∞^*, X, and P. But X and P both vanish for large m, and the first order solution to the narrow ramp problem is found to be

$$R \triangleq \frac{(1-\mu_\infty^*) - i\frac{\pi}{m}(1-\mu_\infty^{*2})}{(1+\mu_\infty^*) + i\frac{\pi}{m}(1-\mu_\infty^{*2})} \qquad (6\text{-}102)$$

which reverts to the uniform interface solution as $m \to \infty$:

$$R = \frac{1-\mu_\infty^*}{1+\mu_\infty^*} = \frac{k_0 - k^*}{k_0 + k^*} \qquad (6\text{-}32)$$

Effects of Variable Ramp Width. Numerical evaluations of the exact solutions for $|R|$, φ_R, and ρ were performed on IBM 7094 and 1620 computers,[+] using real algebra and expansions generated from recursion relations similar to the example above. The preparation of adequate computer programs for this task is discussed in Appendix D. The collision frequency ν/ω was taken

---

[+]The assistance of the Princeton University and Guggenheim Laboratories Computing Centers in making the necessary machine computations is gratefully acknowledged. This work made use of computer facilities supported in part by National Science Foundation Grant NSF-GP579.

to be 0.02 for these calculations, the approximately constant value calculated from the experimental data (viz Fig. 6-23) for the quiescent preionized plasma ahead of the current sheet. This value agrees well with predicted initial values of collision frequency based on simple theoretical considerations (Appendix B).

The independent variable in the problem was taken to be the normalized electron density $(\omega_p/\omega)^2_\infty = (n_e/n_p)_\infty$, and ramp width was taken as an adjustable parameter.

To specify the ramp width the folding parameter m was employed, or alternatively the quantity δ, defined by noting that the electron density has reached 99% of its maximum value,

$$\frac{n_e(z)}{n_{e\infty}} = \left(1 - e^{-2m\frac{z}{\lambda_0}}\right) = 0.99 \ldots.$$

by the time the total exponent has reached the value of 5.0. Hence δ represents a useful saturation limit,

$$\delta = \left[\frac{z}{\lambda_0}\right]_{99\%} = \frac{2.5}{m} \qquad (6\text{-}103)$$

which can be physically interpreted as the (99%) thickness of the transition zone in units of λ_0, the free space wavelength.

The computed curves for the phase measurable ρ are displayed in Figs. 6-30 and 6-31 for both high and low mode operation of the interferometer (section 6-4).

In general these curves are well behaved over the range of δ considered (up to δ = 2.5, or 1 cm ramps). The insensitivity of the "cusp" heights to δ, compared with their considerable sensitivity to ν/ω, (Figs. 6-7 and 6-8) implies little interaction between the two effects. Increases in ν should thus be manifested as an overall damping of the family of curves, as

FIGURE 6-30

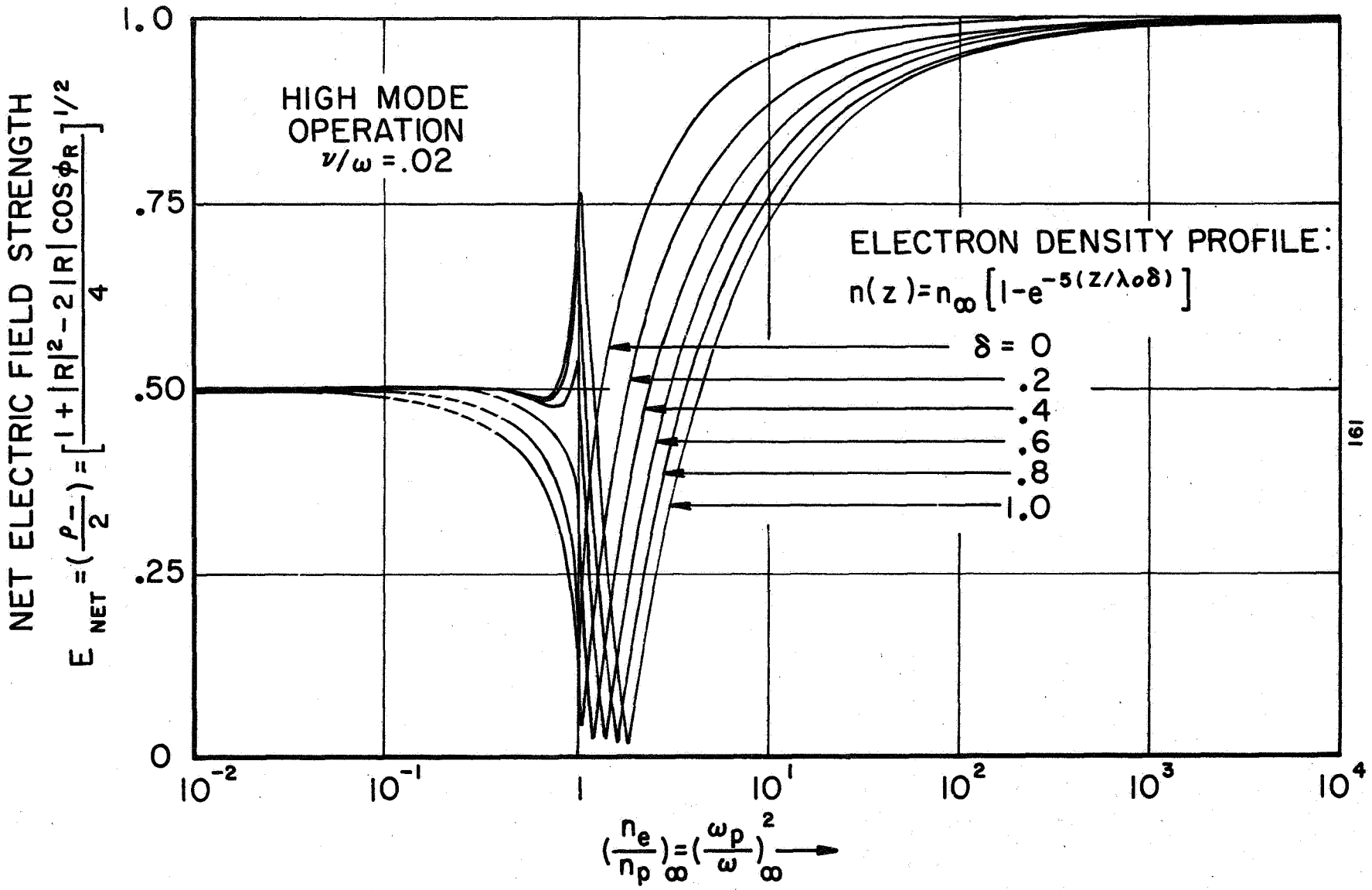

COMPUTED INTERFEROMETER RESPONSE FROM ELECTRON DENSITY GRADIENT

APZS-4179a66

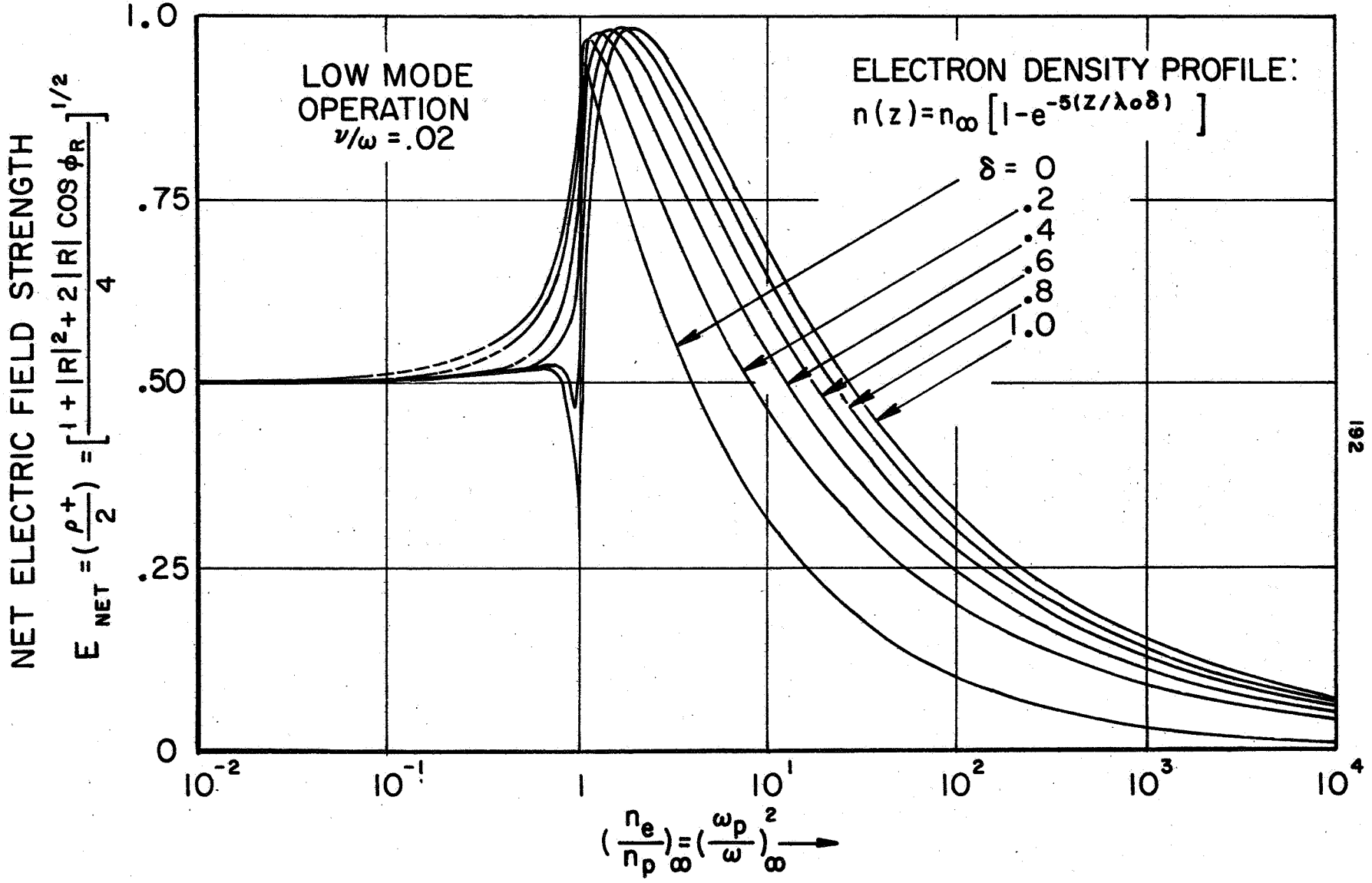

FIGURE 6-31

COMPUTED INTERFEROMETER RESPONSE FROM ELECTRON DENSITY GRADIENT

in the previous uniform plasma model, and computer studies for various ν/ω show this to be the case.

The dashed parts of the curves, in the subcritical density regime, smooth over occasional small spikes which were traced to zeros in one of the Bessel functions in the denominator of R. The machine operation, for low values of n_e, occasionally strayed beyond the valid numerical limits of some of the subroutines, and whether these little spikes were the result of a truncated numerical procedure or had more physical significance was never satisfactorily determined. In any case, interest in the low n_e regime was purely academic for this problem, and the interesting domain $(\omega_p/\omega)^2 > 1$ was monotonic and well behaved. The rightward shift of the "critical" null (or anti-null) for increasing ramp width is reasonable in view of the receding position of the effective reflecting plane and the phase change concommitant with this effect.

The quantity ρ, which represents the net field strength at the detector, was shown in section 6-4 to be related to the reflection coefficient by the law of cosines:

$$\rho_{\pm} = \sqrt{1 + |R|^2 \pm 2|R| \cos \varphi_R} \qquad (6\text{-}50)$$

The nonlinearity of this expression means that use of the two modes independently offers in a sense the utility of two measurables instead of one. The bridge modes produce numerically equal signals when

$$|R| \cos \varphi_R = 0 \qquad (6\text{-}104)$$

which always occurs once for $n_e > n_p$. For example, if $\nu/\omega = 0$, $|R| = 1$, then $\varphi_R = 90^\circ$ and $n_e = 2n_p$ at the match point. $\rho_- > \rho_+$ for densities higher than this value and data obtained in one mode are readily converted to data in the other:

$$\frac{\rho_\pm}{2} = \sqrt{(1 + |R|^2) - \frac{\rho_\mp}{2}} \qquad (6\text{-}105)$$

In low mode, the interferometer "saturates," or becomes insensitive to further increases in n_e, as ρ approaches zero. Thus, if ϵ is the small quantity under the radical in eq. (6-50), near saturation

$$\rho_+ \propto \sqrt{\epsilon} \qquad (6\text{-}106)$$

In high mode, on the other hand, the saturation trend is toward unity

$$\rho_- \propto \sqrt{1-\epsilon} \sim 1 - \frac{\epsilon}{2} \qquad (6\text{-}107)$$

Small changes ϵ in the low mode thus produce large changes in ρ for $n_e/n_p \gg 1$, whereas small changes ϵ in the high mode produce practically negligible changes in ρ, a feature which is obvious from Figs. 6-30 and 6-31. The trivial but important point being made is that the nonlinearities of signal addition have important consequences, one of which is that δ can be uniquely determined.

The procedure to determine δ involves recording ρ from the plasma in both modes, under otherwise identical conditions, as shown in Fig. 6-32. Profiles of n_e vs. t can be calculated from these experimental curves for each mode, using first

T-1740

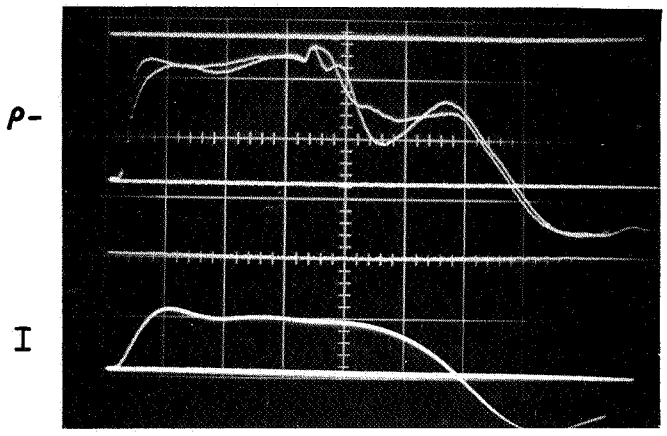

a. HIGH MODE PHASE MEASUREABLE

T-1744

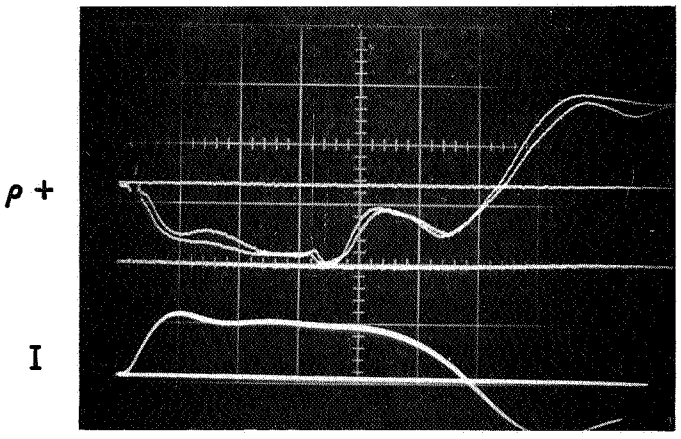

b. LOW MODE PHASE MEASUREABLE

TYPICAL PHASE DATA COMPARING HIGH AND LOW MODES
(DOUBLE OVERLAY, $\frac{R}{R_0}=.5, \frac{z}{h}\cong 0$)

FIGURE 6-32

δ = 0, then δ = .2, and so on, from the theoretical curves of Figs. 6-30 and 6-31. Clearly, for a given measured value of ρ, the predicted electron number density will be higher for large δ; but the predicted density is much more sensitive to the choice of δ in the low mode than in the high mode, because of the nonlinearity just mentioned. Therefore, since the measured electron density must be independent of the particular bridge mode employed, it follows that the profiles which match $n_e(t)$ determine $\delta(t)$. Once δ is known, the necessary curves of $|R|$ and ρ can be generated by the computer to incorporate ν/ω as a free parameter while including the experimentally determined δ implicitly.

The results of this procedure, though unexpected, are quite interesting. Double mode data sets, such as the double-overlay traces of Fig. 6-32, when reduced by the techniques of section 6-7, unambiguously indicated that δ = 0 was the only possible value of ramp parameter consistent with the experimental data. Profiles of $n_e(t)$ obtained from ρ_1 yielded agreement within about 50% for δ = 0; for δ = 0.2 the profiles differed by an order of magnitude, and the discrepancy became rapidly worse for large values of δ. Agreement within 50% is actually very close for this type of calculation, because the low mode was so difficult to calibrate properly; there is no simple way of placing a top reference line, corresponding to total reflection and $\varphi_R = 0^\circ$, without unbalancing the bridge.

This ramp result was checked in another way by constructing aluminum test plates with varying degrees of "surface roughness," an effect achieved by machining perpendicular V-grooves into the

metal to form a matte of tiny square-based metallic pyramids on the surface. It was hoped that these surfaces would adequately represent transition zones of varying thickness. Reflections measured from the smooth surface were found to agree well with $|R|$ from the plasma, but the presence of surface roughness greatly decreased the amount of coherent reflected wave intensity which reentered the horn. The phase measurable was especially sensitive to the surface structure, as expected, and the only surface condition which was compatible with the plasma data was again shown to be $\delta \cong 0$.

Finally, it must logically be argued that the mere fact that wide transition zones (large δ) require very high electron densities to produce the measured near-saturation values of ρ mitigates against them. For example, the $\delta = 0.4$ curves would yield $(n_e)_{max} \cong 10^{18}\text{cm}^{-3}$ from the experimental data, a difficult result to accept in view of the initial gas density, $\sim 10^{15}\text{cm}^{-3}$. Thus the conclusion seems safe that $\delta = 0$ is an adequate, and probably the best, approximation to the experimental conditions prevailing here, and the appropriate curves for data reduction are thus given by the uniform plasma results of Figs. 6-4 through 6-8.

In the following section bridge balancing problems, data reduction techniques, and other practical error sources are discussed.

6.7. Laboratory Sources of Error

Microwave interferometers have their own unique problems from an experimentalist's point of view, which can be described only with difficulty to the uninitiated. Ginzton (ref. 84) is an

adequate introduction to the subject. The problems can generally be ascribed to the presence of standing wave patterns which change from point-to-point in the waveguide interior, the local properties of which are determined by the variety of reflected, transmitted and attenuated dominant and higher mode waves which happen to coincide there.

The reflected phase interferometer of these experiments was designed to handle a reference signal in the "reference" arm, and a reflected signal from the plasma in the remaining, or "reflection" arm. These two signals combine with amplitudes and phases determined by the control settings in the two arms, which include reflection arm attenuator, reference arm attenuator, and two reference arm phase shifters (to assure full 360 degree control), as shown in Fig. 6-10. These circuit components are not ideal, but rather exert several control functions simultaneously; the phase shifters, for example, are lossy and thus attenuate the signal in addition to altering its phase. The control functions thus can not be isolated in practice, and the resulting nonlinear, multi-variable adjustments required to achieve bridge balance are tedious and best handled by a considered systematic approach. An example will illustrate the methods.

Balancing for $|R|$ Measurements. Measurements of reflected amplitude are usually attempted without a bridge arrangement. The microwave detector is conventionally mounted on a reversed directional coupler to the main guide, and with the horn looking at free space, registers some net signal which is the vector sum of all the small internal reflections in the waveguide plus any residual forward coupling. This net internal reflection is con-

stant in time, and can be eliminated under most conditions with a stub or E-H tuner by effectively introducing a compensating signal of equal amplitude and opposite phase. The detector then registers zero net signal, and the presumption is usually that any subsequent detector output during the course of an experiment can be attributed to reflected amplitude from the plasma.

This presumption is false, however, when the reflection coefficient of the load approaches unity, as can easily be proved by replacing the plasma-horn combination by a simple movable metallic plunger at the horn location. (This is conveniently accomplished in practice with the three-port switching arrangement shown in Fig. 6-14). The position of the metallic plunger in the waveguide should be immaterial to the problem, since the modulus by definition is not phase dependent. Thus the detector output should ideally indicate unit reflection, independent of plunger movement. In practice, however, large oscillations in output signal were observed every time the experiment was performed, implying serious phase sensitivity.

The mismatch effect has a simple explanation in terms of reflected waves. The initial null was set by cancelling an internal reflection signal caused by the essentially uni-directional passage of microwave energy along the waveguide and through the matched horn into free space. However when energy is more or less totally reflected back into the waveguide, from either plasma or plunger, the rear-traveling wave which results also undergoes reflections at every small irregularity encountered in the

waveguide, and thus generates a second forward traveling wave, which in turn is totally reflected by the load, etc. The second generation wave is as capable of producing a net signal at the detector, arising from summed internal reflections, as was the original, but its contribution has not been tuned out and so of course it interferes with the plasma (or plunger) signal (the one of interest) at the detector.

It therefore follows that the only practical way to eliminate interference problems of this kind is to tune out the unwanted internal reflections under load conditions, i.e. when a reflecting surface is present at the horn location or its equivalent. The result is a kind of "dynamic" balancing, which is far easier to accomplish with a bridge arrangement than with a series tuner. This led to the concept of a "modulus" bridge, the third bridge mode to be used in the experiments.

Consider the reference arm of the bridge to be initially closed off with the isolation valve shown schematically in Fig. 6-10. The resulting internal reflections from the circuit and the horn-space combination then enter the bridge through the reflection arm, and can be tuned out with a series E-H tuner to give zero diode output. When the horn is replaced by an oscillating metallic plunger in the waveguide, an interference pattern develops as discussed above, and the resulting oscillatory diode output can be displayed on an oscilloscope screen to adapt the bridge to a visual balancing procedure.

A bucking signal of proper amplitude and phase was admitted from the reference arm to exactly cancel the interference and

produce a steady unit reflection independent of plunger motion. Subsequent amplitude experiments with the horn in place exhibited complete insensitivity to the phase of the reflected signal, and thus a serious impediment to valid $|R|$ measurements was removed.

Balancing for ρ Measurements. A host of similar pitfalls arise when the interferometer is used to record the phase measurable ρ. Similar tactics must be employed, with liberal use of ferrite isolators to provide adequate signal isolation. The result of these varied and often tedious balancing procedures is to limit the number of data runs to one or two per day, a time scale on which klystron output variations become an important experimental variable. (Such difficulties constitute an inherent limitation of microwave diagnostics in this application, and should be considered in feasibility studies.)

Calibration and Data Reduction. Reflected amplitude measurements were made with the modulus bridge just described, and the two reference lines $|R| = 0$ and $|R| = 1$ were normally superimposed on the oscillograms. The first was obtained by triggering the oscilloscope prior to the experiment with the bridge connected to the 70 Gc horn, the second by switching to the metallic plunger, shown in Fig. 6-14. These two reference lines were sufficient for calibration when the diode response law was known.

Reflected phase measurements were normally made with the bridge in the high mode arrangement, as shown for example in Fig. 6-23. The three reference lines shown correspond to $\frac{\rho}{2} = 0$, .5, and 1.0, and were obtained by triggering the scope with shorted input, by triggering the scope to record the reference arm signal

only, and by triggering to record reflection from the metallic plunger with the phases adjusted to add from a metal ($\varphi_R = 180^\circ$). The superiority of the high mode arrangement over the low mode is that the latter affords no simple way of obtaining more than two reference lines, since $\left(\frac{\rho}{2}\right)_{max}$ $(i.e.\ \varphi_R = 0^\circ,\ |R| = 1)$ is not an asymptotic limit.

The high mode with its three easily obtained reference lines is essentially self-calibrating, once the diode response law is known. Thus calibrating the diode and placing reference lines on each oscillogram is sufficient to calibrate each shot individually, whether for $|R|$ or ρ.

It should be emphasized that $|R|$ and ρ are not recorded directly, but rather are distorted by the diode; experimental curves are labeled $|R|$ or ρ strictly in the interest of concise expression. The more correct statement is

$$V_{diode} \propto |R|^n \text{ or } \left(\frac{\rho}{2}\right)^n \tag{6-108}$$

where

$$n \cong 2.0$$

for approximate square law response. To obtain $\frac{\rho}{2}$ for graphical data reduction, for example, the relation

$$\frac{\rho}{2} = \left(h_{norm}\right)^{\frac{1}{n}} \tag{6-109}$$

was employed, where $\frac{1}{n} \cong 0.5$ is the power law obtained from the ratio of baselines, and h_{norm} is the normalized measured

trace height as shown in Fig. 6-33:

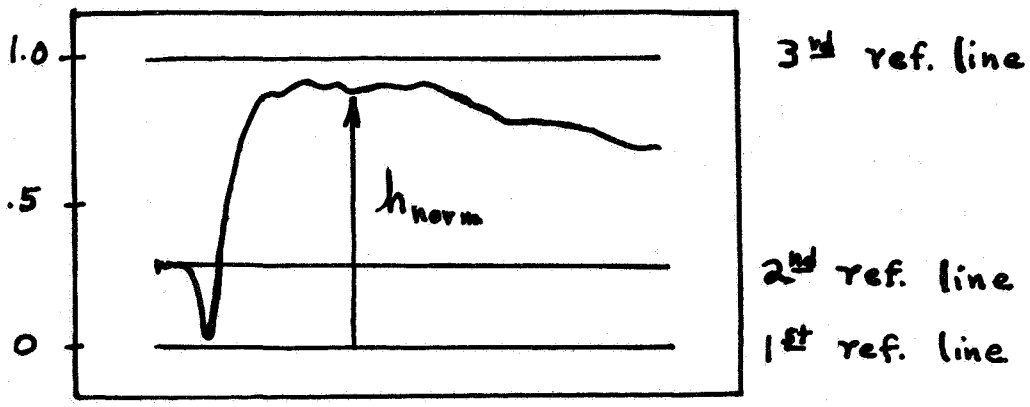

Nomenclature for Data Reduction

Fig. 6-33

Because of the prevailing high electron densities, h_{norm} was normally between 0.75 and 1.0 during the interesting part of the experiment, and in particular was close to unity during the current sheet traverse. Thus little error was incurred from experimental uncertainties in the exponent n, since near unity any exponent in the range $0.5 \leq n \leq 1$ gives essentially the same result, as shown in Fig. 6-34.

The calibrated data curves for $|R|$ and ρ are sufficient in principle to determine n_e and ν. However, since ρ involves $|R|$ explicitly (eq. (6-50)), it is more convenient to use the independent variables $|R|$ and φ_R directly:

$$\varphi_R = \cos^{-1}\left[\frac{4\left(\frac{\rho}{a}\right)^2 - |R|^2 - 1}{2|R|}\right] \qquad (6\text{-}110)$$

The data is then reduced systematically in several steps:

(1) calibrate $|R|$ and ρ traces to obtain h_{norm} and $\frac{1}{n}$ for

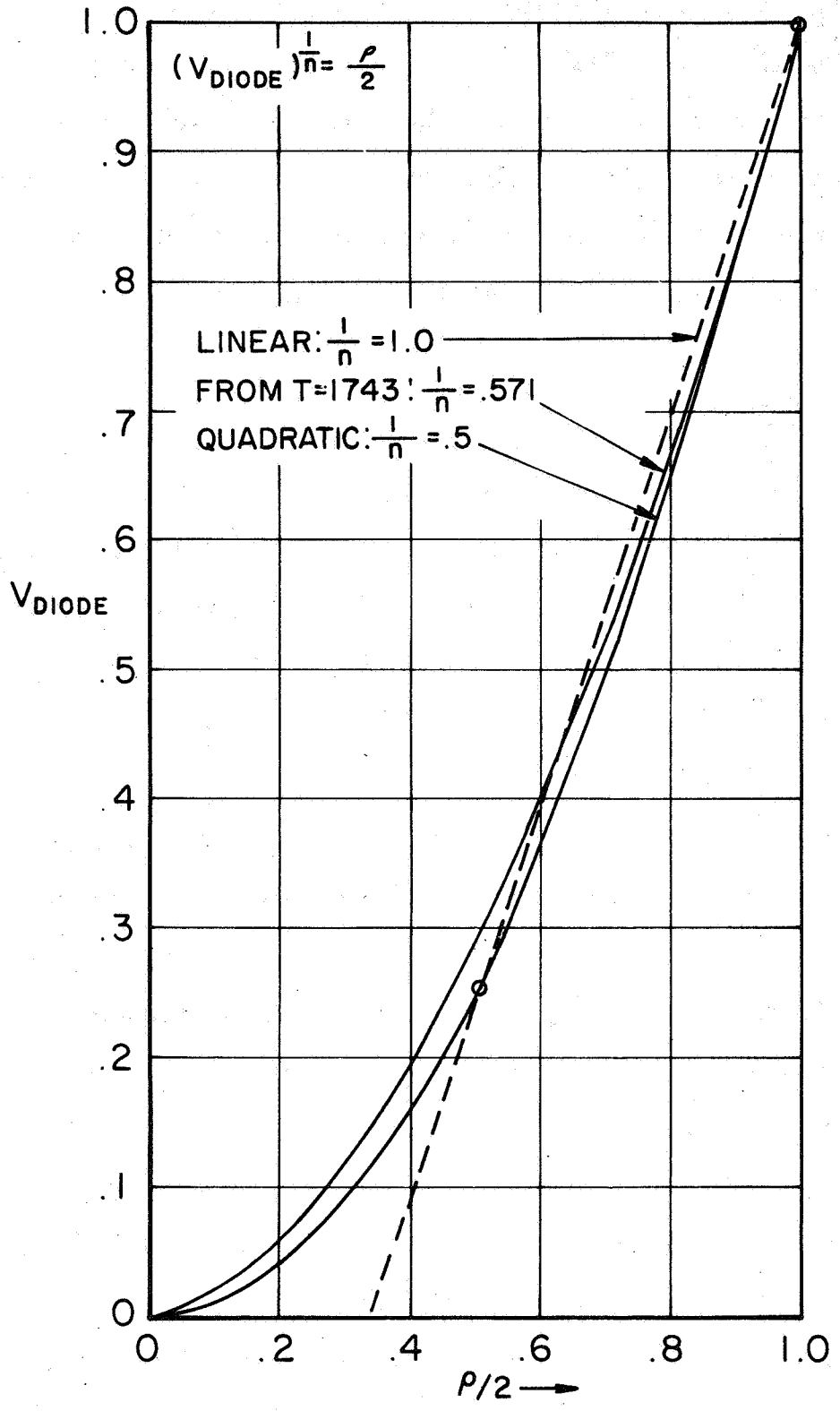

VARIOUS DIODE RESPONSE LAWS COMPARED

FIGURE 6-34

each; (2) calculate $|R|$ and ρ (from eq. (6-109)); (3) calculate φ_R from eq. (6-110); (4) using Figs. 6-4 and 6-5, obtain $(\omega_p/\omega)^2$ and ν/ω graphically for various times; and (5) using the probing frequency, $\omega = 4.4 \times 10^{11} \text{sec}^{-1}$, convert these dimensionless groups into n_e and ν time profiles.

In the last section of this chapter, the data is discussed and methods for determining the true collision frequency are presented.

6.8. Plasma Electron Properties

This chapter has been devoted so far to describing a method for measuring plasma properties. The microwave data presented in previous sections have had more relevance to the diagnostic technique than to the larger problem. In this section the quantitative variation of plasma properties through the current sheet is examined in detail.

Several general pinch chamber surveys were made with the reflection probe to provide correlations with the earlier magnetic probe surveys. The current sheet traverse over the probe under normal conditions was clearly evident on the oscillograms, and the current sheet width estimated from the raw microwave data coincided closely with the B-probe data.

Radial Surveys. A series of radial surveys were made, wherein the probe was inserted a fixed distance axially and the radial coordinate was changed. The probe was always inserted through the exterior electrode (Fig. 2-1), and choice of polarity then made that electrode positive or negative. Unless the probe aperture was flush with the anode or cathode surface, the flow isolator (Fig. 6-20) was added to minimize gas dynamic disturbances.

Radial surveys allowed the progress of the precursor effect and the current sheet to be followed radially inward. The precursor was determined to have a large but finite velocity, roughly an order of magnitude larger than the current sheet. Thus the precursor traveled 2 or 3×10^5 m/sec, or about 0.1% of the velocity of light. The velocity of the current sheet, extracted from the microwave data by following the radial progress of characteristic wiggles in the traces, agreed with the radial progression of the $\dot{B}_\theta$ profiles within experimental error. Thus both probes gave the same value for U_s (section 4-5).

The experimental $|R|$ and ρ traces of Fig. 6-23 were typical of the raw data returned by the microwave probe, and, not unexpectedly, the radial surveys favored the midradius location for more detailed studies. Thus the microwave data reinforced the same conclusions drawn earlier from the other probe surveys. The internal self-consistency of the microwave data has been discussed in several previous instances, and this additional check on experimental procedure was maintained for all the quantitative work discussed below.

Axial Surveys. Axial surveys were made by mounting the probe at a given radial station and varying the axial position of the probe aperture from anode to cathode. The probe was never allowed to extend over 3/4" beyond the electrode surface through which it passed, so that a 2" axial survey from anode to cathode required one polarity reversal, and the probe finished the survey in the opposite polarity electrode from the one in which it began. The centerplane position was not normally accessible to the probe in a 2" high chamber.

A midradius axial survey of reflected amplitude is shown in Fig. 6-35. At midradius the current sheet reached the probe in about three microseconds, the exact time depending on the probe axial coordinate because the sheet was slightly tilted. The degree of tilt estimated from the microwave data agreed closely with the magnetic probe results (Fig. 4-6).

The current density at the cathode is represented by B_θ in part g of Fig. 6-35. (Current densities at the other axial positions can be inferred from the axial $\dot{B}_\theta$ survey of Fig. 4-8.) Part f of the figure shows the corresponding amplitude data from the microwave probe at the cathode. The ambient argon density at 100 mT is 3×10^{15} atoms/cm^3 and the early precursor ionization of a few percent raises the electron density almost immediately above the critical value of 6.1×10^{13} cm^{-3}. $|R|$ remains near unity until the current sheet arrives, at which time a roughly linear decrease in amplitude occurs. The reflected wave then once more assumes a constant amplitude at a value related in some way to the current sheet's passage over the probe. In the center of the linear portion, at the maximum of the current density, a spike or peak in $|R|$ is clearly evident. The effect is shown to be reproducible by the use of double overlays on each trace, and the gradual disappearance of this feature as the probe is moved toward the anode is clear. The general degradation of sharp features in the data from cathode to anode is paralleled by a similar smearing out of axial current density, previously discussed in Chapter IV. At the anode position, Fig. 6-35a, the passage of a discrete sheet is no longer identifiable, in agreement with the magnetic probe data of Fig. 4-8. From these and similar data it could be

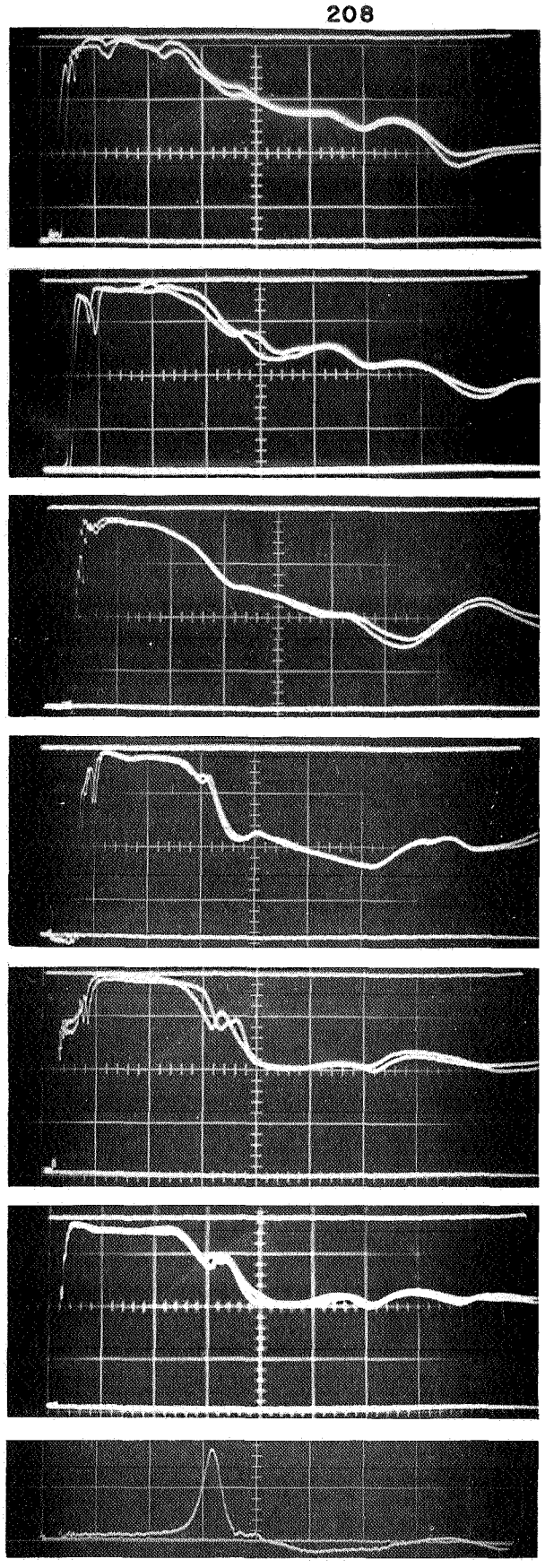

AP 23-P108-GT

AXIAL SURVEY OF REFLECTED AMPLITUDE, $\frac{R}{R_0} = .5$

FIGURE 6-35

concluded that axial variations were smooth and gradual, so that calculations at one axial position could be extrapolated within limits to neighboring positions. This will be helpful because of the extended calculations needed in this and the following chapter. As with the other probe studies, the microwave data exhibits sharper variations and better definition near the cathode than at the other axial positions. Consequently experimental efforts were concentrated there (Fig. 4-4).

Precursor Studies. The microwave probe was the only diagnostic tool employed in the pinch experiments which could be effectively used to study precursor ionization phenomena. Although the details of particular preionizing mechanisms are incidental to the primary research goals, the preionization event itself is of singular importance. Its occurrence preconditions the gas to conduct current, and implies that the current sheet advances into a plasma whose transport properties are already completely dominated by electron-ion encounters. The precursor also represents the first dynamic event associated with the discharge. The following brief digression on observed precursor behavior therefore has some direct relevance to current sheet studies.

Precursor phenomena are of course well-known, and have been studied in a variety of accelerator, shock tube, and gas discharge devices. The particular device employed determines whether the precursor precedes a current sheet, gas dynamic shock wave, hydromagnetic disturbance, etc. Not surprisingly, these various studies have indicated that more than one mechanism may be involved, and a variety of models have appeared in the literature. Electron diffusion ahead of gas dynamic shocks,[78] field-driven electron

waves,[79-81] diffusion of hot electrons from arc-type discharges,[82] photoionization effects,[85-87] and ionizing potential waves,[88] similar to the streamers in electrical breakdown at high pressure, have all been advanced.

In the present linear pinch experiments, it may be concluded from the B-probe studies that the precursor wave does not involve significant current conduction. Electron diffusion ahead of the current sheet can be ruled out for two reasons: typical measured levels of diffusion electron density are $10^7 cm^{-3}$, or about eight orders of magnitude lower than the precursor densities measured in these experiments; and electric probe measurements show no detectable electric fields ahead of the current sheet.

The possibility of ionizing shock waves ahead of the current sheet was investigated with a piezoelectric pressure transducer. If a shock wave is driven ahead of the current sheet at the observed precursor velocities, it will have a Mach number of $\sim$ 1,000, and a pressure ratio of $\sim M^2$, or 10^6. Thus a precursor shock wave would involve a pressure jump from 10^{-4} to 10^2 atmospheres, and could certainly be detected. Fig. 6-36 shows the result of a typical radial pressure probe survey along the cathode, with $\dot{B}_\theta$ displayed simultaneously to locate the current sheet. The rise time of the transducer was quite good, $\sim$ 0.1 μs, as shown by the probe's response to a reflected shock wave in a shock tube, Fig. 6-36a. The oscillations correspond to various ringing frequencies for the probe and should be allowed for in the other traces. Oscillograms 6-36b-e are from the probe mounted flush in the cathode, and show clearly the large pressure pulse associated with the passing current sheet. No leading shock wave or precursor pressure front

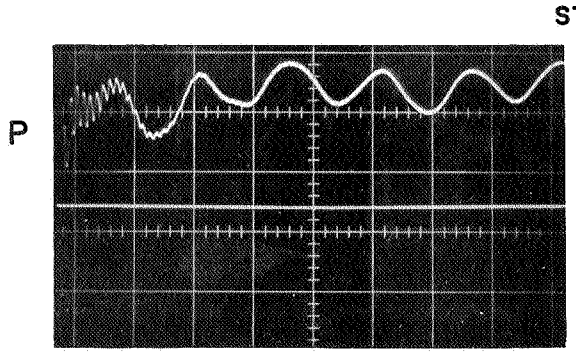

a) RESPONSE OF INSULATED PRESSURE PROBE TO A REFLECTED SHOCK

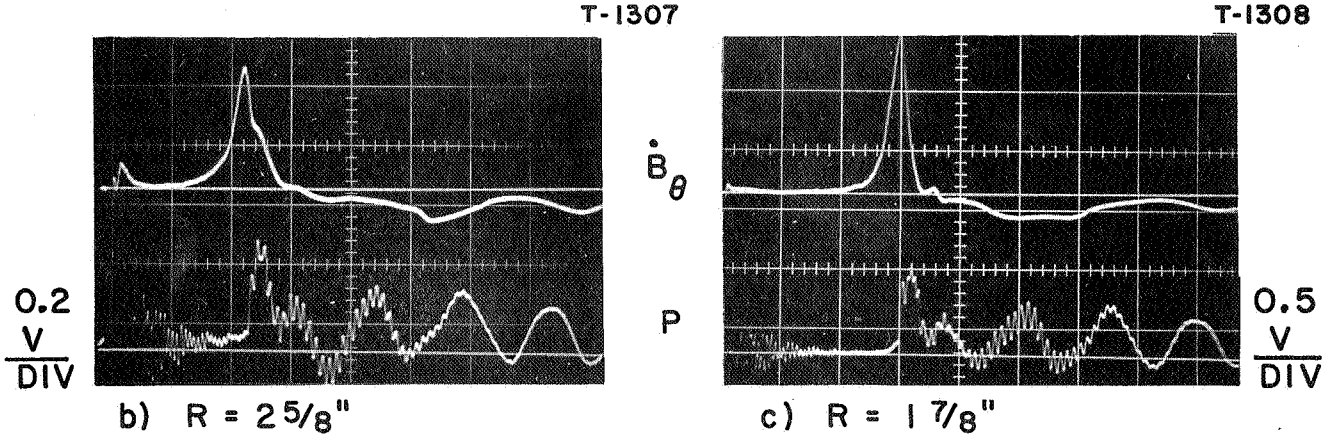

b) R = 2 5/8" c) R = 1 7/8"

(TIME SCALE : 1 μsec/DIV)

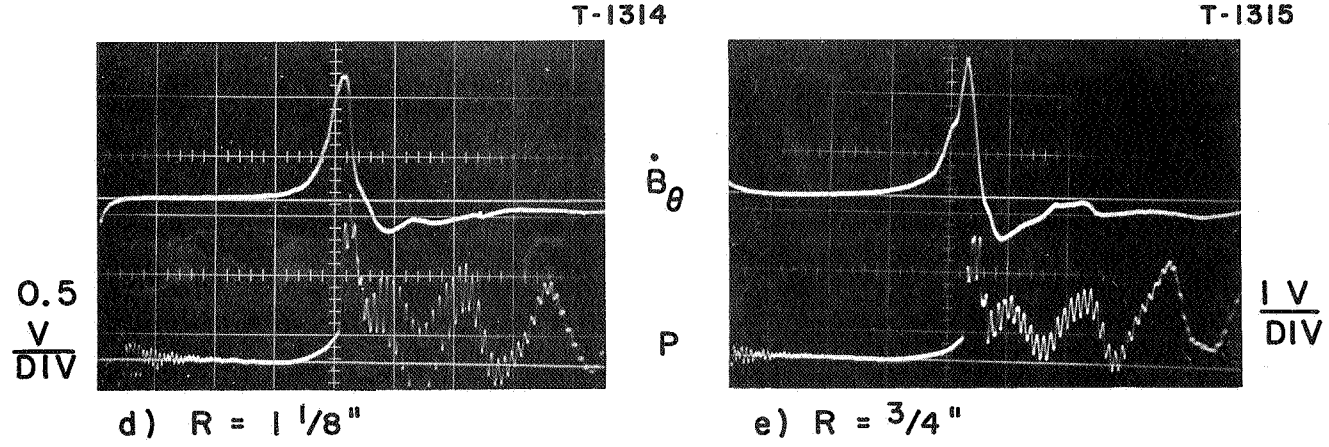

d) R = 1 1/8" e) R = 3/4"

(b) – (e) : SIMULTANEOUS MEASUREMENTS OF $\dot{B}_\theta$ AND PRESSURE AT VARIOUS RADII †

† (DATA BY T.M. YORK, REF. 8)

FIGURE 6-36

of any form was detected, and so were eliminated from further consideration.

The most probable cause for the precursor in these experiments seems to be photoionization. A number of authors[89 - 92] present evidence linking precursor ionizing waves with radiative mechanisms ahead of traveling electrical discharges and shock waves. Trace impurities in the noble gases have been shown to participate significantly under ultraviolet irradiation, and wall effects have also been noted. These phenomena are compatible with the data of the present experiments. The initial cylindrical discharge near the outer wall of the pinch chamber generates a very hot, intense sheet of plasma, and presents a large radiating surface to the gas it encloses. Radiation from the sheet can be absorbed by argon or impurity atoms in the gas or by the metal electrodes, and thus it might be postulated that one effective ionization front could pass through the gas and another along the electrodes.

The axial survey data of Fig. 6-35 conforms to this picture. At first glance the precursor front seems to be concave, since ionization is detected almost immediately along the electrodes, slightly later at interior points. However the oscillogram of Fig. 6-35e appears to preclude the nonplanar model since a multiple event is indicated. It is more likely that the original burst of radiation from the discharge region ejects electrons from the electrodes more readily than from the relatively dispersed argon atoms. Thus oscillogram 6-35e would indicate an early electron population of a few $x10^{13} cm^{-3}$, arising from photoemission from the cathode surface, and a subsequent boost, to above $10^{14} cm^{-3}$, from

the increasing ionization level in the ambient argon. More precise estimates of precursor ionization levels, and electron density increases in the current sheet itself, will be given in the data figures.

One additional feature of the precursor was investigated, to determine how closely the progression of significant ionization could be identified with a true propagating front. The motivation for these experiments was an observed phase discrepancy in the probe's response to the precursor near either electrode. According to the slab model, where the electron density is assumed to vary in time uniformly in front of the horn aperture, $|R|_{max} \geq 1$ should occur exactly at the critical null of ρ . Thus corresponding oscillograms of the two measurables should exhibit this correlation, and failure to do so indicates that the slab model might not be valid for the precursor event. In particular, if large variations near the critical electron density occur over a distance comparable to the horn aperture, then normal averaging over the probe dimension becomes untenable and the finite spatial resolution of the probe becomes important. A phase shift in the measurables is also accompanied by a distortion of the critical null in ρ , since ρ involves $|R|$ explicitly (cf. Fig. 6-37).

A series of bench tests were undertaken to duplicate the precursor phase anomaly by advancing various discrete and grooved metallic interfaces past the horn aperture with a micrometer drive apparatus. The experimentally observed phase anomaly and critical-null distortion from the precursor were simultaneously duplicated in these bench tests when the metallic interface deviated from a smooth surface by less than half the aperture dimension. This finding

strongly suggests that the preionization phenomenon can be adequately represented in this instance by a wave front whose diffuseness is on the order of a millimeter. Such a strong radial n_e gradation in the leading edge of the precursor would satisfactorily explain the observed propagation characteristics of the front, and is compatible with the photoionization model and the corresponding very high precursor velocity near either electrode where the anomaly was most severe.

Signficance of ν/ω. Error analyses in previous chapters have dealt with the influence of the measuring device itself on the desired measurement, i.e. probe interference. This effect was also present in the microwave experiments, due to the proximity of the horn window surface to the plasma under study. One example of the problem has already been suggested under precursor effects, where evidence was presented that precursor ionization levels were influenced by the proximity of an electrode surface. In a sense the microwave horn represents an extension of the electrode surface, and in this capacity its influence may not be negligible. In particular, since the wave interaction takes place within such a short distance of the aperture, it was suggested that the surface condition of the aperture window could play a dominant role.(83)

This suspicion was verified in a series of experiments which investigated data sensitivity to the type of window surface. Fig. 6-37 shows the effect on $|R|$ and ρ data of two different window surfaces, taken under otherwise identical conditions. Typical reproducibility is illustrated by the double overlay. Set B was obtained using the quartz surface, which had been cleaned with acetone and outgassed under vacuum ($\sim 10^{-3}$ Torr) for 24 hours.

|R|

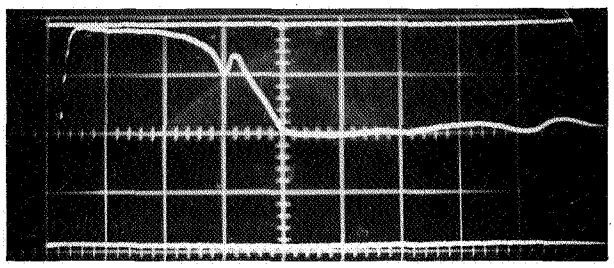

T-1855

ρ (HIGH MODE)

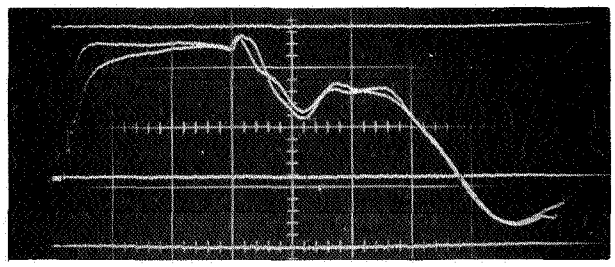

T-1743

SET A: LACQUERED WINDOW SURFACE

|R|

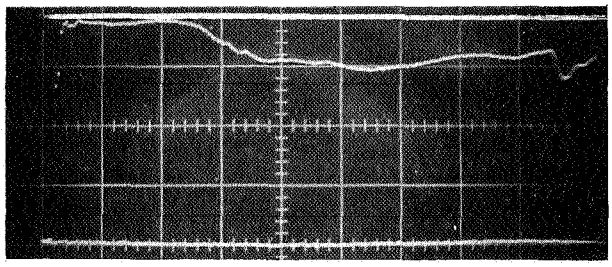

T-1796

ρ (HIGH MODE)

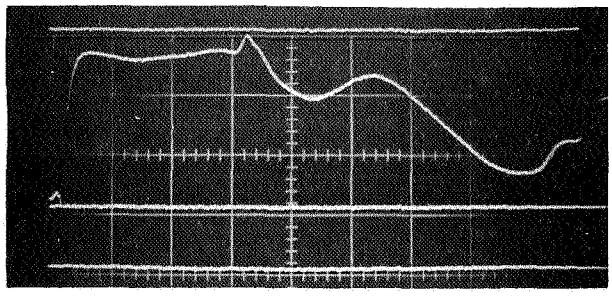

T-1802

SET B: QUARTZ WINDOW SURFACE

$\dot{B}_\theta$

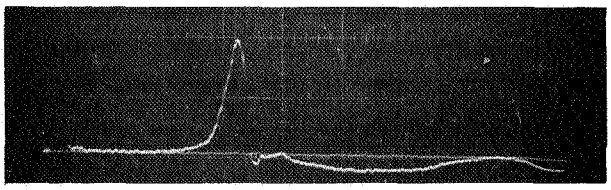

T-1993

INFLUENCE OF HORN WINDOW SURFACE ON AMPLITUDE AND PHASE MEASURABLES

FIGURE 6-37

Set A was obtained after coating the quartz surface with a thin transparent coat of high voltage insulating dope (Hi-Voltage Clear Spra-Koat, mfg. by General Electronics), also outgassed under vacuum. This latter arrangement was the usual operating condition when setting up experiments, because the insulating cover protected the horn from arc damage. A thin, hard drying coat of dope applied to the horn's exterior surfaces provided effective protection without disturbing the horn match. Shot-to-shot damage from local arc strikes was not so great, however, that the coating could not be eliminated for individual experiments.

These two sets of oscillograms are essentially indistinguishable prior to current sheet arrival (indicated in the figure by $\dot{B}_\theta$), but during the transit of the sheet over the probe the traces of set A exhibit apparently greater damping. The indication is that outgassing, vaporization, occluded impurities, etc., have significantly influenced the effective values of ν/ω. This is confirmed by Figs. 6-38 and 6-39, which are plots of n_e and ν from these oscillograms. The calculated electron density profiles are seen to be independent of the window coating, but the calculated total collision frequencies are significantly higher for the coated window case beginning with the arrival of the current sheet. The important conclusion is thus reached that impurities which leave the window surface, through radiation boil-off, sputtering, etc., although playing an important role in the overall collision description, do not ionize on the time scale of the experiment. The local electron density is thus insensitive to the increased level of impurities for at least the first few microseconds, and the

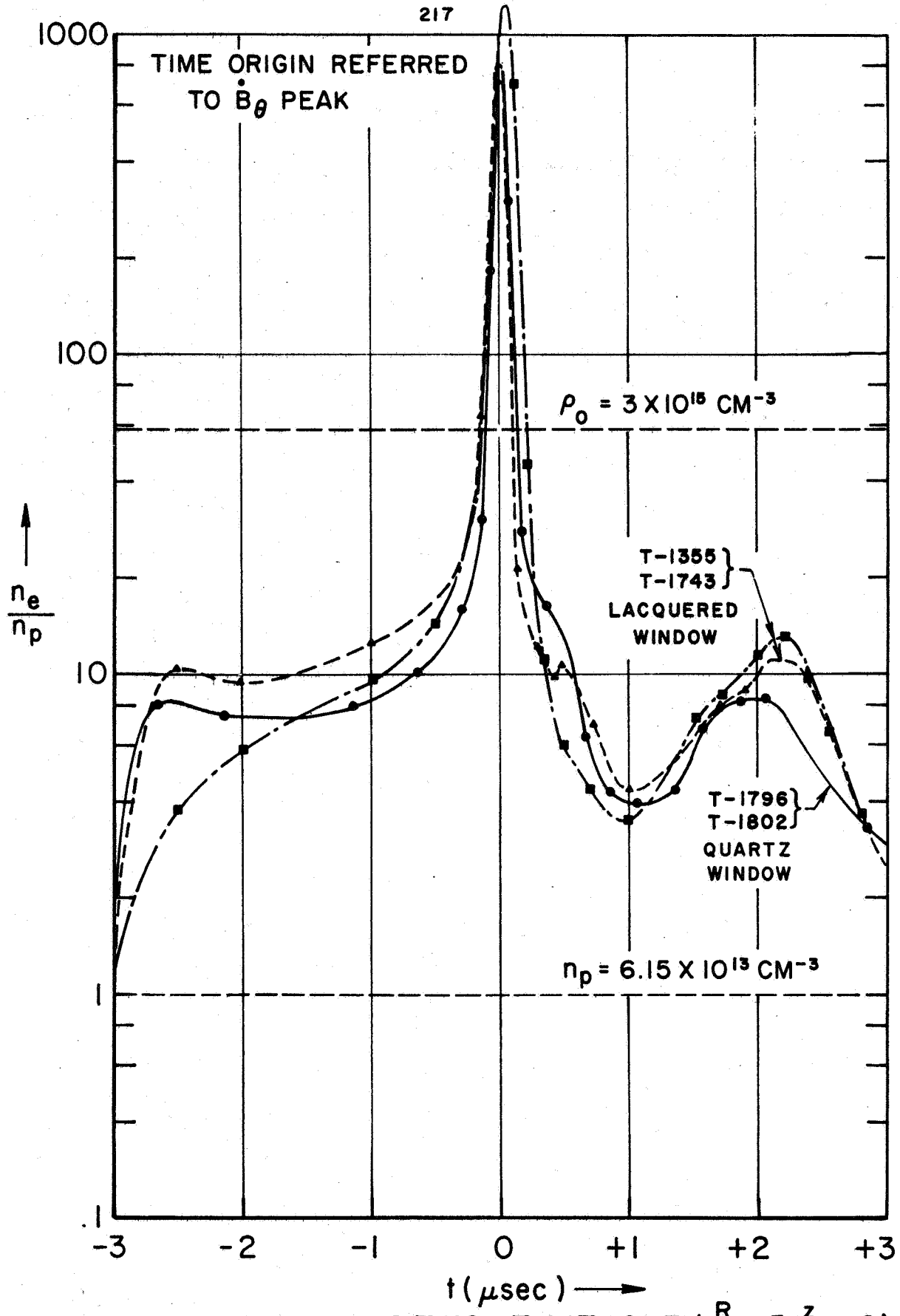

MEASURED ELECTRON DENSITIES AT CATHODE, ($\frac{R}{R_0} = .5, \frac{z}{h} \cong 0$)

FIGURE 6-38

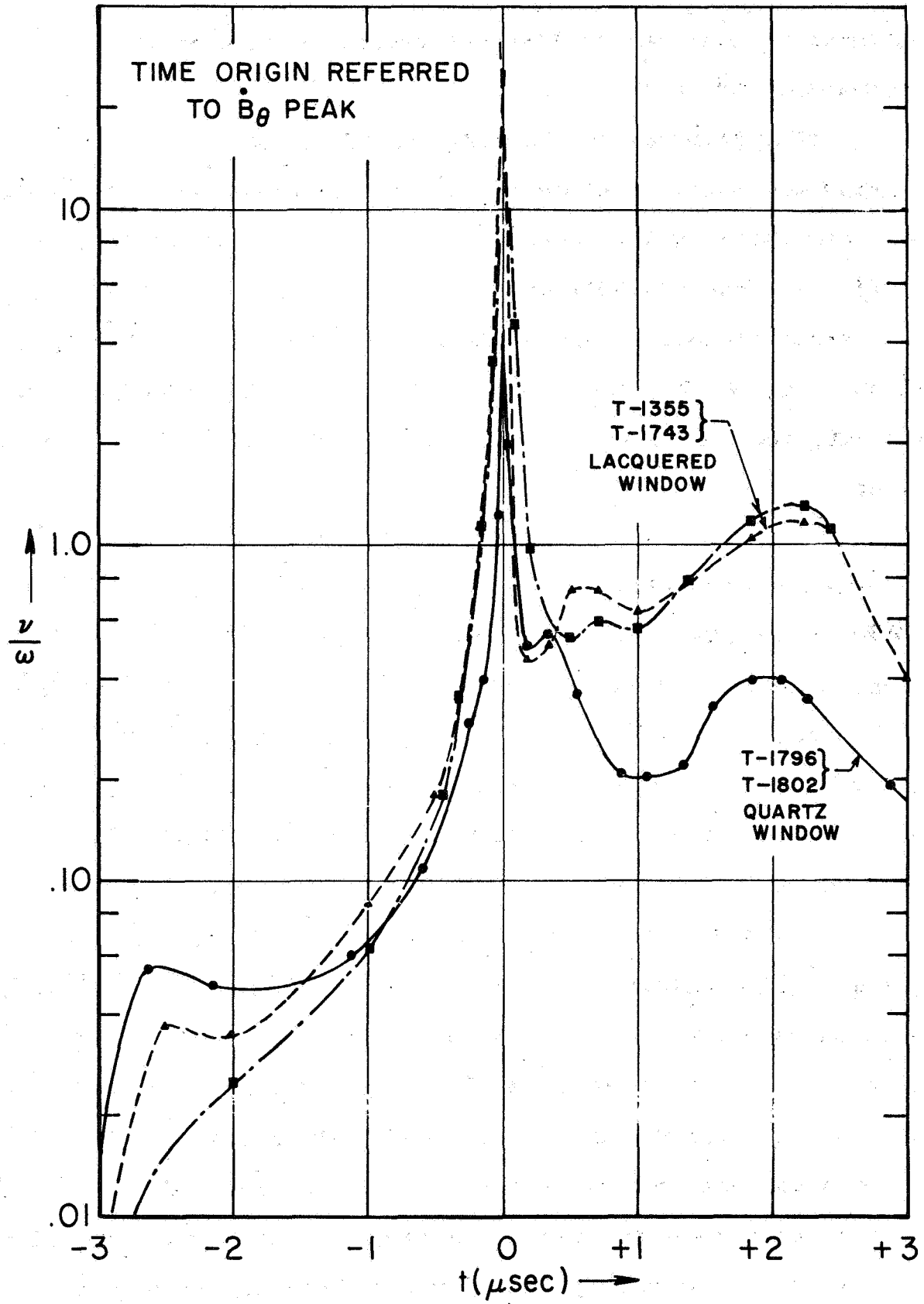

MEASURED COLLISION FREQUENCIES AT CATHODE

$(\frac{R}{R_o} = .5, \frac{z}{h} \cong 0)$

FIGURE 6-39

measured values may be taken as representative of the true conditions in the plasma.

The problem thus becomes one of minimizing the impurity contribution of the probe to the overall measurement of ν/ω, and compensating for the remainder. The lesser effect of the pure quartz surface should logically be more representative of the undisturbed plasma, and so attention will be concentrated on the data of set A, Fig. 6-37, and the corresponding measured profiles of n_e and ν, reproduced for convenience in Figs. 6-40 and 6-41.

The actual nature of the surface impurities is not essential to the graphical data reduction techniques described below, because ν/ω is an effective collision frequency which includes contributions from electron-argon, electron-ion, and electron-impurity collisions. Therefore the impurity contribution can be handled as an effective addition to the argon components without regard to the specific colliding species involved. It is probable, however, that the impurities ejected into the plasma are other argon atoms, air molecules, and water vapor, etc., occluded on the surface. The observed slow ablation rate of the quartz would seem to preclude serious vaporization problems, and large chunks of foreign material in the plasma would not present a very effective target to the oscillating electron swarm. The observation that impurity damping becomes serious only after current sheet arrival, and does not increase significantly after its passage, suggests that the effect is basically a sputtering phenomenon. Even at the pump-down pressure of $\sim 10^{-3}$ torr (1 μ), at which the surfaces were outgassed, about 10^{18} particles per cm^2 per second bombard the surface, and it seems

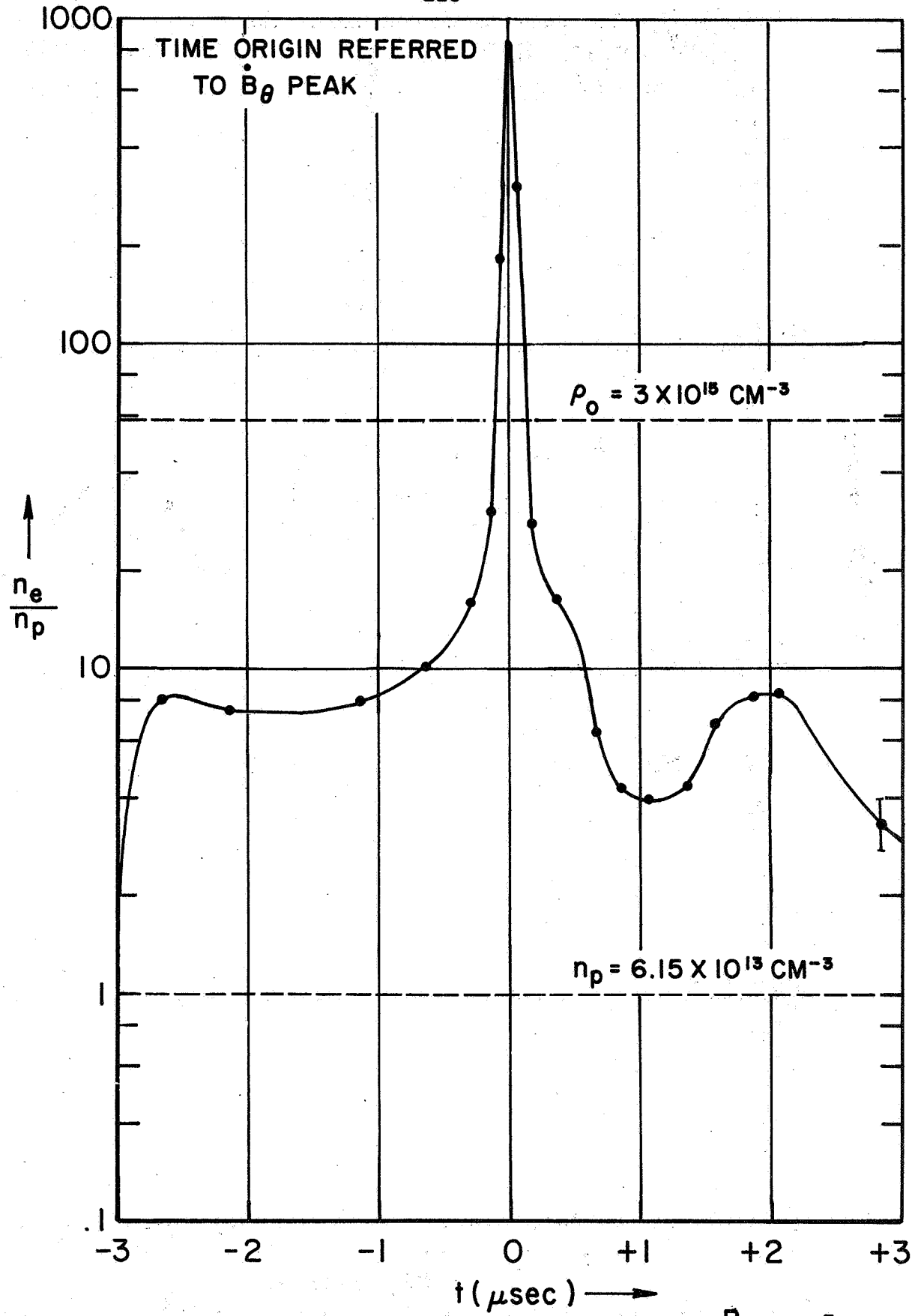

ELECTRON DENSITY AT CATHODE, ($\frac{R}{R_0} = .5, \frac{z}{h} \cong 0$)

FIGURE 6-40

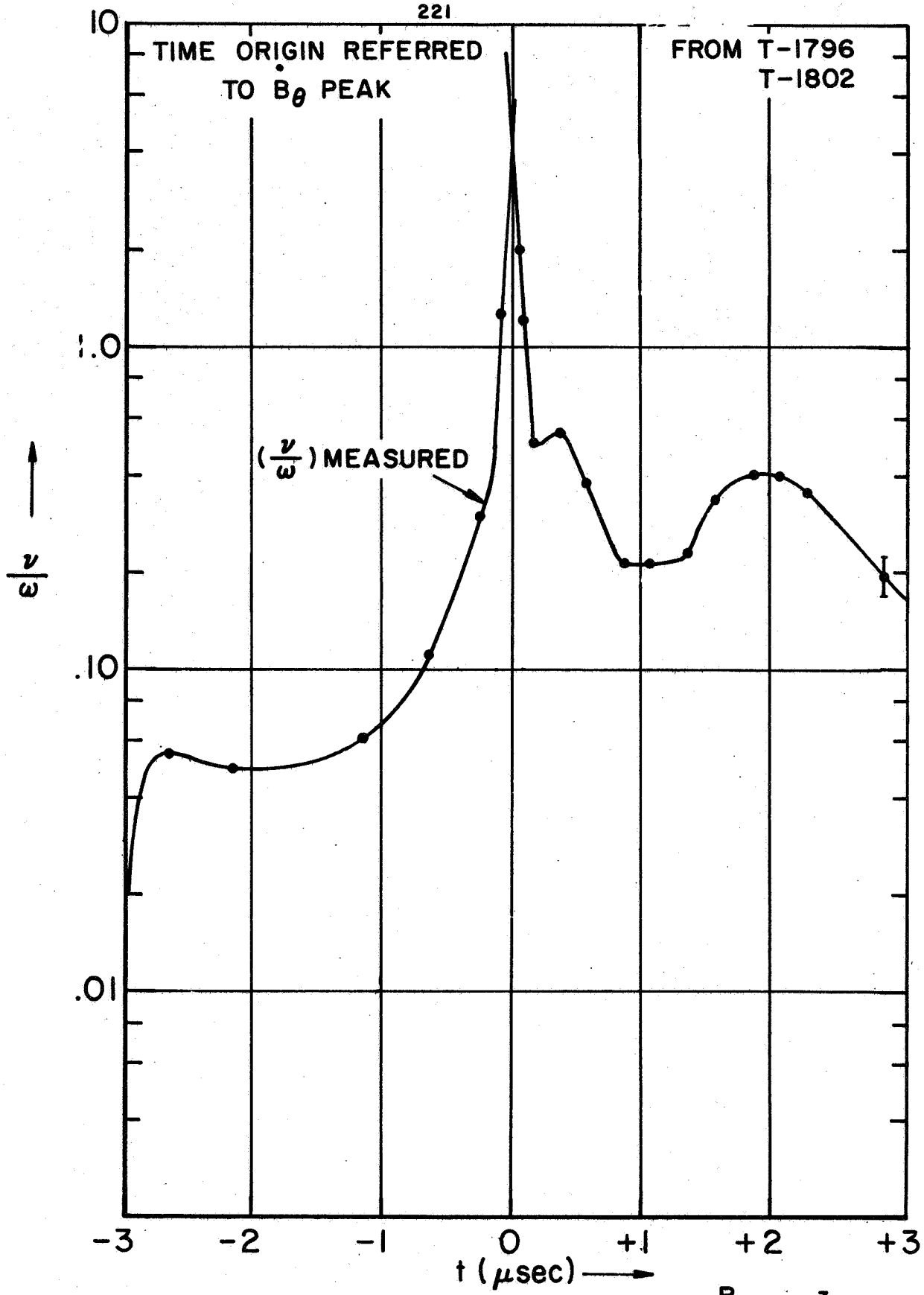

COLLISION FREQUENCY AT CATHODE, $(\frac{R}{R_0} = .5, \frac{z}{h} \cong 0)$

FIGURE 6-41

reasonable that a fraction of these will be absorbed. The high temperatures and particle energies associated with the current sheet would be sufficient to loosen some of this occluded material while the current sheet is passing over the probe.

A few remarks on the last several data figures are in order before passing. The axial survey of Fig. 6-35 showed $|R|$ to have two generally constant plateau regions separated by a linear decrease in amplitude when the sheet passed. Fig. 6-37 shows that this feature occurs for both types of window surface, with the greater damping from the softer surface as would be expected. The peaked profile in this linear region is not common to both, however, and illustrates how the same peaked electron density profile appears under two conditions of collisional damping. The more weakly damped trace of set B, obtained with the quartz surface, exhibits less sensitivity to density changes just as the theoretical curves of Fig. 6-4 predict. Thus softer, more volatile horn coatings appear to exert a rather unique biasing effect, through the mechanism of a controllable damping factor, which shifts the operating domain further from the saturation density limits and shows up the electron density peak in a particularly graphic way. In subsequent experiments, employing deliberately soft window coatings, this biasing effect was exaggerated to the extreme of near total damping with dramatic results. This method of tailoring the probe output is a useful technique for easy visualization of the electron density profile, and can furnish useful qualitative information without detailed data reduction. On the other hand, the absence of a spike does not mean the absence of a peaked density profile, cf Fig. 6-37b. The phase measurable is a much better visual guide to

the profile than is $|R|$, and the axial gradation of $|R|$ data in Fig. 6-35, for example, must be interpreted with this in mind. ρ data, such as Fig. 6-23b, show the electron density profiles to be consistent with the known variations of the sheet structure with position in the chamber.

It should also be noted that φ_R as well as $|R|$ has a predicted sensitivity to collisional damping (cf Figs. 6-4 and 6-5). Thus the phase measureable ρ should exhibit distinctly different behavior for different window surfaces, instead of simply incorporating different values for $|R|$. This is seen to be the case in Fig. 6-37, where ρ from set A makes the larger excursions even though incorporating the smaller $|R|$.

The electron density profile of Fig. 6-40 shows a number of interesting features. The density remains above critical for all times of interest, including the regions behind the sheet, so that the plasma is always strongly reflecting. The preionization is around 10%, and the ambient density line is shown for reference. The preionization calculated from many similar data records generally fell within the limits bracketed by the several curves of Fig. 6-38. The maximum density of $\sim 5\times10^{16}\text{cm}^{-3}$ was estimated by extrapolating the curve, since densities above $\sim 10^{16}\text{cm}^{-3}$, corresponding to $\varphi_R > 170^\circ$, are difficult to calculate accurately. The maximum electron density is thus over an order of magnitude higher than the ambient density, indicative of compression and possibly multiple ionization. The rapid drop in n_e behind the sheet, implying a corresponding drop in n_I , strongly suggests that the bulk of the ionized argon has been swept up by the current sheet. Referring to Fig. 6-40 then, the sequence of events recorded

by the probe can be roughly divided into five time periods: the precursor event, which ionizes about 10% of the ambient gas; a relatively quiescent period, during which the density slowly increases as the sheet approaches; the interior of the current sheet, marked by a rapid buildup in electron number density; the subsequent decline in n_e, indicative of efficient sweeping; and finally a gentle density swell in the downstream region of the current sheet. This second density maximum is about 1% of the first, and corresponds to a small pulse of current which the B-probes also detect, cf. Fig. 4-15. In fact the entire n_e profile exhibits many points of similarity with the J_z profile of Fig. 4-15, even to the extent of duplicating the small shoulder at the rear of the current sheet. It should be noted, however, that the number density profile is generally narrower than the current density profile. This will have important consequences.

Electron Temperature Calculations. If the measured ν/ω values represented only the electron-ion encounters in the plasma, the electron temperature profile could be calculated directly, using the well-known coulombic cross section [eq. (B-8)]

$$\frac{\nu_{ei}}{\omega} = 4.61 \times 10^{-17} \frac{n_e(cm^{-3})}{[kT_e(eV)]^{3/2}} \qquad (6\text{-}111)$$

where $\ln \Lambda$ has been taken to be 7.0. The direct approach is ruled out in this case since ν/ω also contains an unknown contribution from the impurity term, and the sputtering characteristics of the quartz window are not well enough known under the conditions of the experiment to permit quantitative compensation. The measured

collision frequency actually includes three contributions

$$\frac{\nu}{\omega} = \frac{\nu_{ei}}{\omega} + \left(\frac{\nu_{en}}{\omega}\right)_{imp.} + \left(\frac{\nu_{en}}{\omega}\right)_{A} \qquad (6\text{-}112)$$

where the third term represents electron-argon neutral collisions. From Appendix B, the Maxwell-averaged expression

$$\left(\frac{\nu_{en}}{\omega}\right)_{A} = 6.68 \times 10^{-8} \left[kT_e(eV)\right]^{3/2} \qquad (6\text{-}113)$$

shows this term to be directly proportional to the electron temperature, but orders of magnitude smaller than the measured ν/ω values for any reasonable temperature. Hence only the electron-ion and electron-impurity contributions need be considered for the present.

It has already been shown that ν/ω is independent of horn surface, and hence of boiled off impurity contributions, until current sheet arrival at the probe position. It therefore follows that the precursor event is not effective in ejecting impurity atoms from the probe surface, and thus that the 2nd term of eq. (6-112) can be neglected for the first few microseconds. It has also been shown that precursor ionization levels far ahead of the current sheet are around 10^{-1}, whereas electron-ion collisions dominate over electron-neutral collisions at the much lower levels of about 10^{-3}. This reconfirms that the third term in eq. (6-112) can be neglected compared to the first. Thus electron collisions behind the precursor are coulombic, and the electron temperature far ahead of the sheet can be accurately estimated from eq. 6-111. Using measured values of ν/ω and n_e, the electron temperature

immediately behind the precursor is

$$kT_e\Big)_{-2.75\,\mu s} \cong 0.57 \quad eV \tag{6-114}$$

This value is not too far from the 1 eV values anticipated in the sheet, and so as a first approximation consider T_e to be constant at this value. Then ν_{ei}/ω can be calculated from the n_e profile, and the result is shown in Fig. 6-42. Notice that ν_{ei}/ω is less than ν/ω everywhere except the initial match point, as it should be, since the difference between these curves represents the impurity, or effective electron-neutral, contribution. This difference quantity is plotted separately in Fig. 6-43, for clarity. The initial linearity of ν_{en}/ω implies an exponential growth rate of impurity concentrations as the current sheet approaches the probe, a reasonable behavior. The latter parts of this curve, for positive times, also seem reasonable. The portion near t = 0, however, corresponding to the center of the current sheet, seems anomalous. The current sheet has been shown to drive impurities off of the probe surface, which do not ionize immediately. Therefore the expectation is for a peaked profile of ν_{en}/ω, not the reverse. Note, however, that this peculiar ν_{en}/ω profile is a direct consequence of the assumed constant temperature profile. If T_e is assumed to increase through the sheet, which is of course a more realistic approximation, then ν_{ei}/ω will be correspondingly reduced (cf eq. (6-111)) and ν_{en}/ω increased.

Thus a graphical construction is indicated, to yield an estimate of T_e. It might appear at first glance that a T_e profile can be selected rather arbitrarily, but this is not the case.

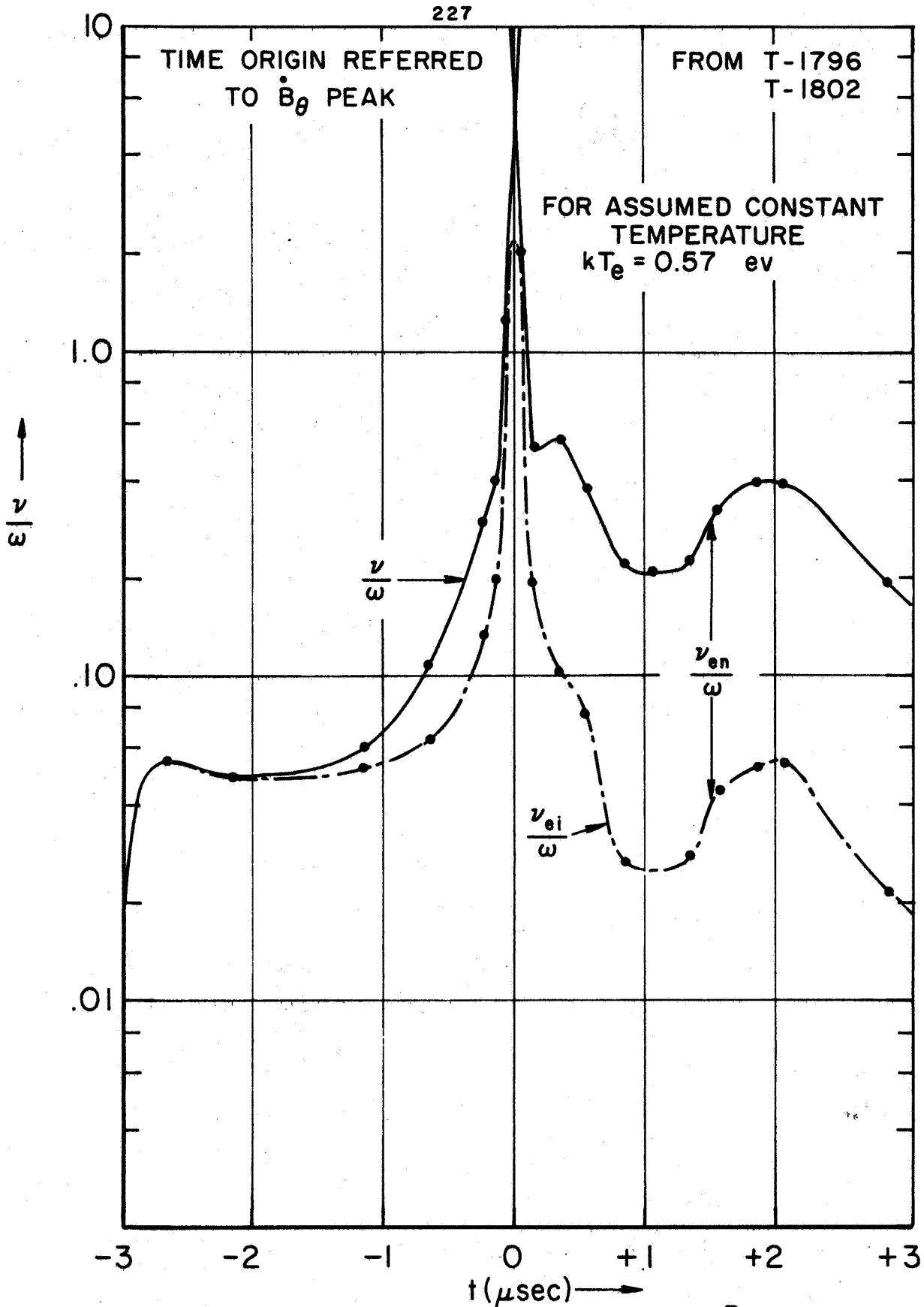

COLLISION FREQUENCIES AT CATHODE, ($\frac{R}{R_o} = .5, \frac{z}{h} \cong 0$)

FIGURE 6-42

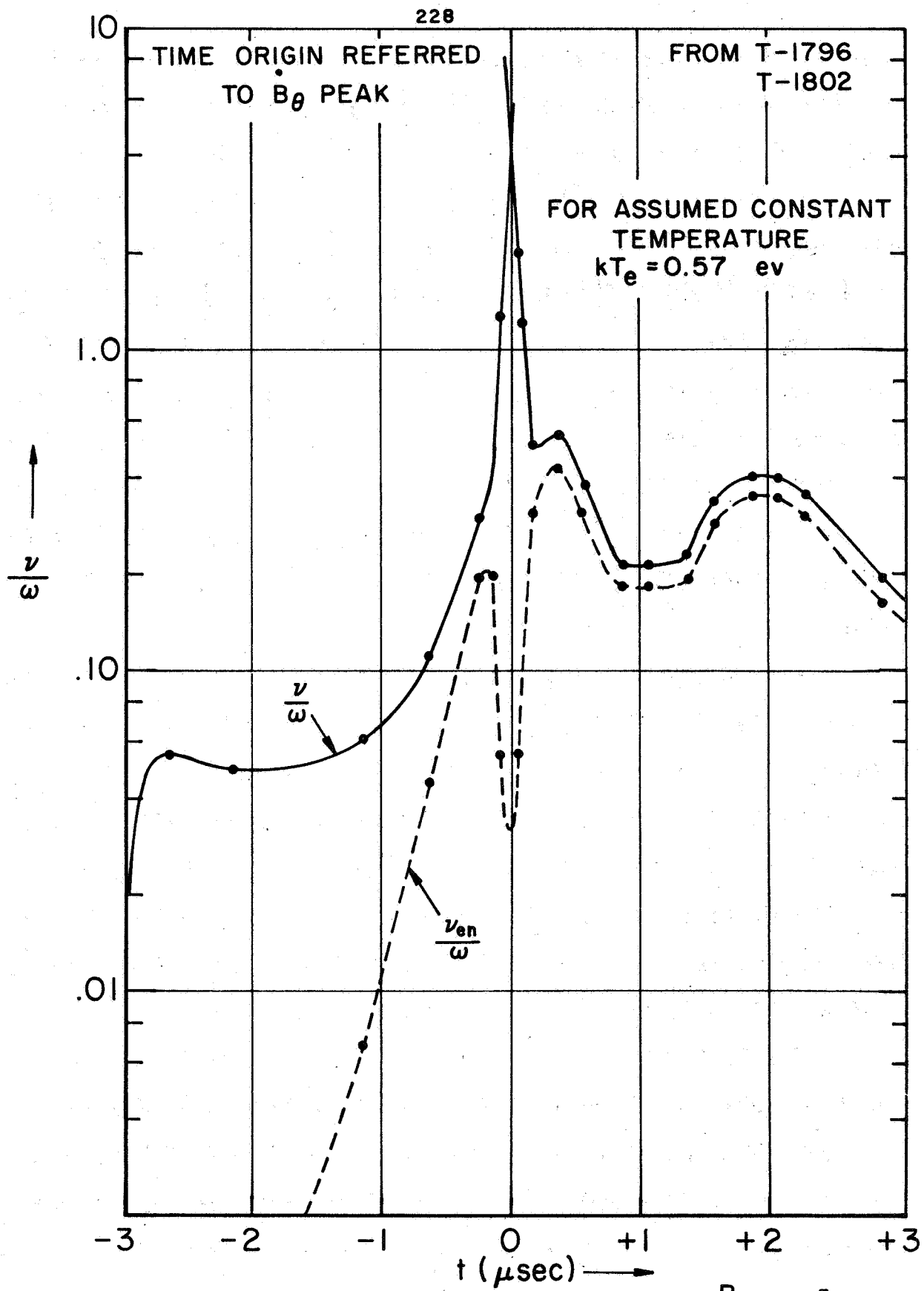

COLLISION FREQUENCIES AT CATHODE, ($\frac{R}{R_0} = .5, \frac{z}{h} \cong 0$)

FIGURE 6-43

With the five mild constraints that (1) ν_{en}/ω have a peaked profile in the current sheet, (2) ν_{ei}/ω retain a reasonably peaked profile in the sheet, to reflect the greatly increased electron density, (3) T_e increase in a reasonable way at least half way through the sheet, (4) $kT_e = 0.57$ at $-2.75\ \mu s$, (5) $\nu/\omega \cong \nu_{ei}/\omega + \nu_{en}/\omega$, it is a straightforward matter to show that T_e has the unique profile given in Fig. 6-44. The corresponding collision frequencies are shown in Fig. 6-45, and the argon neutral contribution calculated from eq. 6-113 is shown in Fig. 6-46. The fact that T_e exhibits sharply peaked behavior in the sheet, reaching a maximum of about 1.5 eV, is consistent with the other experimental data and conforms closely to previous estimates.

Assignment of Error Bars. The profiles of Figs. 6-38 to 6-45 are felt to represent adequately the fundamental electron properties of the plasma, and to offer a method for compensating the troublesome effects of probe impurities. The rather elaborate data reduction necessary to combat this problem would perhaps be unnecessary if strictly local measurements were not the goal of the experiments. Had transmission experiments been possible, for example, the effects might have been less severe.

Due to the large number of mathematical operations on the raw data, and the large number of experimental factors entering in complicated ways, it is difficult to assign error bars with confidence. Repetition afforded one indication of errors, and the multiple overlay traces (cf Fig. 6-35) and superimposed profiles (cf Figs. 6-38 and 6-39) allow certain error estimates to be made. Another method involved data perturbation, in which an

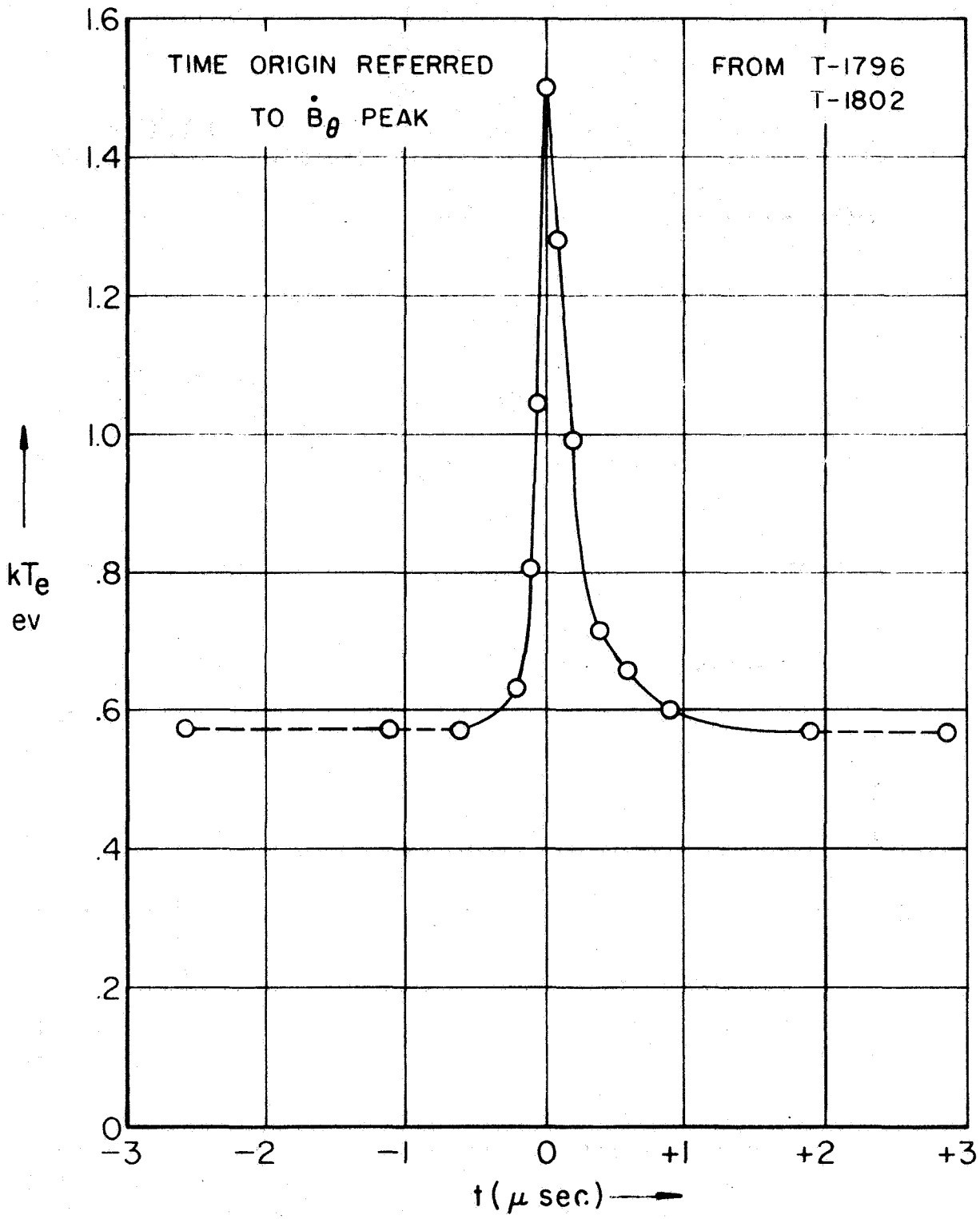

ELECTRON TEMPERATURE AT CATHODE, ($\frac{R}{R_o}$=.5, $\frac{z}{h}\cong 0$)

FIGURE 6-44

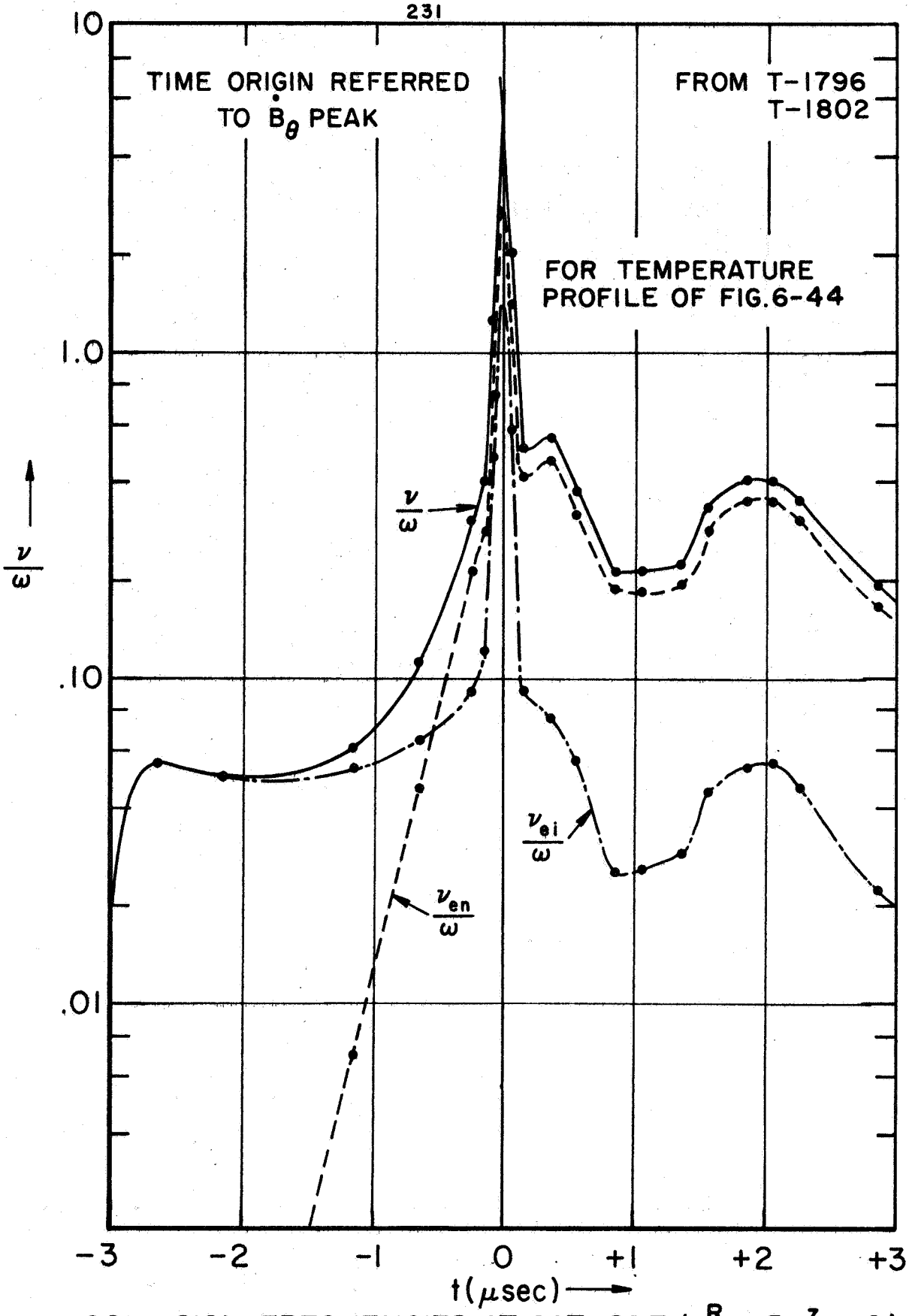

COLLISION FREQUENCIES AT CATHODE, ($\frac{R}{R_o}$ = .5, $\frac{z}{h} \cong 0$)

FIGURE 6-45

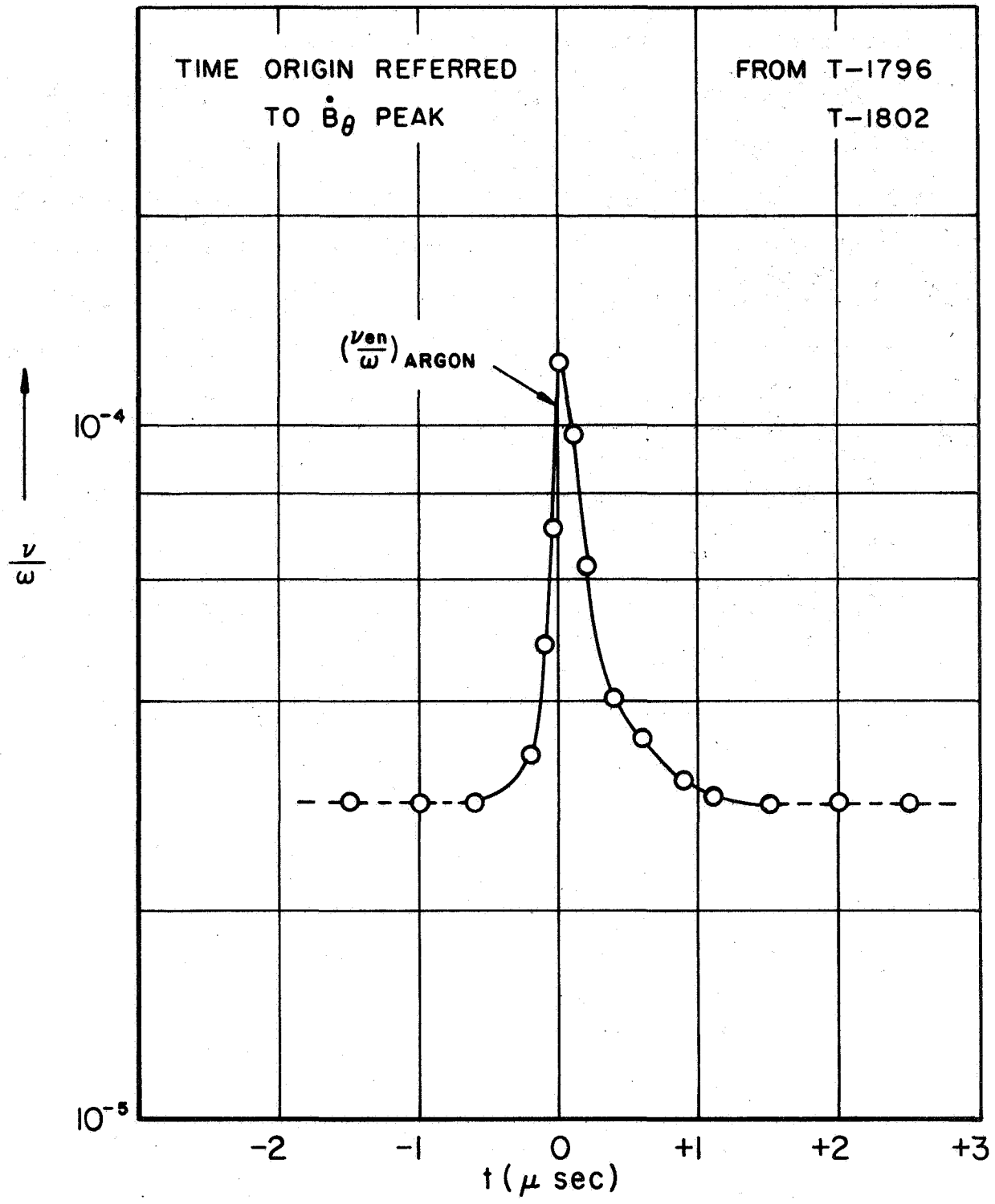

COLLISION FREQUENCY AT CATHODE , ($\frac{R}{R_0}$ =.5, $\frac{z}{h} \cong 0$)

FIGURE 6-46

assumed small change in raw data was traced through the calculations at various stages in the analysis to determine its ultimate influence. Even so, precision was elusive.

The electron density profile is probably correct within about 20% except near t = 0, where the indicated values may possibly be in error by a factor of two or three. The measured values of ν/ω share about the same degree of accuracy. The temperature profile is probably more accurate than the absolute values involved. In particular, the initial value with which the graphical construction was started may be in error by as much as 50%. This error, if it exists, would probably mean the indicated value of $\sim$ 0.6 eV is too low.

In the following chapter these electron parameters are combined with the field measurements of Chapters IV and V to provide further information on interior processes in the current sheet.

Chapter VII

DISCUSSION AND THEORETICAL MODELS

7.1 Introduction

In this chapter the experimental data is examined within the framework of various simplified models of the current sheet, in an attempt to identify some of the physical mechanisms and properties of interest to propulsion.

To review, the current sheet has been probed at half radius, the midpoint of its 10 cm trajectory to the chamber axis. The sheet was found to be slightly under 4 cm wide at this position, as defined by the sensible axial current density J_z, with a nearly constant propagation velocity of $\sim 2.5 \times 10^4$ m/sec. The magnetic field was found to be almost entirely azimuthal, increasing smoothly and monotonically through the sheet. The interior electric field was found to have both axial and radial components, the former being small in the sheet coordinate system.

The electron density was found to have a very steep profile at maximum J_z, and a rapid falloff to the back of the sheet. The electron temperature was computed to reach a maximum value of $\sim$ 1.5 ev at maximum current density, but was not a particularly sensitive function of position. The electron-ion collision frequency was consequently a steep profile through the sheet, and a relative importance of charged specie collisions can be anticipated near maximum current. In particular, since ν_{ei} peaks in the sheet while B_θ increases almost linearly, a variable Hall parameter can be expected in the current sheet,

and interior regions may develop where scalar and Hall currents participate in different degree.

7.2 Discussion of Models

Compared to the 2 mm spatial resolution of the probes, the current sheet width was some 20 probe diameters. If calculations are made at, say, 0.1 μ sec intervals, the data points are spaced $\sim$ 2.5 mm apart in the sheet and each can be regarded as the average value over a small volume $\sim$ $(2.5\ \text{mm})^3$, which contains at least 5×10^{13} particles. Since the calculated mean free paths are a small fraction of a mm under the conditions of the experiment[14], the medium is properly described as continuum and fluid concepts are appropriate to the problem.

Consider a coordinate system moving with the sheet. We can envisage the flow entering the front of the sheet at sheet velocity and there encountering crossed electric and magnetic fields. The entering plasma is $\sim$ 10% ionized from precursor photoionization (Chapter VI), and the fields at the front of the sheet are small, just measurable by definition. The three constituent fluids of electrons, ions, and neutrals, which are comingled when they enter the sensible sheet, begin to respond variously to the electromagnetic and gas dynamic forces which are developing. The ion stream initially begins a simple deceleration in the opposing E_r field, and simultaneously gains an axial component of velocity along E_z. The gyro-radius of an ion

$$r_i = \frac{m_i u_i}{|e| B_\theta} \tag{7-1}$$

is several meters at this forward position in the sheet, and hence B_θ is relatively unimportant. To put it another way, the average ion would be only slightly deflected by the magnetic field even if it moved on a collisionless trajectory and was unhindered in its turning motion.

The neutrals, feeling no electromagnetic forces, would maintain their incoming velocity in the absence of collisions. However, they are tightly collision-coupled to the decelerating ion stream, since any significant velocity difference between the two streams would result in greatly increased streamwise collision rates, and a corresponding velocity adjustment. As the ion and neutral streams move further into the sheet, the combined effects of decreasing velocity and increasing magnetic field render the ions, and thereby the neutrals, increasingly vulnerable to magnetic field deflection, since both effects reduce the ion gyro-radius. In the back of the sheet, where the ions have lost much of their streaming energy and B_θ is a maximum, the ion gyro-radius is estimated to decrease to less than 1 cm and magnetic field influence on the heavy particles can be important in this region. The general picture is thus one of a radially decelerating ion stream, which at the same time acts to brake the streaming neutrals and develops axial fluid motion appropriate to the applied E_z field and deflection in B_θ .

A model which satisfactorily treats these basic mechanisms, while also incorporating a proper description of the nonlinear collision phenomena, gas dynamic effects such compression and

rarefaction, and characteristic lengths involving the discharge chamber and current sheet dimensions would be very difficult to formulate and solve in any generality. In the remainder of this chapter various simplified models, which incorporate one or more of the features mentioned above, will be examined to gain some insight into the physics of the problem; e.g. regions of scalar or Hall current, the importance of ion conduction to the overall current pattern, variation of ionization through the sheet, ionization processes, and mechanisms of gas acceleration.

7.3 Collisionless Model of Ion Deceleration

Consider a very simple model of the ion fluid, wherein the motion of a typical ion is considered representative of the mean fluid motion. As this ion decelerates in the E_r field, it under goes collisions with typical neutrals, braking them as discussed above. The net effect of such collisional coupling is to slow an average ion less than would be predicted from collisionless deceleration in E_r. On the other hand the ion is increasingly turned by B_θ as it decelerates, and consequently loses more forward velocity than would be predicted from E_r alone. Thus the two effects are in opposite directions, and for a first approximation to the radial ion motion we will neglect both and examine the effects of collisionless deceleration in E_r.

Consider an ion entering the sheet at velocity U_s in the $+\hat{r}$ direction of Fig. 4-2. The potential difference retarding the ion is given by

$$\Delta\varphi = \int_0^{\hat{r}} E_r \, dr \qquad (7\text{-}2)$$

since E_r is zero ahead of the sheet. Assuming U_s to be constant over a distance Δr comparable to the sheet width (cf Fig. 4-5), and assuming the invariance of E_r with transit time over the probe, E_r vs t data profiles can be interpreted as radial probe traverses through the sheet. Invoking the Galilean transformation $\Delta r \cong U_s \Delta t$, the ion velocity is obtained in current sheet coordinates:

$$u_i = u_s - \left[\frac{2|e|u_s}{m_i}\int E_r\, dt\right]^{\frac{1}{2}} \qquad (7\text{-}3)$$

From this equation, using measured values of U_s (Chap. IV) and $E_r(t)$ (Chap. V), the radial ion velocity can be calculated at both axial positions (cathode and midplane) as a function of position through the current sheet. The results are given by the solid curves of Figs. 7-1 and 7-2, and show a significant difference between the two probe positions. In both cases the ion decelerates to $\sim 1/2\ U_s$ at $t = 0$, which we can define for convenience as the center of the sheet, but thereafter the reversed electric field at the cathode (cf Figs. 5-6a and 5-7) causes the ion to leave the sheet with a velocity comparable to U_s, while at the center plane the ion continues to decelerate. Recalling that the anode regions of the sheet were earlier rejected for detailed study because of the diffuse, irreproducible fields there, the implication is that an ion near the chamber midplane can receive a very considerable velocity increment in passing through the current sheet, perhaps even being entrained, but that near an electrode the sheet is not very efficient at accelerating the ambient gas.

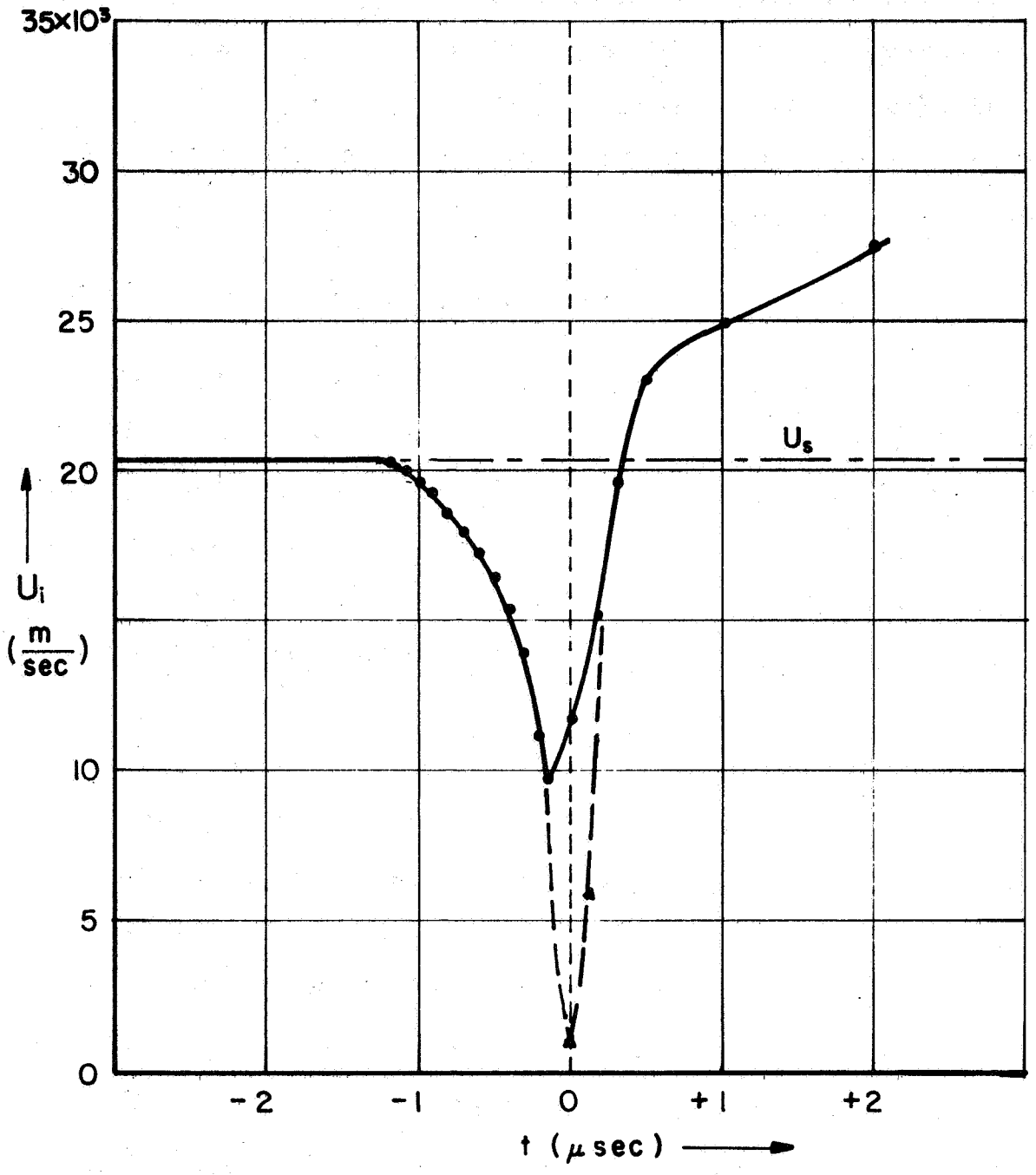

ION VELOCITY AT CATHODE

FIGURE 7-1

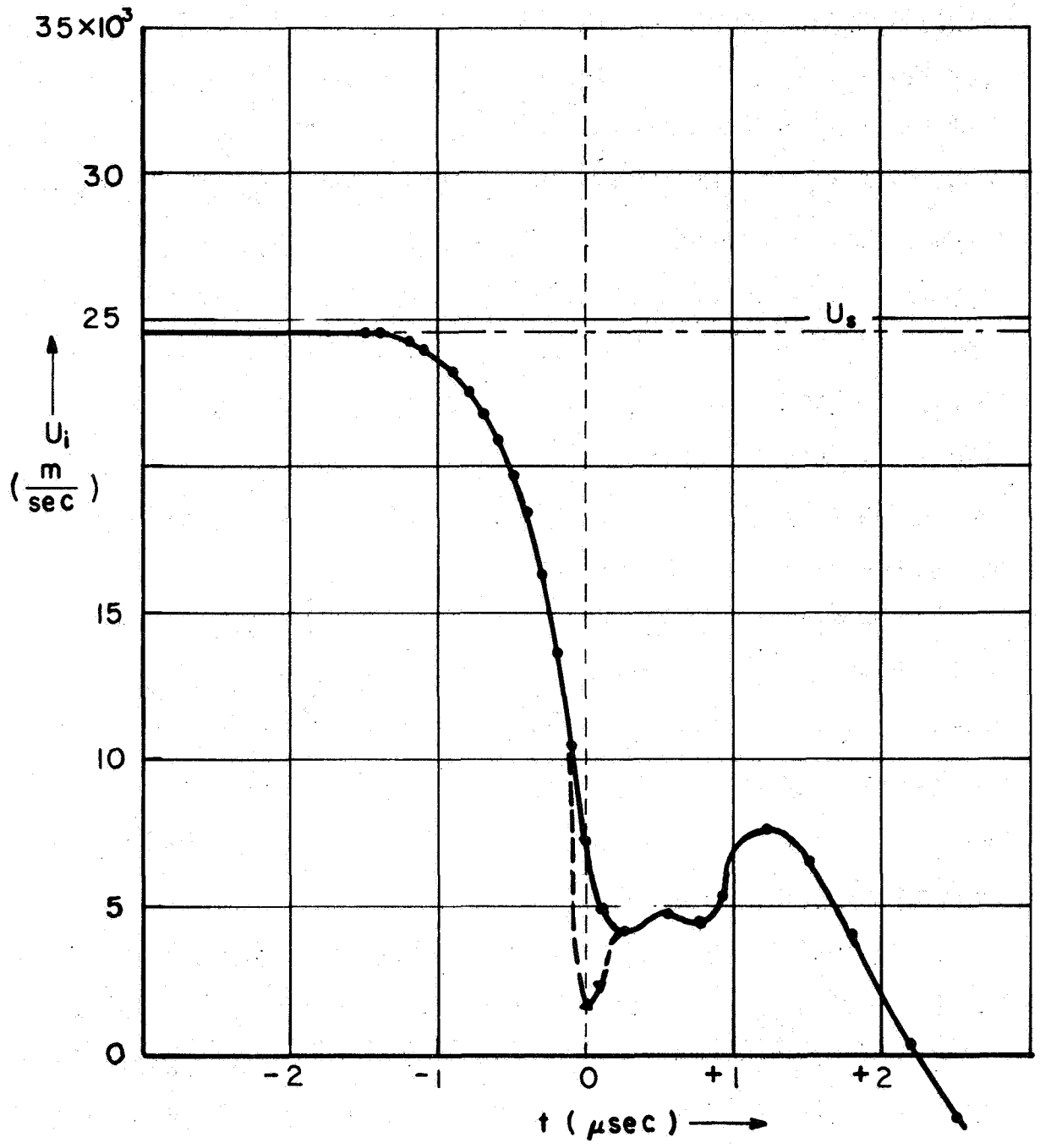

ION VELOCITY AT MIDPLANE

FIGURE 7-2

7.4 An Ionization Model

The possibility of gas entrainment in the current sheet, suggested by the radial ion trajectories of Figs. 7-1 and 7-2, reinforces earlier inferences based on electron density profiles (Chap. VI). Other studies[13] have shown that current sheet trajectories can be predicted rather well by simple snowplow models, although there is some question whether total mass entrainment can be deduced from agreement with snowplow predictions[22]. If there is a region of entrained gas in the sheet, the ion velocity profiles should reasonably reflect this fact. A check on the validity of the profiles of Figs. 7-1 and 7-2 can be made by invoking a simple model of mass continuity and the quasi-neutral approximation.

It was shown in section 5.5 that the measured electric field divergence was consistent with a very small charge imbalance, $(n_i - n_e)/n_e < 10^{-7}$. Thus for purposes other than the Poisson equation, n_i can be assumed equal to n_e to a very good approximation and measured electron density profiles used equally well for ion density.

Define the electron (or ion) density ahead of the sheet as n_{e0} (or n_{i0}), as determined by the early precursor event (Chap. VI). As the ion stream decelerates in the sheet, assume that the local ion density increases to satisfy steady flow mass continuity:

$$n_i = n_{i0} \frac{u_s}{u_i} + n_{is} \tag{7-4}$$

where the first term represents deceleration and the second term is a "source" term, to allow for increasing ionization. Consistent with our assumption that the neutral stream is also decelerated, an equivalent expression can be written for the neutrals

$$n_n = n_{no} \frac{u_s}{u_i} - n_{is} \tag{7-5}$$

with the "source" term in this case just the negative of the ion source term. With the usual definition of the ionization fraction,

$$\alpha = \frac{n_i}{n_i + n_n} \tag{7-6}$$

the last three equations can be combined to give

$$\alpha = \frac{n_i}{N_0} \frac{u_i}{u_s} \tag{7-7}$$

where $N_0 = n_{i0} + n_{n0}$ is just the ambient gas density, 3.55×10^{15} cm^{-3} in this case. Rewriting the ion fraction in terms of the nondimensional electron density, we obtain

$$\alpha = \frac{1}{58} \times \left(\frac{n_e}{n_p}\right) \times \frac{u_i}{u_s} \tag{7-8}$$

α is plotted in Fig. 7-3 for both axial positions, using measured values of (n_e/n_p) and the ion trajectories of Figs. 7-1 and 7-2. The ionization level rises slowly from $\sim$12% ahead of the sheet, where the calculation was started, to $\sim$17% less than half-way into the sheet; then it rises quite rapidly to large values near the maximum current density, and falls more slowly behind the sheet. Ionization levels somewhat

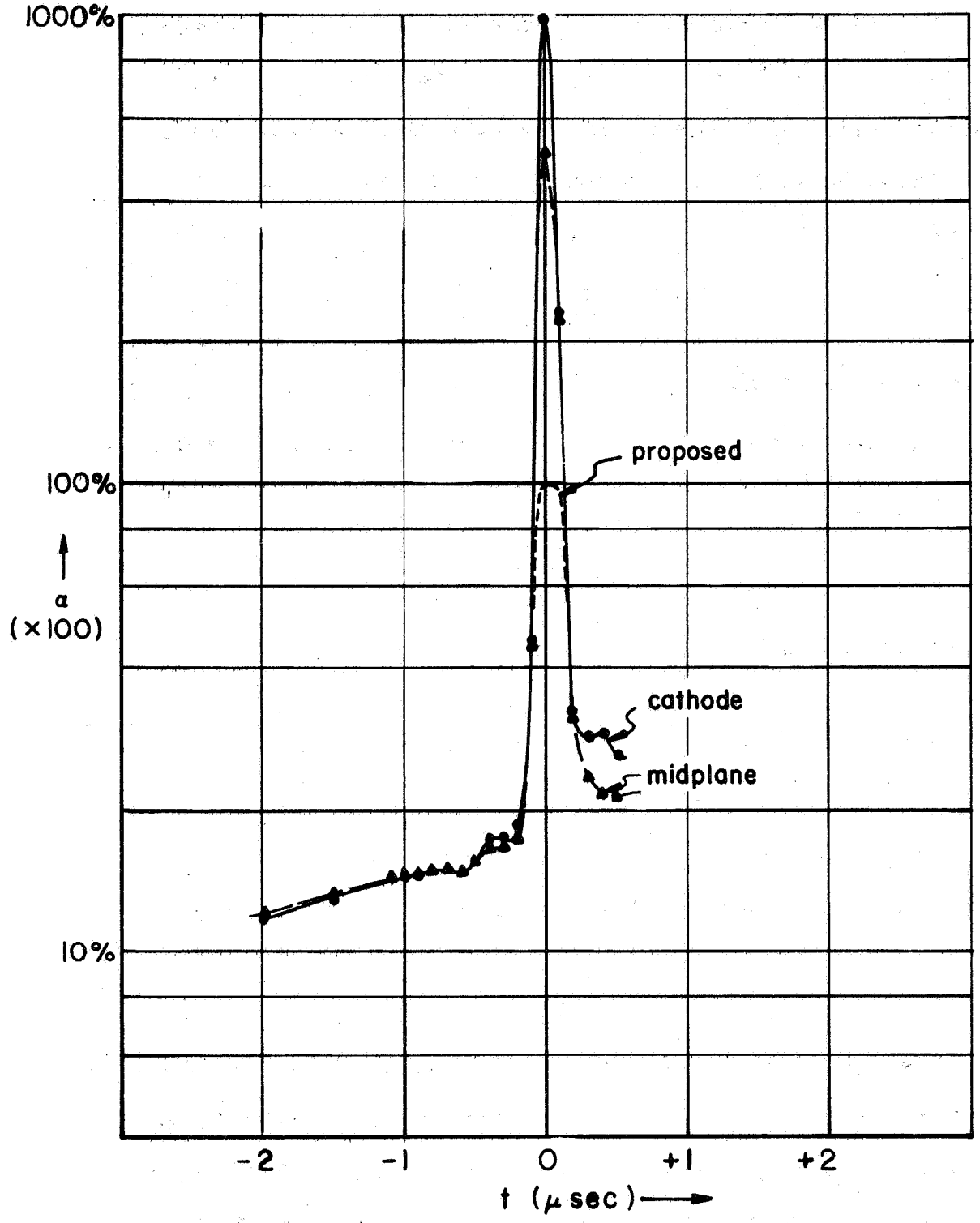

IONIZATION PROFILES, MIDPLANE & CATHODE

FIGURE 7-3

larger than 100% might be anticipated in the sheet, from multiple ionization, but certainly nothing of the order of the 1000% predicted by the calculation. This anomalously high value probably indicates a failure of the steady, collisionless ion model adequately to represent ion velocities in this region, and the indicated correction is toward lower velocities in the center of the sheet. In particular, if the ionization at maximum current density is limited to $\sim$ 100%, the dashed correction curves of Figs. 7-1, 7-2 and 7-3 are obtained. These may be regarded as first order corrections to the solid curves, and may be attributed to either of two effects: the randomization of ion streaming energy via collisions, or the unsteady accumulation of mass in the sheet itself. In the former case, we refer to ion collisions with entrained or nearly stationary particles (i.e. ions, since the ionization is high) in the sheet, analogous to the randomization which accompanies the compression of gas flow through a shock front. This is to be distinguished from the ion-neutral collision phenomena which we have previously mentioned, and the inference is that the ions in the center of the current sheet are properly to be considered in collision dominated flow. This model would agree with the indicated high concentration of ions at $t = 0$ from the microwave data, and it also suggests that the ion temperature may exceed the electron temperature in this region. A randomization of ion streaming energy by collisions with slower moving or entrained ions would be a much more efficient process than ion energy equilibration with the light electrons. Since ions enter this region with 30-40 ev

of their original 100 or so ev of streaming energy, the ion temperature could approach 50% of this value[13], $(T_i)_{max} \backsim 15 - 20$ ev. This is an order of magnitude higher than the 1.5 ev maximum value calculated for T_e in Chapter VI.

The question of how much mass has actually been entrained cannot be answered on the basis of the present data, since detailed studies of the radial progression of the various profiles particularly pressure, are needed. It is possible that local flow conditions in the high density region are approximately steady, i.e. that only a small fraction of the mass flow is actually accumulated. The distinction is not a vital one to propulsion interest, since the difference between total gas entrainment, wherein U_i actually goes to zero in the sheet, and efficient gas acceleration, wherein U_i is small but non-zero at the back of the sheet, is small in terms of total momentum. In our case the ion stream emerges from the center-plane sheet with $\backsim 1/5$ of its entering velocity, corresponding to a "sweeping" efficiency of 80% and an acceleration to 2×10^4 m/sec in the laboratory.

The fact that the ion accelerates somewhat in leaving the high density regions of the sheet implies that a rarefaction occurs there. This would be consistent with the low charge densities and electron temperature at the back of the sheet, from Chap. VI. Thus, within the limitations of the model, the ion stream appears to encounter a compression-rarefaction wave imbedded in the sheet, which participates in the gas acceleration process. This description is suggestive of a peaked shock

wave, a common gas dynamic wave in cylindrical geometries. The similarity between the cathode and centerplane ionization profiles is interesting since the sheet velocity, number density, electric fields, retarding potentials, sweeping efficiencies, etc., are different for the two locations. They combine together in such a way as to describe a current sheet of fixed ionization profile.

We will return to the question of ionization mechanisms in a later section.

7.5 Current Conduction Models

We now wish to examine modes of current conduction in the sheet. Consider the electron fluid entering the sheet at velocity U_s. Because of the mass ratio, $\sim 10^{-5}$, electrons are much more easily deflected by the magnetic field than are ions, and at the first measurable values of B_θ the electron gyro-radius is calculated from eq. (7-1) to be a small fraction of a millimeter. Electrons are also undergoing momentum exchange collisions with ions at the rate of $\sim 10^{10}$ sec^{-1} as they enter the sheet, from Chapter VI. Therefore it is unrealistic to treat electron motion in a collisionless, electrostatic framework in any regions of the sheet, and we must look to continuum models.

In a continuum framework the fields and particle velocities are related by an Ohm's law for the plasma. The simplest serviceable approach is perhaps through the Langevin equation (B-2) which incorporates collisional and magnetic field effects into

an effective equation of motion for electrons in a viscous, anisotropic medium. This equation yields a tensor form for σ which is discussed in some detail in Appendix B under the heading Tensor Conductivity Models. Both electron and ion current components are examined, and it is shown that Hall currents, or cross-field charge motions, are dominant for Hall parameters greater than unity. It is further shown that ion participation in the total current density is favored to develop as Hall conduction itself becomes important, and we next examine Hall parameters in the current sheet.

The electron Hall parameter [eq. (B-17)] is the quantity of interest in the analysis to follow, and can be calculated from the electron ion collision frequency, modified for this limit as discussed in Appendix B, and the magnetic field data. Ω_- is plotted in Figs. 7-4 and 7-5 for both axial positions. The increasing values of Ω_- from front to back of the sheet reflect the influence of the rising B field, and the Hall parameter is depressed nearly to zero in the center of the sheet because of the high electron density and electron-ion collision frequency there. The similarities in Ω_- for the two axial positions near the front of the sheet reflect the similar profiles measured for n_e and B_θ, and likewise the lower values of Ω_- at the rear of the sheet at midplane result from the higher electron and current densities.

From these data, the current sheet is seen to have two well defined regions where the electron Hall parameter is small and two regions where it is large. It is therefore useful to

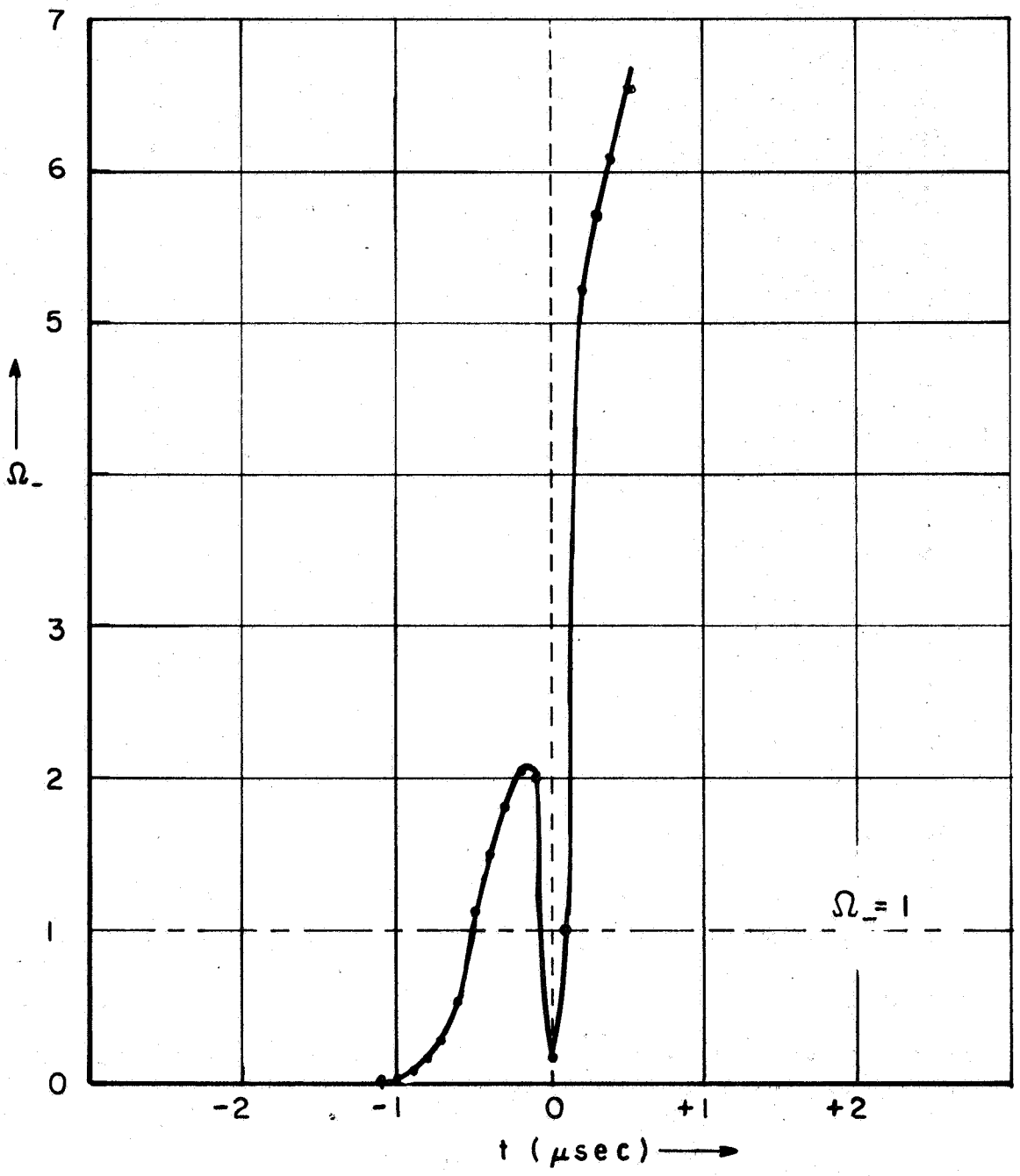

HALL PARAMETER AT CATHODE

FIGURE 7 - 4

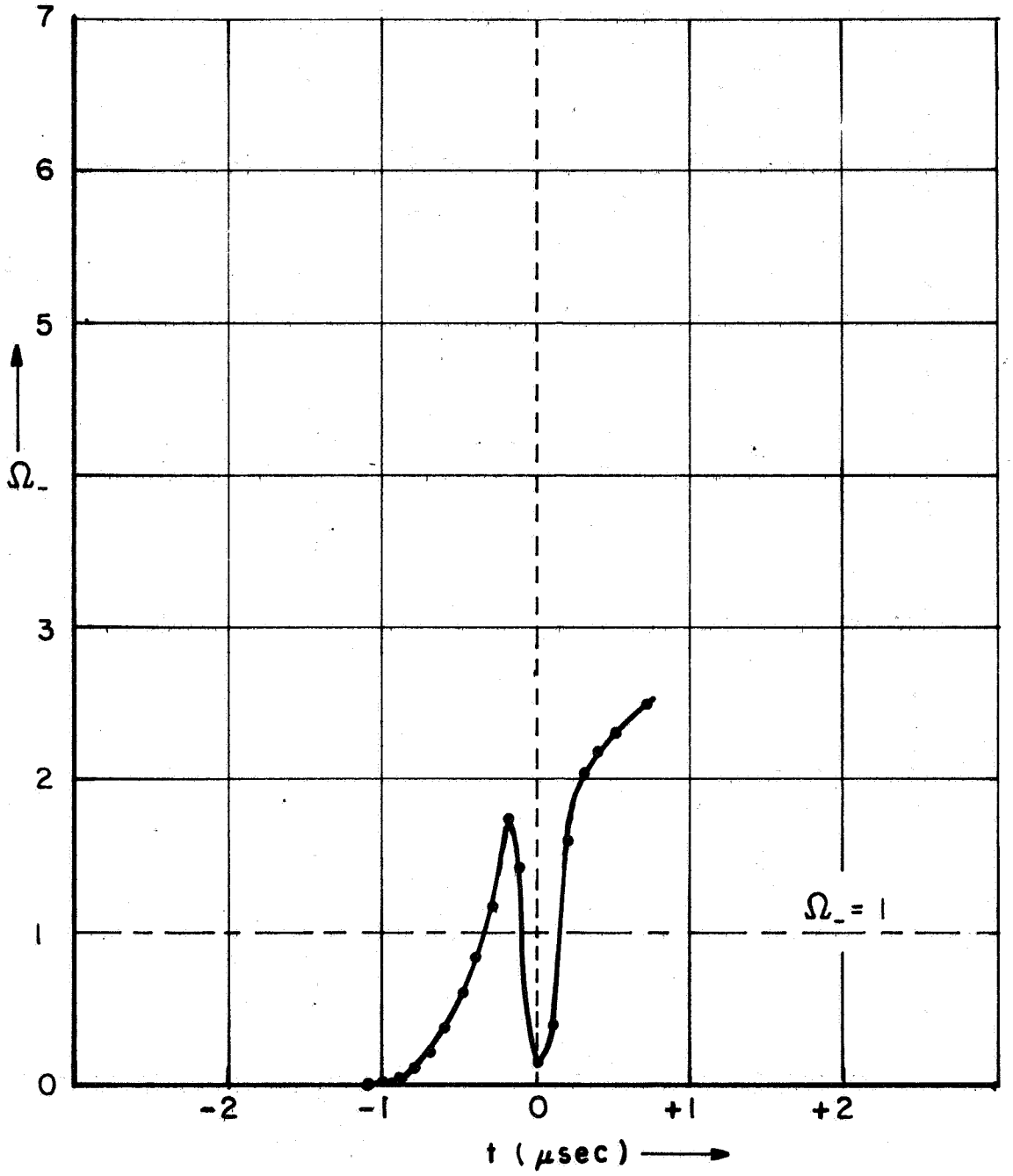

HALL PARAMETER AT MIDPLANE

FIGURE 7 - 5

subdivide the current sheet into four zones where different current mechanisms can be expected to predominate. In the first zone, the first cm or so into the sheet, the B_θ field is small enough that electron-ion collisions determine the electron motion. Scalar currents should be conducted here, and electrons entering the sheet should initially follow the resultant electric field. With B_θ increasing faster than n_e, the particles move into the second zone, less than 1 cm wide, where the Hall parameter is greater than unity. Here substantial Hall currents can be anticipated, and ion conduction may become significant. Zone three, about the same width, brackets the maximum current density and because of the high electron density and collision frequency, electron currents should be large and scalar. Finally, moving to the back of the sheet, the Hall parameter becomes and remains large, and this portion of the sheet should carry predominantly Hall currents with possibly large ion participation. Thus as the flow moves through the sheet the charged species respond first to the electric field, then to the electric and magnetic fields combined, then to the electric field alone, and finally to the combined fields once more.

The existence of ion currents is investigated more explicitly in the following section.

7.6 Magnetohydrodynamic Models

The question of ion currents, flow deflection, etc., can more properly be addressed by calculating the various flow velocities through the current sheet. In this section we seek to derive expressions for velocity components which include all

components of the electric field and first order gas dynamic effects in the analysis. One way to approach this problem is through the so-called Lorentz conductivity tensors of Appendix B, but pressure gradients are neglected in that formulation and the ion collision rates are not well known.

A more rigorous analysis can be based on the three fluid charge transport equations for a partially ionized gas, through a so-called generalized Ohm's law formulation. From Sutton and Sherman, Magnetohydrodynamics[16], the total current density can be shown to take the form

$$\bar{J} = \sigma_0 \left(\bar{E}^* + \frac{\nabla P_e}{n_e |e|} \right) - \frac{\Omega_-}{|B|} \bar{J} \times \bar{B} + (1-\alpha)^2 \Omega_- \Omega_+ \left[\frac{\bar{B}(\bar{B}\cdot\bar{J})}{|B|^2} - \bar{J} \right] \qquad (7\text{-}9)$$

where $(1-\alpha)$ is the fraction of un-ionized argon (cf Fig. 7-3), Ω_- and Ω_+ are the electron and ion Hall parameters, and ∇P_e is the electron pressure gradient.

The first term of eq. (7-9) gives the effect of electric fields and electron pressure gradients on the current density, and $\bar{E}^*$ is the electric field which would be measured in coordinates moving with the mass-average gas velocity. $\bar{E}^*$ is related to the laboratory measured field by

$$\bar{E}^* = \bar{E} + \bar{V} \times \bar{B} \qquad (7\text{-}10)$$

where $\bar{V}$ is the mass-average gas velocity relative to the laboratory. The second term of eq. (7-9) is the Hall effect, and the third term is "ion slip." This last effect is usually important only for low density flows where the magnetic fields

are large and the ionized fraction is small. It allows for the possibility of different flow velocities for the ions and neutrals, which would give rise to a net ion current in a coordinate system moving with the mass-average fluid velocity. Ion slip is estimated to be small in the sheet, and consistent with our earlier assumptions on the close streamwise collision coupling between ions and neutrals, it will be neglected. The fluid velocity is thus assumed to be identical with the ion velocity,

$$\bar{V} \equiv \bar{V}_i = \hat{r} u_i + \hat{\theta} v_i + \hat{z} w_i \qquad (7\text{-}11)$$

and to this approximation eq. (7-9) becomes

$$\bar{J} = \sigma_0 \left(\bar{E} + \bar{V}_i \times \bar{B} + \frac{\nabla P_e}{n_e |e|} \right) - \frac{\Omega}{|B|} \bar{J} \times \bar{B} \qquad (7\text{-}12)$$

where the subscript on Ω_- has been dropped.

The current sheet is a region of rather severe radial variations in most properties, as compared to their axial variations, and the radial electron pressure gradient should be much larger than the axial gradient except possibly near the electrodes, where heat transfer and other effects may also become important. We will consider midplane flow here, and neglect these effects. To evaluate the radial pressure gradient the electron partial pressure can be calculated from the perfect gas law,

$$P_e = n_e k T_e \qquad (7\text{-}13)$$

using measured values of n_e and the electron temperature profile of Fig. 6-44. A radial plot of P_e through the sheet is shown in Fig. 7-6, and the radial pressure gradient calculated from this profile reverses sign through the sheet, because of the changing slope. The electron pressure reaches a maximum of $\sim 10^4$ n/m^2, and the maximum pressure gradient is calculated to be $\sim 2 \times 10^6$ n/m^3 on either side of the maximum current density, a 30% contribution to the total charge transport in these regions of the sheet.

The scalar conductivity σ_0, eq. (B-10), has been plotted through the sheet in Fig. 7-7. It remains in the range 10^3 - 10^4 mho/meter in most regions of the sheet, and the maximum value indicates a plasma conductivity about midway between a semiconductor (~ 1 mho/m for germanium) and a metal ($\sim 10^8$ mho/m for copper).

Assuming $\bar{B} = \hat{\theta} B_\theta$, $\bar{E} = \hat{r} E_r + \hat{z} E_z$, and $\bar{V}_i = \hat{r} u_i + \hat{\theta} v_i + \hat{z} w_i$, the generalized Ohm's law, eq. (7-12), can be expanded into components

$$J_r = \sigma_0 \left(E_r + \frac{1}{n_e e} \frac{\partial P_e}{\partial r} - w_i B_\theta \right) + \Omega J_z \qquad (7\text{-}14)$$

$$J_\theta = 0 \qquad (7\text{-}15)$$

$$J_z = \sigma_0 \left(E_z + u_i B_\theta \right) - \Omega J_r \qquad (7\text{-}16)$$

from which the current density components are obtained:

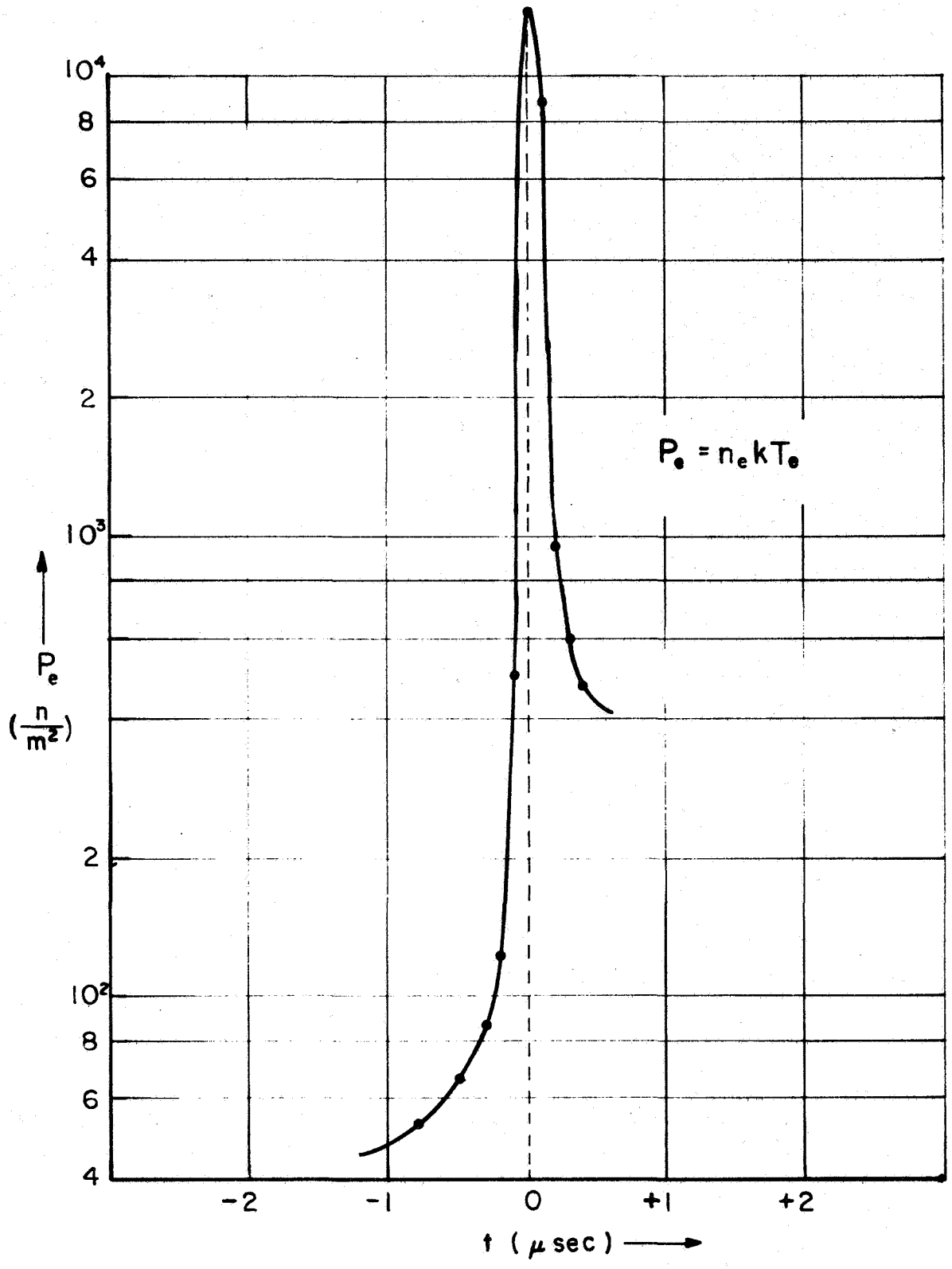

ELECTRON PRESSURE AT MIDPLANE

FIGURE 7 - 6

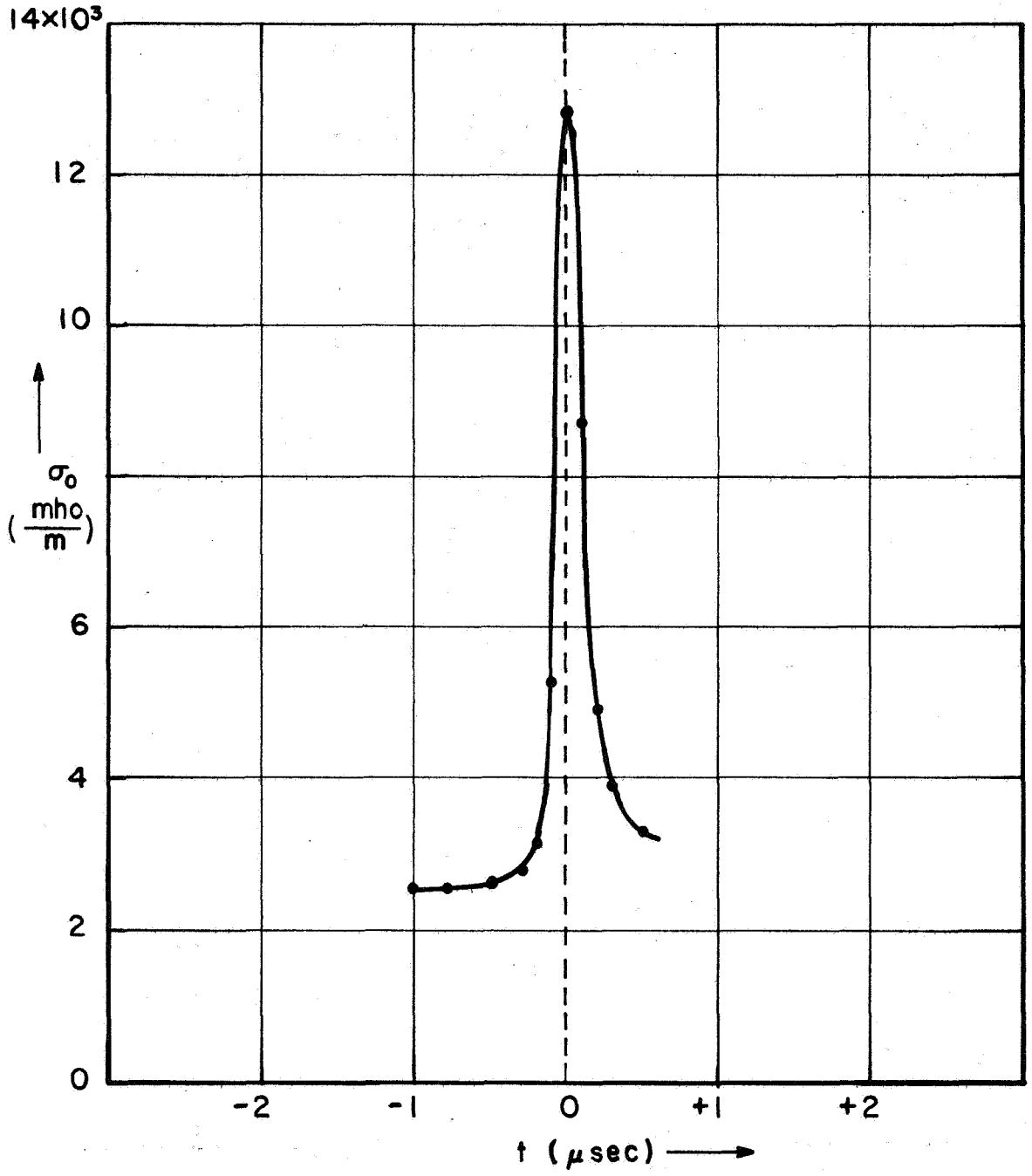

CONDUCTIVITY AT MIDPLANE

FIGURE 7-7

$$J_r = \frac{\sigma_0}{1+\Omega^2}\left[\left(E_r + \frac{1}{n_e e}\frac{\partial P_e}{\partial r} - w_i B_\theta\right) + \Omega\left(E_z + u_i B_\theta\right)\right] \quad (7\text{-}17)$$

and

$$J_z = \frac{\sigma_0}{1+\Omega^2}\left[\left(E_z + u_i B_\theta\right) - \Omega\left(E_r + \frac{1}{n_e e}\frac{\partial P_e}{\partial r} - w_i B_\theta\right)\right] \quad (7\text{-}18)$$

There are several choices which can be made at this point. One could, for example, specify both of the current density profiles and use the experimental field and electron plasma profiles to calculate ion velocity components. An expression was derived in Chapter IV relating J_z to direct magnetic probe measurements

$$J_z = -\frac{1}{\mu_0 u_s}\left[\dot{B}_\theta - \left(\frac{\dot{I}}{I}\right) B_\theta\right] \quad (4\text{-}19)$$

but J_r is more difficult to calculate accurately from B-probe data. Instead we will employ the radial ion velocity profile previously calculated in sections 7.3 and 7.4 and displayed in Fig. 7-2, and calculate the resulting J_r currents required by the equations. Adopting this procedure, eq. (7-18) can be solved for the axial ion velocity in terms of known measured quantities:

$$w_i = \left(\frac{1+\Omega^2}{\sigma_0 \Omega B_\theta}\right) J_z - \frac{1}{\Omega}\left(\frac{E_z}{B_\theta} + u_i\right) + \frac{E_r}{B_\theta} + \frac{1}{n_e e B_\theta}\frac{\partial P_e}{\partial r} \quad (7\text{-}19)$$

The direct relationship between axial ion velocity and total axial current density can be seen from this expression, and the various E/B cross-field Hall components [cf eq. (B-37)] can also be identified.

From the defining equations

$$J_r = n_e|e|(u_i - u_e) \tag{7-20}$$

and

$$J_z = n_e|e|(w_i - w_e) \tag{7-21}$$

and the identity derived in Appendix B,

$$\frac{\sigma_0 B_\theta}{\Omega} = n_e|e| \tag{B-18}$$

(note that Ω is a "spinor" quantity, and takes the sign of B_θ) the axial electron velocity is also obtained in terms of known quantities,

$$w_e = \left(\frac{E_r}{B_\theta} + \frac{1}{n_e|e|}\frac{\partial P_e}{\partial r}\right) - \frac{1}{\Omega}\left(\frac{E_z}{B_\theta} + u_i\right) + \frac{1}{\Omega^2}\frac{J_z}{n_e|e|} \tag{7-22}$$

This expression resembles an expansion in the reciprocal Hall parameter, and contains the simple E_r/B_θ cross field drift solution as a special case for $\Omega \to \infty$ and negligible radial pressure gradients. In the limit $B_\theta \to 0$, this equation reverts to the familiar scalar result

$$J_z \longrightarrow \frac{\Omega n_e|e|}{B_\theta} E_z \equiv \sigma_0 E_z \tag{7-23}$$

We now have axial velocity equations for both charged species; the radial ion velocity has previously been obtained, and the radial electron velocity follows from combining eqs. (7-16) and (7-20):

$$u_e = \frac{J_z}{\sigma_0 B_\theta} - \frac{E_z}{B_\theta} \tag{7-24}$$

If we had elected to derive w_e in terms of J_r instead of U_i, we would have found

$$w_e = \frac{E_r}{B_\theta} + \frac{1}{n_e |e| B_\theta} \frac{\partial P_e}{\partial r} - \frac{J_r}{\sigma_0 B_\theta} \tag{7-25}$$

If we interpret the electric field and pressure gradient together as the total effective electric field,

$$E_r' = E_r + \frac{1}{n_e |e|} \frac{\partial P_e}{\partial r} \tag{7-26}$$

this last may be written

$$w_e = \frac{E_r'}{B_\theta} - \frac{J_r}{\sigma_0 B_\theta} \tag{7-27}$$

which has interesting formal similarity to eq. (7-24).

7.7 Numerical Results

The equations developed in the last section were evaluated in 0.1 μs steps through the sheet using the experimental data of Chapters I - VI. The large number of mathematical operations which had to be performed on the data requires that the results

be interpreted rather more qualitatively than quantitatively, but in general the calculated velocity components show quite reasonable behavior through the sheet. Figure 7-8 repeats the radial velocity profile for the ions from Fig. 7-2, on which is superimposed the radial electron velocity profile from eq. (7-24). Both particles enter the sheet at velocity U_s, the ions decelerating as discussed in section 7.3, and the electrons accelerating slightly. The observation that the electrons are not immediately turned or decelerated by the B_θ field could also have been concluded from the Hall parameter, Fig. 7-5, which is very small in the first part of the sheet. The indication that the electrons tend to accelerate in the radial electric field raises a problem. The difficulty revolves around reconciling the predicted electron acceleration in the prescribed (i.e. measured) field with the maintenance of this field as the sheet propagates. Viewed from the laboratory, the electron population must be weighted slightly ahead of the ion population (albeit by an immeasurably small amount) to establish E_r in the measured direction. It is not clear if this can be accomplished by an electron stream which initially accelerates in the sheet coordinate system. In any event the resultant electromagnetic and gas dynamic forces soon combine to brake the electron fluid faster than the ions, reversing the sign of J_r (the difference between U_i and U_e) near the center of the sheet. The electron fluid also undergoes an acceleration out of the maximum current regions, lending support to the model of a rarefaction wave there, and the electron and ion streams

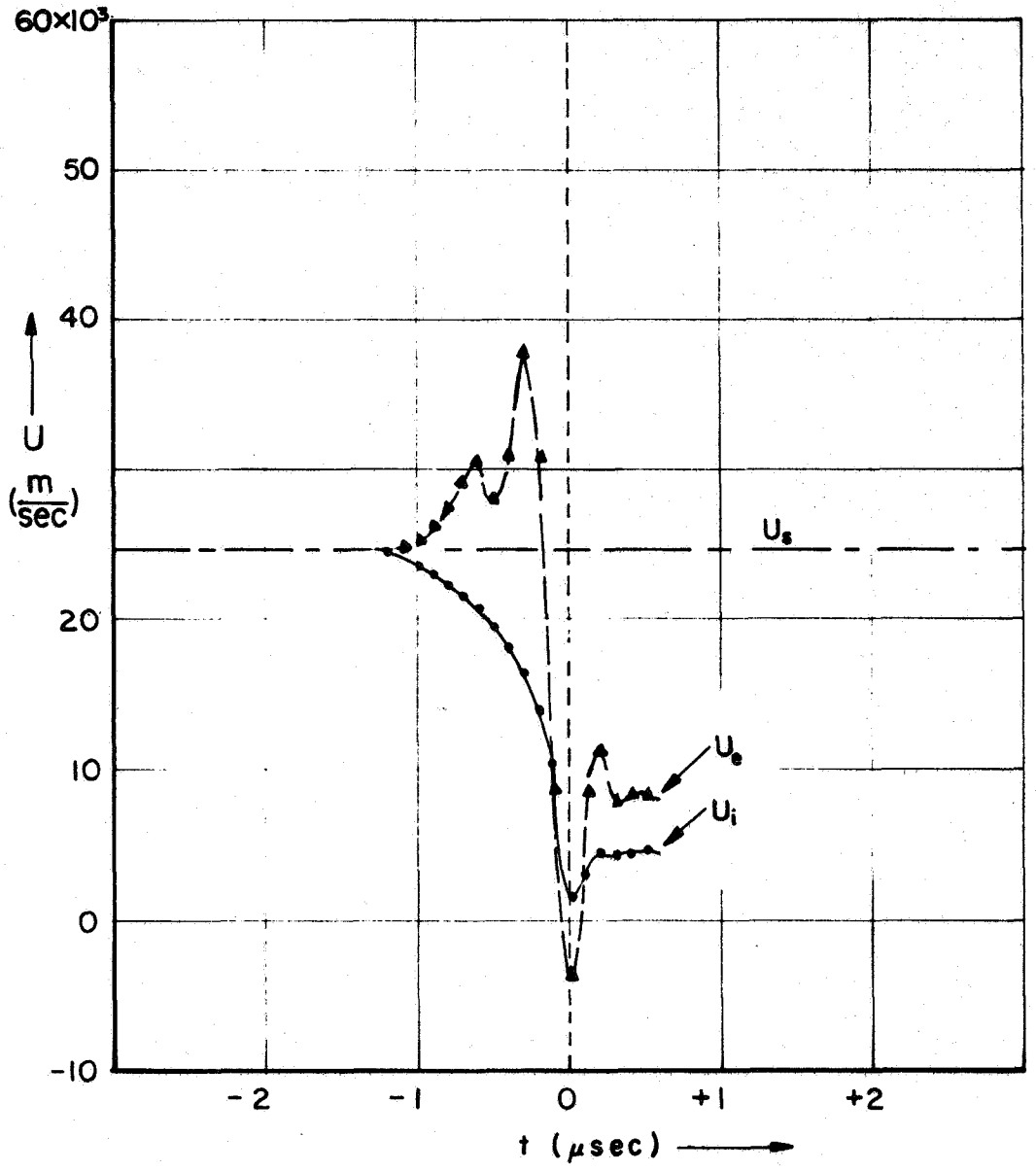

CALCULATED RADIAL VELOCITIES, MIDPLANE

FIGURE 7-8

are rather close together as they emerge from the sheet. This, together with the decreasing values of n_e, indicates generally small radial current behind the sheet.

The radial current density is plotted in Fig. 7-9, and illustrates the oscillatory or reversal effect mentioned above. The direction of J_r at the center of the sheet is correct to produce the observed tilt of the current sheet, with the leading attachment on the anode. The magnitude is somewhat questionable there, however, due to uncertainties in the peak magnitudes of the experimental data and the evaluation of γ_E in the conductivity (Appendix B). J_r can easily be made to fit the experimental tilt of the sheet, as indicated by the dotted lines. [The indicated magnitudes of J_r, a few x 10^6 amp/m^2, shows the validity of neglecting polarization currents arising from the convection of the slight net charge imbalance (section 7.4) past the probes. This neglected component is of magnitude $\rho V_n (n_i - n_e) U_s$, and accounts for an error of ~ 1 amp/m^2].

Figure 7-10 shows the axial electron and ion velocity profiles through the sheet calculated from eqs. (7-19) and (7-22). The solid curve, $J_z/n_e|e|$, is simply the total velocity necessary to supply the measured axial current density, and thus represents the sum of w_i and $-w_e$. The total velocity requirement is severly reduced at $t = 0$, reflecting the measured high charge densities there. The ion contribution to J_z is seen to be considerable in a rather narrow zone near the front of the sheet, and at the rear. This is better illustrated in Fig. 7-11, which is a plot of the total axial current density together with its ion and electron components. The regions of ion participation

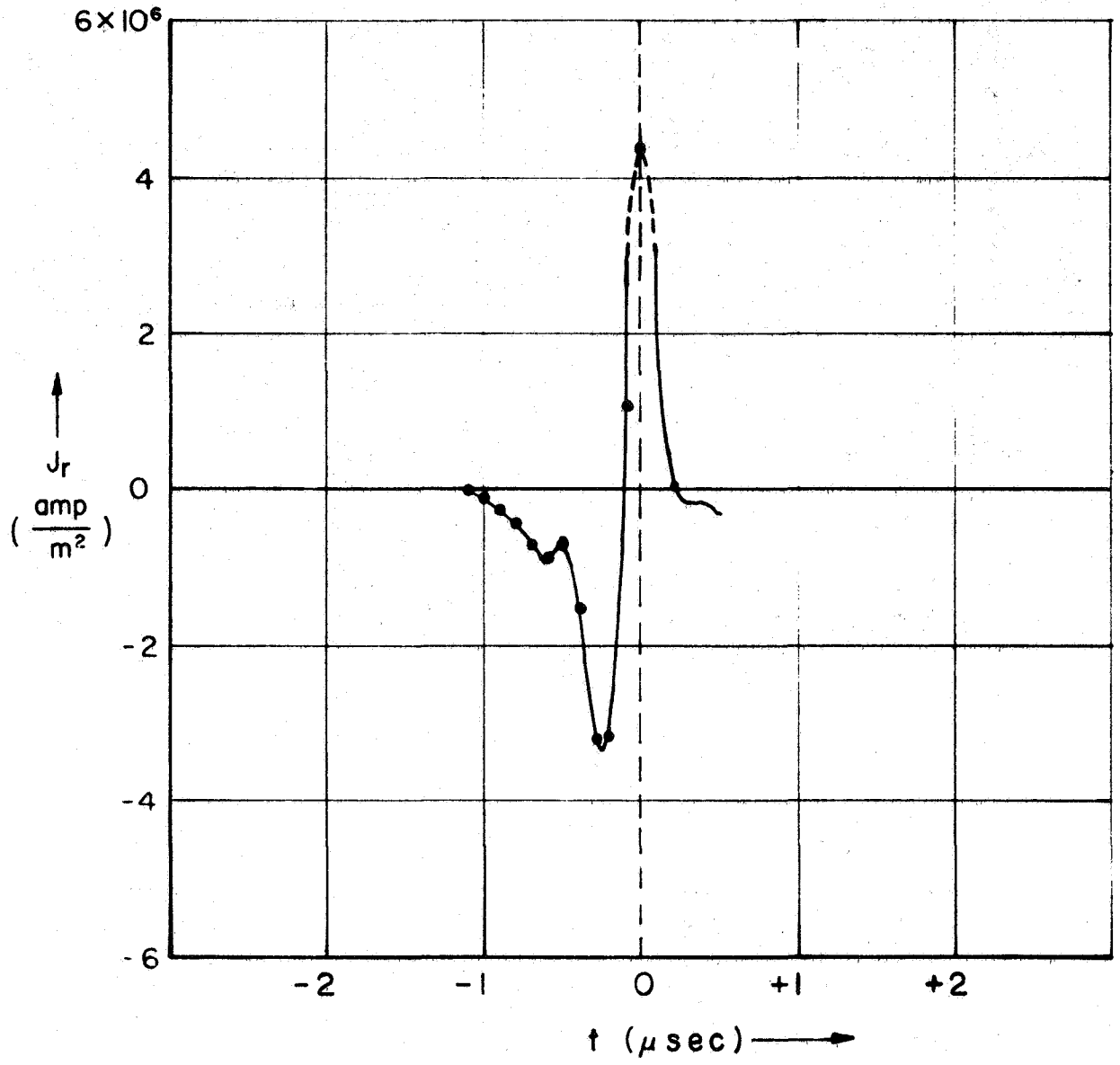

RADIAL CURRENT DENSITY , MIDPLANE

FIGURE 7-9

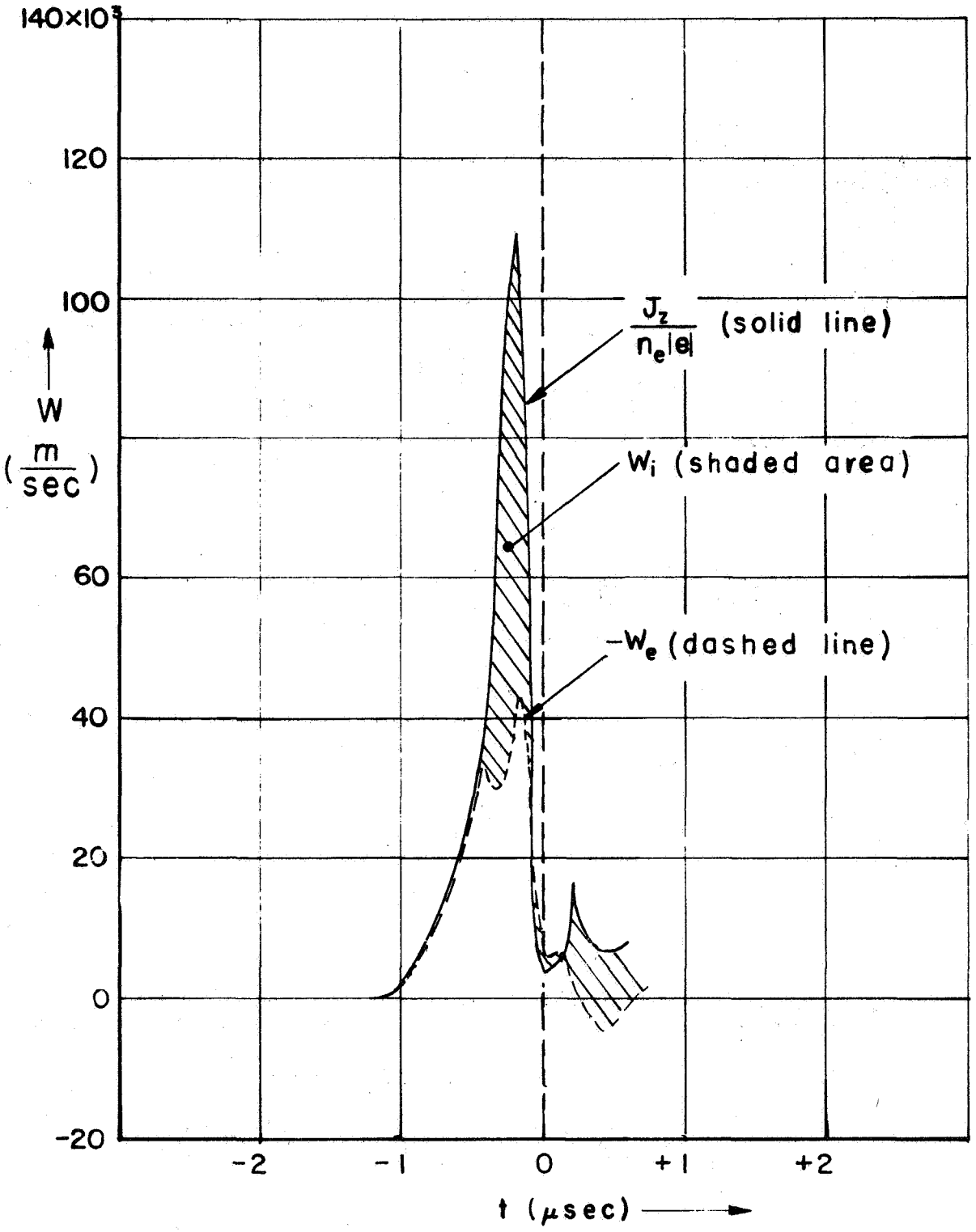

CALCULATED AXIAL VELOCITIES, MIDPLANE

FIGURE 7-10

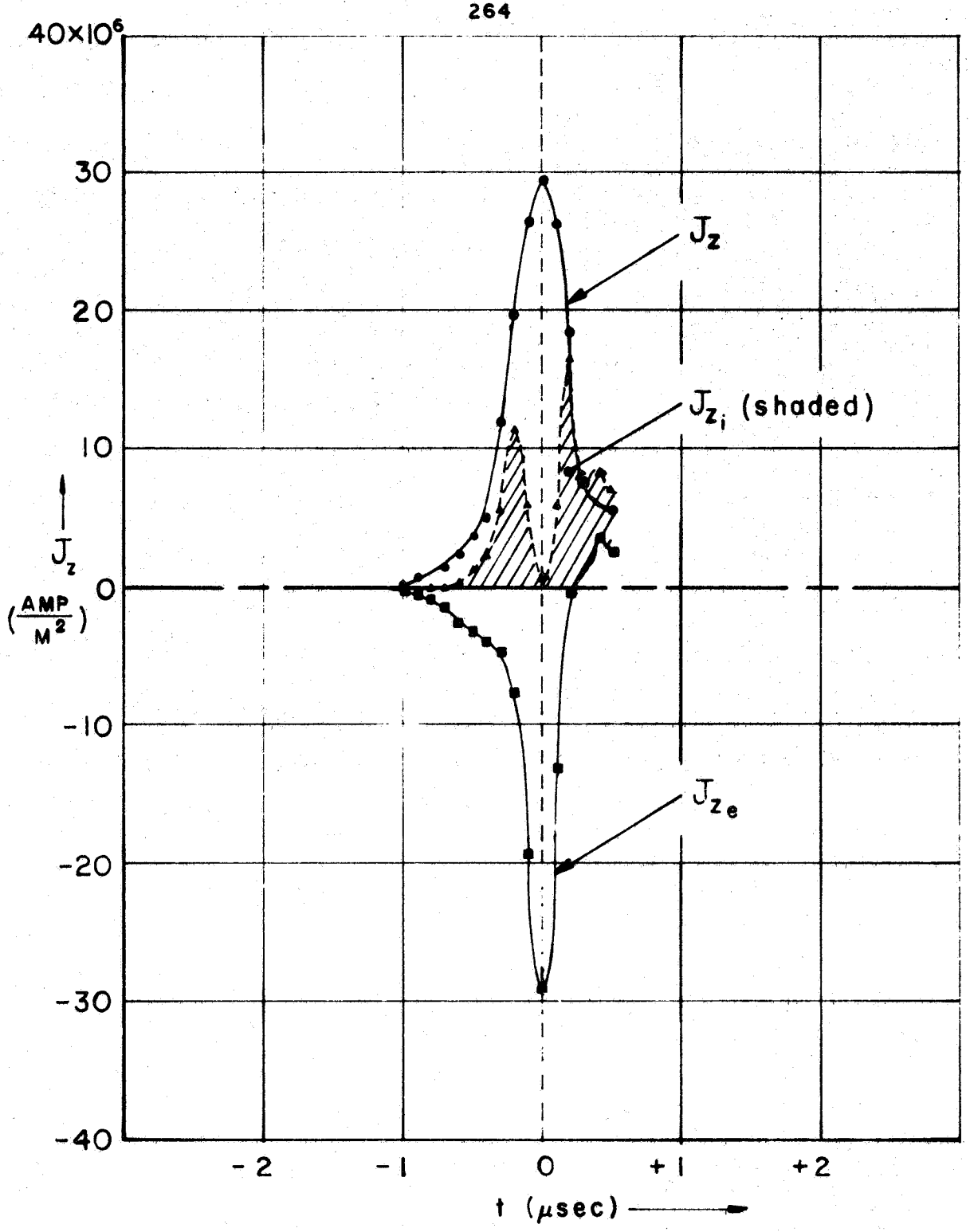

AXIAL CURRENT DENSITY COMPONENTS, MIDPLANE

FIGURE 7-11

are seen to be very similar to the regions of large electron Hall parameter, cf zones 2 and 4 of Fig. 7-5, suggesting that Ω_e may be a useful guideline for quick estimates of both Hall currents and ion components. The indication that the massive component of the plasma emerges from the sheet with an axial velocity approximately one fourth of the radial velocity (in the lab frame) means that the flow has undergone relatively small (i.e. 15°) deflection during the acceleration process.

The electron current density distribution, from Fig. 7-11, is somewhat narrower than the total current density, and bears a close resemblence to the ionization profiles of Fig. 7-3. Hence it seems likely that the increased ionization in the sheet interior arises from ionizing collisions by the axially streaming electrons, and the overall ionization picture would thus be a two step process: initial photoionization of the ambient argon, to $\sim$ 10%, followed by collisional ionization where the electron current is large.

Appendix A

UNITS AND NOTATION

A-1 Units. Rationalized MKS units (m, kg, sec, joule, watt, newton, K^o, amp, volt, ohm, coul, weber) are used throughout, with the following exceptions. Densities are given in m^{-3} or cm^{-3}, the conversion being: $n_e\ (cm^{-3}) = 10^{-6}\ n_e\ (m^{-3})$. Particle energies are given in joules or electron volts, 1 eV = 1.602×10^{-19} joule. Particle temperatures are given in K^o or in eV, 1 eV = 11,600 ^oK.

A-2 Physical Constants. The required physical constants (MKS) are:

c	=	speed of light in vacuum	=	2.99793×10^{8} m/sec
ϵ_0	=	permittivity of vacuum	=	8.854×10^{-12} farad/m
μ_0	=	permeability of vacuum	=	1.257×10^{-6} henry/m
k	=	Boltzmann's constant	=	1.3804×10^{-23} joule/^oK
$\|e\|$	=	charge of proton	=	1.6021×10^{-19} coulomb
m_e	=	rest mass of electron	=	9.108×10^{-31} kg
m_p	=	rest mass of proton	=	1.672×10^{-27} kg

A-3 Description of the Medium. Maxwell's equations for a macroscopic medium, in rationalized MKS units,

$$\nabla \times \bar{E} = -\frac{\partial \bar{B}}{\partial t} \tag{A-1}$$

$$\nabla \times \bar{H} = \bar{J} + \frac{\partial \bar{D}}{\partial t} \tag{A-2}$$

$$\nabla \cdot \bar{D} = \rho \tag{A-3}$$

$$\nabla \cdot \bar{B} = 0 \tag{A-4}$$

relate the time and space dependence of the four field vectors $\bar{E}$, $\bar{H}$, $\bar{D}$, $\bar{B}$ to the net free charge density ρ and the total current density $\bar{J}$, which are themselves related by the continuity equation

$$\nabla \cdot \bar{J} = -\frac{\partial \rho}{\partial t} \tag{A-5}$$

Equations (A-3) and (A-4) are directly derivable from (A-1), (A-2), and (A-5) and hence the entire group constitutes only seven independent scalar relations among sixteen scalar quantities. The remaining constraints derive from the constitutive relations:

$$\bar{D} = \epsilon_0 \bar{E} + \bar{P} \tag{A-6}$$

$$\bar{H} = \frac{\bar{B}}{\mu_0} - \bar{M} \tag{A-7}$$

and Ohm's law, which, in its simplest form for a linear isotropic stationary medium, may be written

$$\bar{J} = \sigma \bar{E} \tag{A-8}$$

In these expressions, $\bar{P}$ and $\bar{M}$ are the polarization and magnetization (net dipole moments per unit volume) respectively, and σ is defined as the conductivity.

For linear isotropic media,

$$\bar{P} = \epsilon_0 \chi_e \bar{E} \tag{A-9}$$

$$\bar{M} = \chi_m \bar{H} \tag{A-10}$$

where χ_e and χ_m are the electric and magnetic susceptibilities,

constants of the medium. The constitutive relations are then compactly expressed as

$$\bar{D} = \epsilon \bar{E} = \epsilon_0 \chi_e \bar{E} \tag{A-11}$$

$$\bar{H} = \frac{\bar{B}}{\mu_0} = \frac{\bar{B}}{\mu_0 \chi_m} \tag{A-12}$$

ϵ and μ are identified as the permittivity and permeability of the medium, and we have the defining equations

$$K_e = 1 + \chi_e \tag{A-13}$$

$$K_m = 1 + \chi_m \tag{A-14}$$

for the relative permittivity (dielectric constant) and relative permeability respectively.

By specifying the three independent quantitites K_e, K_m, and σ (or equivalently ϵ, μ, σ) we completely specify the electromagnetic properties of the medium. In the most general case, K_e, K_m, and σ can take the form of nonlinear, space-, time-, and frequency-dependent tensors and still retain physical meaning. If the medium is linear, isotropic, homogeneous, and unchanging in time, they reduce to scalar functions of the time derivatives of the field vectors.

Because several different notations are prevalent in the literature, the significance of the three parameters K_e, K_m, and σ is easily lost. As defined, they are independent and thus all three must be incorporated into any complete description of the medium. The following discussion (after Heald and Wharton, ref. 35), shows how this is usually accomplished.

The accessibility of the conductivity parameter to direct microwave measurement (see Appendix B) is the basic for the usual practice of deriving information on plasma characteristics in terms of the conductivity. In most cases of practical interest, κ_m is unity or at worst nearly constant. Of the two remaining parameters, κ_e may be regarded physically as a measure of the polarization, or charge separation, of the medium, and hence as a reactive or "stored energy" term, whereas σ measures the dissipative (collisional) or "resistive" properties. Thus we can incorporate both quantities into a single complex term, completely analogous to the complex impedance concept of elementary circuit theory. This has traditionally been done in either of two ways.

Consider fields with harmonic time dependence, $e^{i\omega t}$. Faraday's and Ampere's laws (A-1) and (A-2) in terms of $\bar{E}$ and $\bar{H}$ become

$$\nabla \times \bar{E} = -i\omega\mu_0 \kappa_m \bar{H} \qquad \text{(A-15)}$$

$$\nabla \times \bar{H} = (\sigma + i\omega\epsilon_0 \kappa_e)\bar{E} \qquad \text{(A-16)}$$

In the theory of dielectrics, it is customary to define a complex dielectric constant κ^{*+} such that

$$\sigma + i\omega\epsilon_0\kappa_e \longrightarrow i\omega\epsilon_0\kappa^* \qquad \text{(A-17}$$

or

$$\kappa^* = \kappa_r - i\kappa_i = \kappa_e - i\frac{\sigma}{\epsilon_0\omega} \qquad \text{(A-18)}$$

+The symbol * will sometimes be used to denote explicitly complex quantities, in the interest of clarity.

In ionized gas theory, on the other hand, an explicitly complex conductivity is usually employed

$$\sigma + i\omega\epsilon_0\chi_e \longrightarrow \sigma^* + i\omega\epsilon_0 \tag{A-19}$$

or

$$\sigma^* = \sigma_r + i\,\sigma_i = \sigma + i\,\omega\epsilon_0(\chi_e - 1) \tag{A-20}$$

For correlation with the literature, the interrelations

$$\chi^* = \left(1 + \frac{\sigma_i}{\omega\epsilon_0}\right) - i\left(\frac{\sigma_r}{\omega\epsilon_0}\right) \tag{A-21}$$

and

$$\sigma^* = \omega\epsilon_0\chi_i + i\,\omega\epsilon_0(\chi_r - 1) \tag{A-22}$$

make transition from one notation to the other a straightforward matter.

It is to be emphasized that equations (A-17) and (A-19) are alternative, equivalent mathematical statements of the same phenomena, and must not be employed simultaneously.

If the complex dielectric constant notation of eq. (A-17) is used, the harmonic Maxwell equations take the form

$$\nabla \times \bar{E} = -i\,\omega\mu_0\bar{H} \tag{A-23a}$$

$$\nabla \times \bar{H} = i\,\omega\epsilon_0\chi^*\bar{E} \tag{A-23b}$$

$$\nabla\cdot(\epsilon_0\chi^*\bar{E}) = 0 \tag{A-23c}$$

$$\nabla\cdot(\mu_0\bar{H}) = 0 \tag{A-23d}$$

and neither the net current density nor the net charge density appear explicitly.

If, on the other hand, the complex conductivity notation of eq. (A-21) is used, the appropriate Maxwell relations are

$$\nabla \times \bar{E} = -i\omega\mu_0 \bar{H} \tag{A-24a}$$

$$\nabla \times \bar{H} = (\sigma^* + i\omega\epsilon_0)\bar{E} \tag{A-24b}$$

$$\nabla \cdot (\epsilon_0 \chi_e \bar{E}) = \rho \tag{A-24c}$$

$$\nabla \cdot (\mu_0 \bar{H}) = 0 \tag{A-24d}$$

Although the mathematical development furnishes little basis for choice, physically the concept of a polarized plasma seems a bit wide of the mark, and the complex conductivity convention was adopted for this work.

Using this formalism, an immediate simplification results by noting that, in a partially ionized gas at microwave frequencies, the constitutive and Ohm's law relations can be taken to a very good approximation as those of a stationary conducting medium with vacuum permittivity and permeability:

$$\bar{D} = \epsilon_0 \bar{E} \tag{A-25a}$$

$$\bar{H} = \frac{\bar{B}}{\mu_0} \tag{A-25b}$$

$$\bar{J} = \sigma \bar{E} \tag{A-25c}$$

To this approximation the dielectric constant of the plasma is unity, and the conductivity from eq. (A-20) is no longer explicitly complex:

$$\sigma^* \equiv \sigma \tag{A-26}$$

and the * symbol will be dropped.

The conductivity of an ionized gas is a very complicated concept at best, however, and even under the simplest assumptions is an implicitly complex function, denoting in-phase and out-of-phase components of current. When a magnetic field is present in the plasma, the simplest meaningful form assignable to σ is that of a second rank tensor, implying that the complex current flow is no longer even colinear with the driving electric field (Appendix C).

In our notation the complex refractive index of the plasma,[35]

$$\mu^* = (K^* K_m)^{\frac{1}{2}} \tag{A-27}$$

can be written

$$\mu^* = \left(1 - i\frac{\sigma}{\epsilon_0 \omega}\right)^{\frac{1}{2}} \tag{A-28}$$

The resulting formalism is presented in section 6.2.

Appendix B

COLLISION FREQUENCIES AND PLASMA CONDUCTIVITY

The concept of electrical conductivity in a partially ionized gas is a useful one, and as a macroscopic transport property, it seems to be well-defined. The transport of charge in a conducting fluid is basically a diffusion process, and is properly handled by rigorous solution of the Boltzmann equation. (Conduction can also occur by charge exchange between colliding particles, but normally this is not important.) A major problem in the use of the Boltzmann equation, however, is the evaluation of the collision term $\left(\frac{\partial f}{\partial t}\right)_{coll.}$, which in general is an integral not only over $f(\bar{r}, \bar{v}, t)$ for the class of particles in question, but also over the corresponding distribution functions for all other classes of particles with which interactions occur. Thus the solution of a complicated vector integro-differential equation is required, and this has not yet been accomplished in any generality. Because of this complication, among others, there is at present no exact theory for current conduction in ionized gases. Instead a variety of expressions, with differing assumptions and various degrees of sophistication, have been put forward. Thus, analytically at least, the subject of gas conductivity requires some simplifying assumptions to be serviceable.

The simplest set of assumptions is called the "Lorentz model," wherein only the electron conductivity is calculated by assuming that the electrons undergo momentum-exchange collisions with other particles, which can be described by an average momentum transfer collision frequency. Since $mv\nu$ represents

the average rate of change of forward momentum due to collisions, one can write the equation of motion of a "typical," or ensemble-average, electron in the form

$$m\bar{\dot{v}} + m\bar{v}\nu = -|e|\bar{E}(t) \qquad \text{(B-1)}$$

Thus if the electron averages ν collisions per second, the damping term represents the statistical average force exerted on the electron by the massive ion-neutral component of the plasma, and the electron effectively moves through a viscous medium.

Eq. (B-1) is a simplified version of the more general Langevin equation

$$m\bar{\dot{v}} + m\bar{v}\nu = -|e|(\bar{E} + \bar{v} \times \bar{B}) \qquad \text{(B-2)}$$

which includes the effects of $\bar{j} \times \bar{B}$ forces on electron motion. In both of these equations the electric field appearing on the right as a forcing function is the effective electric field felt by the electron swarm. There has always been some controversy over whether this field ought to be simply the applied field $\bar{E}$, or $\bar{E} + \frac{\bar{P}}{3\epsilon_0}$, as in the case of common dielectrics. A variety of experimental evidence now seems to strongly favor the choice of $\bar{E}$ alone,[35] which yields the Sellmeir form of the conductivity.

By invoking harmonic time dependence of the form $e^{i\omega t}$, neglecting the magnetic field associated with the oscillating $\bar{E}$ field, and applying Ohm's law ($\bar{J} = -n_e|e|\bar{v} = \sigma\bar{E}$), eq. (B-1) can be integrated directly (section 6.2) to yield

$$\sigma = \frac{n_e|e|^2}{m_e(\nu + i\omega)} \qquad \text{(B-3)}$$

The conductivity of the plasma to microwave frequency fields is represented by eq. (B-3). For the purpose of calculating particle motions in the current sheet fields, we use the DC limit:

$$\sigma_0 = \frac{n_e e^2}{m_e \nu} \qquad \text{(B-4)}$$

This result can also be obtained from the Boltzmann equation, under restrictive assumptions. Expanding the distribution function in spherical harmonics in velocity space and retaining first order terms (ref. 35, Chap. 2) leads to

$$\sigma = -\frac{4\pi}{3} \frac{n_e e^2}{m_e} \int_0^\infty \frac{1}{\nu(v) + i\omega} \frac{df_0(v)}{dv} v^3 \, dv \qquad \text{(B-5)}$$

For the special case of ν independent of velocity, we recover our former result, eq. (B-4), independent of $f_0(v)$ (the equilibrium distribution function is isotropic but not necessarily Maxwellian). Most real collision processes are not of this special case and the conductivity more accurately involves an integration over $\nu(v)$ and $f_0(v)$. Because of the relative simplicity of the Sellmeir (or Lorentz) formula, eq. (B-4), and the vast literature employing it, it is convenient to define an effective collision frequency, in terms of actual particle-particle encounters, which can be used directly in eq. (B-4). In general, ν will have both electron-neutral and electron-ion components.

Electron-ion Collisions. Electron-ion collisions dominate in the plasma for ionization levels above $\sim 10^{-3}$. Thus the only effective contribution to ν in eq. (B-4) is ν_{ei}. Due to the long range nature of coulomb interactions, electron-ion encounters must be summed carefully. Spitzer[40] defines a

"90° deflection time," the reciprocal of which is

$$\nu_D = \frac{1}{\tau_D} = 8\pi\left(\frac{1e^2}{4\pi\epsilon_0 m_e}\right)^2 \frac{Z n_e \ln\Lambda}{v^3} \qquad \text{(B-5)}$$

where

$$\Lambda = 1.55 \times 10^{10} \frac{[kT_e(eV)]^{3/2}}{Z\,[n_e(cm^{-3})]^{1/2}} \qquad \text{(B-6)}$$

In terms of ν_D, which is the basis for calculating most electron-ion collision frequencies, Heald and Wharton (ref. 35, Chap. 2) show that the effective electron-ion collision frequency in eq. (B-3) takes the form

$$\nu \cong \nu_{ei} = 2.90 \times 10^{-6} \frac{Z n_e(cm^{-3}) \ln\Lambda}{[kT_e(eV)]^{3/2}} \quad sec^{-1} \qquad \text{(B-7)}$$

Thus, for $\ln\Lambda \cong 7$, $\omega = 4.4 \times 10^{11} sec^{-1}$, we find

$$\frac{\nu_{ei}}{\omega} = 4.6 \times 10^{-17} \frac{n_e(cm^{-3})}{[kT_e(eV)]^{3/2}} \qquad \text{(B-8)}$$

for the effective value of ν/ω at microwave frequencies, with no impurities present and ionization levels above 10^{-3}. The assumption of stationary field particles (ions) is generally valid even when the ion temperature is greater than the electron temperature, unless the ratio exceeds $\left(\frac{m_i}{m_e}\right)^{1/2}$ (35).

In the DC limit, appropriate to eq. (B-4), ν_{ei} of eq. (B-7) takes a modifier:(35)

$$\nu \cong \frac{g(0)}{\gamma_E} \nu_{ei} = \frac{3\pi}{32\gamma_E} \nu_{ei} \qquad \text{(B-9)}$$

so that

$$\sigma_0 \cong 3.3\times10^{4}\,\gamma_E\,\frac{[kT_e(eV)]^{3/2}}{Z\ln\Lambda}\quad \frac{mhos}{m} \qquad \text{(B-10)}$$

γ_E is a modifier representing the effects of electron-electron collisions, $0.582 \leq \gamma_E \leq 1.0$. It differs from unity for very low frequencies, very high ionization levels, and single (as opposed to multiple) ionization [see discussions in Spitzer,[40] Heald and Wharton,[35] and Sutton and Sherman[16]]. Except where the ionization was near 100% (Chapter VII), γ_E was taken to be unity.

Electron-Neutral Collisions. The cross-section for electron-neutral momentum exchange collisions is not as simple as the well-known coulomb cross-section and, in general, empirical determinations of the cross-section are superior to theoretical treatments. From the argon data of De Voto,[97-99] the electron neutral cross section is well represented by a linear relationship,

$$Q(\text{Å}^2) = 1.5\,E(eV) \qquad \text{(B-11)}$$

over the range of energies $0.2 \leq E \leq 4.0$ eV (this is the high energy side of the Ramseur well). Thus

$$Q \propto v^2 \qquad \text{(B-12)}$$

and

$$\nu_{en} = n_n Q v \propto v^3 \qquad \text{(B-13)}$$

In terms of the r.m.s. velocity of the electrons,

$$v \cong \left(\frac{3kT_e}{m_e}\right)^{\frac{1}{2}} \quad m/sec \qquad \text{(B-14)}$$

it is straightforward to show that

$$\nu_{en}(T_e) = 23.5\,[T_e(^\circ K)]^{3/2} = 2.94\times10^{7}\,[kT_e(eV)]^{3/2} \qquad \text{(B-15)}$$

and

$$\frac{\nu_{en}}{\omega} = 6.68\times10^{-5}\,[kT_e(eV)]^{3/2} \qquad \text{(B-16)}$$

For the temperatures ($\sim$ 1 eV) and densities ($\sim 10^{15}\,cm^{-3}$) of interest, a comparison of eqs. (B-16) and (B-8) shows the electron-ion collision frequency to be clearly dominant.

The Hall Parameter. The Hall parameter is defined as

$$\Omega = \frac{\omega_b}{\nu} = \frac{|e|B}{m\nu} \qquad \text{(B-17)}$$

where the collision frequency is the effective value as discussed above. Combining eqs. (B-17) and (B-4) we find the useful identity,

$$\frac{\sigma_0 B}{\Omega} = n_e|e| \qquad \text{(B-18)}$$

Eq. (B-18) allows the various parameters to be combined in consistent groups, as discussed in Chapter VII.

Tensor Conductivity Models. The first integral of the Lorentz equation of motion [eq. (B-1)] yields a complex but scalar form for the conductivity of an ionized gas [eq. (B-3)]. The corresponding harmonic integration of the Langevin equation of motion [eq. (B-2)] is the subject of Appendix C, where it is

shown that the simplest meaningful form assignable to σ is that of a second rank tensor. The results derived there for microwave frequency fields and currents can be adopted for current sheet analyses by taking the D.C. limit, $\omega/\nu \ll 1$. Then eqs. (C-4) and (C-5) take the form

$$\bar{J} = \bar{\bar{\sigma}} \cdot \bar{E} \tag{B-19}$$

and

$$\bar{\bar{\sigma}} = \frac{\sigma_0}{1+\Omega^2} \begin{pmatrix} 1 & 0 & \Omega \\ 0 & 1+\Omega^2 & 0 \\ -\Omega & 0 & 1 \end{pmatrix} \tag{B-20}$$

where σ_0 is the scalar conductivity defined by eq. (B-4), and Ω is the electron Hall parameter, by eq. (B-17). The effective collision frequency ν which appears in these parameters is defined by eq. (B-9). This form of $\bar{\bar{\sigma}}$ is appropriate to $\bar{B}$ along the y-axis of a Cartesian coordinate system, Fig. C-1. This orientation allows the (x,y,z) and (r, θ, z) coordinate systems to be used interchangably with a common z-z-axis, and $\bar{B}$ can be correctly identified with $\hat{\theta} B_\theta$.

It is obvious from the mathematical form of $\bar{\bar{\sigma}}$ that electron fluid motion depends on the value of Ω relative to unity, i.e. the ratio of qyro-frequency to collision frequency. To be more explicit, consider the simple case of electron motion in the E_r and B_θ fields of the current sheet, neglecting for the moment the smaller E_z component of electric field. The current components from eq. (B-19) are

$$J_r = \frac{\sigma_0}{1+\Omega^2} E_r \tag{B-21}$$

$$J_\theta = 0 \tag{B-22}$$

$$J_z = \frac{\sigma_0}{1+\Omega^2}(-\Omega E_r) \tag{B-23}$$

and the total current density is of magnitude

$$|J| = \left(J_r^2 + J_z^2\right)^{\frac{1}{2}} = \frac{\sigma_0}{(1+\Omega^2)^{1/2}} E_r \tag{B-24}$$

and lies in the r-z plane at an angle θ to E_r :

$$\theta = \tan^{-1}\left|\frac{J_z}{J_r}\right| = \tan^{-1}\Omega \tag{B-25}$$

Thus when the Hall parameter is unity the current makes an angle of 45° with respect to the applied field; if $\Omega << 1$, collisions override the magnetic deflection, and the current follows the applied field; and if $\Omega >> 1$, the magnetic field controls the drift and the current is perpendicular to the applied field.

The above remarks pertain to electron current, but an entirely analogous development can be carried through for ion current. Ions generally carry little current at microwave frequencies, and so are neglected in the analysis of Appendix C; but in the D.C. limit ions normally carry a fraction of the current and an analogous Langevin equation for ions can be written. The resulting ion conductivity tensor is found to be

$$\bar{\bar{\sigma}}_+ = \frac{\sigma_{0+}}{1+\Omega_+^2}\begin{pmatrix} 1 & 0 & -\Omega_+ \\ 0 & 1+\Omega_+^2 & 0 \\ \Omega_+ & 0 & 1 \end{pmatrix} \tag{B-26}$$

(+ and - will be used here instead of i and e , to avoid double letter subscripts) and the total current density sums the two components,

$$\bar{J} = (\bar{J}_- + \bar{J}_+) = (\bar{\bar{\sigma}}_- + \bar{\bar{\sigma}}_+) \cdot \bar{E}_n \qquad \text{(B-27)}$$

where J_- and $\bar{\bar{\sigma}}_-$ are given by eqs. (B-19) and (B-20).

The off-diagonal elements of $\bar{\bar{\sigma}}$ are proportional to the charge of the particles, and since ω_b and Ω are defined in terms of $|e|$, these have opposite signs for ions and electrons.

Consider again the simple cross-field case, $\bar{B} = \hat{\theta} B_\theta$ and $\bar{E} = \hat{r} E_r$. The electron current density components are, as before,

$$J_{n-} = \frac{\sigma_{o-}}{1+\Omega_-^2} E_n \qquad \text{(B-28)}$$

$$J_{z-} = \frac{\sigma_{o-}}{1+\Omega_-^2} (-\Omega_-) E_n \qquad \text{(B-29)}$$

and the ion components are

$$J_{n+} = \frac{\sigma_{o+}}{1+\Omega_+^2} E_n \qquad \text{(B-30)}$$

and

$$J_{z+} = \frac{\sigma_{o+}}{1+\Omega_+^2} (\Omega_+) E_n \qquad \text{(B-31)}$$

In the scalar limit, $\Omega_\pm \ll 1$, the current components primarily follow the (radial) field:

$$J_{n-} \simeq \frac{J_{z-}}{\Omega_-} \gg J_{z-} \qquad \text{(B-32)}$$

$$J_{n+} \simeq \frac{J_{z+}}{\Omega_+} \gg J_{z+} \qquad \text{(B-33)}$$

and electrons and ions participate in the ratio

$$\frac{J_{n-}}{J_{n+}} \simeq \frac{m_+ \nu_+}{m_- \nu_-} = \frac{\Omega_-}{\Omega_+} \gg 1 \qquad \text{(B-34)}$$

Electrons are generally assumed to dominate this case, on the grounds that the mass ratio overrides the collision frequency ratio. To what extent this occurs is difficult to argue because of the uncertainty regarding the effective ion collision frequency (momentum transfer with neutrals) in the current sheet, where heavy particle velocities are not primarily thermal.

In the other limit, $\Omega_\pm \gg 1$, a more interesting situation arises. Neither type of particle follows the applied (radial) field:

$$J_{n-} \simeq \frac{J_{z-}}{\Omega_-} \ll J_{z-} \qquad \text{(B-35)}$$

$$J_{n+} \simeq \frac{J_{z+}}{\Omega_+} \ll J_{z+} \qquad \text{(B-36)}$$

indicating well developed cross-field drifts. Collisionless Hall drift is well known to be independent of charge sign, and indeed, to our approximation, the axial components of current are equal and opposite:

$$J_{z-} \simeq -\left(\frac{\sigma_{o-}}{\Omega_-}\right) E_r = -n_e|e| \frac{E_r}{B_o} \simeq -J_{z-} \qquad \text{(B-37)}$$

Thus, in this case, electrons and ions participate equally in the dominant Hall mode.

The radial currents along the applied field are small, and in the ratio

$$\frac{J_{r-}}{J_{r+}} \simeq \left(\frac{\sigma_{o-}}{\Omega_-^2}\right)\left(\frac{\Omega_+^2}{\sigma_{o+}}\right) = \frac{m_-\nu_-}{m_+\nu_+} \gtrsim 1 \qquad \text{(B-38)}$$

Thus, to the extent that electrons carry scalar current in the small Hall parameter limit, eq. (B-34), ions carry it here.

We can thus conclude that ion participation in the overall current conduction picture is likely to become important as Hall conduction itself becomes important, i.e. when the Hall parameter is greater than unity.

The Hall parameter for the electrons can be calculated from the data of these experiments, and this quantity is discussed in detail in section 7.5 of Chapter VII.

The Hall parameter for ions in the current sheet is more difficult to evaluate precisely because it involves a nonlinear, nonisotropic ion-neutral collision frequency as discussed in section 7.2. If the neutral momentum-exchange

collision cross section is assumed to be geometric, and thus approximately equal for both ions and electrons, then in thermal equilibrium we find

$$\frac{\nu_{in}}{\nu_{en}} = \frac{\nu_+}{\nu_{en}} = \frac{n_n Q_+ V_+}{n_n Q_- V_-} \sim \left(\frac{m_-}{m_+}\right)^{\frac{1}{2}} \qquad \text{(B-39)}$$

But it is shown in Chapter VI that, in the current sheet plasma, $\nu_- \doteq \nu_{ei} \sim 10^4\, \nu_{en}$. Substituting these results into eq. (B-34) for the ratio of electron to ion Hall parameters gives a result of order unity for the thermal equilibrium case.

Appendix C

REFLECTION COEFFICIENT FROM AN ANISOTROPIC PLASMA

The presence of a static magnetic field makes a plasma medium anisotropic to microwave propagation, and considerably complicates its refractive index. The index is nonunique in general, and various plane wave motions must be superposed to obtain a general solution to the wave equation. Currents in the plasma will in general not be colinear with the driving fields, leading to a nonscalar conductivity. For these reasons a convenient mathematical approach to the anisotropy problem is through the component equations and the use of tensor notation.

Consider wave propagating along the Z-axis normal to the magnetic field vector, so that $\theta = 90^{\circ}$ in the coordinate system of Fig. C-1, and $\overline{B} = \hat{y}\, B_y$:

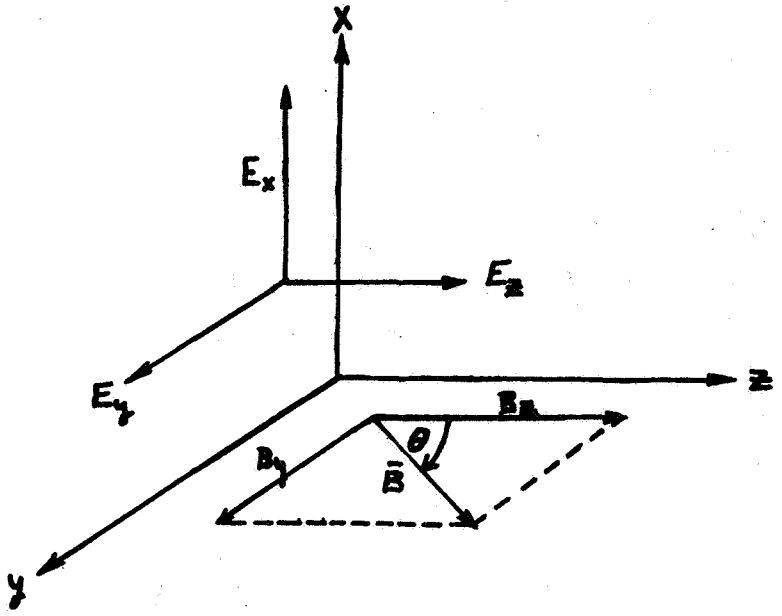

Coordinate System

Figure C-1

The experimental situation can be recovered by identifying Z with the axial dimension in the pinch chamber and B_y with the local B_θ field.

Expansion of the Langevin force equation (Appendix B) then yields the harmonic equations of motion for the plasma electrons:

$$\begin{aligned} i\, m_e \omega V_x + \nu m_e V_x - |e| B_y V_z &= -|e| E_x \\ i\, m_e \omega V_y + \nu m_e V_y &= -|e| E_y \\ i\, m_e \omega V_z + \nu m_e V_z + |e| B_y V_x &= -|e| E_z \end{aligned} \tag{C-1}$$

Identifying the cyclotron frequency (eq. (6-56)) and the plasma frequency (eq. (6-12)), and replacing velocity by current density ($\bar{J} = -n_e |e| \bar{V}$) yields

$$\begin{aligned} (i\omega + \nu) J_x - \omega_b J_z &= \epsilon_0 \omega_p^2 E_x \\ (i\omega + \nu) J_y &= \epsilon_0 \omega_p^2 E_y \\ (i\omega + \nu) J_z + \omega_b J_x &= \epsilon_0 \omega_p^2 E_z \end{aligned} \tag{C-2}$$

or in matrix notation

$$\frac{1}{\epsilon_0 \omega_p^2} \begin{pmatrix} i\omega+\nu & 0 & -\omega_b \\ 0 & i\omega+\nu & 0 \\ \omega_b & 0 & i\omega+\nu \end{pmatrix} \begin{pmatrix} J_x \\ J_y \\ J_z \end{pmatrix} = \begin{pmatrix} E_x \\ E_y \\ E_z \end{pmatrix} \tag{C-3}$$

which is Ohm's law in the inverted form

$$\bar{\bar{\sigma}}^{-1} \cdot \bar{J} = \bar{E} \tag{C-4}$$

The conductivity tensor can be obtained by inverting the matrix of eq. (C-3):

$$\bar{\bar{\sigma}} = \frac{\epsilon_0 \omega_p^2}{(i\omega+\nu)\left[(i\omega+\nu)^2+\omega_b^2\right]} \begin{pmatrix} (i\omega+\nu)^2 & 0 & \omega_b(i\omega+\nu) \\ 0 & (i\omega+\nu)^2+\omega_b^2 & 0 \\ -\omega_b(i\omega+\nu) & 0 & (i\omega+\nu)^2 \end{pmatrix} \tag{C-5}$$

The appearance of off-diagonal elements in $\bar{\bar{\sigma}}$ corresponds to the development of Hall currents in the plasma, a well-known consequence of $\bar{B}$ field anisotropy, signifying that the current density and electric field are generally in different directions as well as out of phase.

All currents and fields in the plasma must also satisfy Maxwell's equations, which may or may not be possible with simple plane waves. This can be checked by assuming transverse harmonic wave motion of the usual form

$$\bar{E} = \bar{E}_0 \, e^{i(\omega t - k^* z)} \tag{C-6}$$

and expanding the Faraday law (eq. (A-1))

$$\begin{aligned} i k^* E_y &= -i \mu_0 \omega H_x \\ -i k^* E_x &= -i \mu_0 \omega H_y \\ 0 &= -i \mu_0 \omega H_z \end{aligned} \tag{C-7}$$

and Ampere's law (eq. (A-2))

$$\begin{aligned} i k^* H_y &= i \epsilon_0 \omega E_x + J_x \\ -i k^* H_x &= i \epsilon_0 \omega E_y + J_y \\ 0 &= i \epsilon_0 \omega E_z + J_z \end{aligned} \tag{C-8}$$

into their component equations. Eliminating the H components and recalling the definition of the refractive index from section 6-2 and Appendix A

$$\mu^* = \frac{k^*}{k_0} \tag{C-9}$$

$$k_0 = \frac{\omega}{c} = \frac{\omega}{\sqrt{\epsilon_0 \mu_0}} \tag{C-10}$$

yields a set of equations relating $\bar{E}$ and $\bar{J}$:

$$\begin{aligned} i \epsilon_0 \omega (\mu^{*2} - 1) E_x &= J_x \\ i \epsilon_0 \omega (\mu^{*2} - 1) E_y &= J_y \\ -i \epsilon_0 \omega E_z &= J_z \end{aligned} \tag{C-11}$$

which is a kind of Ohm's law for plane waves. In maxtrix form,

$$i \epsilon_0 \omega \begin{pmatrix} \mu^{*2}-1 & 0 & 0 \\ 0 & \mu^{*2}-1 & 0 \\ 0 & 0 & -1 \end{pmatrix} \begin{pmatrix} E_x \\ E_y \\ E_z \end{pmatrix} = \begin{pmatrix} J_x \\ J_y \\ J_z \end{pmatrix} \tag{C-12}$$

The fact that $\bar{\bar{\sigma}}$ from eq. (C-12) is diagonal, as opposed to eq. (C-5), illustrates the impossibility of finding a unique refractive index to satisfy both the Langevin equation and Maxwell's equations simultaneously for the assumed plane wave, even for the restricted case of transverse propagation. The smallest number of distinct refractive indices which may be assigned to the plasma under these circumstances is two, corresponding to the two characteristic waves[+] which the plasma will support.

Combining the two matrix equations for $\bar{J}$ and $\bar{E}$ yields

$$\bar{J} = \left(\bar{\bar{\sigma}}^{-1}\right)^{-1} \cdot \bar{E} = \bar{\bar{\sigma}} \cdot \bar{E} \qquad \text{(C-13)}$$

or

$$\left(\bar{\bar{\sigma}}^{-1} \cdot \bar{\bar{\sigma}} - 1\right) \cdot \bar{E} = 0 \qquad \text{(C-14)}$$

Substituting $\bar{\bar{\sigma}}$ from eq. (C-12) and $\bar{\bar{\sigma}}^{-1}$ from eq. (C-3) and carrying out the indicated operations,

$$\frac{\omega}{\omega_p^2}\begin{pmatrix} (i\omega+\nu)(\mu^2-1)+i\frac{\omega_b^2}{\omega} & 0 & \omega_b \\ 0 & (i\omega+\nu)(\mu^2-1)+i\frac{\omega_b^2}{\omega} & 0 \\ \omega_b(\mu^2-1) & 0 & -(i\omega+\nu)+i\frac{\omega_p^2}{\omega} \end{pmatrix}\begin{pmatrix} E_x \\ E_y \\ E_z \end{pmatrix} = 0 \qquad \text{(C-15)}$$

[+]A characteristic wave is defined as one which does not change its state of polarization as it propagates, thus characterizing a fundamental mode of propagation.

This set of three scalar equations among the electric field components has a general solution for μ^* provided the determinant of the coefficients vanishes. The solution of the determinental equation in this case yields a simplified form (i.e. $\theta = 90^\circ$) of the more general Appleton-Hartree equation for the refractive index,

$$\mu^{*2} = 1 - \frac{(\omega_p/\omega)^2}{(1 - i\nu/\omega) - \frac{(\omega_b/\omega)^2}{2\left[1 - \left(\frac{\omega_p}{\omega}\right)^2 - i\frac{\nu}{\omega}\right]} \pm \frac{(\omega_b/\omega)^2}{2\left[1 - \left(\frac{\omega_p}{\omega}\right)^2 - i\frac{\nu}{\omega}\right]}} \qquad \text{(C-16)}$$

from which the appropriate index for the two characteristic waves can be recovered directly. However it is more useful for the present purposes to derive the index from the individual equations.

The second of the three eqs. (C-15) requires either

$$E_y = 0 \qquad \text{(C-17)}$$

or

$$\mu^*_{ord} = 1 - \frac{(\omega_p/\omega)^2}{1 - i\nu/\omega} \qquad \text{(C-18)}$$

where μ^*_{ord} is conventionally identified with the "ordinary" wave, a characteristic wave whose polarization is colinear with the applied magnetic field. In this case the parallel alignment of the electric wave vector with the $\overline{B}$ field allows the electrons to oscillate without restriction, so that the magnetic field does not appear explicitly in eq. (C-18), and the refractive index is identical with the isotropic, or "ordinary," plasma result of eq. (6-17).

If the electric vector is not parallel to $\overline{B}$, the plasma will support the wave motion only if the field components are

related by the first equation

$$\frac{E_z}{E_x} = \frac{(i+\nu/\omega)(\mu^{*2}-1)+i(\omega_p/\omega)^2}{(\omega_b/\omega)} \tag{C-19}$$

and the third equation

$$\frac{E_z}{E_x} = \frac{(\omega_b/\omega)(\mu^{*2}-1)}{(i+\nu/\omega)-i(\omega_p/\omega)^2} \tag{C-20}$$

of (C-15).

For these to be compatible they must be equal, yielding the refractive index

$$\mu^{*2}_{ex} = 1 - \frac{(\omega_p/\omega)^2}{(1-i\nu/\omega) - \dfrac{(\omega_b/\omega)^2}{1-(\omega_p/\omega)^2 - i(\nu/\omega)}} \tag{C-21}$$

in the so-called "extraordinary" mode. This characteristic wave is polarized perpendicular to the applied magnetic field, and clearly develops a longitudinal component E_z, given by substituting eq. (C-21) into either eq. (C-19) or (C-20). The resulting ratio is complex even for the collisionless case, $\nu/\omega \to 0$:

$$\frac{E_z}{E_x} = i\,\frac{(\omega_b/\omega)(\omega_p/\omega)^2}{1-(\omega_p/\omega)^2-(\omega_b/\omega)^2} \tag{C-22}$$

indicating a degree of elliptical polarization in the propagation direction which is approximately linear in B_θ for high electron densities.

It is instructive to consider the collisionless limit of the refractive index,

$$\mu^*_{ex} = \left\{ \frac{\left[1-(\omega_p/\omega)^2\right]^2 - (\omega_b/\omega)^2}{1-(\omega_p/\omega)^2 - (\omega_b/\omega)^2} \right\}^{\frac{1}{2}} \qquad \text{(C-23)}$$

From the usual definitions of the zeros and poles of the index,

cutoff: $\mu^* \to 0, \quad \lambda \to \infty$ (C-24)

resonance: $\mu^* \to \infty, \quad \lambda \to 0$ (C-25)

the extraordinary wave cutoffs

$$\left[1-(\omega_p/\omega)^2\right]^2 - (\omega_b/\omega)^2 = 0 \qquad \text{(C-26)}$$

or

$$\left(\frac{\omega_p}{\omega}\right)^2 \pm \left(\frac{\omega_b}{\omega}\right) = 1 \qquad \text{(C-27)}$$

and resonances

$$1-(\omega_p/\omega)^2 - (\omega_b/\omega)^2 = 0 \qquad \text{(C-28)}$$

or

$$(\omega_p/\omega)^2 + (\omega_b/\omega)^2 = 1 \qquad \text{(C-29)}$$

are found. The resulting propagation domains are displayed in Fig. 6-24 and discussed in section 6-5.

A cutoff plasma permits wave penetration to a distance given approximately by the skin depth (eq. (6-48)). For the extraordinary wave in a collisionless plasma, the skin depth is defined for all real β, and in general exhibits strong dependence on the magnetic field:

$$d_p = \frac{1}{\beta} = \frac{1}{k_0}\left\{\frac{\left(\frac{\omega_b}{\omega}\right)^2 + \left(\frac{\omega_p}{\omega}\right)^2 - 1}{\left[1-\left(\frac{\omega_p}{\omega}\right)^2\right]^2 - \left(\frac{\omega_b}{\omega}\right)^2}\right\}^{\frac{1}{2}} \qquad \text{(C-30)}$$

(see section 6-5).

The conductivity of the plasma to the extraordinary mode is found by combining eq. (6-14) and eq. (C-23),

$$\sigma_{ex} = -i\epsilon_0\omega\left\{\frac{\left(\frac{\omega_p}{\omega}\right)^2\left[1-\left(\frac{\omega_p}{\omega}\right)^2\right]}{1-\left(\frac{\omega_p}{\omega}\right)^2-\left(\frac{\omega_b}{\omega}\right)^2}\right\} \qquad \text{(C-31)}$$

an expression which relates the current density and electric field components normal to the applied magnetic field. Since the normal electric field also drives Hall currents, this conductivity must be effectively smaller than σ_{ord}, for $\overline{B}$ effectively absent. Using eq. (6-11), in the collisionless limit, the ratio can be formed:

$$\frac{\sigma_{ex}}{\sigma_{ord}} = \frac{\omega^2-\omega_p^2}{\omega^2-\omega_p^2-\omega_b^2} = \frac{1}{1-\dfrac{(\omega_b/\omega)^2}{1-(\omega_p/\omega)^2}} \qquad \text{(C-32)}$$

which confirms this result quantitatively.

The reflection coefficient from an anisotropic plasma interface can be calculated as in section 6-3, by solving the appropriate boundary value problem. However certain new and rather subtle features arise in the extraordinary wave problem involving the wave polarizations. Consider a plane wave to be incident on the plasma interface at Z = 0 from the left, as shown in Fig. C-1. The incident wave is assumed to be linearly polarized along $\hat{x}$, thus exciting the extraordinary mode in the plasma which has both transverse and longitudinal components, as given by eq. (C-22). The problem is thus how to match a linearly polarized wave to an elliptically polarized wave, i.e. a TEM wave to a TM wave. Several authors[63,64,65] have recently dealt with this problem in varying degrees of generality, and have shown that the reflection coefficient can be uniquely and consistently defined as

$$R_{ex} = \frac{1-\mu^*_{ex}}{1+\mu^*_{ex}} \tag{C-33}$$

within a possible sign ambiguity depending on whether the amplitude coefficients are defined in terms of $\overline{E}$ or $\overline{H}$.[54] It is a straightforward matter to show that

$$R_{ord} = \frac{1-\mu^*_{ord}}{1+\mu^*_{ord}} \tag{C-34}$$

similar to the isotropic result of section 6-3. Computed curves for R_{ex} are displayed and discussed in section 6-5.

Appendix D

COMPUTER PROGRAM TO EVALUATE COMPLEX REFLECTION COEFFICIENTS FROM AN INVERSE EXPONENTIAL ELECTRON DENSITY GRADIENT

The derivation of complex reflection coefficients for the exponential profile [eq. (6-71)] is discussed in section 6.6. The exact solution for R involves Bessel functions of complex order and argument [eq. (6-95)], while the narrow ramp approximation [eq. (6-102)] is an algebraic equation in μ^*_{eo}, the refractive index of the (uniform) plasma [eqs. (6-18) and (6-19)]. Both the exact and approximate expressions for R involve the ramp parameter m [eq. (6-71)], or alternately δ [eq. (6-103)], and the familiar quantities $(\omega_p/\omega)^2$ and ν/ω, through μ^*_{eo} [re eq. (6-80) and (6-86)]. Thus by specifying δ, $(\omega_p/\omega)^2$, and ν/ω, the quantities of interest, $|R|$, φ_R, $\beta_\pm$ can in principle be calculated.

The computer program used for calculating these quantities is given below. The complex Bessel function subroutine is based on SHARE program NYU BES4,[93] with several modifications. The iteration scheme to generate the functions is based on familiar recursion relations, discussed in section 6.6 and the references (76, 77, 94). The acceptable range of parameters which could be handled by the subroutine was extended and the call statement to the subroutine, incorrectly published in SHARE, was corrected.

A new subroutine was needed to calculate the natural logarithm of gamma functions of complex argument and this was added to the program. The method involved an expansion in terms of continued fractions,[95] and sample calculations agreed with published tables[96] to six significant figures.

The overall Bessel function routine was checked in two ways, both indirect since general tables of the complex function do not exist and hand calculations are prohibitively long. First, the routine was checked against the limited tables which do exist, particularly for real values of order and argument; and second, every calculated value used in computing R was tested against the various recursion relations to assure internal consistency.

The output of the listed program was in the form of printed tables and punched cards. The latter were used as the input data for CALCOMP plotter programs, not listed here, which automatically plotted $|R|$, φ_R and ρ as functions of $(\omega_p/\omega)^2$ for given ν/ω and δ (Figs. 6-30 and 6-31).

```
C      EXPONENTIAL RAMP MICROWAVE COMPUTATION (VERSION II)
C      INVERSE EXPONENTIAL DENSITY PROFILE
C      THE PURPOSE OF THIS PROGRAM IS TO CALCULATE COMPLEX REFLECTION
C       COEFFICIENTS FROM A DUFFUSE PLASMA BOUNDARY
C      THIS PROGRAM MAKES NO USE OF FORTRAN COMPLEX ARITHMETIC
C      AUTHORS   W. R. ELLIS, JR.   AND   L. HOFFMAN
C      DATE      13 FEB   1966


CNAME    SOURCE PROGRAM
       DIMENSION OMPSQT(225)
       DIMENSION BJRE(400),BJIM(400),YRE(400),YIM(400)
       COMMON CHECK1,CHECK2
     1 FORMAT(8F10.0)
     2 FORMAT(I5)
     3 FORMAT(E10.4)
    10 FORMAT(1H1,12X,10HZNU=NU/W= ,F4.2)
    11 FORMAT(12X,3HZ*=,F4.2)
    15 FORMAT(3X,5HOMPSQ,6X,4HCHI1,6X,4HCHI2,7X,2HP1,8X,2HP2,4X,
      1 8HRE JP(X),2X,8HIM JP(X),1X,10HRE JP+1(X),1X,10HIM JP+1(X),4X,
      2 3HPRP,7X,3HPRN,6X,4HRMAG,6X,4HPHIR)
    16 FORMAT(1P13E10.3,2A1)
    17 FORMAT(1H1)
    18 FORMAT(1P7E10.3,0P2F5.2,    2A1)
       CALL FPTEST(DUMMY)
       RIT5,1,ZNU
       RIT5,2,NN
       RIT5,3,(OMPSQT(I),I=1,NN)
    99 RIT5,1,ZMIN
C      ZSTAR = DELTA = RAMP PARAMETER = 2.5/M
       ZSTAR=2.5*ZMIN
       LINE=50
       WOT 6,10,ZNU
       WOT6,11,ZSTAR
       WOT6,15
       DO 4 I=1,NN
       CHECK1=1H
       CHECK2=1H
       OMPSQ=OMPSQT(I)
       ZNUSQ=ZNU*ZNU
       A=1.-OMPSQ/(1.+ZNUSQ)
       B=SQRTF(ABSF(A**2+ZNUSQ*(1.-A)**2))
       ALPHA=SQRTF(ABSF(.5*(A+B)))
       BETA=SQRTF(ABSF(.5*(-A+B)))
C      ZK=ALPHA-I BETA
C      ZK1=ALPHA
C      ZK2=-BETA
C      ZA=1+K
       ZA1=1.+ALPHA
C      ZA2=-BETA
C      ZB=1-K
       ZB1=1.-ALPHA
C      ZB2=BETA
C      ZC=K**2
       ZC1=ALPHA**2-BETA**2
```

```
      ZC2=-2.*ALPHA*BETA
C     ZD=1-K**2
      ZD1=1.-ZC1
      ZD2=-ZC2
C     ZE=(1-K**2)**1/2
      T1=ZD1*ZD1 + ZD2*ZD2
      ZE1=.707106781    *SQRTF(ABSF( ZD1+SQRTF(T1)))
      ZE2=.707106781    *SQRTF(ABSF(-ZD1+SQRTF(T1)))
C     CHI=(2 PIE/M)(1-K**2)**1/2
      PIE=3.14159265358979323846
      ZCON=2.*PIE*ZMIN
      CHI1=ZCON*ZE1
      CHI2=ZCON*ZE2
C     P=(2 PIE/M)K
      P1=ZCON*BETA
      P2=ZCON*ALPHA
      IF (ZMIN) 20,22,20
   20 CONTINUE
      N=P1
      C=N
      PF=P1-C
C      PF  = FRACTIONAL PART OF P1
      CALL COMBES(CHI1,CHI2,PF,P2,N,BJRE,BJIM,YRE,YIM)
      B1=BJRE(N+1)
      B2=BJIM(N+1)
      B3=BJRE(N+2)
      B4=BJIM(N+2)
C     R=( (1-K)JP(X)-I(1-K**2)**1/2JP+1(X) )/( (1+K)JP(X)+I(1-K**2)
C        **1/2 JP+1(X))
C     R=RNUM/RDEN
      T2=B2*BETA
      T3=B3*ZE2
      T4=B4*ZE1
      T5=B1*BETA
      T6=B2*ZB1
      T7=B3*ZE1
      T8=B4*ZE2
      T9=-T2+T3+T4
      T10=T5-T7+T8
      RNUM1=B1*ZB1+T9
      RNUM2=T6+T10
      RDEN1=B1*ZA1-T9
      RDEN2=T6-T10
C       R=R1 + IR2
      SMSQ=RDEN1*RDEN1+RDEN2*RDEN2
      R1=(RNUM1*RDEN1+RNUM2*RDEN2)/SMSQ
      R2=(RNUM2*RDEN1-RNUM1*RDEN2)/SMSQ
      RMAGSQ=R1*R1+R2*R2
      RMAG=SQRTF(RMAGSQ)
      TT=ATANF(R2/R1)
      IF (R1) 240,205,205
  205 PHIR=TT
      GO TO 8888
  240 IF (R2) 207,203,203
  203 PHIR=TT + PIE
```

```
      GO TO 8888
  207 PHIR=TT-PIE
 8888 CONTINUE
      T11=1.+RMAGSQ
      T12=2.*RMAG*COSF(PHIR)
      PRP=T11+T12
      PRN=T11-T12
C     RX=( (1-K)-I(PIE/M)(1-K**2) )/( (1PK)+I(PIE/M)(1-K**2) )
   22 RNUM1X=ZB1+P1*ALPHA
      RNUM2X=BETA-ZCON*ZD1*.5
      RDEN1X=ZA1-ALPHA*P1
      RDEN2X=-RNUM2X
      SMSQX=RDEN1X*RDEN1X+RNUM2X*RNUM2X
      R1X=(RNUM1X*RDEN1X-RNUM2X*RNUM2X)/SMSQX
      R2X=RNUM2X*(RDEN1X+RNUM1X)/SMSQX
      RMGSQX=R1X*R1X + R2X*R2X
      RMAGX=SQRTF(RMGSQX)
      TTT=ATANF(R2X/R1X)
      IF (R1X) 140,105,105
  105 PHIRX=TTT
      GO TO 9999
  140 IF (R2X) 107,103,103
  103 PHIRX=TTT+PIE
      GO TO 9999
  107 PHIRX=TTT-PIE
 9999 CONTINUE
      T11X=1.+RMGSQX
      T12X=2.*RMAGX*COSF(PHIRX)
      PRPX=T11X+T12X
      PRNX=T11X-T12X
      RAD=57.2957795
      PHIR=PHIR*RAD
      PHIRX=PHIRX*RAD
      IF(DUMMY) 301,300,301
  301 DUMMY=0.
      CHECK1=1H*
  300 CONTINUE
      IF(ZMIN)25,26,25
   26 CONTINUE
      RMAG=RMAGX
      PHIR=PHIRX
      PRP=PRPX
      PRN=PRNX
   25 CONTINUE
      PDQ=PRP**.707107
      WOT6,16,OMPSQ,CHI1,CHI2, P1,P2,B1,B2,B3,B4,PRP,PRN,RMAG,PHIR
     1  ,CHECK1,CHECK2
      PUNCH 18,OMPSQ,RMAG,PHIR,PRP,PRN,B1,PDQ,ZNU,ZSTAR,CHECK1,CHECK2
      LINE=LINE-1
      IF(LINE) 30,30,4
   30 CONTINUE
      WOT6,17
      WOT6,15
      LINE=50
    4 CONTINUE
```

```
      GO TO 99
      END


CNAME    COMPLEX BESSEL FUNCTION SUBROUTINE      PART 1 OF  17
C     BASED ON SHARE LIBRARY ROUTINE NYUBES4
C        THIS ROUTINE MAKES NO USE OF FORTRAN COMPLEX ARITHMETIC
      SUBROUTINE COMBES(X,Y,ALPHA,BETA,N,BJRE,BJIM,YRE,YIM)
      DIMENSION BJRE(100),BJIM(100),YRE(50),YIM(50)
      CALL START(X,Y,N,K,R)
      CALL JRECUR(X,Y,ALPHA,BETA,K,R,BJRE,BJIM)
      CALL JSUM(ALPHA,BETA,K,BJRE,BJIM,SUMRA,SUMIA)
      CALL FACTOR(X,Y,ALPHA,BETA,Q,R)
      CALL JNORM(K,Q,R,SUMRA,SUMIA,BJRE,BJIM)
 7    CALL YSUM (X,Y,ALPHA,BETA,K,BJRE,BJIM,ASUMR,ASUMI)
 8    CALL YGNU (X,Y,ALPHA,BETA,Q,R,ASUMR,ASUMI,BJRE,BJIM,YRE,YIM)
 9    CALL WRONSK (X,Y,BJRE,BJIM,YRE,YIM)
       BJSQ=BJRE(1)**2+BJIM(1)**2
       IF(BJSQ-.00000005) 14,14,15
 14   CALL YSUMP(X,Y,ALPHA,BETA,K,BJRE,BJIM,ASUMR,ASUMI)
      CALL YGNUP(X,Y,ALPHA,BETA,Q,R,ASUMR,ASUMI,BJRE,BJIM,YRE,YIM)
 15   IF (N-1)10,12,11
 10   IF (N)13,12,12
 13   CALL NEGN (X,Y,ALPHA,BETA,N,BJRE,BJIM,YRE,YIM)
      GO TO 12
   11 CALL YRECUR(X,Y,N,BJRE,BJIM,YRE,YIM)
 12   RETURN
       END
CNAME    START SUBROUTINE                        PART 2 OF 17
      SUBROUTINE START(X,Y,N,K,R)
      SSQ=X**2+Y**2
      KTEN=SQRTF(SSQ)+20.0
      NTEN=XABSF(N)+10
      M=XMAXOF(KTEN,NTEN) /2
      K=2*M+1
          R = K + 1
      RETURN
      END
CNAME    JRECUR SUBROUTINE                       PART 3 OF 17
      SUBROUTINE JRECUR(X,Y,ALPHA,BETA,K,R,BJRE,BJIM)
      DIMENSION BJRE(100),BJIM(100)
      RALPHA=R+ALPHA
      SSQ=X**2+Y**2
      BJRE(K+2)=0
      BJIM(K+2)=0
      BJRE(K+1)=1.0E-37
      BJIM(K+1)=0.0
      DO4I=1,K
      L1=K+1-I
      RALPHA=RALPHA-1.0
      A=((2.0*X*RALPHA)+(2.0*BETA*Y))/SSQ
      B=((-2.0*Y*RALPHA)+(2.0*BETA*X))/SSQ
      BJRE(L1)=(A*BJRE(L1+1))-(B*BJIM(L1+1))-BJRE(L1+2)
 4    BJIM(L1)=(B*BJRE(L1+1))+(A*BJIM(L1+1))-BJIM(L1+2)
      RETURN
      END
```

```
CNAME    JSUM SUBROUTINENE                                  PART 4 OF 17
      SUBROUTINE JSUM(ALPHA,BETA,K,BJRE,BJIM,SUMRA,SUMIA)
      DIMENSION BJRE(100),BJIM(100)
 801  SUMRA=(BJRE(3)*(ALPHA+2.0))-(BJIM(3)*BETA)
      SUMIA=(BETA*BJRE(3))+((ALPHA+2.0)*BJIM(3))
      GRE=1.0
      GIM=0
      S=1.0
      DO6I=5,K,2
      S=S+1.0
      GREN=((GRE*(ALPHA+S-1.0))-(BETA*GIM))/S
      GIM=((GIM*(ALPHA+S-1.0))+(BETA*GRE))/S
      GRE=GREN
      ALPTS=ALPHA+2.0*S
      GJR=GRE*BJRE(I)
      GJI=GIM*BJIM(I)
      GJRI=GRE*BJIM(I)
      GJIR=GIM*BJRE(I)
      SUMRB=ALPTS*(GJR-GJI)-BETA*(GJIR+GJRI)+SUMRA
      SUMIB=ALPTS*(GJIR+GJRI)-BETA*(GJI-GJR)+SUMIA
      IF(ABSF((SUMRB/SUMRA)-1.0)-.00000005)21,21,10
 21   IF(SUMIA)20,11,20
 20   IF(ABSF((SUMIB/SUMIA)-1.0)-.00000005)11,11,10
 10   SUMRA=SUMRB
 6    SUMIA=SUMIB
   11 RETURN
       END
CNAME    FACTOR SUBROUTINE                                  PART 5 OF 17
      SUBROUTINE FACTOR(X,Y,ALPHA,BETA,Q,R)
      CALL LOGGAM(ALPHA+1.0,BETA,U,V)
      CALL COMLOG(X,Y,A1,B1)
      A2=ALPHA*A1-BETA*B1
      B2=BETA*A1+ALPHA*B1
      A2=-A2
      B2=-B2
      CALL COMEXP(A2,B2,A3,B3)
      A4=.6931471806*ALPHA
      B4=.6931471806*BETA
      CALL COMEXP(A4,B4,A5,B5)
      A6=A3*A5-B3*B5
      B6=B3*A5+A3*B5
      CALL COMEXP(U,V,A7,B7)
      Q=A6*A7-B6*B7
      R=B6*A7+A6*B7
      RETURN
       END
CNAME    COMLOG SUBROUTINE                                  PART 6 OF 17
C     COMPLEX LOGARITHM - BRANCH CUT ON NEGATIVE REAL AXIS
      SUBROUTINE COMLOG(X,Y,A,B)
      PI=3.141592654
      A=.5*LOGF(X*X+Y*Y)
      IF(X)5,1,4
 1    B=.5*PI
      IF(Y)2,3,8
 2    B=-B
```

```
      GO TO 8
 3    B=0.
      GO TO 8
 4    B=ATANF(Y/X)
      GO TO 8
 5    B=ATANF(Y/X)
      IF(Y)6,7,7
 6    B=B-PI
      GO TO 8
 7    B=B+PI
 8    RETURN
       END
CNAME     COMEXP SUBROUTINE                          PART 7 OF 17
      SUBROUTINE COMEXP(X,Y,A,B)
      COMMON CHECK1,CHECK2
      IF(ABSF(X)-88.) 1,1,2
    2 C=EXPF(88.*X/ABSF(X))
      CHECK2=1H*
      GO TO 3
    1 CONTINUE
      C=EXPF(X)
    3 CONTINUE
      A=C*COSF(Y)
      B=C*SINF(Y)
      RETURN
       END
CNAME     JNORM SUBROUTINE                           PART 8 OF 17
      SUBROUTINE JNORM(K,Q,R,SUMRA,SUMIA,BJRE,BJIM)
      DIMENSION BJRE(100),BJIM(100)
      S=((SUMRA+BJRE(1))*Q)-((SUMIA+BJIM(1))*R)
      T=((SUMIA+BJIM(1))*Q)+((SUMRA+BJRE(1))*R)
      IF(ABSF(S)-ABSF(T))100,101,101
 101  TS=T/S
      TSSQ=S*(1.0+(TS**2))
 12   DO13I=1,K
      BJREN=(BJRE(I)+BJIM(I)*TS)/TSSQ
      BJIM(I)=(BJIM(I)-BJRE(I)*TS)/TSSQ
 13   BJRE(I)=BJREN
      GO  TO  14
 100  ST=S/T
      STSQ=T*((ST**2)+1.0)
 102  DO103I=1,K
      BJREN=(BJRE(I)*ST+BJIM(I))/STSQ
      BJIM(I)=(BJIM(I)*ST-BJRE(I))/STSQ
 103  BJRE(I)=BJREN
   14 RETURN
       END
CNAME     YSUM SUBROUTINE                            PART 9 OF 17
      SUBROUTINE YSUM (X,Y,ALPHA,BETA,K,BJRE,BJIM,ASUMR,ASUMI)
      DIMENSION BJRE(100),BJIM(100)
      A1=ALPHA-1.0
      A2=A1-1.0
      A3=A1+ALPHA
      A4=BETA**2
      A5=2.0*A4
```

```
      ABSQ=(-A1)**2+A4
      GAMRE=((2.0+ALPHA)*(-A1)-A4)/ABSQ
      GAMIM=(BETA*3.0)/ABSQ
      ASUMR=GAMRE*BJRE(3)-GAMIM*BJIM(3)
      ASUMI=GAMIM*BJRE(3)+GAMRE*BJIM(3)
      T=1.0
      DO 500 I=5,K,2
      T=T+1.0
      B1=2.0*T
      F1=B1+ALPHA
      F2=A3+T
      F3=A1+T
      F5=T-ALPHA
      F6=A2+B1
      G1=F1*F2-A5
      G2=(F2+2.0*F1)*BETA
      H1=G1*F3-G2*BETA
      H2=G2*F3+G1*BETA
      P1=F5*F6+A4
      P2=(F5-F6)*BETA
      P3=P1**2+P2**2
      CRE=((H1*P1+H2*P2)/P3)/T
      CIM=((H2*P1-H1*P2)/P3)/T
      TEMP=-(CRE*GAMRE-CIM*GAMIM)
      GAMIM=-(CIM*GAMRE+CRE*GAMIM)
      GAMRE=TEMP
      BSUMR=GAMRE*BJRE(I)-GAMIM*BJIM(I)+ASUMR
      BSUMI=GAMIM*BJRE(I)+GAMRE*BJIM(I)+ASUMI
      IF(ABSF((BSUMR/ASUMR)-1.0)-.00000005)521,521,510
  521 IF(ASUMI)520,511,520
  520 IF(ABSF((BSUMI/ASUMI)-1.0)-.00000005)511,511,510
  510 ASUMR=BSUMR
  500 ASUMI=BSUMI
  511 RETURN
       END
CNAME    YGNU SUBROUTINE                                PART 10 OF 17
      SUBROUTINE YGNU(X,Y,ALPHA,BETA,Q,R,ASUMR,ASUMI,BJRE,BJIM,YRE,YIM)
      DIMENSION BJRE(100),BJIM(100),YRE(50),YIM(50)
      PI=3.141592654
      TPI=2.0/PI
      QRE=TPI*(Q**2-R**2)
      QIM=TPI*2.0*Q*R
      DRE=QRE*ASUMR-QIM*ASUMI
      DIM=QIM*ASUMR+QRE*ASUMI
      IF(ALPHA)1,2,1
    2 IF(BETA)1,3,1
    3 CALL YZERO(X,Y,ALPRE,ALPIM)
      GO TO 720
    1 PALPHA=PI*ALPHA
      COX=COSF(PALPHA)
      SIX=SINF(PALPHA)
      EXY=EXPF(PI*BETA)
      EXY1=1.0/EXY
      COSH=.5*(EXY+EXY1)
      SINH=.5*(EXY-EXY1)
```

```
      DEN=(SIX*COSH)**2+(COX*SINH)**2
      ERE=(SIX*COX)/DEN
      EIM=(-COSH*SINH)/DEN
      ABSQ3=2.0*(ALPHA**2+BETA**2)
      ALPRE=ERE-((QRE*ALPHA+BETA*QIM)/ABSQ3)
      ALPIM=EIM-((QIM*ALPHA-BETA*QRE)/ABSQ3)
  720 YRE(1)=ALPRE*BJRE(1)-ALPIM*BJIM(1)+DRE
      YIM(1)=ALPIM*BJRE(1)+ALPRE*BJIM(1)+DIM
      RETURN
       END
CNAME    YZERO SUBROUTINE                              PART 11 OF 17
      SUBROUTINE YZERO(X,Y,ALPRE,ALPIM)
      TPI=2.0/3.141592654
      CALL COMLOG(X,Y,A,B)
      ALPRE=TPI*(-.1159315157+A)
      ALPIM=TPI*B
      RETURN
       END
CNAME    WRONSK SUBROUTINE                             PART 12 OF 17
      SUBROUTINE WRONSK(X,Y,BJRE,BJIM,YRE,YIM)
      DIMENSION BJRE(100),BJIM(100),YRE(50),YIM(50)
      SSQ=X**2+Y**2
      TPI=2.0/3.141592654
      AZRE=TPI*X/SSQ
      AZIM=-TPI*Y/SSQ
      ZRE=BJRE(2)*YRE(1)-BJIM(2)*YIM(1)
      ZIM=BJIM(2)*YRE(1)+BJRE(2)*YIM(1)
      BZRE=ZRE-AZRE
      BZIM=ZIM-AZIM
      BJSQ=BJRE(1)**2+BJIM(1)**2
      CZRE=BJRE(1)/BJSQ
      CZIM=(-BJIM(1))/BJSQ
      YRE(2)=BZRE*CZRE-BZIM*CZIM
      YIM(2)=BZIM*CZRE+BZRE*CZIM
      RETURN
       END
CNAME    NEGN SUBROUTINE                               PART 13 OF 17
      SUBROUTINE NEGN(X,Y,ALPHA,BETA,N,BJRE,BJIM,YRE,YIM)
      DIMENSION BJRE(100),BJIM(100),YRE(50),YIM(50)
      L=XABSF(N)+1
      SSQ=X**2+Y**2
      TX=2.0*X
      TY=2.0*Y
      RALPHA=ALPHA
      A=(TX*RALPHA+TY*BETA)/SSQ
      B=(-TY*RALPHA+TX*BETA)/SSQ
      BJRE(2)=A*BJRE(1)-B*BJIM(1)-BJRE(2)
      BJIM(2)=B*BJRE(1)+A*BJIM(1)-BJIM(2)
      YRE(2)=A*YRE(1)-B*YIM(1)-YRE(2)
      YIM(2)=B*YRE(1)+A*YIM(1)-YIM(2)
      DO 1 I=3,L
      RALPHA=RALPHA-1.0
      A=(TX*RALPHA+TY*BETA)/SSQ
      B=(-TY*RALPHA+TX*BETA)/SSQ
```

```
      BJRE(I)=A*BJRE(I-1)-B*BJIM(I-1)-BJRE(I-2)
      BJIM(I)=B*BJRE(I-1)+A*BJIM(I-1)-BJIM(I-2)
      YRE(I)=A*YRE(I-1)-B*YIM(I-1)-YRE(I-2)
 1    YIM(I)=B*YRE(I-1)+A*YIM(I-1)-YIM(I-2)
      RETURN
       END
CNAME    YRECUR SUBROUTINE                                  PART 14 OF 17
      SUBROUTINE YRECUR(X,Y,N,BJRE,BJIM,YRE,YIM)
      DIMENSION BJRE(100),BJIM(100),YRE(50),YIM(50)
      SSQ=X**2+Y**2
      TPI=2.0/3.141592654
      AZRE=TPI*X/SSQ
      AZIM=-TPI*Y/SSQ
      L=N+1
      DO 1 I=3,L
      ZRE=BJRE(I)*YRE(I-1)-BJIM(I)*YIM(I-1)
      ZIM=BJIM(I)*YRE(I-1)+BJRE(I)*YIM(I-1)
      BZRE=ZRE-AZRE
      BZIM=ZIM-AZIM
      BJSQ=BJRE(I-1)**2+BJIM(I-1)**2
      CZRE=BJRE(I-1)/BJSQ
      CZIM=(-BJIM(I-1))/BJSQ
      YRE(I)=BZRE*CZRE-BZIM*CZIM
    1 YIM(I)=BZIM*CZRE+BZRE*CZIM
      RETURN
       END
CNAME    YGNUP SUBROUTINE                                   PART 15 OF 17
      SUBROUTINE YGNUP(X,Y,ALPHA,BETA,Q,R,ASUMR,ASUMI,BJRE,BJIM,YRE,YIM)
      DIMENSION BJRE(100),BJIM(100),YRE(50),YIM(50)
      PI=3.141592654
      TPI=2.0/PI
      QRE=TPI*(Q**2-R**2)
      QIM=TPI*2.0*Q*R
      DRE=QRE*ASUMR-QIM*ASUMI
      DIM=QIM*ASUMR+QRE*ASUMI
      IF(ALPHA)1,2,1
 2    IF(BETA)1,3,1
 3    CALL YZERO(X,Y,ALPRE,ALPIM)
      GO TO 720
 1    PALPHA=PI*ALPHA
      COX=COSF(PALPHA)
      SIX=SINF(PALPHA)
      EXY=EXPF(PI*BETA)
      EXY1=1.0/EXY
      COSH=.5*(EXY+EXY1)
      SINH=.5*(EXY-EXY1)
      DEN=(SIX*COSH)**2+(COX*SINH)**2
      ERE=(SIX*COX)/DEN
      EIM=(-COSH*SINH)/DEN
      ABSQ3=2.0*(ALPHA**2+BETA**2)
      ALPRE=ERE-((QRE*ALPHA+BETA*QIM)/ABSQ3)
      ALPIM=EIM-((QIM*ALPHA-BETA*QRE)/ABSQ3)
 720  TRE=ALPRE*BJRE(2)-ALPIM*BJIM(2)+DRE
      TIM=ALPIM*BJRE(2)+ALPRE*BJIM(2)+DIM
      ALPRE=-(Q*X+R*Y)/(X**2+Y**2)
      ALPIM=-(X*R-Q*Y)/(X**2+Y**2)
```

```
      YRE(2)=ALPRE*BJRE(1)-ALPIM*BJIM(1)+TRE
      YIM(2)=ALPIM*BJRE(1)+ALPRE*BJIM(1)+TIM
      RETURN
       END
CNAME    YSUMP SUBROUTINE                                  PART 16 OF 17
      SUBROUTINE YSUMP(X,Y,ALPHA,BETA,K,BJRE,BJIM,ASUMR,ASUMI)
      DIMENSION BJRE(100),BJIM(100)
      A1=ALPHA-1.0
      A2=A1-1.0
      A3=A1+ALPHA
      A4=BETA**2
      A5=2.0*A4
      ABSQ=(-A1)**2+A4
      ROLDRE=((2.0+ALPHA)*(-A1)-A4)/ABSQ
      ROLDIM=(BETA*3.0)/ABSQ
      RES1=-ROLDRE/2.0
      VMS1=-ROLDIM/2.0
      STORE=3.*(ALPHA*X+BETA*Y)/(X**2+Y**2)
      STOIM=3.*(X*BETA-ALPHA*Y)/(X**2+Y**2)
      RES2=(ROLDRE*STORE-ROLDIM*STOIM)
      VMS2=(ROLDRE*STOIM+ROLDIM*STORE)
      ASUMR=RES1*BJRE(2)-VMS1*BJIM(2)
      ASUMR=ASUMR+RES2*BJRE(3)-VMS2*BJIM(3)
      ASUMI=VMS1*BJRE(2)+RES1*BJIM(2)
      ASUMI=ASUMI+VMS2*BJRE(3)+RES2*BJIM(3)
      T=1.0
      DO 500 I=3,K,2
      T=T+1.0
      B1=2.0*T
      F1=B1+ALPHA
      F2=A3+T
      F3=A1+T
      F5=T-ALPHA
      F6=A2+B1
      G1=F1*F2-A5
      G2=(F2+2.0*F1)*BETA
      H1=G1*F3-G2*BETA
      H2=G2*F3+G1*BETA
      P1=F5*F6+A4
      P2=(F5-F6)*BETA
      P3=P1**2+P2**2
      CRE=((H1*P1+H2*P2)/P3)/T
      CIM=((H2*P1-H1*P2)/P3)/T
      TEMP=-(CRE*ROLDRE-CIM*ROLDIM)
      RNEWIM=-(CIM*ROLDRE+CRE*ROLDIM)
      RNEWRE=TEMP
      RES1=(ROLDRE-RNEWRE)/2.0
      VMS1=(ROLDIM-RNEWIM)/2.0
      RES2=(RNEWRE*STORE-RNEWIM*STOIM)
      VMS2=(RNEWRE*STOIM+RNEWIM*STORE)
      BSUMR=RES1*BJRE(I+1)-VMS1*BJIM(I+1)+ASUMR
      BSUMI=VMS1*BJRE(I+1)+RES1*BJIM(I+1)+ASUMI
      BSUMR=RES2*BJRE(I+2)-VMS2*BJIM(I+2)+BSUMR
      BSUMI=VMS2*BJRE(I+2)+RES2*BJIM(I+2)+BSUMI
      IF(ABSF((BSUMR/ASUMR)-1.0)-.00000005)521,521,510
```

```
521   IF(ASUMI)520,511,520
520   IF(ABSF((BSUMI/ASUMI)-1.0)-.00000005)511,511,510
510   ASUMR=BSUMR
      ASUMI=BSUMI
      ROLDIM=RNEWIM
500   ROLDRE=RNEWRE
511   RETURN
       END
;NAME     LOGGAM SUBROUTINE                          PART 17 OF 17
      SUBROUTINE LOGGAM(ZRE,ZIM,FZRE,FZIM)
      DIMENSION BJRE(100),BJIM(100)
      DIMENSION C(7)
      COMMON BJRE,BJIM,C
      C(1)=.83333333333333E-01
      C(2)=.33333333333333E-01
      C(3)=.25238095238095E-00
      C(4)=.52560646900269 54E-00
      C(5)=.10115230681268 41E+01
      C(6)=.15174736491532 87E+01
      C(7)=.22694889742049 59E+01
      Q4=.91893853320467 25E+00
      X=ZRE
      Y=ZIM
    9 ACCR=0.
      ACCI=0.
   22 IF(X-2.)20,21,21
   20 ACCR=ACCR+.5*LOGF(X**2+Y**2)
      ACCI=ACCI+ATANF(Y/X)
      X=X+1.
      GO TO 22
   21 ZRE1=X
      ZIM1=Y
      DO1 I=1,7,1
      J=8-I
      DENOM= ZRE1*ZRE1+ZIM1*ZIM1
      ZRE2=ZRE1/DENOM*C(J)
      ZIM2=-ZIM1/DENOM*C(J)
      IF(I-7)11,2,2
   11 ZRE1=X+ZRE2
      ZIM1=Y+ZIM2
      GO TO 1
    2 ZRE1=ZRE2
      ZIM1=ZIM2
    1 CONTINUE
      Q3=X-.5
      Q1=.5*LOGF(X**2+Y**2)
      Q2=ATANF(Y/X)
      FZRE=-X+Q1*Q3-Y*Q2+Q4+ZRE1-ACCR
      FZIM=-Y+Y*Q1+Q2*Q3+ZIM1-ACCI
      RETURN
      END
```

References

1. R. G. Jahn, The Physics of Electric Propulsion, McGraw-Hill Book Company, New York (1967).

2. R. H. Goddard, An Autobiography, Robert H. Goddard Notebook dated September 6, 1906; Astronautics 4, 24 (1959).

3. E. Stuhlinger, Ion Propulsion for Space Flight, McGraw-Hill, New York (1964).

4. R. G. Jahn and W. von Jaskowsky, "The Plasma Pinch as a Gas Accelerator," AIAA Paper No. 63013, March 1963.

5. R. G. Jahn and W. von Jaskowsky, "Structure of a Large-Radius Pinch Discharge," AIAA J. 1-8, 1809-1814 (August 1963).

6. R. G. Jahn and W. von Jaskowsky, "Current Distributions in Large-Radius Pinch Discharges," AIAA J. 2-10, 1749-1753 (October 1964).

7. R. G. Jahn, W. von Jaskowsky, and R. L. Burton, "Ejection of a Pinched Plasma From an Axial Orifice," AIAA J. 3, 10 (October 1965).

8. "Pulsed Electromagnetic Gas Acceleration," Eighth Semi-Annual Progress Report, Princeton University, Guggenheim Laboratories for the Aerospace Propulsion Sciences, Report No. 634g (1967).

9. M. Rosenbluth, et al., "Infinite Conductivity Theory of the Pinch," Los Alamos Scientific Laboratory Report LA-1850 (1954).

10. L. A. Artsimovitch, "Controlled Thermonuclear Reactions," p. 127, Gordon Breach, New York (1964).

11. K. Millsaps and K. Pohlhausen, "The Linear Acceleration of Large Masses by Electrical Means," Air Force Missile Defense Center Tech. Rept. 60-11 (June 1960).

12. S. A. Colgate, "Initial Conditions for the Dynamic Pinch," A.E.C. UCRL 4895 (1957).

13. N. A. Black, "Dynamics of a Pinch Discharge Driven by a High Current Pulse-Forming Network," Princeton University Ph.D. Thesis (1966).

14. R. L. Burton, "Structure of the Current Sheet in a Pinch Discharge," Princeton University Ph.D. Thesis (1966).

15. M. Rosenbluth, "Pinch Dynamics," Research Establishment Riso Report No. 18 (1957).

16. G. W. Sutton and A. Sherman, Engineering Magnetohydrodynamics, McGraw-Hill, New York (1965).

References-continued

17. G. G. Chernyi, Introduction to Hypersonic Flow, Translated and edited by R. F. Probstein, Academic Press, New York (1961).

18. G. A. Rowell, "Cylindrical Shock Model of the Plasma Pinch," Princeton University M.S.E. Thesis (1966).

19. J. E. Allen, "An Elementary Theory of the Transient Pinched Discharge," Proc. Phys. Soc. B, 70, 24 (1957).

20. G. C. Vlases, "Experiments in a Cylindrical Magnetic Shock Tube," Caltech Ph.D. Thesis (1963).

21. G. C. Vlases, "Experiments in a Cylindrical Magnetic Shock Tube," J. Fluid Mech. 16, Part 1, 82 (1963).

22. F. Y. Sorrel, "On the Generation of Shock Waves in an Inverse Pinch," Caltech Ph.D. Thesis (1966).

23. S. C. Lin, E. L. Resler, A. R. Kantrowitz, "Electrical Conductivity of Highly Ionized Argon Produced by Shock Waves," J. Appl. Phys, 26, 95 (1955).

24. R. H. Lovberg, Acceleration of Plasma by Displacement Currents Resulting from Ionization, Proc. VI, Int. Conf. on Ionization Phenomena in Gases, Vol. IV, p. 235 (Paris, 1963).

25. R. H. Lovberg, "Inference of Plasma Parameters from Measurement of $\vec{E}$ and $\vec{B}$ Fields in a Coaxial Accelerator," Phys. Fluids 7, 857 (1964).

26. R. H. Lovberg, "Schlieren Photography of a Coaxial Accelerator Discharge," Phys. Fluids 8, 177 (1965).

27. L. C. Burkhardt and R. H. Lovberg, "Current Sheet in a Coaxial Plasma Gun," Phys. Fluids 5, 341 (1962).

28. J. C. Keck, "Current Distribution in a Magnetic Annular Shock Tube," Phys. Fluids 5, 630 (1962).

29. R. B. Johansson, "Current Sheet Tilt in a Radial Magnetic Shock Tube," Phys. Fluids 8, 866 (1965).

30. R. G. Jahn, W. von Jaskowsky, and A. L. Casini, "Gas-Triggered Inverse Pinch Switch," Rev. Sci. Instr. 34-12, 1439-1440 (December 1963).

31. R. G. Jahn, W. von Jaskowsky, and A. L. Casini, "Gas-Triggered Pinch Discharge Switch," Rev. Sci. Instr. 36-1, 101-102 (January 1965).

32. N. Black, "Linear Pinch Driven by a High Current Pulse-Forming Network," AIAA Bulletin 2, 6, 309 (1965).

References-continued

33. "Pulsed Electromagnetic Gas Acceleration," Fifth Semi-annual Progress Report, Princeton University, Guggenheim Laboratories for the Aerospace Propulsion Sciences, Report No. 634d (1965).

34. R. H. Huddlestone and S. L. Leonard, ed., Plasma Diagnostic Techniques, Academic Press, New York (1965).

35. M. A. Heald and C. B. Wharton, Plasma Diagnostics With Microwaves, John Wiley and Sons, New York (1965).

36. Malmstadt, Enke, and Toren, Electronics for Scientists, W. A. Benjamin, Inc., New York (1962).

37. "Pulsed Electromagnetic Gas Acceleration," Sixth Semi-annual Progress Report, Princeton University, Guggenheim Laboratories for the Aerospace Propulsion Sciences, Report No. 634e (1965).

38. S. H. Lam and M. Greenblatt, "Flow of a Collisionless Plasma Over a Cone," AIAA J. 3, 1850 (1965).

39. I. Langmuir and H. M. Mott-Smith, "Studies of Electrical Discharges in Gases of Low Pressure," General Electric Review 27, 449-810 (1924).

40. L. Spitzer, Physics of Fully-Ionized Gases, 2nd ed., Interscience, New York (1962).

41. R. H. Dicke, private communication.

42. E. O. Johnson and L. Malter, "A Floating Double-Probe Method for Measurements in Gas Discharges," Phys. Rev. 80, 58 (January 1950).

43. J. M. Corr, "Double Probe Studies in an 8" Pinch Discharge," Princeton University M.S.E. Thesis (1964).

44. R. G. Jahn, "Interaction of Electromagnetic Waves With Slightly Ionized Gases," Guggenheim Jet Propulsion Center, California Institute of Technology, TN-2, August 1960.

45. S. Chapman and T. G. Cowling, The Mathematical Theory of Non-Uniform Gases," 2nd ed. University Press, Cambridge (1952), Chap. 18.

46. H. Margenau, "Conduction and Dispersion of Ionized Gases at High Frequencies," Phys. Rev. 69, 508 (1946).

47. H. Margenau, "Conductivity of Plasmas to Microwaves," Phys. Rev. 109, 6 (1958).

48. R. G. Jahn, "Microwave Probing of Ionized Gas Flows," Phys. Fluids 5, 678 (1962).

References-continued

49. S. Takeda and M. Roux, "A Method for Measuring High Electron Densities in Plasmas," J. Phys. Soc. Japan 16, 95 (Jan. 1961).

50. T. Tsukishima and S. Takeda, "Microwave Reflection by Uniform Dense Plasmas," J. of Appl. Phys. 33, 3290 (November 1962).

51. S. Takeda and T. Tsukishima, "Microwave Study of Plasmas Produced by Electromagnetically Driven Shock Waves," J. Phys. Soc. Japan 18, 426 (March 1963).

52. S. Takeda and T. Tsukishima, "Microwave Reflection Techniques for Dense Plasma Diagnostics," U. S. National Bureau of Standards Technical Report NBS-256 (March 1965).

53. H. Hermansdorfer, "Measurement of High Electron Densities on a Linear Z-Pinch Using a New Microwave Reflection Probe," Institut für Plasmaphysik Report No. IPP 1/37 (June 1965).

54. J. C. Slater, Microwave Transmission - 1942, Dover Publications, New York (1959).

55. S. Silver, Microwave Antennae Theory and Design, M.I.T. Radiation Lab. Series, Vol. 12, McGraw-Hill, New York (1949).

56. L. J. Chu, "Calculation of the Radiation Properties of Hollow Pipes and Horns," J. Appl. Phys. 11, 603 (1940).

57. F. B. Harris, Jr., "Prediction of Radiation Intensities in the Fresnel and Near-Zone Regions of Microwave Aperture Antennas," RADC-TN-58-252 (October 1958).

58. J. A. Stratton, Electromagnetic Theory, McGraw-Hill, New York (1941).

59. C. G. Montgomery, et al., ed., Principles of Microwave Circuits, M.I.T. Radiation Lab. Series, Vol. 11, McGraw-Hill, New York (1948).

60. S. C. Lin, "Rate of Ionization Behind Shock Waves in Air," AVCO Research Note 170 (December 1959).

61. H. Hermansdorfer, "Untersuchung der Elektronendichte Bein Linearen Pinch mit 8, 7 mm-Wellen," Z. Naturforschg. 15a, 979 (1960).

62. J. A. Ratcliffe, The Magneto-Ionic Theory and Its Applications to the Ionosphere, University Press, Cambridge (1959).

63. K. G. Budden, Radio Waves in the Ionosphere, University Press, Cambridge (1961).

64. J. R. Wait, Electromagnetic Waves in Stratified Media, Pergamon Press, New York (1962).

References-continued

65. V. L. Ginsberg, Propagation of Electromagnetic Waves in Plasmas, translated by Sykes and Taylor, Pergamon Press, New York (1964).

66. M. P. Bachynski, "Nature of Electromagnetic Waves in Nonhomogeneous, Anisotropic Plasmas," Rept. 7-801, 7, RCA Victor Research Laboratories, Montreal (1960).

67. F. A. Albini and R. G. Jahn, "Reflection and Transmission of Electromagnetic Waves at Electron Density Gradients," J. Appl. Phys. 32, 75 (1961).

68. P. Epstein, "Reflection of Waves in an Inhomogeneous Absorbing Medium" Proc. Nat. Acad. Sci. U.S.A., XVI (1930).

69. P. Poincelot, Compt. Rend. 244, 2031, 2298, 3045 (1957).

70. L. S. Taylor, "Electromagnetic Propagation in an Exponential Ionization Density," IRE Trans. AP-9, 483 (1961).

71. L. S. Taylor, "Reflection of Electromagnetic Waves at Electron Density Ramps," J. Appl. Phys. 32, 1796 (1961).

72. L. S. Taylor, "Reflection of a TE Wave from an Inverse Parabolic Ionization Density," IRE Trans. AP-9, 582 (1961).

73. K. T. Yen, "Microwave Reflection by Nonuniform Plasmas with Exponential Electron Distribution," J. Appl. Phys. 35, 290 (1964).

74. C. B. Wharton and D. M. Slager, "Microwave Determination of Electron Density Profiles," J. Appl. Phys. 31, 428 (1960).

75. E. Greene and D. Hornig, J. Chem. Phys. 21, 617 (1953).

76. F. B. Hildebrand, Advanced Calculus for Applications, Prentice-Hall, Englewood Cliffs, N. J. (1963).

77. G. N. Watson, A Treatise on the Theory of Bessel Functions, Cambridge University Press, New York (1952).

78. H. D. Wyemann, Phys. Fluids 3, 545 (1960).

79. E. W. Paxton and R. G. Fowler, Phys. Rev. 128, 993 (1962).

80. J. P. Barach and J. P. Sivinski, Phys. Fluids 7, 1075 (1964).

81. J. P. Barach and J. P. Sivinski, Phys. Fluids 8, 2158 (1965).

82. R. G. Fowler and J. D. Hood, Phys. Rev. 128, 991 (1962).

83. M. A. Heald, private communication.

84. E. L. Ginzton, Microwave Measurements, McGraw-Hill, New York (1957).

References-continued

85. E. A. McLean, et al., Phys. Fluids 3, 843 (1960).

86. R. A. Nelson, Phys. Fluids 8, 23 (1965).

87. R. D. Metford, et al., Nature 196, 32 (1962).

88. A. Haberstitch, Ph.D. Thesis, University of Maryland (1964).

89. D. L. Jones, "Precursor Electrons Ahead of Cylindrical Shock Waves," Phys. Fluids 5, 1121 (September 1962).

90. J. B. Gerardo, et al., "Microwave Studies of Electrically Driven Shock Waves," Phys. Fluids 6, 1222 (September 1963).

91. L. Wetzel, "Far-Flow Approximations for Precursor Ionization Profiles," AIAA J. 2, 1208 (July 1964).

92. H. G. Alstrom, et al., "Precursor and Other Effects in the Electrically Driven Shock Tube," Boeing Scientific Research Laboratories Report DI-82-0321 (1963).

93. Share Program Librarian, IBM, 690 Madison Avenue, New York 22, New York.

94. M. Goldstein and R. M. Thaler, "Recurrence Techniques for the Calculation of Bessel Functions," MTAC, Vol. XIII, No. 66, 102 (April 1959).

95. Wall, Analytic Theory of Continued Functions, p. 364, formula 93.9.

96. National Bureau of Standards, Applied Math. Series 34, Government Printing Office.

97. R. S. DeVoto, "Argon Plasma Transport Properties," Stanford University report SU DAER No. 217 (1965).

98. R. S. DeVoto, "Transport Properties of Ionized Monotomic Gases," Phys. Fluids 9, 1230 (June 1966).

99. R. S. DeVoto, "Transport Properties of Partially Ionized Argon," Phys. Fluids 10, 354 (Feb. 1967).

100. M. A. Uman, Introduction to Plasma Physics, McGraw-Hill, New York (1964).